FIELD, TEXTURAL, AND GEOCHRONOLOGICAL INVESTIGATIONS INTO THE INTRUSION DYNAMICS AND CRYSTALLIZATION HISTORIES OF THE SEPARATION RAPIDS RARE-METAL PEGMATITES, NORTHWESTERN ONTARIO

By

J. Garnet W. Ching

A Thesis

Submitted to the Faculty of Graduate Studies of

The University of Manitoba

In Partial Fulfillment

Of the Requirements For

the Degree of

MASTER OF SCIENCE

Department

of Earth Sciences

University of Manitoba

Winnipeg, Canada

Abstract

The Separation Lake greenstone belt (SLgb) is host to a suite of potentially economic Neoarchean Lithium – Cesium – Tantalum (LCT) complex type, petalite subtype granitic pegmatites (Big Whopper, Big Mack, Snowbank, Glitter and Marko's). Field observations on these pegmatites such as well-developed layering, ptygmatic folds, boudins, and mullions have in the past led investigators to infer that the pegmatites experienced pervasive high-strain deformation after emplacement.

In this study, we reinterpret the field relations between the pegmatites and country rock, incorporate pegmatite microtextures, and date, by the U-Pb method, the time of crystallization to reassess the role of regional-scale deformation in the distribution and morphology of these pegmatites. Uranium-Pb ratios in monazite and titanite were measured, in-situ, by LA-ICP-MS to establish the timing of regional metamorphism and pegmatite intrusion. Monazite in the country rock yields the same age, within error, of the ca. 2650 Ma Separation Rapids pluton and suggests intrusion and metamorphism were coeval in the area. The range of monazite U-Pb ages of ca. 2637 Ma, ca. 2617 Ma, and ca. 2602 Ma indicate that the pegmatites crystallized after metamorphism / deformation and may not be related to one magmatic event.

Field relationships and microtextural data indicate that deformation is induced locally (i.e., not regional) and results from emplacement mechanisms during pegmatite intrusion. The dominant fabric in the country rock is defined by the alignment of hornblende and is cut by the pegmatite. Moreover, all pegmatites have a metasomatic halo of biotite that overprints the S_2 fabric in the country rock. Essentially, the pegmatites acted as viscous indenters into fluidized, weakened, ductile country rock. Recognizing the fact that deformation is not a result of regional-scale deformation has important implications for exploration including: 1) pegmatites need not intrude along structural corridors, 2) the dominant direction of propagation is now oriented subvertical with the surface expression of several pegmatites suggesting the bulk of the intrusions lies buried under the current erosional surface; and 3) undiscovered LCT pegmatites may lie within other segments of metavolcanic rocks along the English River – Winnipeg River subprovincial boundary, as similar emplacement ages across the SLgb and Bird River belt of eastern Manitoba (e.g. Big Mack at ca. 2637 Ma and Tanco at ca. 2640 Ma) may infer continuous mineralization along the boundary.

Acknowledgements

I would like to firstly thank my Advisor, Dr. Alfredo Camacho and co-advisors, Dr. Scott Anderson and Dr. Christian Bohm for their support in the preparation of this thesis. Thank you to J. Chris Pedersen for his wealth of knowledge on the Separation Lake pegmatites and local geology of the area. Thank you to Karen Ferreira for review of this thesis. In addition, thank you to Nicolas Piette-Lauziere and the University of British Columbia – Okanagan for preparatory work, SEM imaging, EBSD analyses and plotting as well as Scott Andrew Dufrane from the University of Alberta at the Centre for Isotopic Microanalysis for completion of the LA-ICP-MS analyses.

This project was funded through the Geological Survey of Canada Targeted Geoscience Initiative (TGI 4) in conjunction with Avalon Advanced Materials.

Many obstacles were overcome and setbacks to success were abundant, but thank you to my partner, Erin Ward, for your continued support as I worked through and completed this thesis.

Table of Contents

List of Figures

List of Tables

1.0 Introduction

Lithium, historically used for ceramic and high-strength glass, has increased in demand in recent years, especially for use in rechargeable batteries in personal electronics and the electrification of our industrial and transportation systems (USGS, 2021; NRCan, 2022). Deemed a critical metal by Natural Resources Canada (NRCan, 2020, 2022), increased exploration and development are required to establish a domestic supply for use in the manufacturing, communications, aerospace, defence, and clean technology sectors. Kesler *et al*. (2012) estimated lithium resources in several mineral deposit types: brines (69%), pegmatites (13%), hectorite and jadarite deposits (11%), and oilfield and geothermal brines (6%). Although relatively minor in relation to brines, pegmatite deposits provide wider geographic distribution to insulate against supply disruptions, possess market flexibility and contain other critical metals as byproducts (Kesler *et al*., 2012). While pegmatite deposits account for 25% of the world's lithium production, they also provide 10% of beryllium, the majority of tantalum, and all the cesium production (USGS, 2011; Bradley *et al.*, 2017).

Rare-element–enriched pegmatites are categorized broadly as belonging to either the lithium-cesium-tantalum (LCT) or niobium-yttrium-fluorine (NYF) compositional classes or a mixed LCT-NYF class (Cerny and Ercit, 2005). LCT pegmatites, considered to be derived from extreme fractionation of mostly S-type orogenic granites, can be highly enriched in not only lithium, cesium and tantalum, but also rubidium, beryllium, tin, niobium (Tantalum>Niobium), boron, phosphorus and fluorine (London, 2008, 2016). Spodumene, petalite and lepidolite are the principal ore minerals of lithium in pegmatite deposits, whereas pollucite and columbite-tantalite represent the main ore minerals of cesium and tantalum-niobium, respectively. Beryl, once the

main source of beryllium, is still used as an indicator mineral for prospective fertile granitoids (Breaks *et al*., 2003; Selway *et al*., 2005).

In Canada, nearly all production of tantalum, lithium and cesium is derived from LCT pegmatites (Sinclair, 1996). The best-known LCT pegmatite is the world-class TANCO pegmatite in southeastern Manitoba (Figure 1.1). Mined by Tantalum Mining Corp. of Canada Ltd. since 1969, currently a wholly-owned subsidiary of Sinomine Resource Group Co. Ltd., the mine is the world's largest supplier of cesium, and produces spodumene and columbite-tantalite concentrates. Pre-production reserves totalled 2.07 Mt at 0.216% Ta_2O_5, 7.30 Mt at 2.76% Li_2O, 0.35 Mt at 23.3% Cs_2O, 0.92 Mt at 0.20% BeO, 0.78 Mt of quartz, and additionally, 0.11 mt Li_2O and 3% Rb_2O in lepidolite (Cerny *et al.*, 1996, 1998). TANCO is part of the Winnipeg River – Cat Lake pegmatite field in the Bird River supracrustal belt, Bird River Subprovince (Card and Ciesielski, 1986). Linked by a thin, continuous septum of greenstone to the Bird River belt, the Separation Lake greenstone belt (SLgb) forms the thickest part of the Bird River Subprovince east of the Manitoba – Ontario border (Fig. 1.1; Sanborne-Barrie, 1988). In the SLgb, granitoids hosting beryl were first noted by Stockwell (1932) and LCT pegmatites first reported by Breaks (1993). Mineral exploration by Champion Bear Resources (L. Chastko, pers comm. to C.E. Blackburn *in* Breaks, 1993) and reconnaissance mapping by the Ontario Geological Survey in 1992 resulted in the discovery of numerous LCT pegmatites in the SLgb. These pegmatites comprise the Separation Rapids pegmatite field and constitute the greatest known resource of petalite in Ontario (Cerny, 1989a; Breaks and Tindle, 1996a, 1996b, 1997; Breaks *et al.*, 1999; Cerny and Ercit, 2005; Cerny *et al.*, 2012).

The foremost known intrusion in this pegmatite field is the Big Whopper which hosts measured and indicated resources of 8.41 Mt at 1.41% Li_2O and inferred resources of 1.79 Mt at

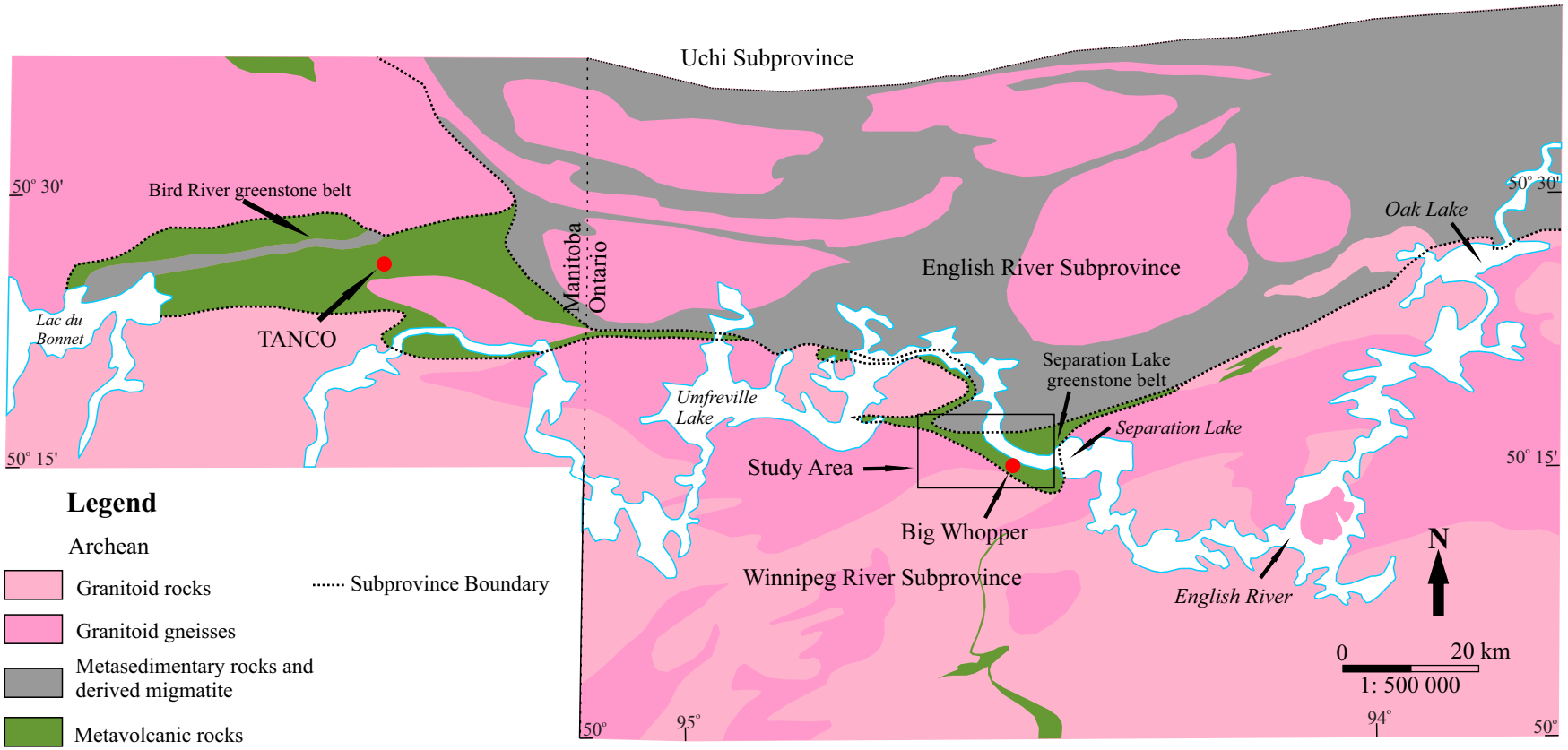

Figure 1.1 Regional Geology, *modified from* Sanborne-Barrie (1988). The Bird River and Separation Lake greenstone belts are components of the Bird River Subprovince (Card and Ciesielski, 1986). TANCO and the Big Whopper (red dots) are the largest known pegmatites in the Bird River Subprovince.

1.35% Li_2O (Gowans *et al.*, 2018). Additional drilling in 2023 has increased the measured and indicated resources to 10.08 Mt at 1.35% Li_2O and inferred resources of 2.81 Mt at 1.38% Li_2O (Avalon Advanced Materials, [News Release], 2023). Several other petalite-bearing intrusions of lesser size include the Glitter, Big Mack, Snowbank, and Marko's pegmatites. These pegmatites are described in OGS (Breaks and Tindle, 1994, 1996a, 1996b, 1997; Breaks and Pan, 1995; Tindle *et al.*, 1998; Tindle and Breaks, 1998, 2000a, 2000b) and industry reports (Galeschuk, 1998; de la Fuente, 1998; Pedersen, 1998, 2017; Pedersen *et al.,* 2018; Sears and Pryslak, 1999, 2001; Chastko, 2001; Pryslak and Chastko, 2001; Aiken *et al.*, 2016; Clark and Siemieniuk, 2016; Gowans *et al.*, 2018).

Guidelines for exploration and evaluation of LCT pegmatites in the Bird River and Separation Lake greenstone belts have been summarized by Truman and Cerny (1982), Selway *et al*. (2005), and Galeschuk and Vanstone (2005, 2007). Developed largely during exploration in the Winnipeg River – Cat Lake pegmatite field in southeastern Manitoba, these guidelines provide a framework for prospect generation. The first step in LCT pegmatite exploration involves identification of the potential for fertile source granitoids in mafic metavolcanic or metasedimentary host rocks (Selway *et al*., 2005). These S-type granitoids may contain green muscovite, garnet, tourmaline, apatite, cordierite, and rare andalusite and topaz (Cerny, 1989a, b; Breaks and Tindle, 1997, Breaks *et al*., 2003). Textures may include graphic K-feldspar or graphic muscovite that form plumose books in outcrop (Selway *et al*., 2005). More highly evolved granitoids may contain beryl. Pegmatites commonly define regional mineralogical or geochemical zonation around the exposed or inferred source granitoid with the greatest enrichment in rare elements up to 10 km from the intrusion (Trueman and Cerny, 1982).

Additional challenges occur where the granitoid source and/or pegmatites are buried, as they typically do not possess distinctive geophysical signatures and are thus not conducive to geophysical exploration techniques (Trueman and Cerny, 1982; Galeschuk and Vanstone, 2005, 2007; Selway *et al.,* 2005; Bradley *et al*., 2017). LCT pegmatites typically lack significant concentrations of magnetic minerals, conductive metallic minerals and terrane dependant density/mass contrast with the country rock, thus making most common geophysical methods of exploration of limited practicality (Trueman and Cerny, 1982). For pegmatites that lack a surface expression, lithogeochemical and biogeochemical surveys may assist in pegmatite discovery (Galeschuk and Vanstone, 2007).

Pegmatites within the SLgb have been widely interpreted by previous authors to have experienced extensive solid-state deformation based on the presence of complex fold geometries, mylonites, boudins, tectonic layering, and "flame and mullion" structures (Breaks and Tindle, 1994, 1996a, 1996b, 1997; Barclay, 1998; Galeschuk, 1998; Pedersen, 1998, 2017, 2018; Breaks *et al.*, 1999; Sears and Pryslak, 1999, 2001; Chastko, 2001; Aiken *et al.*, 2016; Clark and Siemieniuk, 2016; Gowans *et al.*, 2018). This interpretation requires that pegmatite emplacement occurred prior to or during regional deformation. Hence, the analysis of deformation structures has strongly influenced predictive exploration strategies for pegmatites in the belt. For example, the current exploration model is applied under the premise that overprinting fabrics can be used to search for undiscovered LCT pegmatites in the SLgb (Pedersen, 1998; Barclay, 1998). In contrast, de la Fuente (1998, *in* Galeschuk, 1998) recognized pegmatite intrusions that cross-cut regional folia in the SLgb, including the Big Whopper, and suggested that crystallization of some pegmatite phases post-date regional-scale deformation and metamorphism.

The main objectives of this thesis are to document the nature and extent of solid-state deformation that the pegmatites of the SLgb may have experienced, in order to constrain the mechanisms and controls on pegmatite emplacement and inform exploration models for pegmatites in the SLgb. Documentation of pegmatite morphology and geometry may also help understand intrusion mechanisms and structural controls, which would have important implications for resource modeling and estimation. In order to meet these objectives, the following aspects are the main focus of this study:

(1) determine the nature and extent of solid-state deformation in pegmatites of the SLgb, by qualitative field and petrographic studies, coupled with quantitative electron back-scatter diffraction (EBSD) analyses;

(2) document the crystallization histories of the rare-element enriched intrusions of the SLgb, using *in-situ* U-Pb geochronology; and

(3) define the timing of metamorphism and associated deformation within the SLgb, through *in-situ* U-Pb geochronology of mineral growth phases associated with deformation.

To make these determinations, data were collected from two fertile granitoids (the Skidder and Separation Rapids pluton), five lithium pegmatites (the Big Whopper, Big Mack, Snowbank, Glitter and Marko's), and a deformed aplite northwest of the Big Whopper.

Chapter 2 Geological Setting

2.1 Regional Geology

The Separation Lake greenstone belt (SLgb) represents a collection of attenuated lenses of metavolcanic and metasedimentary rocks that define, in part, the Bird River Subprovince of the Superior Province of the Canadian Shield (Card and Ciesielski, 1986). The Bird River Subprovince is bounded to the north by metasedimentary rocks, migmatites, and felsic plutonic rocks of the English River Subprovince, and to the south by the felsic to intermediate plutonic rocks of the Winnipeg River Subprovince (Beakhouse, 1977, 1991; Breaks, 1991). Deformation and metamorphism at amphibolite-facies has influenced, to some extent, the original textures and structures of the rocks of the Bird River, English River, and Winnipeg River Subprovinces. Nevertheless, preservation of original textures and structures has permitted previous workers to use pre-metamorphic nomenclature to describe the rocks; this practice is used herein.

The rocks of the English River Subprovince are predominantly clastic sedimentary rocks with subordinate metaluminous diorite, tonalite and granodiorite intrusions, migmatites, and peraluminous granitic rocks (Breaks, 1991; Breaks and Bond, 1993; Corfu *et al.*, 1995). Greywacke and mudstones, ca. 2720 – 2705 Ma (Corfu *et al.,* 1995), sourced from the Uchi Subprovince farther to the north form the sedimentary rocks of the English River Subprovince (Fig. 1.1; Breaks, 1991; Breaks and Bond, 1993). The youngest age of sedimentation in the English River Subprovince is limited by *ca.* 2698 Ma dioritic to granodioritic intrusions (Corfu *et al.*, 1995). Deformation commenced during the Kenoran orogeny (2717- 2650 Ma; Melnyk *et al.*, 2006) along the boundary between the English River and Winnipeg River Subprovinces with folding and intrusive activity *ca.* 2698 Ma, followed by the development of a major east-west, subvertical

fabric and dextral shear zones along the Uchi – English River boundary to at least ca. 2650 Ma (Corfu *et al.*, 1995; Hrabi and Cruden, 2006; Melnyk *et al.,* 2006). Coeval with east-west fabric development, peraluminous granite and migmatite formed by partial melting of the metasedimentary rocks of the English River Subprovince (Corfu *et al.*, 1995). Protracted metamorphism at ~5.4 kbar and ~725-750ºC (Breaks *et al*., 1978; Breaks, 1991) occurred at ca. 2687 Ma and ca. 2669 Ma (Corfu *et al.*, 1995). This influx of heat is proposed by Hrabi and Cruden (2006) to have resulted from a period of extension in the English River Subprovince. Late, retrograde, dextral, transcurrent faults (<2663 Ma) are recorded as discrete mylonitic zones along its northern boundary with the Uchi and as variably broad zones along its southern boundary with the Winnipeg River Subprovince (Breaks *et al.*, 1978; Breaks, 1991; Breaks and Bond, 1993; Hrabi and Cruden, 2006).

The Winnipeg River Subprovince is dominated by gneissic and plutonic tonalitic rocks ranging in age from *ca.* 3200 to 2800 Ma (Fig. 1.1; Beakhouse, 1991; Corfu *et al.*, 1995) and dioritic to granitic plutons emplaced between *ca.* 2710 and 2690 Ma (Corfu *et al.*, 1995). Supracrustal remnants of massive to pillowed basalt and iron-bearing sedimentary rocks are the oldest rocks within the Winnipeg River Subprovince, deformed and metamorphosed under peak amphibolite- or granulite-facies conditions. The Kenoran orogeny (*ca.* 2717– 2650 Ma) tectonically thickened the Winnipeg River Subprovince by large thrusts and folds (Melnyk *et al.*, 2006). Associated metamorphic conditions reached ~630-800ºC and ~4-7 kbar and were coupled with a 40 m.y. period of granodioritic to granitic plutonism (Beakhouse, 1991; Corfu *et al.*, 1995; Menard *et al.*, 1997; Melnyk *et al.*, 2006).

The Bird River Subprovince extends from the Bird River greenstone belt in Manitoba eastwards through the SLgb to Oak Lake and beyond to Lac Seul in Ontario (Fig. 1.1; Blackburn

and Young, 1993, 2000; Breaks and Tindle, 1996a, 1996b; Breaks *et al.*, 1999; Card and Ciesielski, 1986). The Bird River Subprovince is defined by attenuated belts of supracrustal rocks that are typically less than ~200 m thick, except near the Bird River where the main belt is ~60 km long and up to ~8 km thick, and at Separation Lake where it is ~45 km long and up to ~5 km thick (Beakhouse, 1991; Blackburn and Young, 2000). The Bird River belt contains the greatest lithologic diversity in the Bird River Subprovince and includes MORB-like basalt, andesite, dacite and rhyolite, volcano-sedimentary rocks, and orogenic sediments that include marine turbidites and fluvial-alluvial sandstone and conglomerate; gabbroic and granitoid intrusions are voluminous and diverse (Trueman, 1980; Cerny *et al.*, 1981; Gilbert, 2008; Gilbert *et al.*, 2008). Continental arc magmatism over an ~80 m.y. period (ca. 2800-2720 Ma) was followed by a period of orogenic sedimentation from ca. 2710 to 2700 Ma (Gilbert *et al.,* 2008).

The Winnipeg River – Cat Lake pegmatite field is notable in the Bird River belt, with highly fractionated LCT and NYF pegmatites documented with crystallization of the TANCO pegmatite ca. 2640 Ma (Baadsgard and Cerny, 1993; Camacho *et al*., 2012). Further details of the geology and pegmatite mineralization in the Bird River greenstone belt can be found in Trueman (1980), Cerny *et al.* (1981), Gilbert (2008), Gilbert *et al.* (2008), and references therein. Less diverse, yet still interpreted to be linked to the Bird River belt (Beakhouse, 1991), the SLgb consists mainly of subaqueous massive to pillowed basalt flows overlain by felsic volcanic rocks and at least three sequences of clastic sedimentary rocks (Blackburn and Young, 2000). Late granitoid intrusions, including LCT pegmatites, are voluminous in the SLgb as well, and are described further below. The Bird River belt has experienced at least three generations of deformation and associated metamorphism attaining amphibolite facies at approximately 550ºC and 4-5 kbar (Gilbert *et al*., 2008). Metamorphic mineral assemblages include hornblende-biotite-

cummingtonite-garnet in mafic rocks, and biotite-garnet-cordierite in felsic rocks, like assemblages documented in the SLgb (Section 2.2; Blackburn and Young, 2000; Blackburn *et al*., 2008; Gilbert *et al*., 2008). The Bird River greenstone belt and the SLgb are connected by a thin, laterally continuous septum of mafic volcanic rocks, minor chert, and chemical sedimentary rocks (Fig. 1.1; Beakhouse, 1991).

2.2 Separation Lake greenstone belt

The SLgb forms the thickest segment of the Bird River Subprovince east of the Manitoba – Ontario border. The rocks of the SLgb consist of pillowed to massive basalt flows with subordinate felsic volcaniclastic rocks and at least three clastic sedimentary sequences (Figure 2.1; Blackburn and Young, 1993, 2000; Blackburn *et al.*, 2008). Pillows, where preserved, are interpreted by Blackburn and Young (2000) to indicate a northerly tops direction. Synvolcanic medium- to coarse-grained mafic sills intrude multiple levels in the stratigraphy and cut a unit of chert-magnetite iron formation near the centre of the belt east of the Separation Rapids pluton (Fig. 2.1; Blackburn and Young, 1993, 2000). Iron formation crops out as ~1 to 5 m thick units interspersed with mafic volcanic lenses (Blackburn and Young, 2000).

At least three units of clastic sedimentary rocks are documented in the SLgb: (1) feldspathic arenite to wacke, (2) alternating sandstone and conglomerate, and (3) conglomerate (Blackburn and Young, 2000). The third unit of sedimentary rocks crops out along the north contact of the SLgb with the English River Subprovince and contains clasts of volcanic rocks, chemical sedimentary rocks, and intrusive and extrusive phases of felsic composition, but does not contain clasts of LCT pegmatite (Blackburn and Young, 2000).

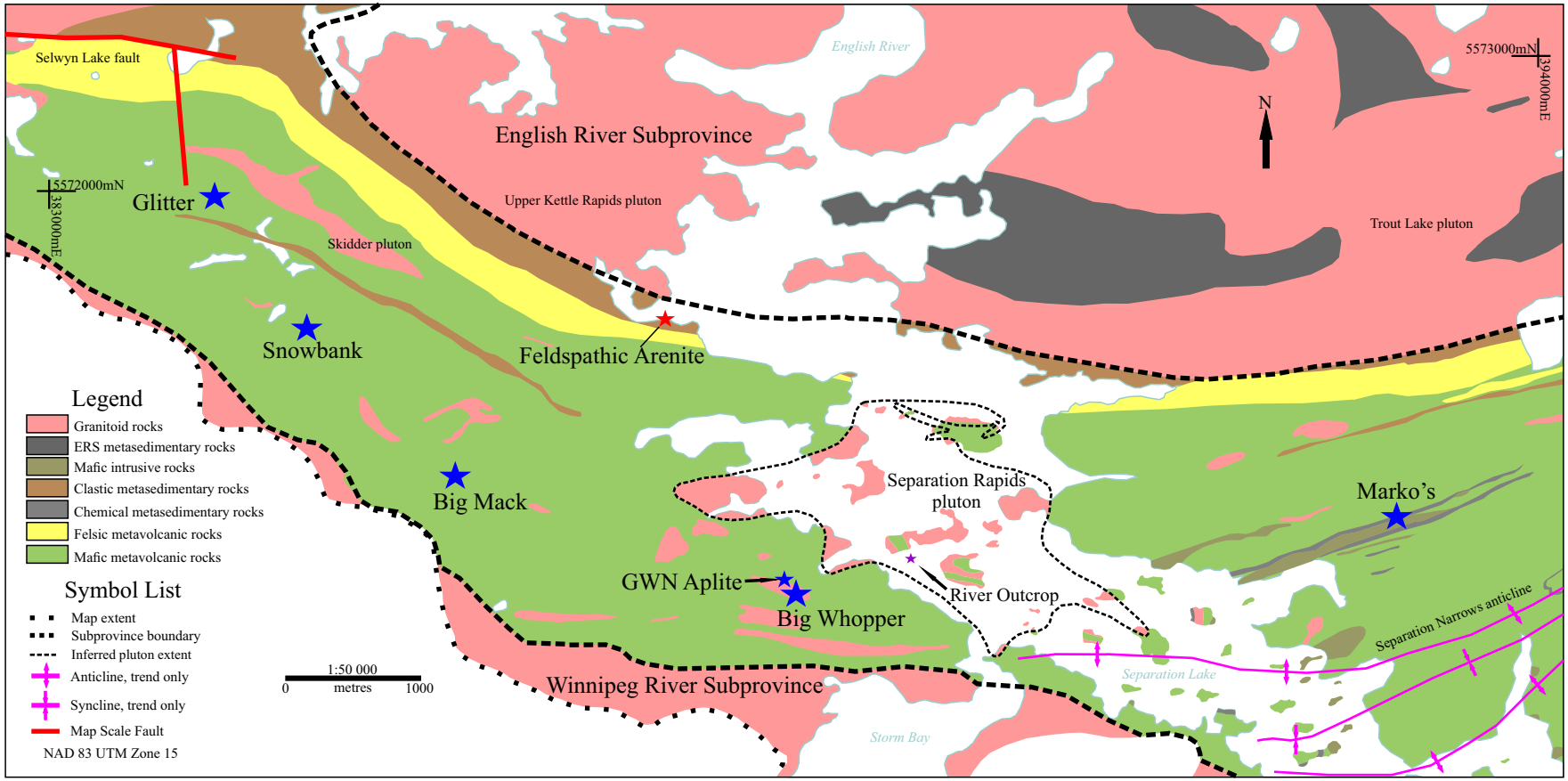

Figure 2.1 Simplified geology of the Separation Lake greenstone belt, *modified after* Blackburn *et al.* (2008). Locations of the five study pegmatites and Great White North (GWN) aplite outcrop given by blue stars. River outcrop location given by purple star.

Granitoid rocks constitute a minor component of the SLgb and are dominated by the Separation Rapids pluton and its presumed, associated pegmatites (Fig. 2.1; Blackburn and Young, 1993, 2000; Blackburn *et al.*, 2008). Breaks and Tindle (1997) and Pan and Breaks (1997) suggested a link between granulite-metamorphism facies with the formation of migmatites in the English River Subprovince and rare-element bearing pegmatites in the SLgb. They made this link based on geochemical similarities in (1) cesium content and potassium/rubidium in K-feldspar and (2) neodymium and erbium anomalies in chondrite-normalized REE patterns. The Treelined Lake granitic complex of which the Upper Kettle Rapids and Trout Lake plutons are members (Fig. 2.1), crop out along the northern margin of the SLgb and are interpreted to be derived from this partial melting event. These intrusions are thought to be the source melts for to the Separation Rapids pluton (2646 ± 2 Ma; Breaks and Tindle, 1997; Pan and Breaks, 1997; Larbi *et al.*, 1999), from which the rare-element pegmatites of the SLgb are thought to be derived (Breaks, 1993; Breaks and Tindle, 1996a, 1996b, 1997; Pan and Breaks, 1997; Tindle and Breaks, 1998, 2000a, b; Selway *et al.*, 2005).

Investigations into the deformation and metamorphism of the SLgb are sparse in literature; a preliminary framework for deformation in the SLgb is provided by Blackburn *et al*. (1992) and Blackburn and Young, (1993). Additional work by Blackburn and Young (2000) and Blackburn *et al*. (2008) further refined the structural framework for the belt. Regional metamorphism in the SLgb attained amphibolite facies, as indicated by the presence of hornblende in the mafic metavolcanic and intrusive rocks (Blackburn and Young, 2000). The degree of deformation increases from south to north in the SLgb, achieving peak intensity at the contact between the SLgb and the English River Subprovince (Blackburn and Young, 2000).

Composite east-trending subvertical fabrics within the SLgb have been interpreted to reflect three deformational events, with a fourth low-grade brittle event documented in the northwest part of the project area near Selwyn Lake (Fig. 2.1; Blackburn and Young, 2000). The first event resulted in a foliation (S_1) that occurs subparallel to pillow layering in basalt (Blackburn and Young, 2000). Hornblende growth in the plane of S_2 during F_2 folding overprints the S_1 foliation. Composite S_1 and S_2 fabrics dip steeply south, locally documented by Blackburn and Young (2000) to be at low angle to each other on the limbs of major F_2 folds. Blackburn and Young (2000) interpret F_2 mineral lineations that plunge 45-70^o to the west to be spatially associated with the Separation Narrows anticline (Fig. 2.1). Barclay (1998) inferred that emplacement of rare-element pegmatites in the SLgb was coeval with D_2, based on observation of S_2 fabrics aligned subparallel to planar elements in the pegmatites.

Late brittle faults (D_3) juxtaposed migmatites of the English River Subprovince with sediments and volcanic rocks of the SLgb, including the Selwyn Lake fault in the northwest part of the project area (Fig. 2.1; Blackburn and Young, 2000; Blackburn *et al.*, 2008). A second brittle event (D_4) recorded by three north-northeast striking faults at high angle to the Selwyn Lake fault is documented by Blackburn and Young (2000), who suggested vertical movement to be dominant (Fig. 2.1, upper left). North-trending faults are present elsewhere in the SLgb; one example is located near the northwest part of the study area, but these faults are otherwise absent. These faults form west-facing scarps and do not offset the Selwyn Lake fault, leading Blackburn and Young (2000) to infer that vertical movement dominated during D_4.

2.3 The Separation Rapids Pegmatite Group

The pegmatites that are the subject of this study are members of the Separation Rapids Pegmatite Group (Fig. 2.1) and are classified as members of the LCT family of rare-element

pegmatites (Breaks, 1993). Following the classification of Cerny (1991), Cerny and Ercit (2005), and Cerny *et al*. (2012), these pegmatites are considered to belong to the 'complex type' of the rare-element class of pegmatites, signifying that they have substantial proportions of lithium aluminosilicate minerals; this type of pegmatite has the most evolved internal zonation and most extreme levels of magmatic fractionation. Further, the Separation Rapids pegmatites are part of the 'petalite subtype' of complex rare-element pegmatites. Pegmatites of this subtype are enriched in Li, Rb, Cs, Be, Ta>Nb and, to a lesser extent, Sn, P, F, ± B. As the name implies, petalite is its dominant lithium aluminosilicate mineral, typically with beryl, columbite-tantalite and lesser amblygonite, lepidolite and pollucite. Investigations into the mineralogy of the pegmatites of the SLgb have led previous authors to infer that the Separation Rapids Pegmatite Group constitutes the eastern limit of the Cat Lake – Winnipeg River pegmatite field (Tindle and Breaks, 1998, 2000a, 2000b; Tindle *et al.*, 1998). Tindle *et al.* (1998) documented a wide range of compositions in wodginites in the SLgb, with a comparable spread recorded only at the Tanco pegmatite.

Pegmatites of the SLgb exhibit internal zonation common to other rare-element pegmatites, including well-developed 1–10 cm thick wall zones that transition into petalite-rich intermediate zones (Pedersen, 1998, 2017; Breaks *et al.,* 1999; Aiken *et al.*, 2016; Gowans *et al.*, 2018). The bulk of the Big Whopper comprises petalite-bearing zones subdivided based on composition and texture (Gowans *et al.*, 2018). Other intermediate zones of the Big Whopper comprise coarse to megacrystic K-feldspar in an albite or K-feldspar–muscovite–quartz or quartz–muscovite groundmass. Both petalite and intermediate zones, including K-feldspar zones, are several to 10's of metres thick (Pedersen, 1998; Aiken *et al*., 2016). Fine- to medium-grained, equigranular, aplitic albitite dikes commonly <1m thick and up to 10's of metres in length are present near all pegmatites.

Tindle and Breaks (1998, 2000a, 2000b) and Tindle *et al.* (1998) proposed that the Separation Rapids pluton and most petalite-bearing pegmatites in the SLgb followed a Fe-rich evolution with the Mn-rich evolutionary path represented primarily by the Marko's pegmatite, which is the only pegmatite known to have pollucite in the SLgb (Breaks and Tindle, 1997, 2002). To explain this variation in the Separation Rapids Pegmatite Group, three hypotheses have been proposed: (1) a layered source magma chamber, (2) successive batches of evolved F-rich melts in the Separation Rapids pluton, or (3) a potential source magma independent of the Separation Rapids pluton (Tindle and Breaks, 1998; Tindle *et al.*, 1998). Crystallization histories have received little attention in literature: Table 2.1 summarizes data from Smith *et al*. (2004) but is inconclusive to discriminate among those hypotheses. Establishing crystallization histories as part of this thesis (see Section 5.2.2) may provide additional information.

Table 2.1. Age determinations in columbite-tantalite in pegmatites of the SLgb; pegmatite classification of Tindle and Breaks, (1998, 2000). Data compiled from Smith *et al* . (2004).

Intrusion	Age (Ma)	MSWD
Fe – Suite beryl pegmatite	2649 ± 5	2.5
Mn – Suite pegmatite (Marko's)	2644 ± 7	29
Pegmatitic segregation of the Separation Rapids pluton	2629 ± 1.5	0.22
Deformed pegmatite, (Big Mack)	Inconclusive	-

Chapter 3 Methodology

In this study, field and microtextural observations and electron back-scatter diffraction (EBSD) analyses were used to assess intrusion mechanisms and solid-state deformation histories. Specimens were selected from four locations internal and external to pegmatites: (1) across internal layering in coarse-grained to pegmatitic domains, (2) in fine-grained marginal domains, (3) across contacts between pegmatite and wallrock, and (4) across contacts where strain would most likely have accumulated during deformation, such as across boudins, folded dikes, or thin attenuated dikes. In addition, U-bearing minerals were analysed *in-situ* by laser ablation inductively coupled mass spectrometry (LA-ICP-MS) to determine the timing of pegmatite crystallization and regional metamorphism. Monazite is utilized to establish the crystallization histories of the pegmatites. To supplement, or where monazite is absent, analyses of wodginite, zircon, cassiterite or microlite were completed. The crystallization history was also analyzed for an aplite dike (GWN Aplite, Fig. 2.1) from northwest of the Big Whopper, using both monazite and cassiterite. Specimens used to determine the timing of regional metamorphism were selected to locate syn-kinematic growth of suitable phases distal and adjacent to pegmatite intrusions, represented by monazite in biotite feldspathic arenite and titanite calc-silicate zones in basalt.

3.1 Field work

3.1.1 Project location

Field investigations took place over several trips to the property from June 2018 through September 2020. Observations were recorded in both field books and using the FieldMove Clino app. Field observations include lithology, mineralogy, textures, primary structures, deformation structures and contact relationships of the pegmatites and wall-rocks. Digital photographs and rock

specimens were collected for subsequent petrographic, geochronological, and microstructural analyses. In the summer of 2019, imaging of the pegmatite outcrops was completed by aerial drone.

Property access is via all-weather roads north of Kenora, Ontario (Figure 3.1). Directions to access the property from the intersection of Highway 17A and Highway 658 are as follows: travel north 23km and turn left at the English River Road junction (398550E 5536013N 15U); then travel north along English River Road, turn left near the 65 km marker at the junction with Sand Lake Road (390984E 5562824N 15U); continue 5.2 km west to the Avalon Road junction (386926E 5563916N 15U); turn right on Avalon Road and continue 8km to the Big Whopper pegmatite. Access to all pegmatites can then be completed by ATV on overgrown logging roads. Secondary access can be made by boat from the Separation Rapids Campground boat launch, located 6 km farther north from the intersection of Sand Lake Road and English River Road.

3.2 Petrography

A total of 128 standard 30 μm thin-sections were produced by Spectrum Petrographics in Vancouver, Washington and Precision Petrographics in Vancouver, Canada. Samples were oriented in the field for petrographic and structural observation. Sample specimens were cut either orthogonal to the contact zone, in vertical profile and in plan, or in the kinematic reference frame. The kinematic reference frame is perpendicular to the foliation (XY plane of the finite strain ellipsoid) and parallel to the stretching lineation (parallel X-direction).

Optical microscopy was completed utilizing a camera-equipped Leica ICC50 W microscope. Mineral assemblages, textural relationships, and deformation textures (if any) were recorded for each thin-section. Textural observations were completed for individual intrusions to identify features characteristic of magmatic crystallization or tectonic deformation in each

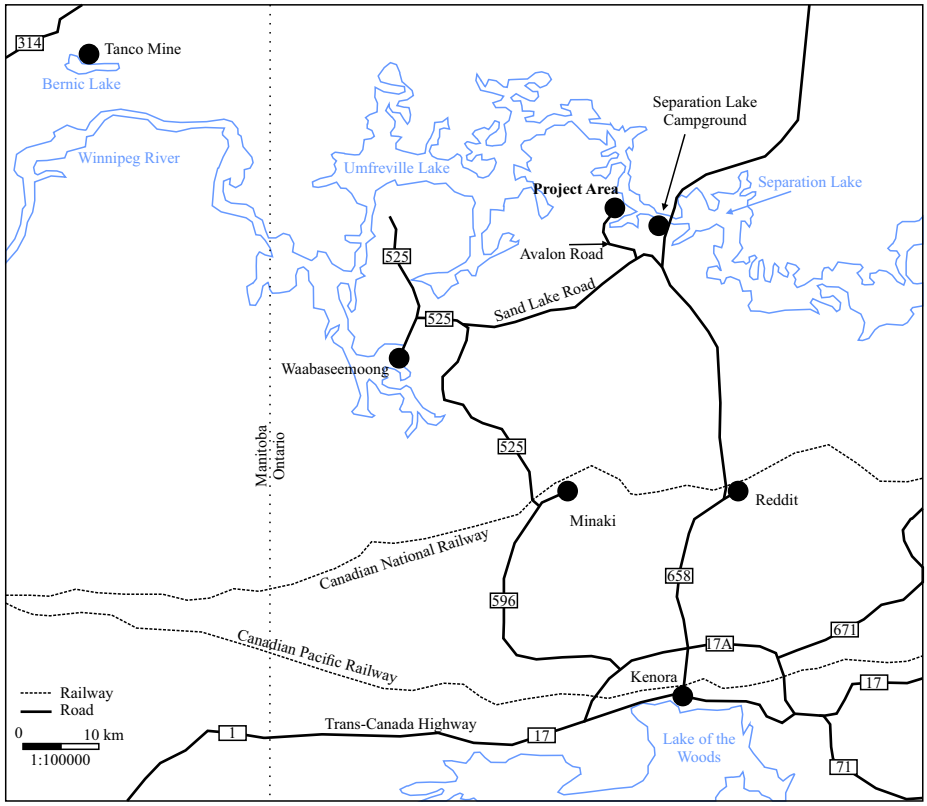

Figure 3.1 Project area location map. *after* Pedersen (1998).

pegmatite and to compare the various pegmatites examined in this study. Spots for EBSD and U-Pb analyses were selected during optical microscopic examination.

3.3 Electron Back-Scatter Diffraction

Thin sections were polished with 0.05 μm alumina suspension using an ATM Saphir Vibro-polisher for three hours, then coated with 6 to 10 nm of graphite. The analytical sites were contoured with copper tape to enhance conductivity on the surface of the specimen and counter charging. The specimens were mapped using a Tescan Mira 3 XMU Field Emission Scanning Electron Microscope (SEM) equipped with an Oxford Instruments Nordlys electron back-scatter diffraction (EBSD) detector at the Fipke Laboratory for Trace Elements Research (University of British Columbia, Okanagan). The SEM was operated at an acceleration voltage of 20kV, a beam current of 20nA, and at a working distance of 15 to 25 mm. The mapping step size was adjusted between 5 to 20 μm, depending on the specimen grain size, with a bin size of 2x2 or 4x4 and frame averaging of 1 to 2, which were independently adjusted to achieve a mapping speed of less than 40 ms per pixel with quartz and feldspar indexing rate greater than 50%. The maps were then individually de-noised using Channel 5 software (Oxford Instruments), which allowed for the removal of spikes and zero-solution pixels by averaging a value from 7 or 8 neighboring pixels.

Using Matlabs toolbox MTEX 5.1.1 software (Hielscher and Schaeben, 2008), individual grains were sectioned along boundaries with a misorientation angle of 10°, and in combined sections along their twin boundaries. This was followed by plotting of grain maps, quartz and feldspar grain orientation spread (GOS) maps, and lattice orientation pole figures projected in the specimen reference frame. The GOS is an angle calculated from the average angle of deviation in orientation between the individual pixels in a grain and the grain average orientation (Wright *et al*., 2011). The GOS quantifies intragranular strain and is not biased by grain size, step size, or

indexing rate (Cross *et al*., 2017a). Because the most abundant contiguous phases in the thin sections were mapped, it is also a qualitative criterion related to the finite strain recorded by the specimens. Preparatory work, SEM imaging, EBSD analyses and plotting were completed by Nicolas Piette-Lauziere at the University of British Columbia, Okanagan.

3.4 Uranium-Lead geochronological analyses

Minerals selected for analyses in this study include titanite, monazite, zircon, wodginite, microlite, and cassiterite. Minerals were identified on each thin section using optical microscopy and sent to the Canadian Center for Isotopic Micro-analysis (CCIM) at the University of Alberta, where LA-ICP-MS analyses were carried out by Scott Andrew DuFrane using procedures modified from Simonetti *et al*. (2005) and Simonetti *et al*. (2006).

3.4.1 Titanite

The analytical setup consisted of a New Wave UP-213 laser ablation system interfaced with a Nu Plasma MC-ICP-MS equipped with three ion counters for static collection of U-Pb isotopes. The laser was operated at a pulse rate of 4 Hz with a beam diameter of 30 μm at a fluence of ~3 J/cm^2. Ablations were conducted in a He atmosphere at a flow rate of 1 L/min through the cell. Output from the cell was joined to the output from a standard Nu Plasma desolvating nebulizer (DSN). On-peak gas + acid blanks (30 s) were measured prior to a set of 10-20 analyses. Data were collected statistically, consisting of thirty 1 s integrations. Before and after each set of analyses, zircon reference materials and Khan titanite (Kinney *et al*., 1994; Ashton *et al*., 1999) were analysed to monitor U-Pb fractionation, reproducibility, and instrument drift. Mass bias for Pb isotopes was corrected by simultaneously measuring $^{205}Tl/^{203}Tl$ from an aspirated 0.5 ppb Tl

solution (NIST SRM 997) using an exponential mass fractionation law and assuming a natural $^{205}Tl/^{203}Tl$ of 2.3871.

All data were reduced offline using an Excel®-based spreadsheet. Unknowns were normalized to the titanite reference material Khan, and the uncertainties reported are a quadratic combination of (1) the standard error of the measured isotope ratio and (2) the standard deviation of the reference material means. Reproducibility of the Khan reference material is estimated to be ~1% for $^{207}Pb/^{206}Pb$ and 3% for $^{206}Pb/^{238}U$. Data points were discarded if it was obvious that an inclusion contributed to analysis, or if the laser penetrated through the grain leaving insufficient data points for a reliable analysis, or if there was an extreme component of common Pb. All plots were generated using the IsoplotR software of Vermeesch (2018).

3.4.2 Monazite

A similar setup to that for titanite was utilized for monazite analyses. Changes to the MC-ICP-MS setup included the addition of 12 Faraday cups and an adjustment of the beam diameter to 8-16 μm yielding a fluence of ~2 J/cm^2. Before and after each set of analyses, in-house monazite references Western Australia (Ashton *et al., 1999*; Simonetti *et al*., 2006) and 44069 (Aleinikoff *et al*., 2006) were analyzed repeatedly to monitor U-Pb fractionation, reproducibility, instrument drift, and to assess data quality. Unknowns were normalized to Western Australia monazite as the primary reference, and 44069 was treated as an unknown to assess data quality. The uncertainties reported are a quadratic combination of the internal measurement precision and the overall reproducibility of the standards during an analytical session. The long-term 2σ reproducibility for the standards is estimated to be ~1% for $^{207}Pb/^{206}Pb$ and 2% for $^{206}Pb/^{238}U$. The data are not corrected for common Pb due to the difficulty in resolving transient contributions of ^{204}Hg present in Ar gas from ^{204}Pb present in either the crystal and/or the acid + gas blank. Thus, reported ^{204}Pb

values are for informational purposes only, but can be useful for identifying and rejecting samples that have obvious amounts of common Pb.

3.4.3 Zircon, Wodginite, Microlite, and Cassiterite

Analyses were completed with a similar setup to that for monazite. The beam setup was comparable to that for titanite. Before and after each set of analyses, zircon reference materials GJ1 (Jackson *et al*., 2004), LH9415 (Ashton *et al.*, 1999), Plesovice (Sláma *et al*., 2008), and OG1 (Stern *et al*., 2009) were analyzed repeatedly to monitor and correct for U-Pb fractionation, reproducibility, instrument drift, and to assess data quality. Standard reproducibility is estimated at ~1% for $^{207}Pb/^{206}Pb$ and 2% for $^{206}Pb/^{238}U$. As with monazite, ^{204}Pb values are for informational purposes only, but can be useful for identifying and rejecting samples that have obvious amounts of common Pb.

Chapter 4 Field and Microtextural Observations

Field investigations for this study were focused on documenting the structure, kinematics and geometry between granitoid intrusions and their mafic volcanic host rocks (Fig. 2.1). The Skidder and Separation Rapids plutons, as well as a dike swarm that crops out adjacent to the Separation Rapids pluton at the "River Outcrop" (Figure 4.1), were studied to facilitate comparisons to the spatially associated granitic pegmatites (Fig. 2.1). Field work also included investigations of four other pegmatites, incorporating mapping by previous authors: Big Whopper (Figure 4.2; Pedersen, 1998), Big Mack (Figure 4.3; Pryslak and Chastko, 2001), Snowbank (Figure 4.4; Pedersen *et al.*, 2018), and the Glitter pegmatites (Figure 4.5; Sears and Pryslak, 2001). Field and petrographic work here emphasizes the nature of the contacts between the country rock and pegmatites to determine intrusion dynamics and document solid-state deformation structures.

4.1 Mafic volcanic rocks

Subaqueous basaltic flows are the dominant lithology in the SLgb and comprise both pillowed and massive flows. Dark green to dark green-black in outcrop, the basaltic rock has relatively uniform grain sizes of up to 1 mm with rare albite phenocrysts. Pillowed flow thicknesses are difficult to determine with confidence but appear to be on the order of metres to 10's of metres. Pillows, up to a metre long are elongated by deformation in an east-west direction (Figure 4.6). Where preserved, pillows are defined by dark green-black, 1-2 cm thick, fine-grained, recrystallized pillow selvages. Pillow selvages are curvilinear to arcuate and rarely yield reliable top directions. However, at the River Outcrop, pillows indicate top to the west (Fig. 4.6), suggesting that the primary layering is at least locally oblique to the main deformation fabric (S_2). Quartz amygdules are locally up to several centimetres in diameter and may form morphologies similar to dextral σ-type clasts within the plane of S_2. Centimetre-scale lenses and seams of buff

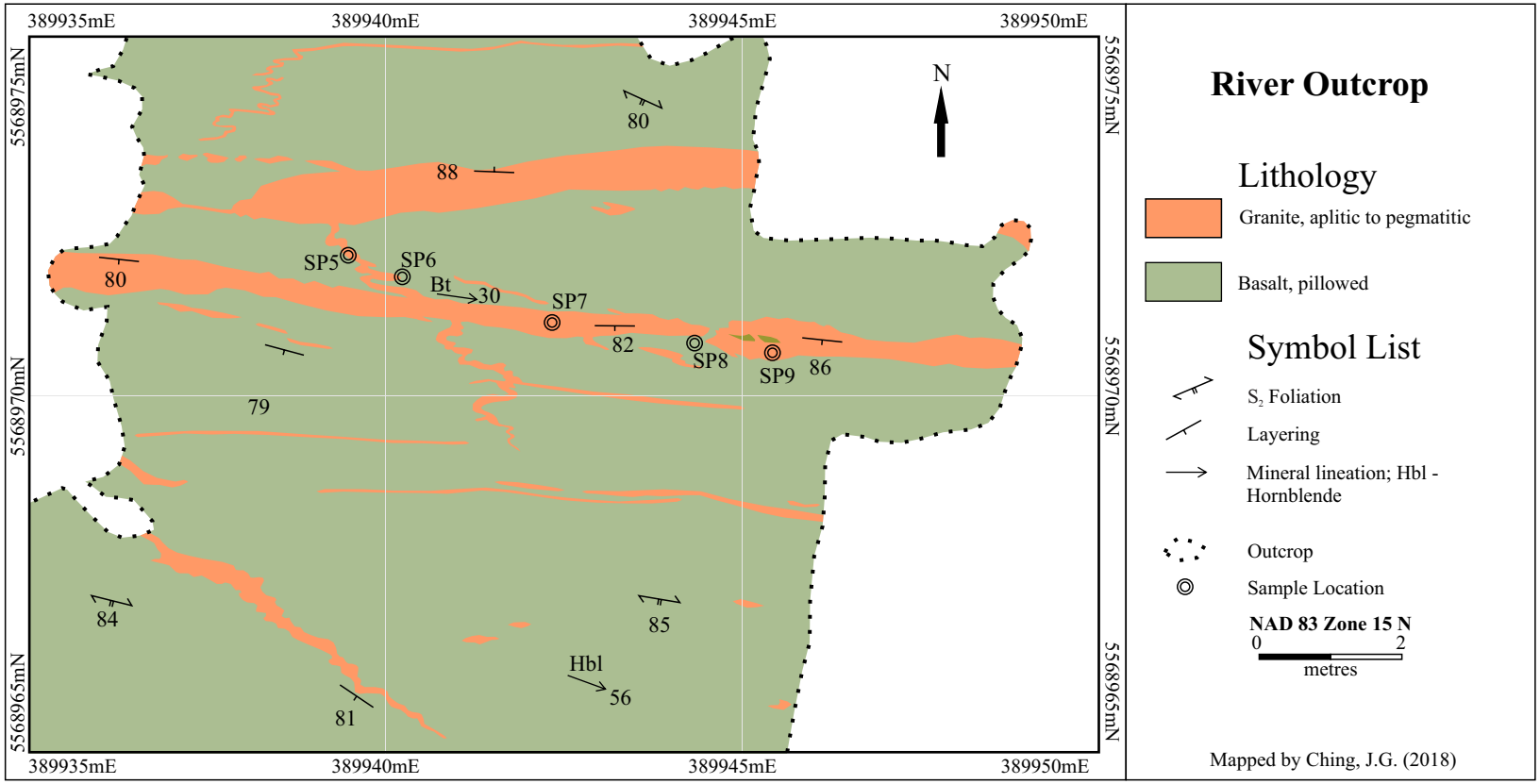

Figure 4.1. Outcrop map of granitoid dikes in basalt along southwestern contact of the Separation Rapids pluton

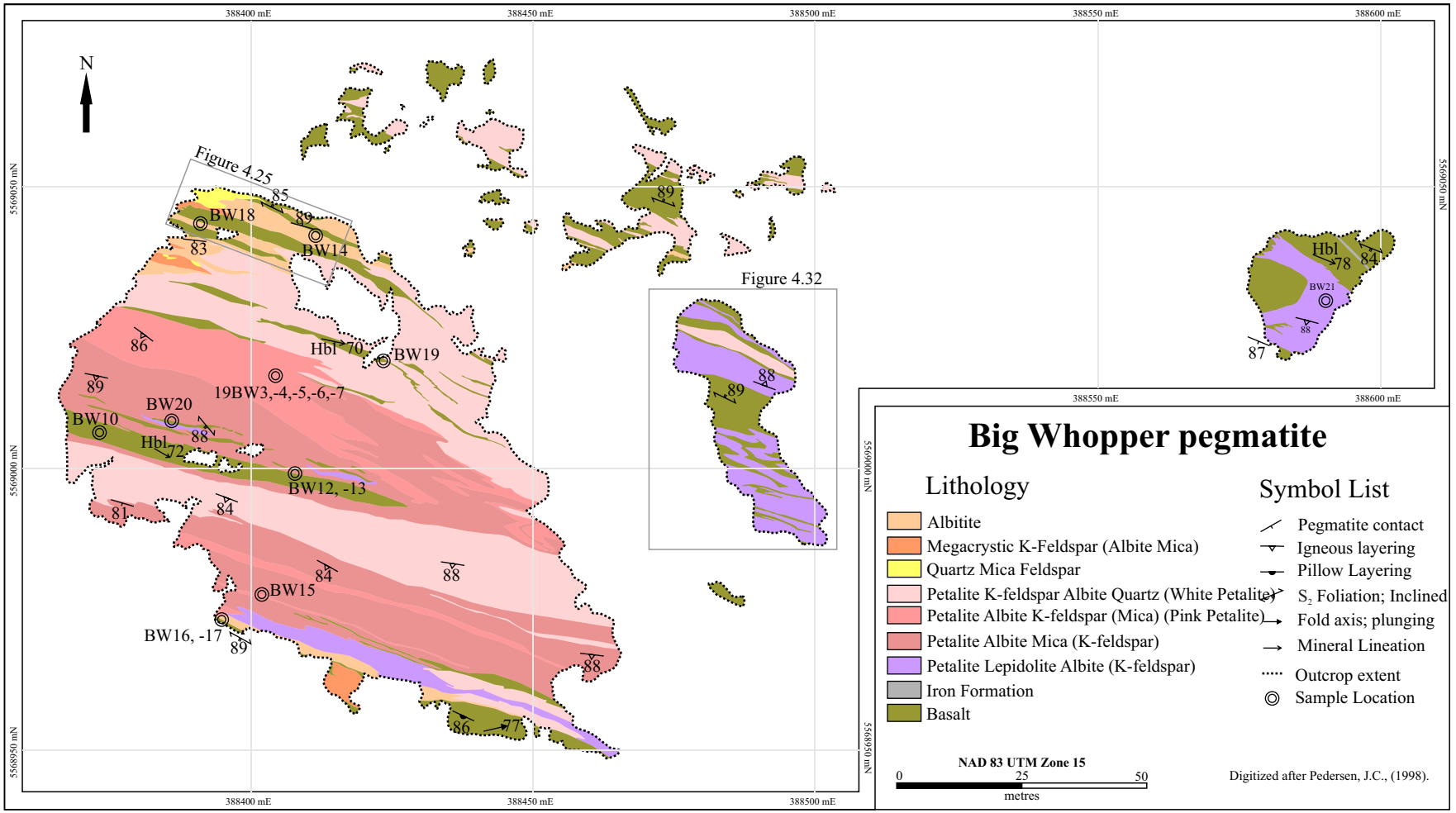

Figure 4.2. The Big Whopper pegmatite. Digitized after outcrop mapping by Pedersen (1998). Labelled rectangles indicate location of two drone images as Figures 4.25 and 4.32 later in this chapter.

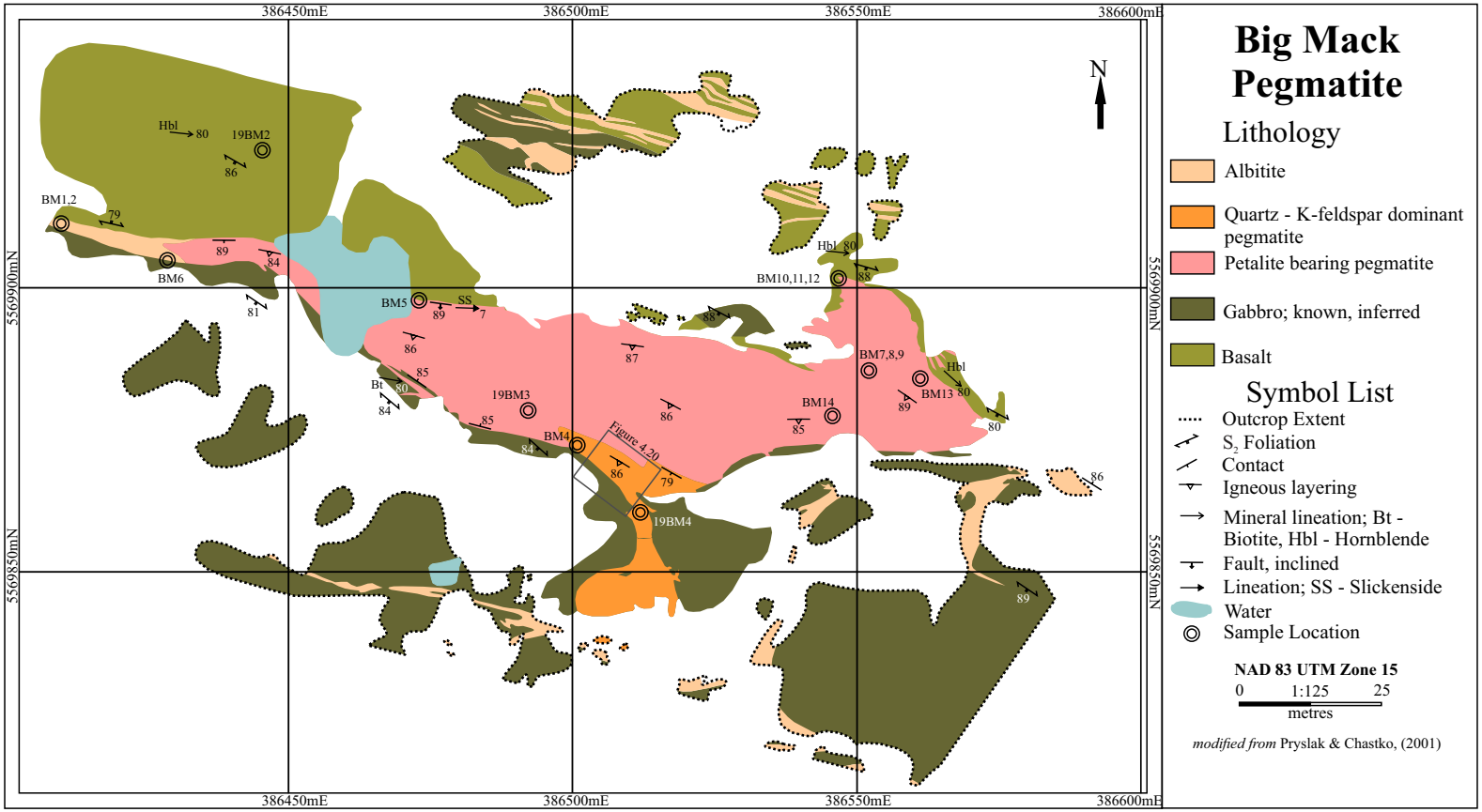

Figure 4.3. The Big Mack pegmatite from mapping by Pryslak and Chastko, (2001). Two additional corresponding drone images are included in Figures 4.20 and 4.34 later in this chapter: (1) contacts between pegmatite units and host gabbro; and (2) an outcrop drone image of mapped area extents.

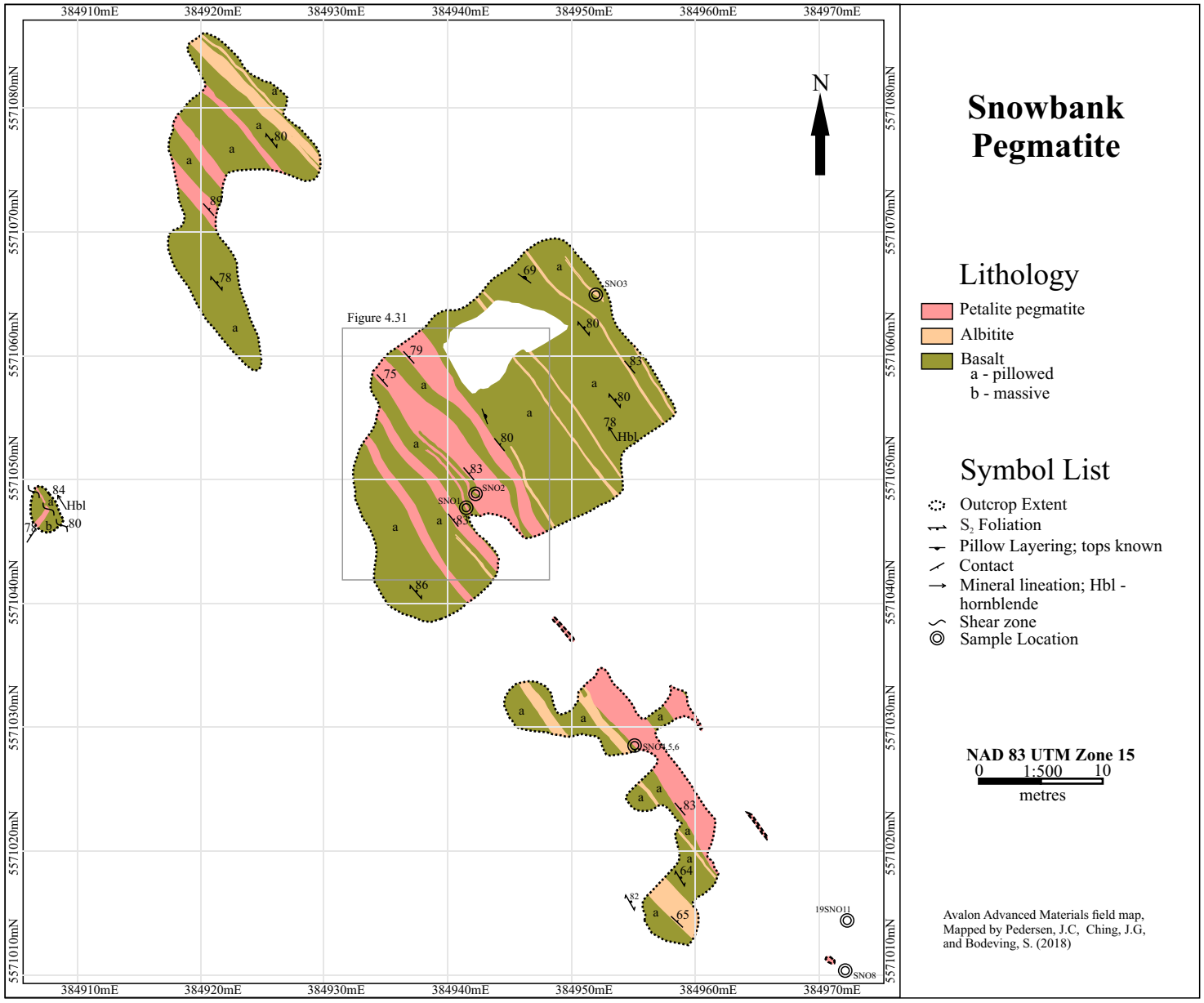

Figure 4.4. The Snowbank pegmatite based on mapping by Pedersen *et al*., (2018). Drone image of central outcrop later in this chapter in Figure 4.31.

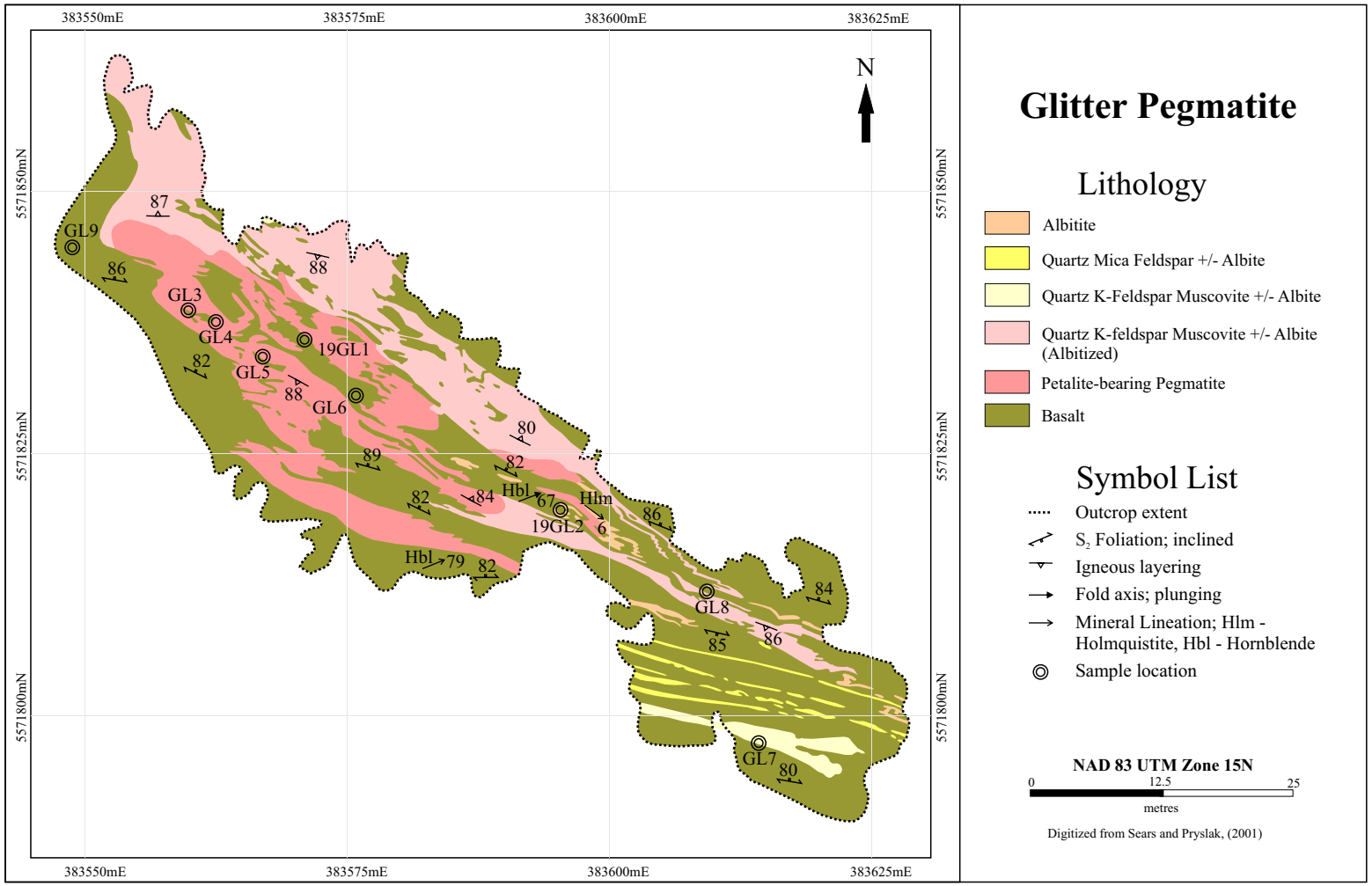

Figure 4.5. The Glitter pegmatite. Sample locations overlain on mapping by previous authors. A drone image of the mapped extents is provided as Figure 4.36 later in this chapter.

Figure 4.6. Basalt along the southwestern margin of the Separation Rapids pluton. Dark green pillow selvedges define pillow morphologies with their long axis oriented east-west; down dip ratios unknown. Pillow rupture (1); tapered pillow roots (2); and convex pillow upper surfaces adjacent to hyaloclastite (3) indicate westerly younging direction.

to tan, fine- to medium-grained hyaloclastite adjacent to pillow margins make up ~1-5% of the pillowed flows. Massive flows up to 10's of metres in thickness are a minor component of the mafic volcanic rocks.

The basaltic country rocks, metamorphosed to amphibolite facies, contain fine grained hornblende ± albite ± clinopyroxene ± garnet. Fine- to medium-grained hornblende ± actinolite ± epidote ± chlorite ± albite ± garnet occurs at the pillow margins. Titanite forms very fine-grained, micron-scale blebs or aggregates and 0.1-0.5 mm, rounded to pill-shaped- crystals in coarser domains (Figure 4.7). Epidote imparts a green-brown colour to the pillow cores on several islands near the River Outcrop (Fig. 2.1).

Contacts between massive and pillowed flows are rarely pristine at the outcrops investigated. Heterogeneous strain is indicated by variable degrees of fabric intensity that includes sigma-type clasts and boudinage (Figure 4.8). Pillows in higher-strain regions are recognized by a banded appearance imparted by the alternation of dark selvages and lighter cores; in places, millimeter-scale bands of hyaloclastite occur between bands. A southeast-trending, penetrative, subvertical composite fabric is defined by alignment of hornblende and titanite and is continuous through pillow cores and selvages. Basalt structures and textures near the mineralized pegmatites studied are summarized in Table 4.1.

4.2 Granitoid plutons

The textural and structural characteristics of the Skidder and Separation Rapids plutons are described here to facilitate comparisons with the observed, spatially associated granitic pegmatites. Compositional details of the plutons are provided in the literature (*cf.* Sears and Pryslak, 1999; Breaks, 1993; Blackburn and Young, 2000). Although Breaks *et al.* (1999) interpreted the Skidder

Table 4.1 Structures and textures evident in outcrop and hand sample in basalt near mineralized pegmatites

Intrusion		Glitter	Snowbank	Big Mack	Big Whopper	GWN Aplites
Volcanic structures	Pillowed flow	x	x	x	x	x
	Massive flow	x	x	x	x	
	Country rock bridges	x	x	x	x	x
Alteration	Biotite	x	x	x	x	x
	Holmquistite	x	x	x	x	x
S2 Foliation	Oblique to intrusion	x	x	x	x	x
	Truncated, dismembered	x	x	x	x	x
Relative strain	High	x				
	Low			x		x
	Variable		x		x	
Sense of Motion	Dextral	x	x	x	x	x
	Sinistral			x		
Deformation structures	Boudinaged pillow cores	x				x
	Drag folds			x		
	Brittle Faults		x	x		
	σ-type clasts					x

x - present

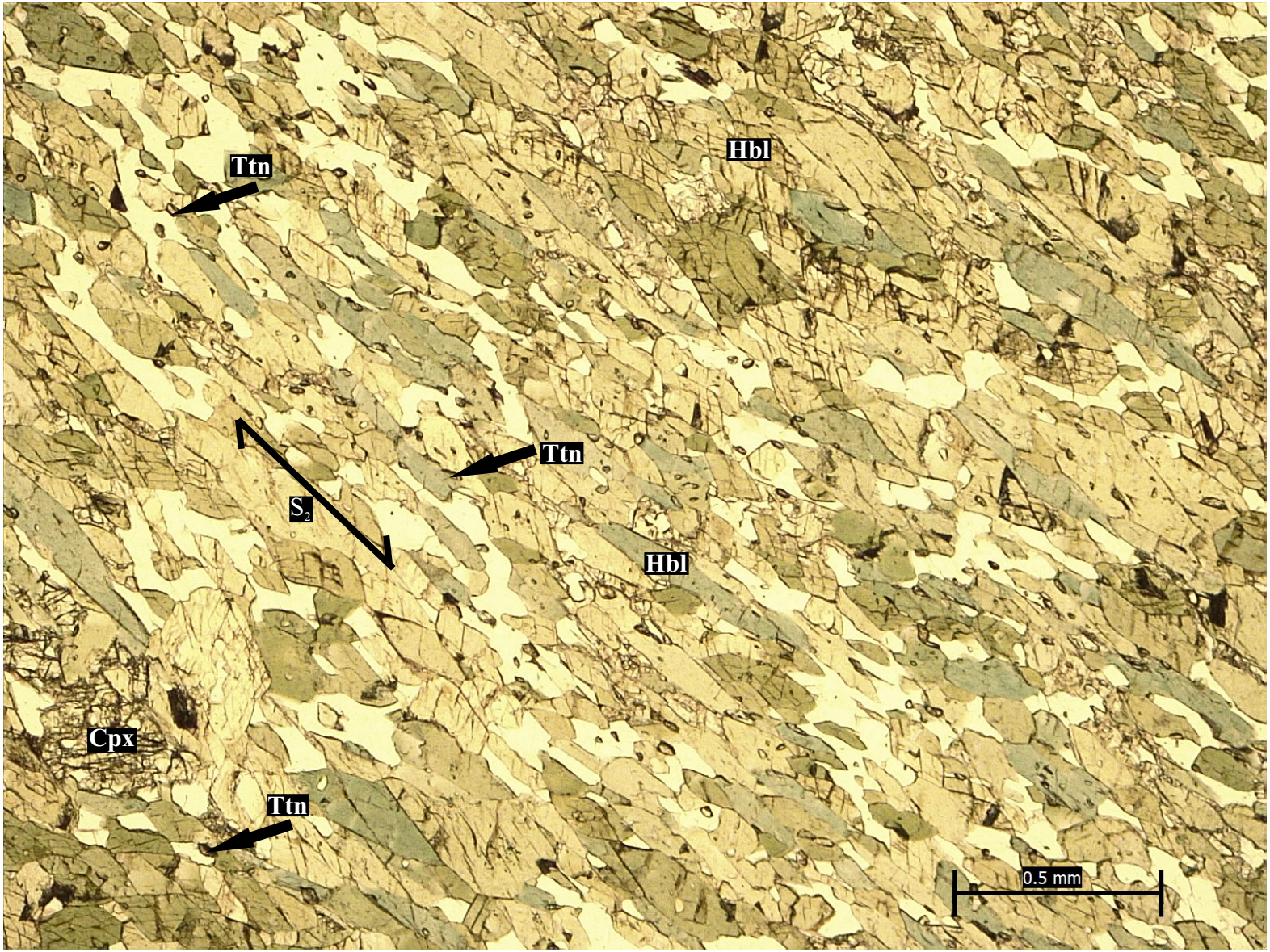

Figure 4.7. Plane polarized light photomicrograph of regional schistosity (S_2) in basalt, defined by the alignment of hornblende. Titanite occurs as disseminated, rounded to pill shaped crystals in this sample.

Figure 4.8. Block boudins in strained basalt adjacent to Snowbank pegmatite dikes. Alternating dark and light green bands (1); and (2) dextral sigma-type clasts, and block boudins infilled by either basalt or recrystallized material (3) occur in east-trending S_2 foliation. Basalt fabrics (4) are disrupted by pegmatite dikes.

pluton as a possible apophysis of the Separation Rapids pluton, the textures and structures of the two plutons differ in outcrop and are described separately. The Separation Rapids pluton crops out immediately north of Storm Bay along the English River and Separation Lake (Fig. 2.1). Lying inland from the English River along the northwestern limb of the SLgb, the Skidder pluton lies ~3 km farther northwest of the Separation Rapids pluton (Fig. 2.1).

4.2.1 Skidder Pluton

The Skidder pluton is an elongate, lenticular body of granodiorite that strikes southeast (Fig. 2.1). Grey-white on weathered surfaces, the granodiorite is medium grained, equigranular, and mineralogically homogeneous, comprising quartz, K-feldspar and albite, with minor biotite ± garnet. Pegmatitic and aplitic phases occur along the margins of the intrusion and where the intrusion is narrower than 20 metres (Sears and Pryslak, 1999).

A penetrative foliation overprints the igneous crystalline texture and trends to the southeast with a subvertical dip, parallel to the regional S_2 schistosity. Microscopically, strain-induced modification of igneous textures shows well in quartz, microcline and albite (Figure 4.9). Quartz grains illustrate the greatest degree of recrystallization; undulatory extinction, bulging at grain boundaries, and grain-size reduction are evident along discontinuous anastomosing networks of very fine-grained quartz ± biotite. Transformation twinning of microcline is evident as near-complete tartan twins (Fig. 4.9). Myrmekite overprints microcline and illustrates directional growth, having apparently nucleated near the very fine-grained quartz ± biotite domains. Albite crystals twinned by the albite law possess equidimensional lamellae with tapered terminations and are bent to arcuate in shape along twin interfaces. Both microcline and albite crystals are dusted by microscopic sericite.

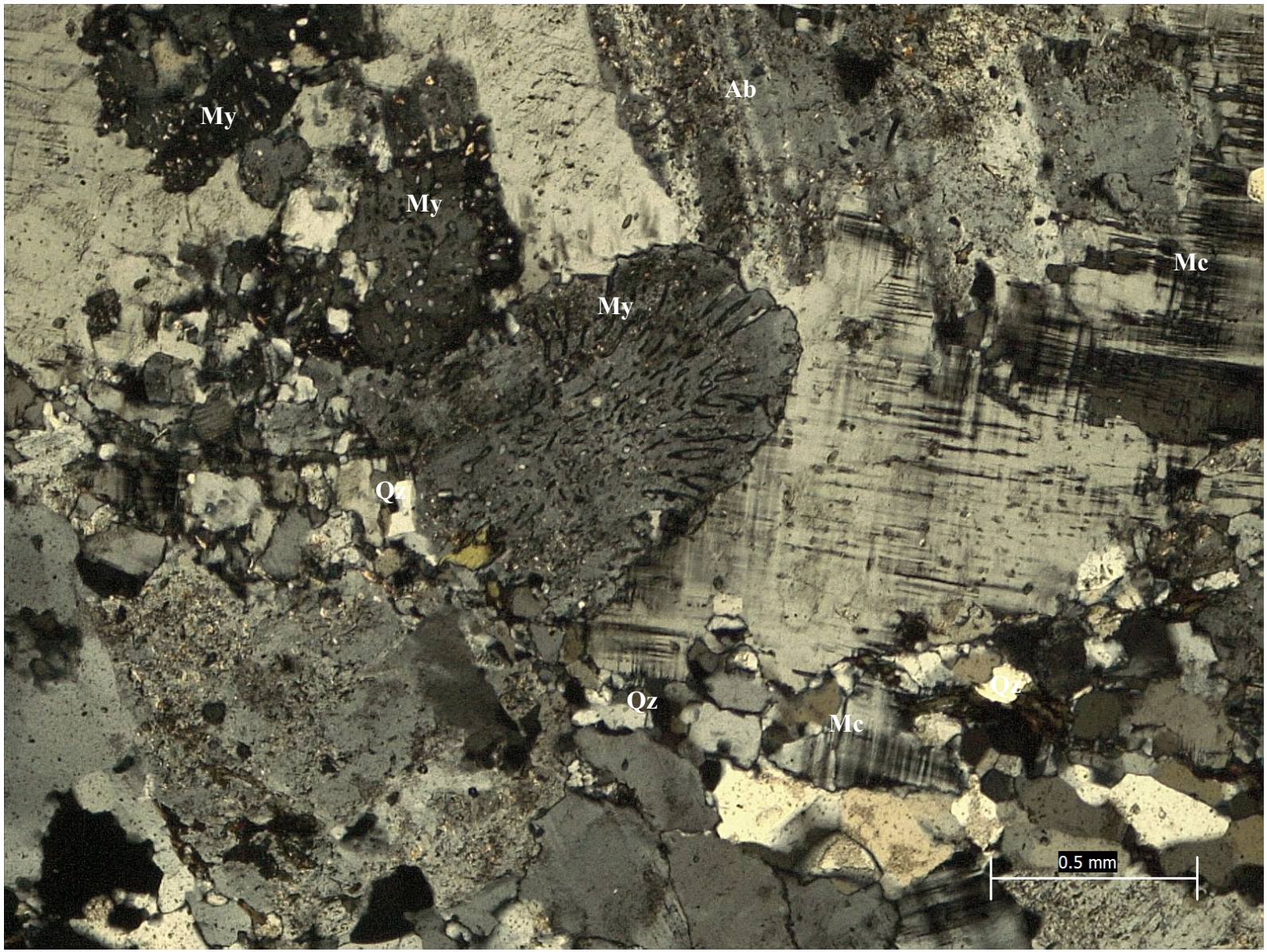

Figure 4.9. Crossed-nicols photomicrograph of deformation microtextures in the Skidder pluton. Partial tartan twinning in microcline (Mc) crystals right of centre. Myrmekite (My) occurs along very fine-grained (<100 micron) anhedral to subhedral bands of quartz (Qz), albite (Ab), and microcline. Sericitic alteration dusts both albite and microcline.

4.2.2 Separation Rapids Pluton

The Separation Rapids pluton crops out in the west-central part of the SLgb and is described in detail by Breaks (1993). Weathering grey-white, the pluton is a pegmatitic to coarse-grained intrusion with minor aplitic phases. Blackburn and Young (2000) described the composition of the Separation Rapids pluton as granitic to granodioritic to tonalitic. Where examined, the main minerals of the Separation Rapids Pluton include quartz ± albite ± K-feldspar with accessory medium-grained euhedral garnet, coarse crystalline books of muscovite, euhedral aquamarine apatite, and dark brown-black biotite. Cordierite and beryl were noted by previous authors (see Breaks, 1993), but are absent at outcrops examined in this study. Textures and structures define three domains in the Separation Rapids pluton. These include (1) coarse-grained to pegmatitic domains with mesoscopic internal layering and textures, (2) a thin, fine-grained porphyritic domain adjacent to basalt country rock, and (3) an area abundant in xenoliths of country rock. These domains are described in greater detail for the pegmatites in Section 4.3, and their features are similar in both the Separation Rapids pluton and the pegmatites.

Magmatic processes have resulted in east-trending textural layering (S_L) along the southern margin of the pluton, locally discordant to regional S_2 in the wall rocks. These metre-scale magmatic layers (Figures 4.10, 4.11) are delineated by differences in texture, mineralogy and grain size, and are manifest as schlieren and crystal cumulates. Linear to arcuate schlieren of biotite ± muscovite are typically medium- to coarse-grained and centimetre-scale in thicknesses. In places, these schlieren form mafic ellipsoids within layers. Where present along schlieren and layer interfaces, centimetre- to decimetre-scale feldspar megacrysts indent and deflect the schlieren (Fig. 4.10). In some layers, the long-axes of megacrysts are aligned perpendicular to the layering. Cumulate layers are up to ~10 m in thickness and host crystals up to one metre in size. Megacrysts

Figure 4.10. Pegmatitic layering along the southern margin of the Separation Rapids pluton. Layering occurs as east-trending, slightly undulating bands of fine to coarse grained crystals. Unevenly distributed coarse to megacrystic (>10cm) subhedral to euhedral k-feldspar cumulates comprise up to 60% of the layer volume. Indicated by green dashed lines, indents and deflections (1) in S_L within finer grained domains suggest a northward younging direction. The groundmass hosting megacrysts is contiguous with finer grained granitic phases.

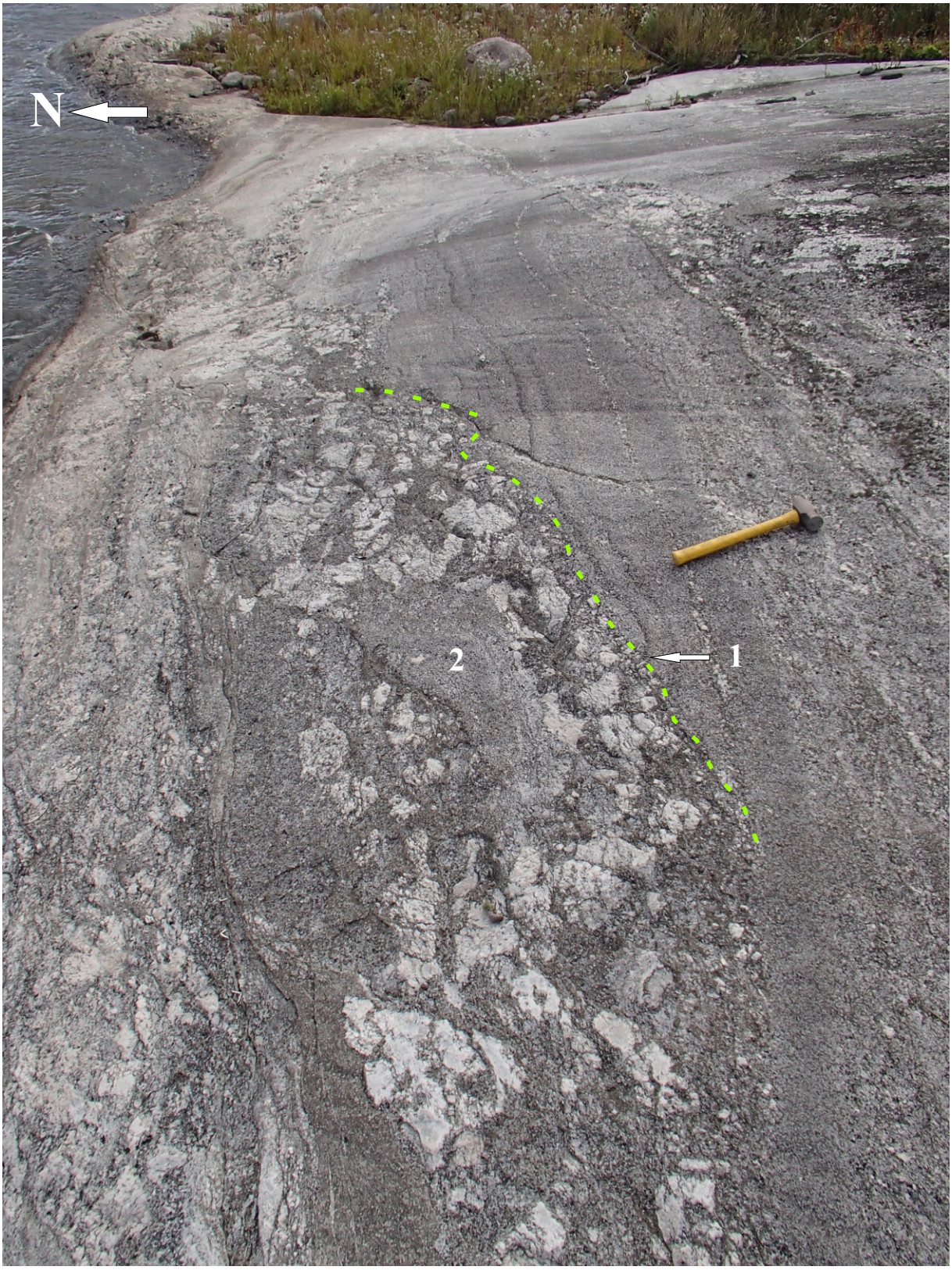

Figure 4.11. Igneous layers and trough-like scour structures (green dashed line) in pegmatitic granite of the Separation Rapids pluton. Trough layering (1), indicated by green dashed line, formed along scour surfaces where east-trending, medium- to coarse-grained granitic domains terminate against coarse grained to pegmatitic domains along southern margin of pluton. Dismembered layered granitic enclave (2) is hosted by younger pegmatitic phase.

are fractured and brecciated, with fractures filled with medium- to coarse-grained albite, K-feldspar and quartz, contiguous with nearby finer-grained layers.

Contacts between individual layers are planar to arcuate, often with cuspate to mullion-shaped structures between coarse- and fine-grained layers. Arcuate contacts define large-scale troughs and scours that consistently indicate a northward younging direction (Fig. 4.11) toward the centre of the pluton along the southern margin of the intrusion.

Along its southern contact with mafic volcanic rocks, the Separation Rapids pluton has a ~1-2 cm wide, porphyritic, fine-grained domain (Figure 4.12). This domain is mineralogically similar to that of the adjacent pegmatite and continuous with branching thin dikes in basalt country rock. Recrystallization textures are not evident here. From outcrop- to thin-section scale, albite and quartz crystals oriented at high angles to the contact with basalt are present in places (Figure 4.13). Primary growth twins in albite show irregular thicknesses of the twin lamellae, angular twin terminations and irregularly distributed poikilitic intergrowths of albite oikocrysts and quartz chadacrysts. These poikilitic intergrowths are common and in places resemble graphic or micrographic symplectites. Linear twin interfaces in albite crystals on {010} define an orientation of the long crystallographic axis at a high angle to the contact. Subhedral to euhedral, simply twinned orthoclase is uncommon. Fine-grained, rounded to blebby apatite decreases in abundance away from the contact. Microtextures are described in more detail with those in the pegmatites in Section 4.3.

Mafic volcanic xenoliths are concentrated near the contact of the pluton. Xenoliths occur as centimetre-size inclusions in thin granitoid dikes, as blocks between metre-scale dike swarms along the southern margin of the pluton, and as rafts hosted within the granitoid intrusions. These blocks increase to lengths on the scale of 10’s of metres, with a large aspect ratio between long

Figure 4.12. Fine-grained to porphyritic domain along the southern contact of the Separation Rapids pluton with basalt. White weathering porphyritic domain (1) is contiguous with thin dikes oblique to the intrusion. Quartz and plagioclase phenocrysts (2) occur at high angles to the contact.

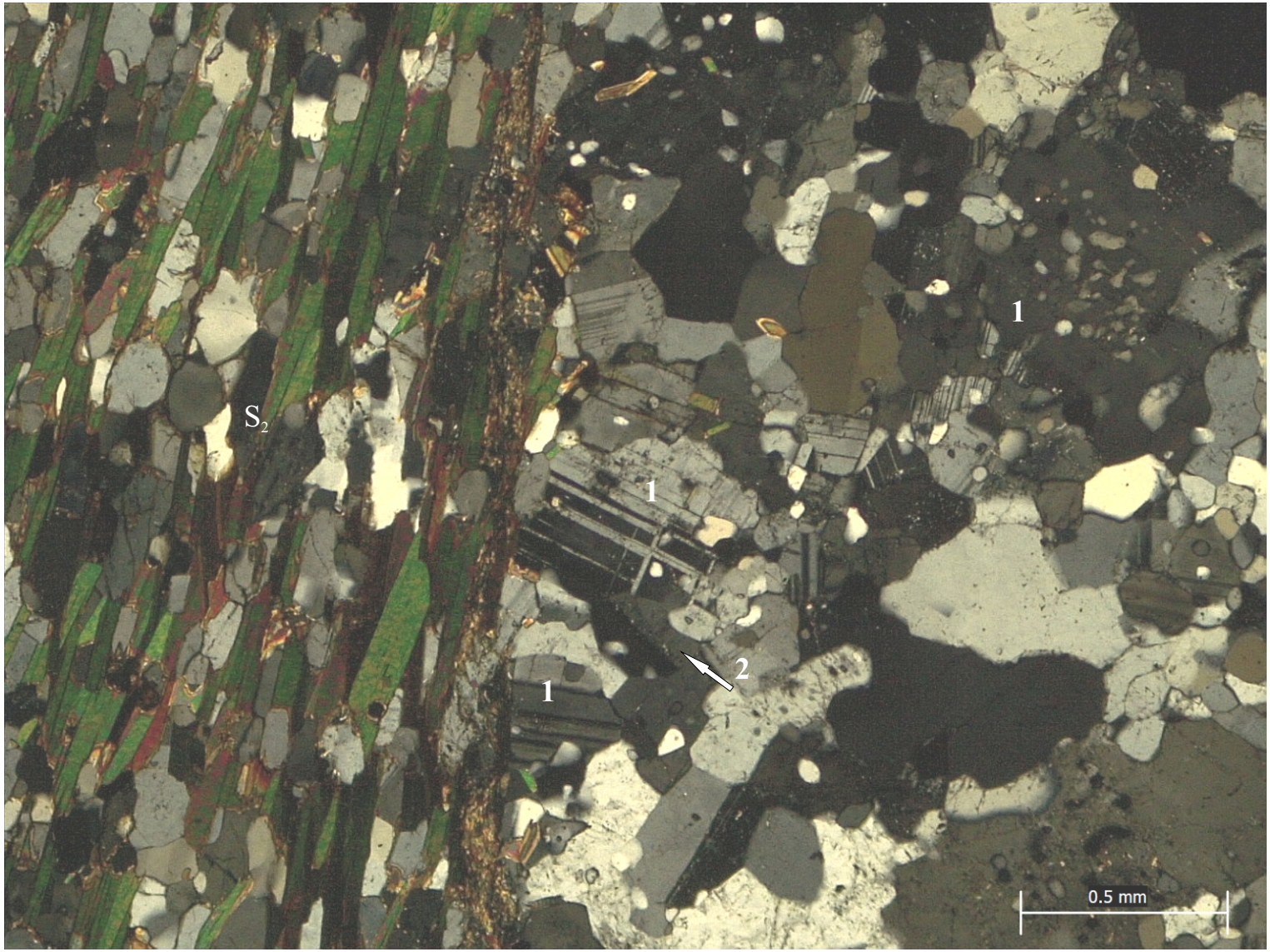

Figure 4.13. Crossed-nicols photomicrograph of the fine-grained domain shown in Fig. 4.12. Poikilitic albite oikocrysts and quartz chadacrysts (1) bounded by simply twinned K-feldspar (2) occur adjacent to basalt contact. Crystals lack a preferred orientation and are in places discordant to S_2 in basalt.

and short axes parallel to the dike trends, and subparallel to S_L. Fabrics such as boudinage and S_2 foliation preserved in the xenoliths are discordant to both the regional S_2 trend and S_L (Figure 4.14), indicating that the xenolith fabrics pre-date emplacement of the pluton.

A dike swarm at the River Outcrop occurs southwest of, and proximal to, the contact of the Separation Rapids pluton with the country rock. In outcrop, two main dikes are joined via thin ptygmatic dikes that transect the primary and composite basalt fabrics to form the swarm. Undulating linear to curvi-linear contacts are common along the east-west contacts in the main dikes with cusps evident along the north-south trending contacts. Composite basalt fabrics along the north-south trending pegmatite contacts are truncated and distorted to obliterated. Sandwiching of basalt occurs in one location, where two dikes deform the basalt into a thin septum (Figure 4.15). Centimetre to decimetre thick ptygmatic dikes are common, possess similar textures to the adjacent granitic pegmatite and occur oblique to the main dike trend (Fig. 4.1, Figure 4.16). These ptygmatic dikes are traced by, and link with, the fine-grained domain described earlier in this section. Crystals are commonly oriented at high angle to the contacts in these dikes (Figure 4.17), with near radial forms at the point of maximum curvature between ptygmatic arms. This dike swarm possesses similar structures and textures to those in regions of the pluton described above and in the mineralized pegmatites studied here (see Section 4.3).

Figure 4.14. Xenolith entrained in the Separation Rapids pluton along the southern extent of the intrusion. Pegmatitic granite truncates S_2 folia in the xenolith at a high angle and has similar fine-grained domains (1) as shown in Figure 4.12.

Figure 4.15. Thin septum of basalt sandwiched between blunted end of two dikes. Adjacent basalt fabrics are distorted from regional S_2 trend to parallel the dike contacts in septum. Regional fabrics are preserved in a xenolith at left but transected by a thin dike. Contacts are curvilinear to arcuate with “Flame” basalt (1) interleaved in pegmatite with cuspate contacts (2) evident. Fine-grained domain (3) mineralogy is contiguous with pegmatite and traces all contacts with basalt, including thin dike (4) that transects xenolith. Branched pegmatite (5) records dextral asymmetry in intrusion.

Figure 4.16. Ptygmatic dike transecting primary structures and composite S_2 foliation in basalt. Boudinaged pillow cores (1) are cut by ptygmatic dike. Ptygmatic dike contacts are arcuate to cuspate (2). Internal crystal growth is orthogonal to contacts in places (3; traced by blue dotted line) and suggests opening vector oblique to dike trend and regional S_2 foliation at this location. Fine-grained domain (4) is continuous from main to ptygmatic dike. Xenoliths of basalt (5) preserve S_2 but occur oblique to regional trend.

Figure 4.17. Regional S2 foliation in basalt cut by thin dike. In places crystals in dike occur orthogonal to the dike contacts discordant to the trend of S_2.

4.3 Pegmatites

Outcrop investigations of four rare-element pegmatites in this study include, with increasing distance from the Separation Rapids pluton: the Big Whopper, Big Mack, Snowbank and Glitter pegmatites. In addition, a zone of aplitic dikes interpreted to be part of the Separation Rapids Lithium Deposit (SRLD) of Aiken *et al.* (2016) and Gowans *et al.* (2018) was examined. These dikes, the Great White North (GWN) aplites, crop out within the SRLD approximately 400 meters northwest of the Big Whopper and lie near the Great White North pegmatite (Fig. 2.1). These intrusions have been described and mapped by previous workers (see section 2.3; Figs. 4.2-4.5). Similar to the Big Whopper, the pegmatites have three domains in which the structures and textures were examined: (1) coarse-grained to pegmatitic domains with mesoscopic internal layering and textures, (2) a thin, fine-grained domain adjacent to basalt country rock, and (3) areas abundant in xenoliths of country rock. Structures and textures are summarized in Table 4.2, and microtextures in Table 4.3.

4.3.1 Layered Pegmatite

Textural and compositional layering (P_L) is developed from centimetre- to decimetre-scale in the Glitter, Big Mack and Big Whopper pegmatites (Table 4.2). Layering is distinguished by differences in mineralogy and grain size: (1) layers rich in megacrystic alkali feldspar, coarse albite and quartz, (2) white to pink petalite-bearing layers, and (3) mica-rich schlieren. Trace euhedral fluorite occurs sporadically in the petalite-bearing layers. The random orientation of minerals along these layers suggests that these are primary and result from magmatic flow. Coarse-grained to megacrystic feldspar and petalite (>2 cm) are present in the Glitter, Snowbank, Big Mack and Big Whopper pegmatites. These subhedral to euhedral megacrysts can occur either as discrete crystals in fine-grained domains or as layer-parallel accumulations (Figure 4.18), which are

Table 4.2. Structures and textures evident in outcrop and hand samples in the SLgb pegmatites and SRLD aplites.

Intrusion		Glitter	Snowbank	Big Mack	Big Whopper	GWN Aplites
Internal components	schlieren	x		x	x	
	magmatic layering (P_L)	x		x	x	x
	crystal clusters	x	x	x	x	x
	plumes[1]	x				
	troughs			x		
	cusps	x		x	x	
	interleaved basalt	x			x	
	xenoliths	x	x	x	x	x
Fine-grained domains	thickness (cm)	1-2	absent to <0.1	<1	1-2	<1
	high-angle crystal growth	x		x	x	
	truncate S_2 in basalt	x	x	x	x	x
Contact Characteristics	linear		x	x	x	x
	undulating	x	x			
	arcuate	x	x	x	x	x
	lobate	x	x	x	x	
Contact Structures	beads[2]	x	x			
	branches	x	x		x	x
	cusps	x	x	x	x	
	interleaved basalt	x			x	
	lobes	x	x	x	x	x
	ptygmatic folds	x	x	x	x	x
	steps[3]	x	x			
Asymmetry	dextral	x	x	x	x	
	sinistral			x		

x – present

Features as defined by [1] - Paterson *et al*., 2019; [2] - Bons *et al*., 2004; [3] - Schofield *et al*., 2012

Table 4.3 Mineralized pegmatite and aplite microtextures in the Separation Lake greenstone belt.

Domain	Mineral	Texture	Glitter	Snowbank	Big Mack	Big Whopper	GWN Aplites
Internal Layers	K-feldspar	Simple	x	x		x	
		Tartan	x	x		x	
	Albite	Growth[1]	x	x	x	x	
		Transformation[1]					x
		Orthogonal to layers	x			x	
		Granophyric	x	x	x	x	
	Petalite	SQUI present	x	x	x	x	
		Mosaic texture	x	x	x	x	
	Lithian mica	Planar cleavage				x	
Fine-grained	Quartz	Skeletal	x	x	x	x	
	Albite	Growth[1]	x	x	x	x	
		Transformation[1]					x
		Orthogonal to layers	x	x	x	x	
		Granophyric	x	x	x	x	
	Biotite	Planar cleavage	x	x	x	x	
	Muscovite	Schlieren	x		x	x	
Basalt margins	Alteration	Biotite	x	x	x	x	x
		Holmquistite	x	x	x	x	
		Garnet	x	x	x	x	
	S_2	Dismembered / obliterated	x	x	x	x	x
		Mullions, cusps	x	x	x	x	x
	Deformation	Dextral shear bands	x	x	x	x	
		Sinistral shear bands			x		
		Mica fish		x			
		Recrystallized quartz	x	x	x	x	

x – present

Features as defined by [1] - Vernon (2004)

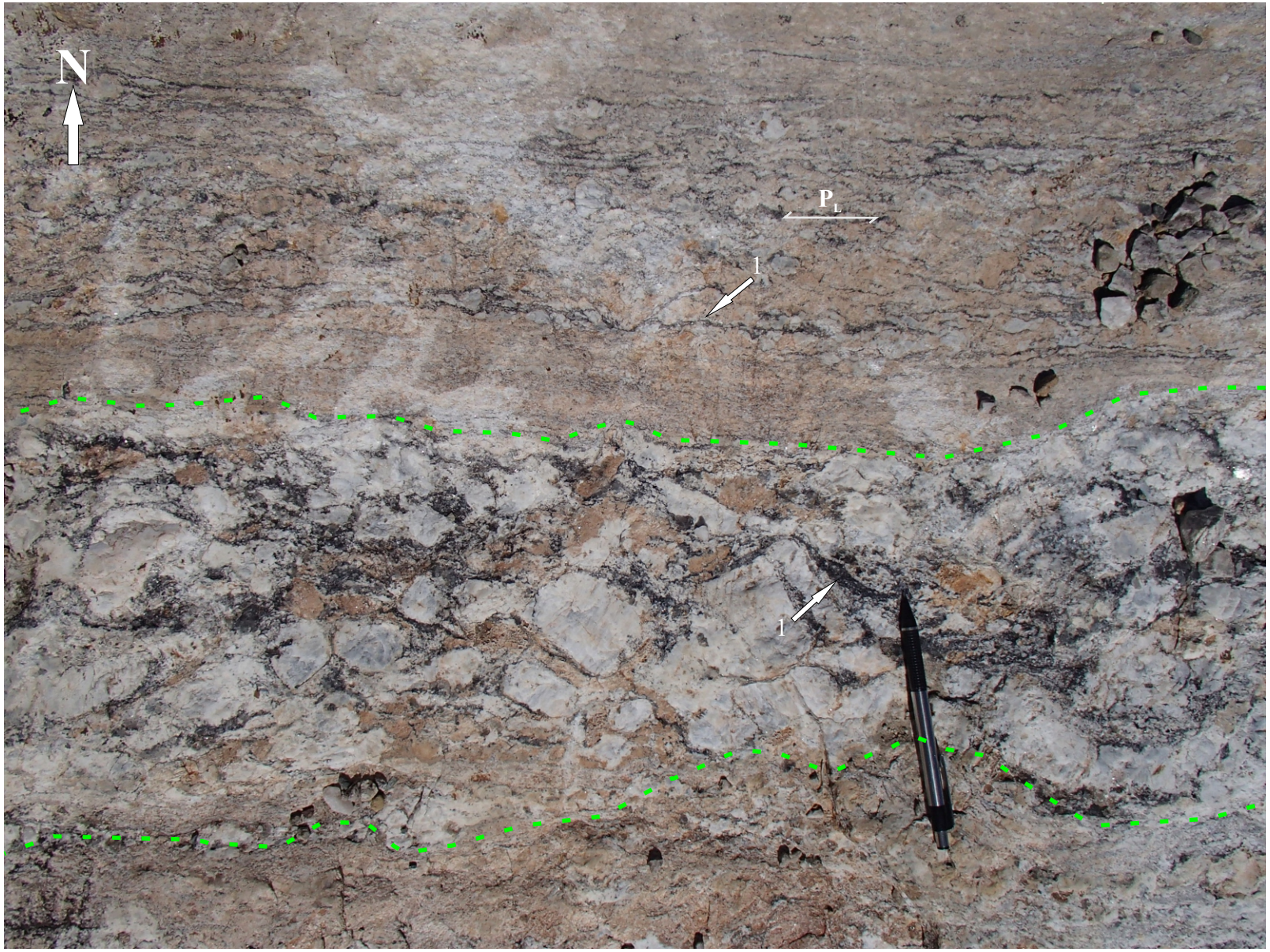

Figure 4.18. Domains of coarse to megacrystic (<10cm) feldspar and petalite occur in contact with, and parallel to, medium to coarse grained domains of similar mineralogy. Biotite schlieren (1) occur along, and partially define P_L in both megacrystic and medium to coarse grained domains.

interpreted to be crystal cumulates. Megacrysts are flanked by fine-grained segregations with similar form to δ-clasts with asymmetry present albeit with inconsistent dextral and sinistral forms. Where present in fine-grained domains, the megacrysts deflect or truncate the easterly trend of the layers. Tails of anastomosing to arcuate, fine-grained feldspar, quartz, biotite, muscovite and petalite form a groundmass to the megacrysts and define grey-blue to pink layers in outcrop at the Big Whopper (Fig. 4.18). Schlieren are predominantly fine-grained muscovite and biotite, and mantle coarse crystals to form pinch-and-swell textures in both horizontal and vertical exposures. Along the northern margin of the Big Whopper, schlieren separate layers of medium- to coarse-grained K-feldspar and albite. Muscovite is the dominant mineral in these schlieren, accompanied by medium to coarse, euhedral red-orange garnet.

At the Big Mack pegmatite, north-younging P_L in a quartz – K–feldspar unit terminates discordant to the basalt contact (Figure 4.19). This unit exhibits structures similar to magmatic cross layering northwards to the scoured contact with petalite-bearing pegmatite (Figure 4.20). This layering infers a north-easterly younging direction towards the core of the intrusion. Scoured pegmatite is not present at the Snowbank or Glitter pegmatites with the latter recording plumose layering (Paterson *et al.,* 2019) to suggest northwesterly propagation.

In thin section, layering is defined more by composition than grain size in <1 cm crystal domains. Domains alternate between albite-rich and -deficient to form layers in all pegmatites. Albite crystals, generally medium- to coarse-grained, have albite growth twins with linear lamellae of unequal thickness and angular internal twin terminations. Albite twins along the (010) plane of the crystals define an alignment parallel to P_L in all samples analyzed. Lenticular, bent and equidimensional lamellae occur in places. Greater proportions of biotite, muscovite and quartz occur in albite-deficient layers. Ribbons of petalite form a mosaic texture in which petalite crystals

Figure 4.19. Sharp curvilinear contact between pegmatite and basalt along southern margin of Big Mack pegmatite. Magmatic foliation P_L of coarse to megacrystic pegmatite grades into an aplitic phase (bottom centre). The aplite and pegmatite possess continuous border zone (1-2cm) adjacent to basalt that is discordant to the magmatic layering and regional schistosity. A thin <10cm zone of shear bands (1) are developed adjacent to, and trace the contact between pegmatite and basalt.

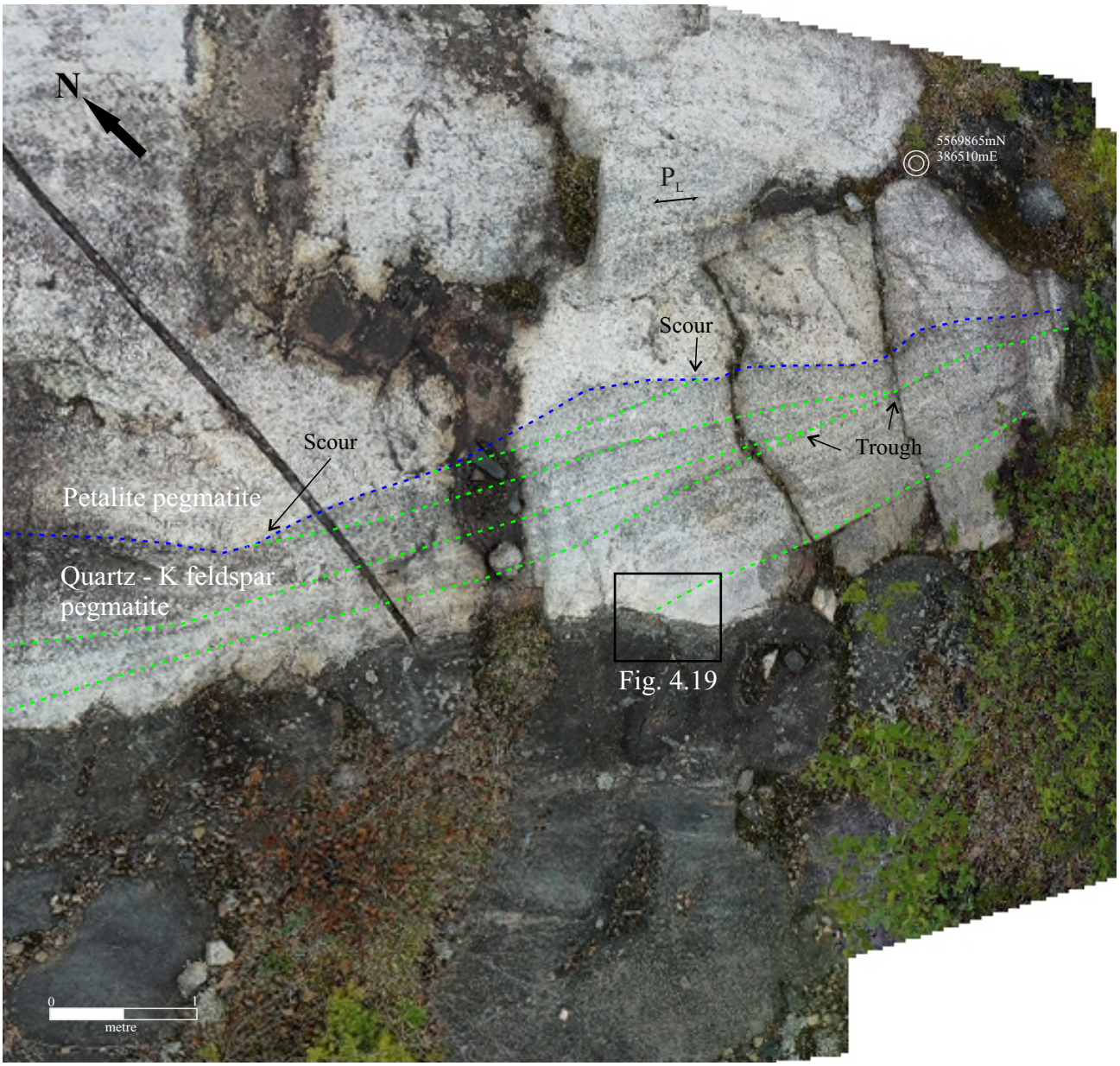

Figure 4.20. Drone image of southern contact of Big Mack pegmatite. Structures similar to magmatic cross-layering in the Quartz - K-feldspar pegmatite (green) is scoured by petalite bearing pegmatite (blue). Both units are discordant to regional S_2 foliation in the basalt (Fig. 4.19)

are rimmed by spodumene-quartz intergrowths (SQUI, Figure 4.21). Along the contacts of petalite-deficient layers, granophyric albite is present (*e.g.*, in the fine-grained porphyritic domain of the Separation Rapids pluton). Granophyre nucleated at the contacts of the petalite ribbon layers, with the direction of growth oriented away from the petalite crystals (Fig. 4.21). Fine- to coarse-grained microcline occurs adjacent to, or within several centimetres of petalite and displays locally fractured, complete, tartan twins. Infrequent fractures in microcline crystals are infilled with fine-grained muscovite and quartz. Anhedral quartz grains occur between microcline and albite within petalite-deficient layers. Quartz grain boundaries are sharp and lack recovery and recrystallization textures except for undulatory extinction.

4.3.2 Fine-grained domains

A narrow (1-2 cm), grey-white weathering, fine- to medium-grained, porphyritic domain traces all external pegmatite contacts, as well as the contacts on mafic xenoliths in pegmatite (Figure 4.22), at the Glitter, Big Mack and Big Whopper pegmatites, and the GWN aplites, but varies depending on the nature of the contact from absent to <5 mm wide at the Snowbank pegmatite (Figure 4.23; Table 4.2). In lieu of the fine-grained domain at the Snowbank pegmatite, locally euhedral, coarser crystalline material is in contact with altered basalt (Fig. 4.23). A lack of preferred orientation of crystals in outcrop and thin section is common in this domain with fine- to medium-grained phenocrysts of albite and quartz are oriented at high angles to the quench margin in places. At the Glitter pegmatite, high-relief crystals form radial patterns around convex arcuate contacts. The groundmass of this domain comprises fine-grained albite, quartz, alkali feldspar and apatite. Apatite is common adjacent to the country rock contact and decreases in frequency away from the country rock. The fine-grained domain is interpreted as the product of rapid cooling and crystallization of the melt (i.e., a quench texture; see Section 6.3).

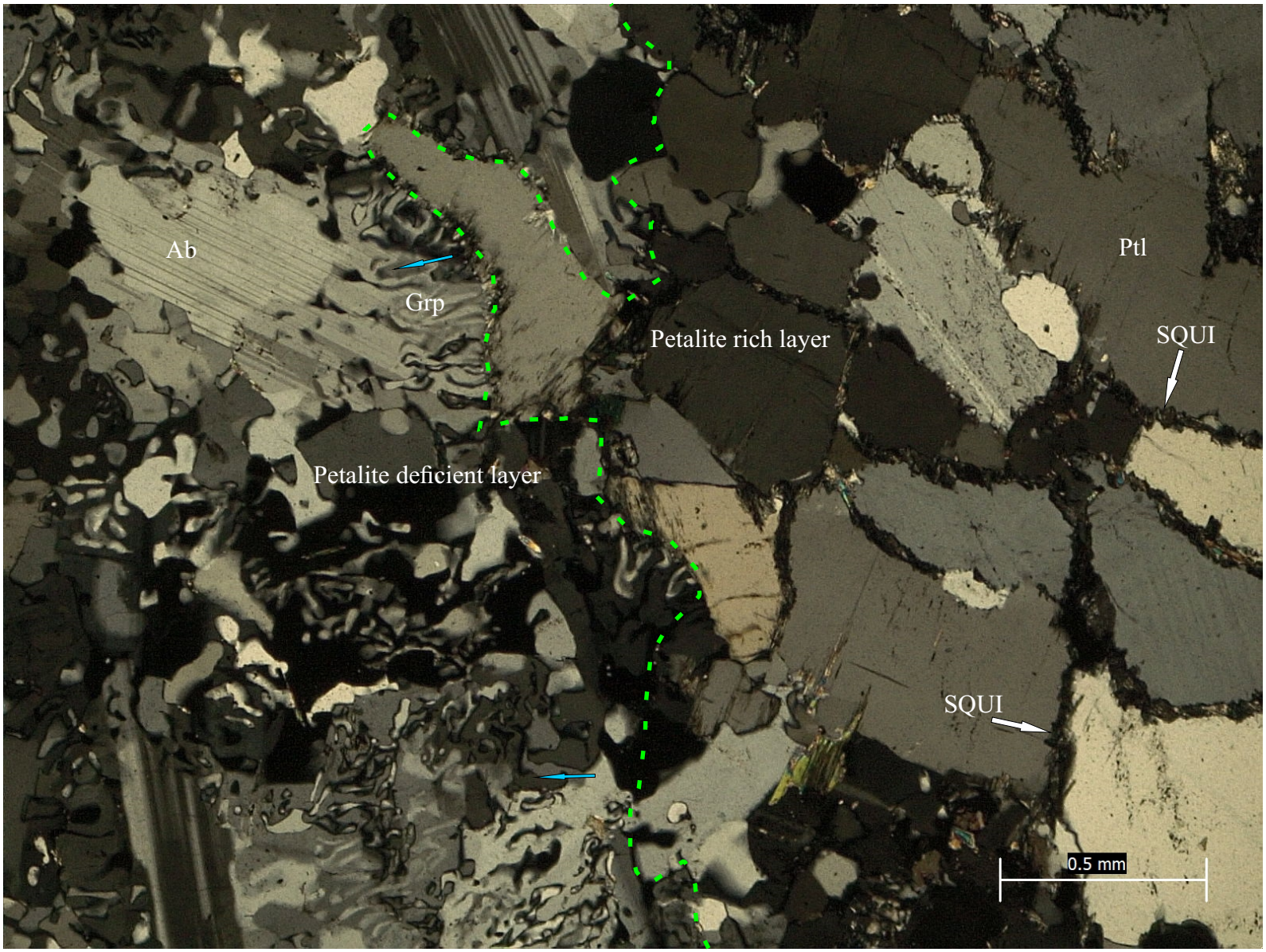

Figure 4.21. Cross-nicols photomicrograph of petalite mantled by micron-scale SQUI. Granophyric albite and quartz intergrowths and graphic alkali feldspar mark the transition between a petalite-rich layer (right) and petalite-deficient layer (left). Directional granophyre growth given by blue arrows. Ptl - petalite; Ab - albite; Grp - granophyre

Figure 4.22. White-weathered fine-grained porphyritic domain in lepidolite-bearing phase of SRp traces all contacts with (1) basalt and (2) xenolith.

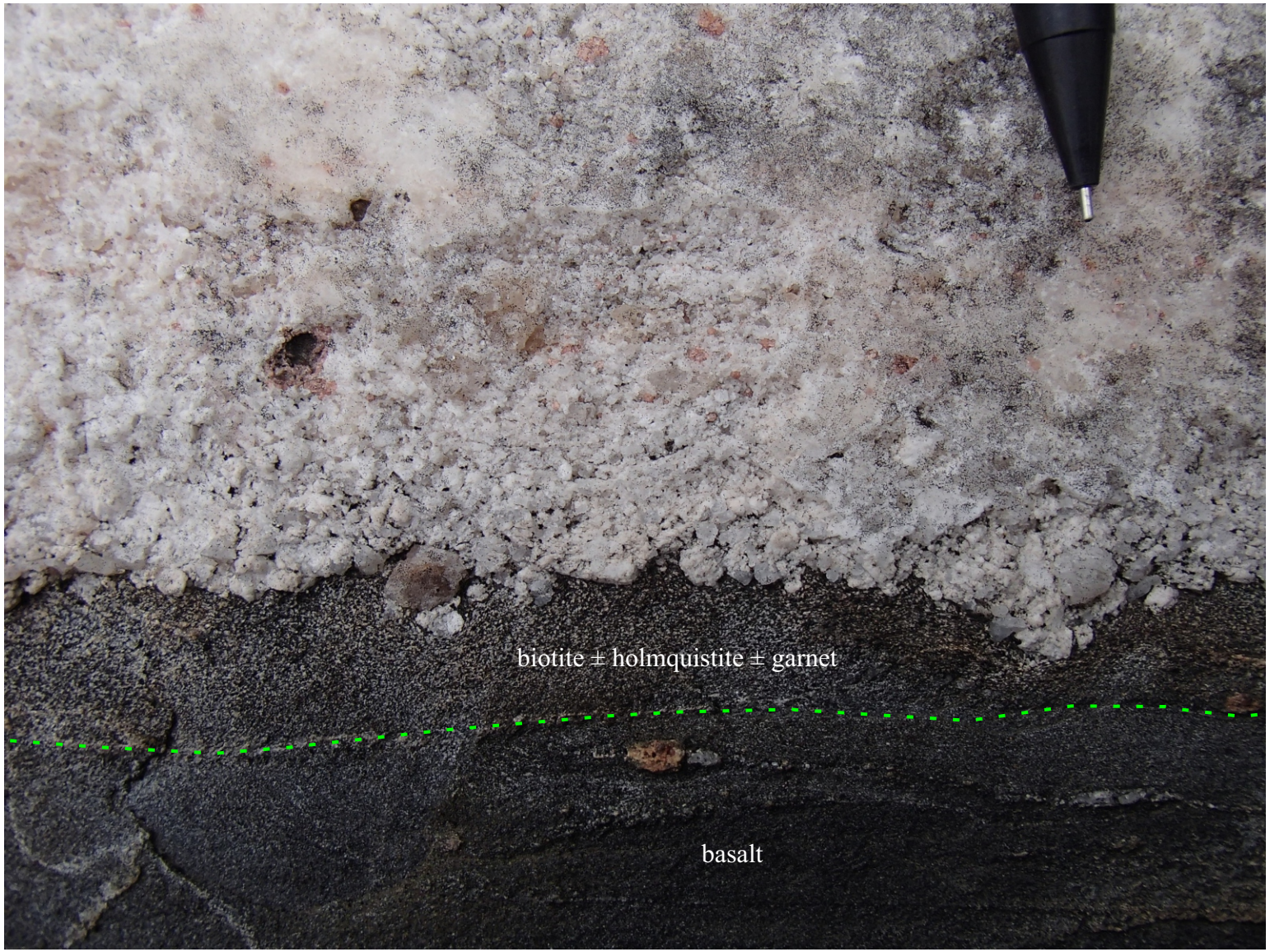

Figure 4.23. Contact absent quenched margin in aplite-pegmatite dike at the Snowbank pegmatite. Sub- to euhedral crystals abut alteration halo in basalt that overprints S2 foliation. Note dextral shear-band boudin bottom right.

In thin section, mineral textures of the fine-grained domains are like those of the internal zones of the pegmatite (Table 4.3). Differences between crystal orientations exist within the quenched material, where (010) in albite is not oriented parallel to P_L, but rather at a high angle to the trend of the domain in places. Granophyre (as defined by London, 2018) is a common texture of the domain and in places makes up to 60% with near-equal portions of quartz and albite. The high granophyre content leads to regions having the appearance of very fine-grained aggregates of quartz and albite. An outlier, the Snowbank pegmatite consists of >80% granophyre in places, infrequently euhedral (Fig. 4.23, Figure 4.24), and locally shows evidence of unidirectional crystallization away from the contacts towards the cores of the dikes.

4.3.3 Xenoliths

Elongate mafic xenoliths are concentrated near the contacts of all pegmatites. Xenoliths are decimetre- to metre-scale with their long axes parallel to either P_L or the external contacts of the pegmatite (Figure 4.25). Xenoliths are locally at an angle to the S_2 fabric in the country rock as observed at the Big Mack, Big Whopper, and Glitter pegmatites. Primary layering in basalt as well as the composite S_2 fabrics are preserved in xenoliths at all intrusions except at the xenolith margins, where alteration obliterates the S_2 foliation (see Section 4.3.6; Figure 4.26).

Fractures in xenoliths were infilled with thin aplitic to pegmatitic dikes continuous with adjacent pegmatite (Figure 4.27). Ptygmatic forms to these dikes are common with dikes up to several centimetres in thickness traced by quench textures continuous with the quenched margins on the xenoliths. Contacts along thin dikes record common cusps, mullions, and local “flame” structures developed between xenolith and pegmatite (Fig. 4.27). In addition, structures like those developed in deformed rocks such as folds and boudinage occur (Figures 4.28, 4.29). Adjacent to these structures, S_2 foliations in xenoliths are truncated and re-oriented by the thin dikes.

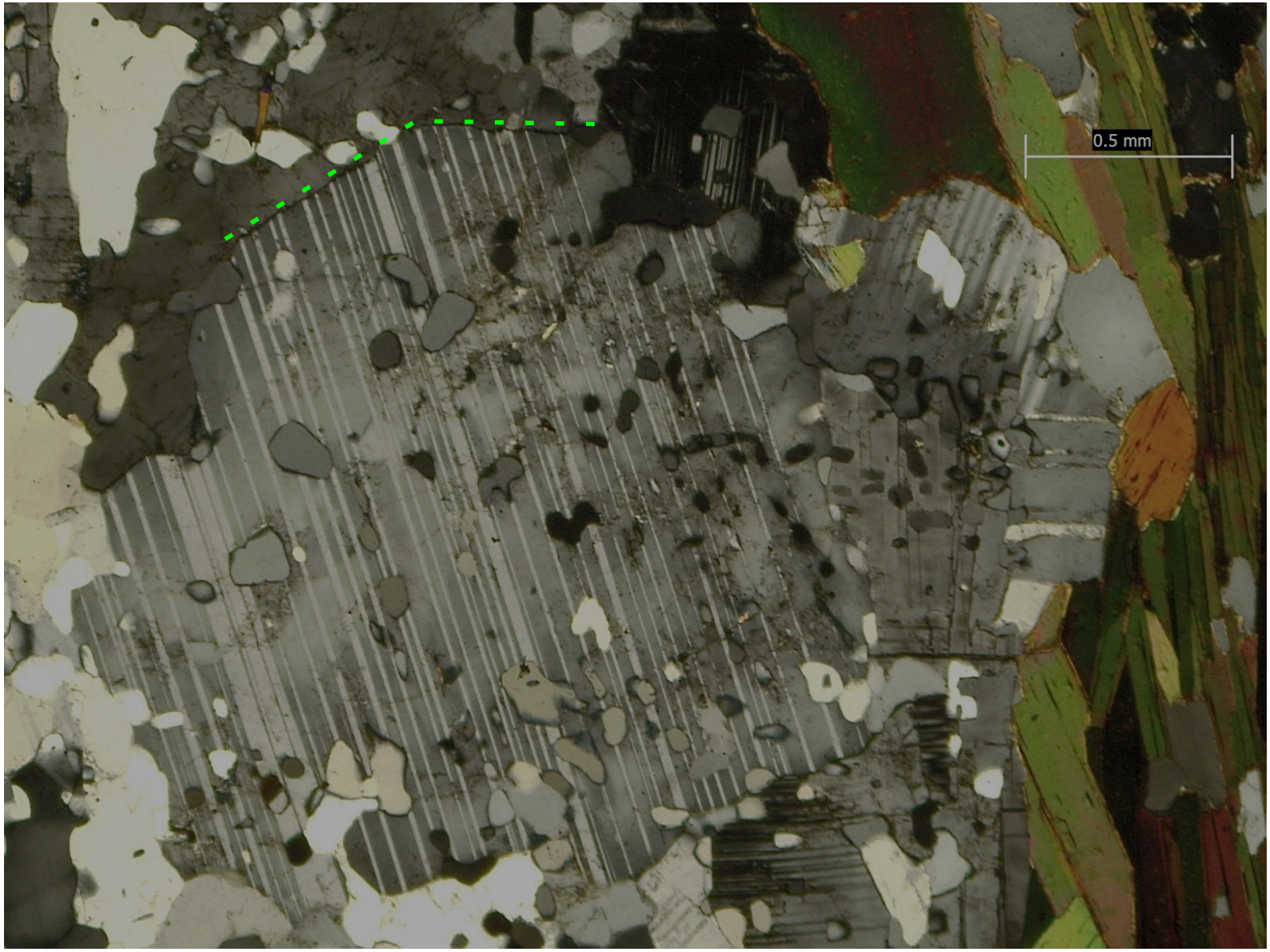

Figure 4.24. Crossed-nicols photomicrograph of euhedral poikilitic albite crystal intergrown with irregularly distributed quartz chadacrysts adjacent to contact with basalt. Albite lamellae are irregular in thickness and terminate at euhedral crystal faces highlighted by green dotted line.

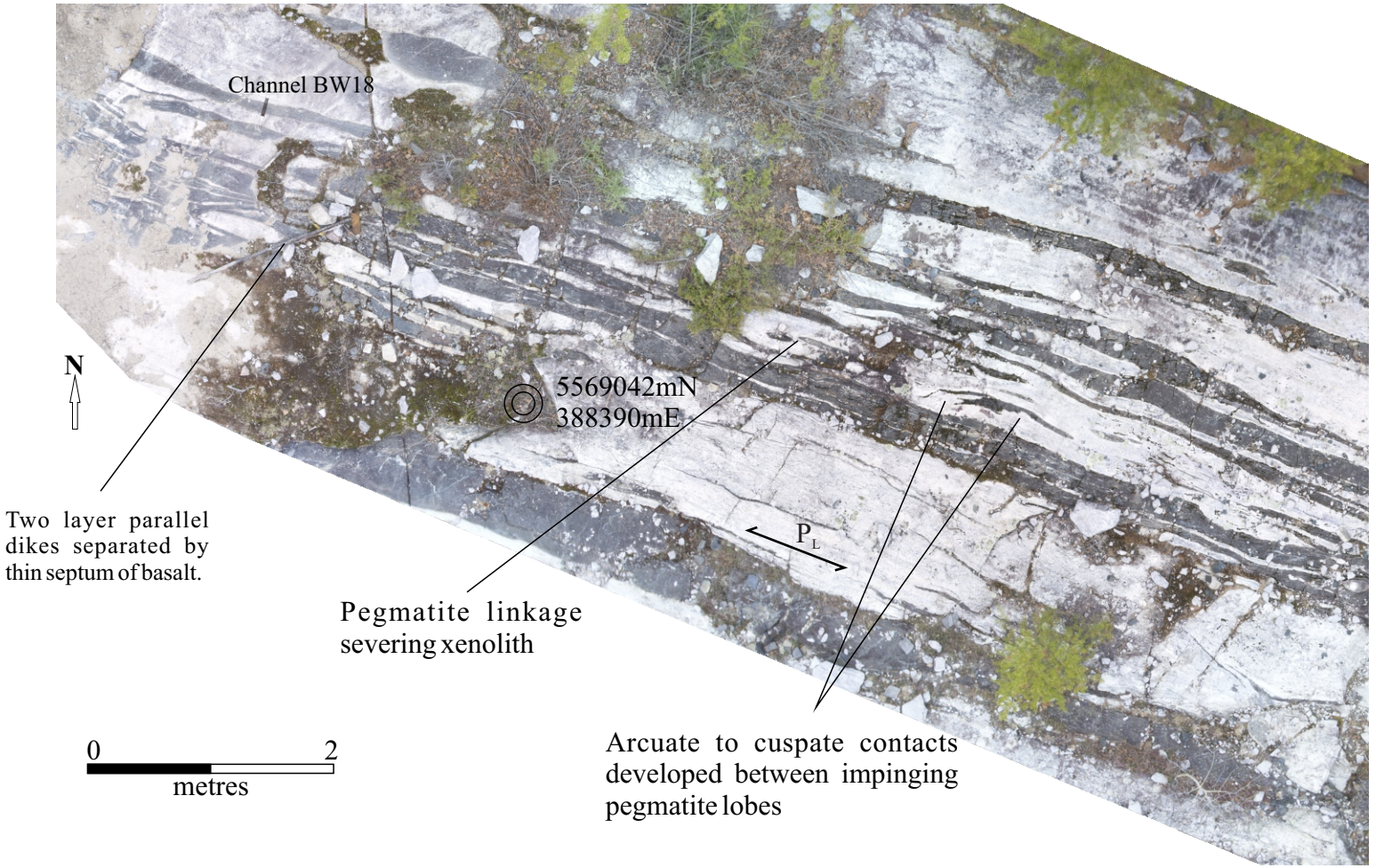

Figure 4.25. Georeferenced drone image along northwest exposure of the Big Whopper. Location given in Figure 4.2. Tabular xenoliths of basalt aligned subparallel to P_L in pegmatite and parallel to inferred long axis of the Big Whopper.

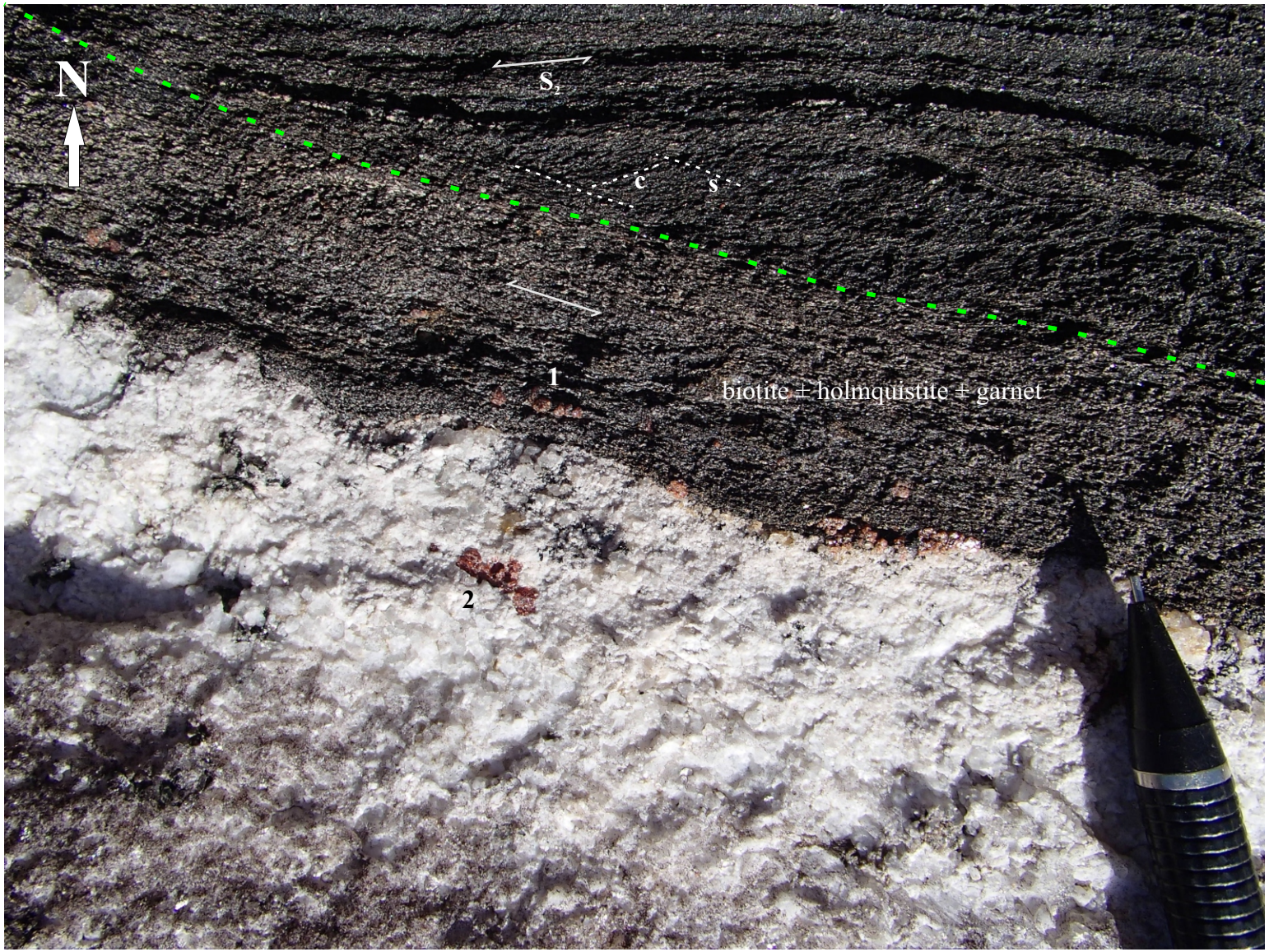

Figure 4.26. Biotite + garnet ± holmquistite alteration overprinting regional foliation in a basalt xenolith at Glitter pegmatite. Regional S_2 foliation and s-c fabrics are obliterated by local deformation and recrystallization within 1-2 cm of the xenolith margin. Garnet crystals present in (1) alteration halo and (2) as crystals in pegmatite.

Figure 4.27. Ptygmatic dikes transecting basalt xenolith in the Big Whopper. Trend of S_2 given by green dashed line is oblique to, deformed by, and terminates on the contact with the 1-2cm thick quenched domain of the dikes. Cusps, mullions, and flame structures (1) developed between interleaved ptygmatic dike and basalt.

Figure 4.28. Minor folds and boudinage of dike apophyses at the Glitter pegmatite. Regional foliation truncated by main dike and small drag fold (1). Boudin train (2) is traced by S_2 fabric into neck of boudin. Irregular boudin core (3) with interleaved basalt with arcuate to cuspate contacts.

Figure 4.29. Folded dike at the Glitter pegmatite. Fabrics in basalt deviate from regional trend. Basalt foliation diverges at fold nose and traces limbs on outer margin of dike and interior southern limb and terminates along interior northern limb of the fold. Sample 19GL2 collected across fold contacts (*see* Section 5.1.3).

4.3.4 Contacts

Contacts between the pegmatites and country rock are similar throughout the field area. (Table 4.2). Contacts are sharp, possess forms ranging from planar to arcuate to lobate, and are adjacent to a biotite ± holmquistite ± garnet alteration halo (see Section 4.3.6; Figs. 4.19, 4.20, 4.22, 4.25-29). Planar to curvilinear contacts are dominant at the Big Mack pegmatite with local arcuate to lobate contacts (*e.g.,* Fig. 4.19; Table 4.2). Curvilinear to arcuate contacts with decimetre-scale pegmatite lobes and interleaved wallrock are typical of the Big Whopper and the Glitter pegmatite (Figs. 4.22, 4.25-29). Curvi-linear to arcuate or irregular undulating contacts are developed at the Snowbank pegmatite with lobate morphologies (Figure 4.30, 4.31). Cusps occur at the Snowbank but are typically on the centimetre scale as opposed to the decimetre scale of the Glitter and Big Whopper.

A change in form of the contacts is recorded in relation to the general easterly trend of the intrusions (Table 4.2). This change in form influences the local interplay between pegmatite and host basalt. Contacts that trend parallel to the long axis of the pegmatite exposures are linear to curvilinear (e.g., Figs. 4.25, 4.31; Figure 4.32). Reorientation of the S_2 foliation in the country rock is minimal along these contacts. Slight undulations and deformation of S_2 follow undulations in the pegmatites, except where thin dikes cut S_2. In contrast, contacts oblique or perpendicular to the trend of the dikes or P_L have two forms; (1) blunted with arcuate to lobate forms that include mullions, cusps, and interleaved basalt and pegmatite in outcrop (e.g., Fig. 4.22, 4.27, Figure 4.33), or (2) tapered with curvi-linear forms with interleaved basalt and pegmatite (*e.g.*, Figs. 4.28, 4.33). Cusps, mullions, and interleaved structures are present in hand sample and at thin section scales. Along the southern contact of the Big Mack pegmatite, contact orientations highlight differences in fabric orientations between S_2 and P_L: P_L, defined here by layering and schlieren in quartz – K-

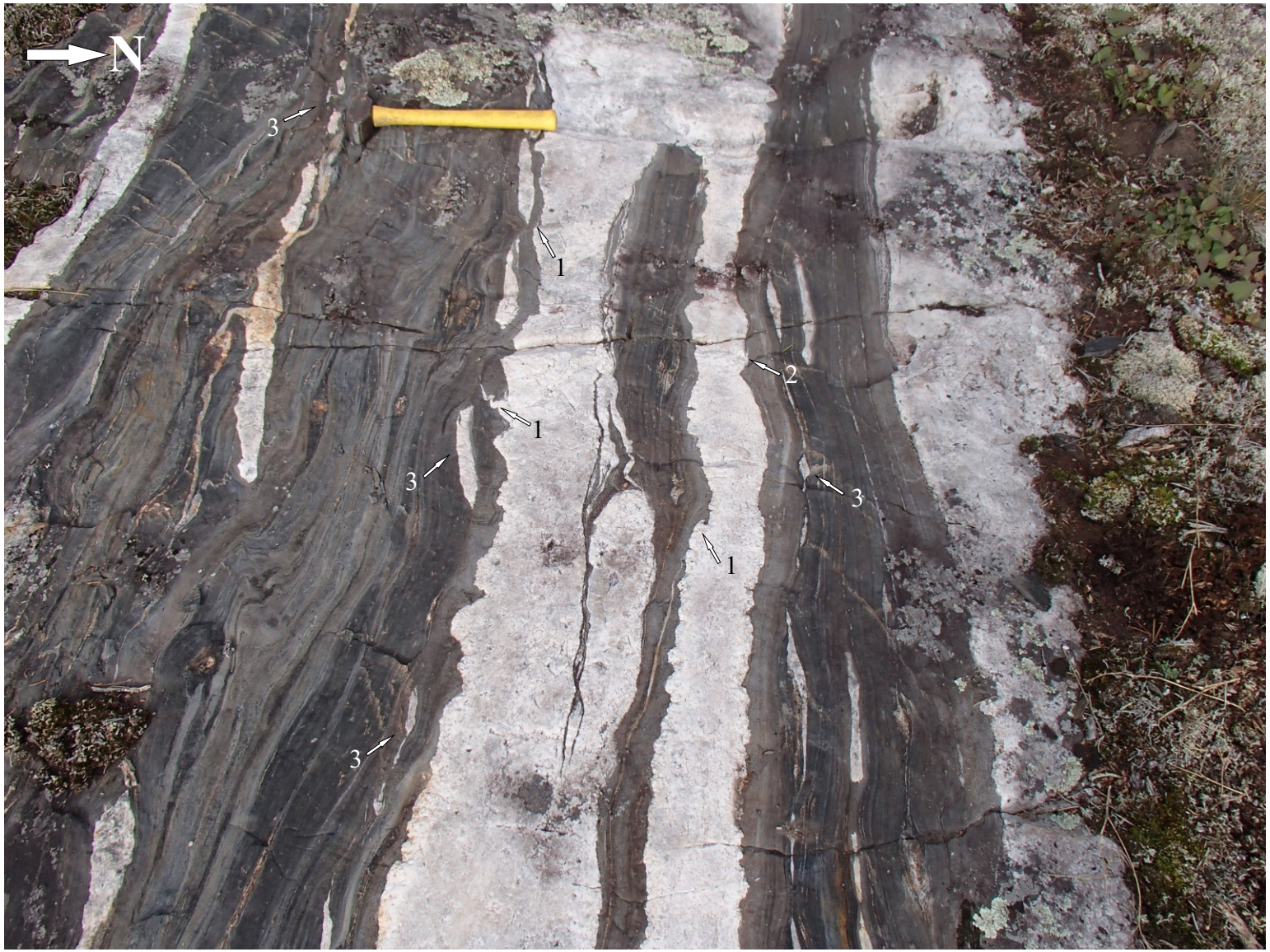

Figure 4.30. Contacts between the Snowbank pegmatite and basalt. Pegmatite contacts along the main dike cut basalt (centre) foliation. Both irregular (central dike) and curvi-linear (dike at right) contacts are present in dikes adjacent to each other. Sinistral asymmetry (1) and weak dextral asymmetry (2) developed by thin injections similar to tension gashes, of pegmatite oblique to P_L. A thin dike swarm flanks the main pegmatite dikes to form tapered, boudin trains with dextral asymmetry (3).

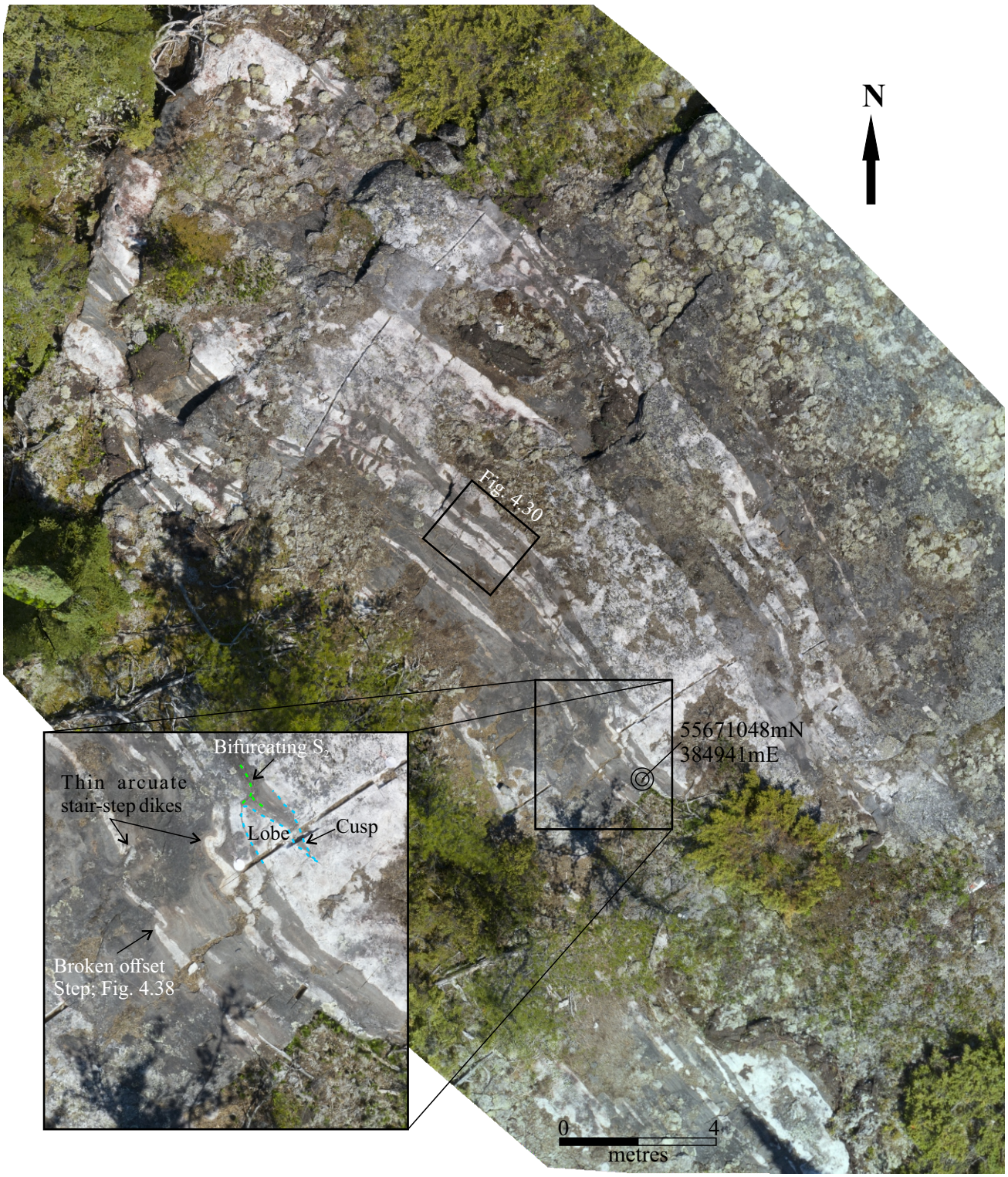

Figure 4.31. Drone image of the central exposure of the Snowbank pegmatite. Inset image of arcuate sinuous dikes. S_2 fabrics are distorted and folded to parallel curve of dikes. Local bifurcation of S_2 traces lobe contacts and terminates in cusp. Offset broken step evident in centre right of inset.

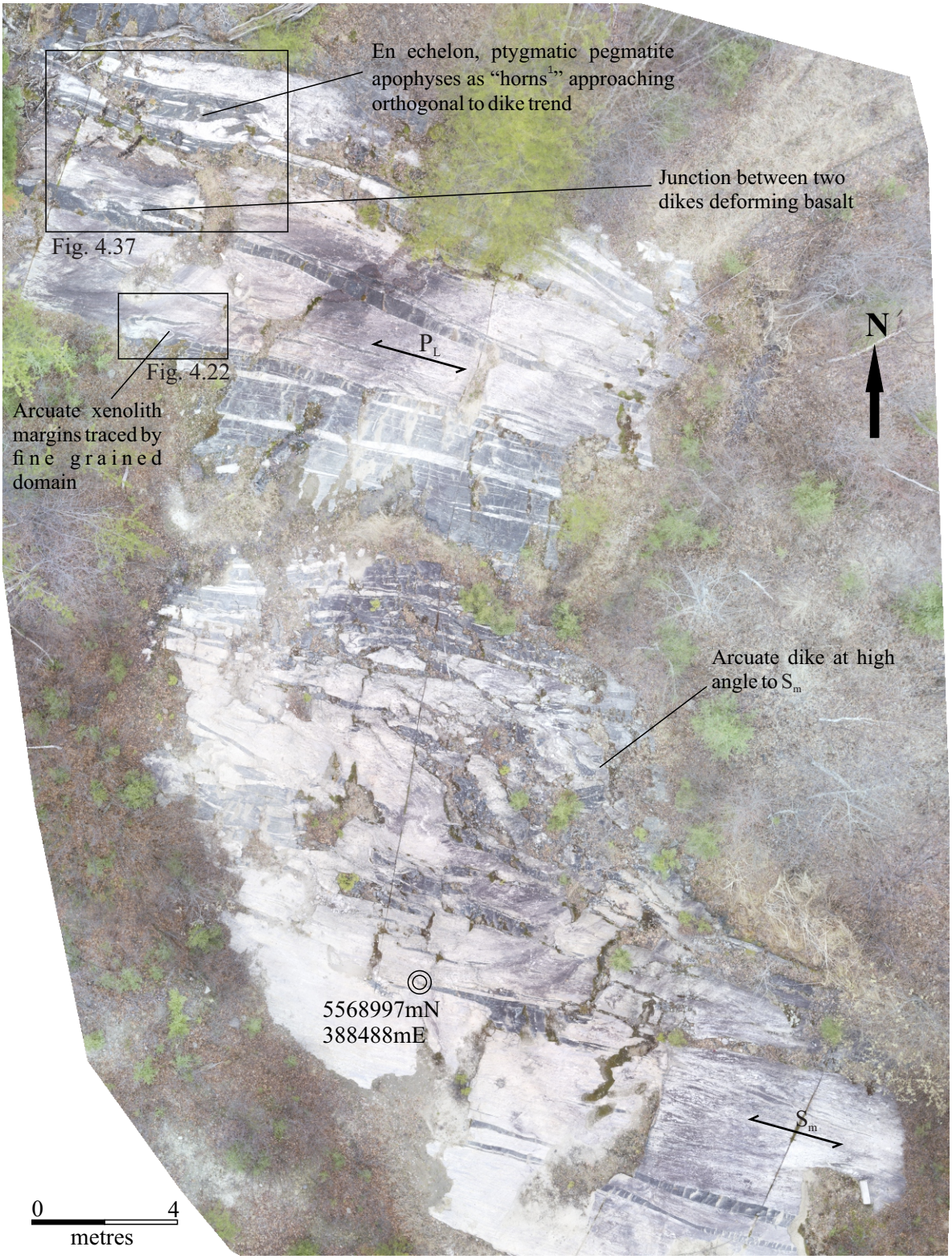

Figure 4.32. Georeferenced drone image along eastern extent of Big Whopper outcrop in lepidolite zone. Arcuate dikes in contact with basalt and basalt xenoliths. Xenolith margins occur at high angle to P_L and are traced by fine-grained porphyritic domain. Location given in Figure 4.2. [1]- Pollard *et al*., 1975

Figure 4.33. Dike contacts that trend orthogonal to S_2 at the Glitter pegmatite that illustrate blunted (1) and tapered forms distorting basalt fabrics. Basalt fabric traces tapers and terminates along blunted contacts at high-angle to fabric trend. Tapered dikes form train of boudins in upper part of image. Interleaved basalt on northern boudin contact (2). Foliation-parallel boudinage and ptygmatic folds cutting basalt fabric evident in <5cm thick dikes bottom right.

feldspar pegmatite, terminates along the contact with basalt, which is discordant to both P_L and S_2 (Figs. 4.19, 4.20).

4.3.5 Asymmetry

Elements of asymmetry are present in all the studied pegmatites from macro to micro-scales. The Big Mack pegmatite appears to be emplaced in a dilational jog that displays macroscale dextral asymmetry (Fig. 4.3, Figures 4.34, 4.35). The main body of the Big Mack pegmatite appears to dissect an earlier pegmatite (northern and southern lobes; Fig 4.34). If this interpretation is correct, the sense of displacement is also dextral. In both instances, paired acute angles exist between the intrusion morphology and the east-west, or north-south plane of symmetry. Mapping by Pryslak and Chastko (2001) indicated flanking albitite dikes lying above and below the main intrusion. These dikes parallel the main body of the intrusion, are oblique to the trend of the northern and southern lobes and may infer a deposit scale dextral s-c geometry with the Big Mack lying in the core of the mapped zone (Fig. 4.35).

At the Snowbank pegmatite, thin injections similar to tension gashes are developed along the margins of the dikes but display conflicting asymmetry across individual dikes with southern and northern contacts possessing tension gashes with sinistral and weak dextral asymmetry, respectively (Fig. 4.30).

Mesoscale asymmetry is also well developed at the Glitter pegmatite (Figure 4.36) with multiple dikes possessing arcuate forms similar to winged inclusions with the trend of the body rotated across the plane of symmetry of the dike (Fig. 4.36; cf. Grasemann and Dabrowski, 2015). In addition, thin dikes coeval with the main intrusion are locally boudinaged into dextral shearband

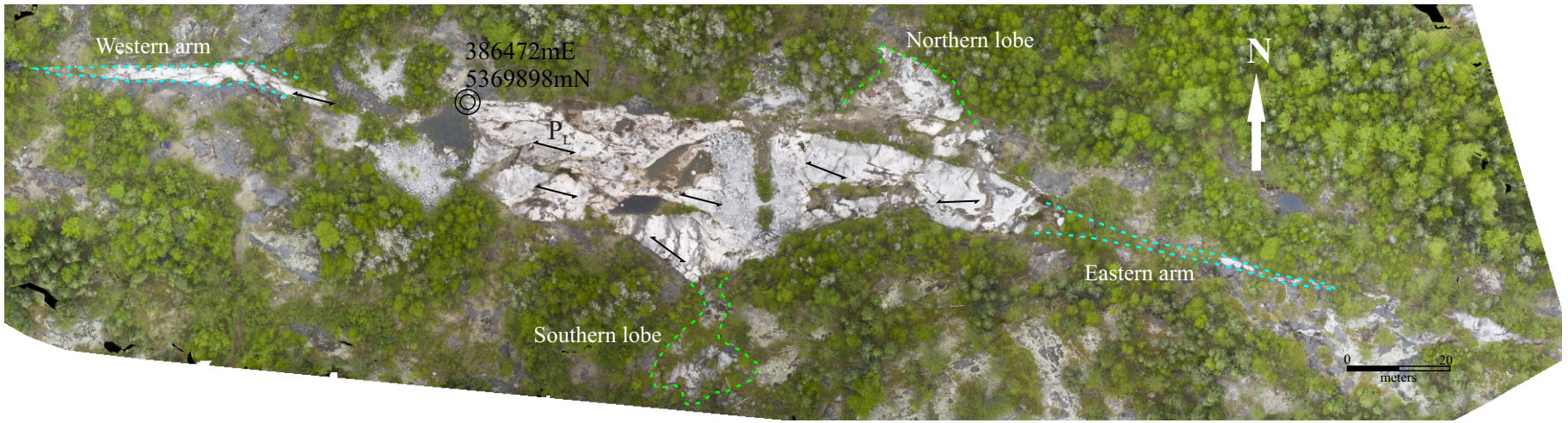

Figure 4.34. Drone image of the Big Mack pegmatite. The eastern and western arms of the pegmatite thin and pinch out away from the central body of the main intrusion. Magmatic foliations (P_L), vary from contact parallel to parallel that of the pegmatite trend. Dextral asymmetry of both the north-south lobes and east-west arms occurs across the east- and north- trending symmetry planes respectively.

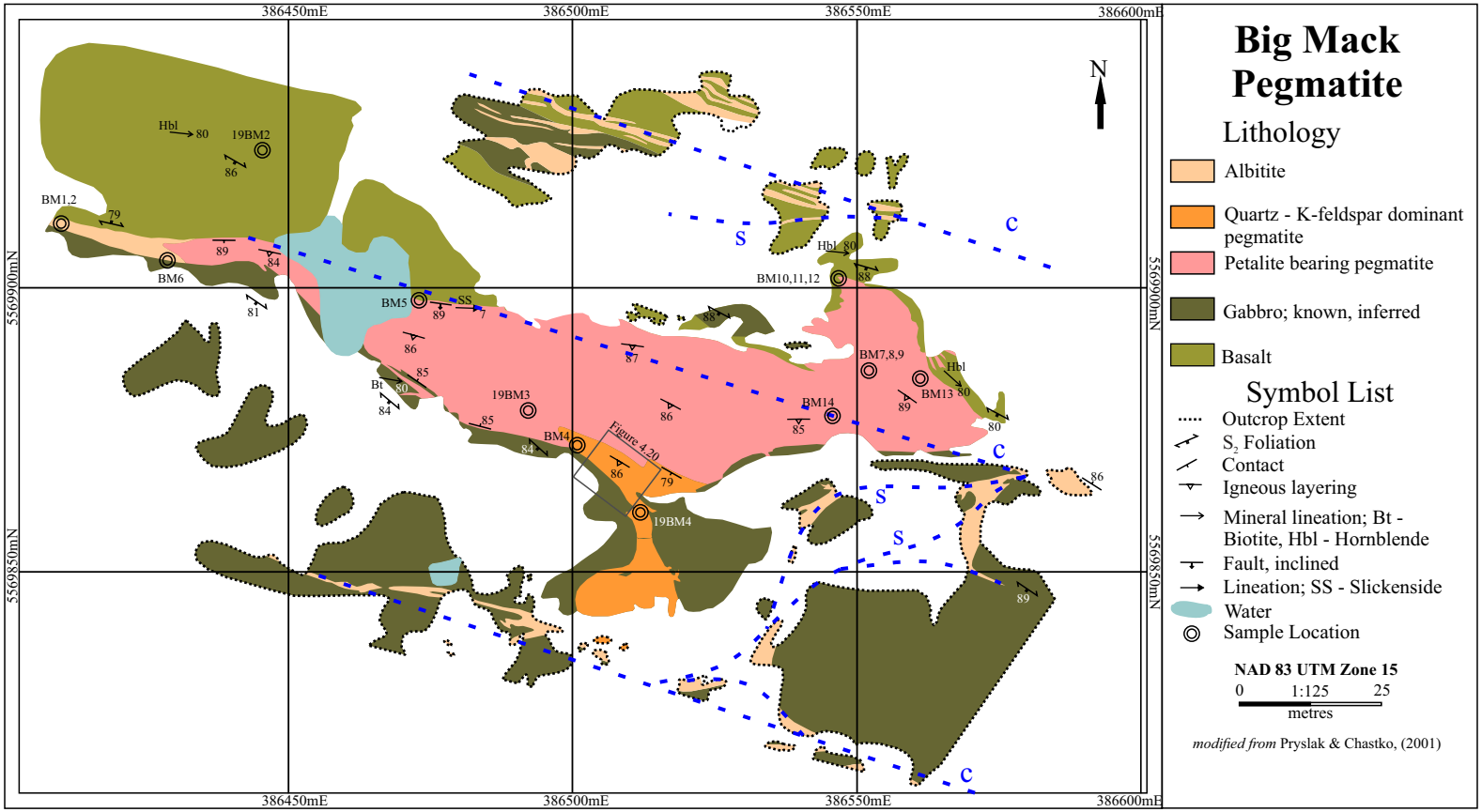

Figure 4.35. The Big Mack pegmatite overlain by interpreted s-c geometries evident from mapped dikes.

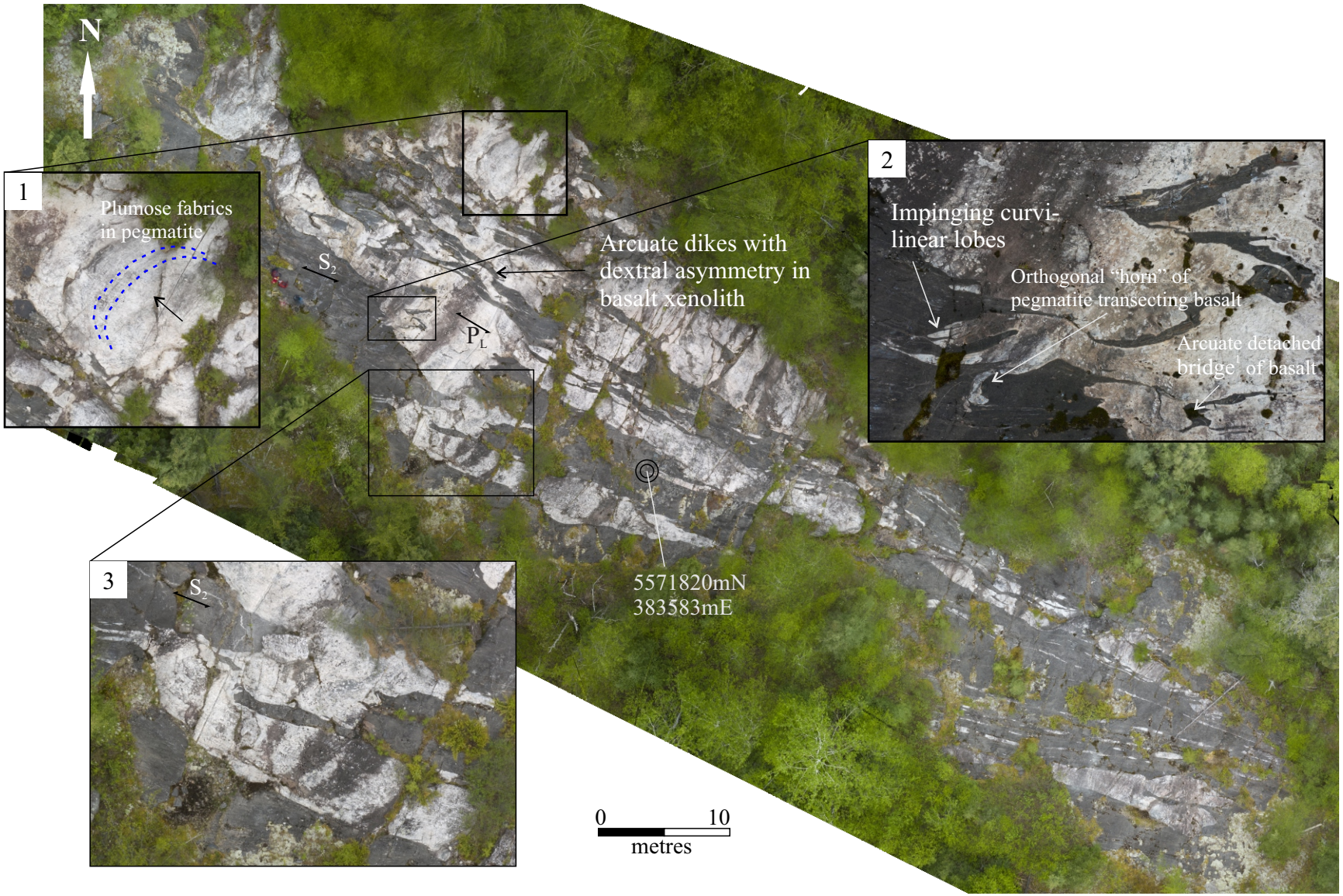

Figure 4.36. Drone image of the Glitter pegmatite. Inset 1 magnifies weakly developed repetitive plumose fabrics and fracture in the northern unit of the Glitter pegmatite, infers northwestern propagation. Inset 2 illustrates impinging fingers[1] of pegmatite along pegmatite contact wedging S_2 with a horn[2] transecting S_2. Severed bridge of basalt evident in bottom right. Inset 3 illustrates arcuate dike cutting regional S_2 folia in basalt and metre-scale cusps developed between pegmatite and basalt.[1] - Schofield *et al.*, (2010), [2] - Pollard *et al.*, (1975)

boudin blocks (Fig. 4.33; cf., Goscombe *et al*., 2004). No solid-state modification of the boudins is apparent at field or hand sample scales.

At the Big Whopper, mesoscale coeval dikes cutting xenoliths form dextral s-c geometries (Figure 4.37). Similarly, at the Snowbank pegmatite mesoscale structures such as shear-band boudin trains (Figs. 4.30, 4.33; Figure 4.38) and folded stair-step morphologies of thin dikes (Fig. 4.31, 4.38) are consistently dextral. At microscales these linkages are visible in both plan and profile, with 19SNO11b (Figure 4.39) recording a similar structure in profile as not broken with a continuous millimetre-scale dike (see Section 5.1.3) Microscale examples of shear-band boudins and s-c dike geometries were not encountered in this study.

4.3.6 Alteration

The S_2 foliation along the margins of xenoliths or in the wallrock adjacent to pegmatite contacts is truncated sharply by pegmatite and obliterated by an alteration halo of biotite ± holmquistite ± garnet (Figs. 4.23, 4.26). The alteration halo is adjacent to all pegmatite margins (Table 4.3), grading 1–5 cm into the country rock. The alteration zone may be thicker where thin, mm-scale, fluid-escape structures penetrate country rock fabrics or in areas where interleaved pegmatite and basalt impinge.

Biotite replaces up to 100% of the hornblende, with the long axis of crystal laths subparallel to the local trend of the pegmatite margin in outcrop (Figs. 4.23, 4.26). Replacement of the hornblende is discordant to the regional S_2 foliation. In outcrop, prismatic holmquistite occurs subparallel to the pegmatite contacts and overprints both biotite and any relict hornblende, locally imparting a violet-blue hue to the alteration halo. In vertical planes perpendicular to the pegmatite contact, holmquistite growth appears random and overprints biotite, whereas in contact-parallel vertical

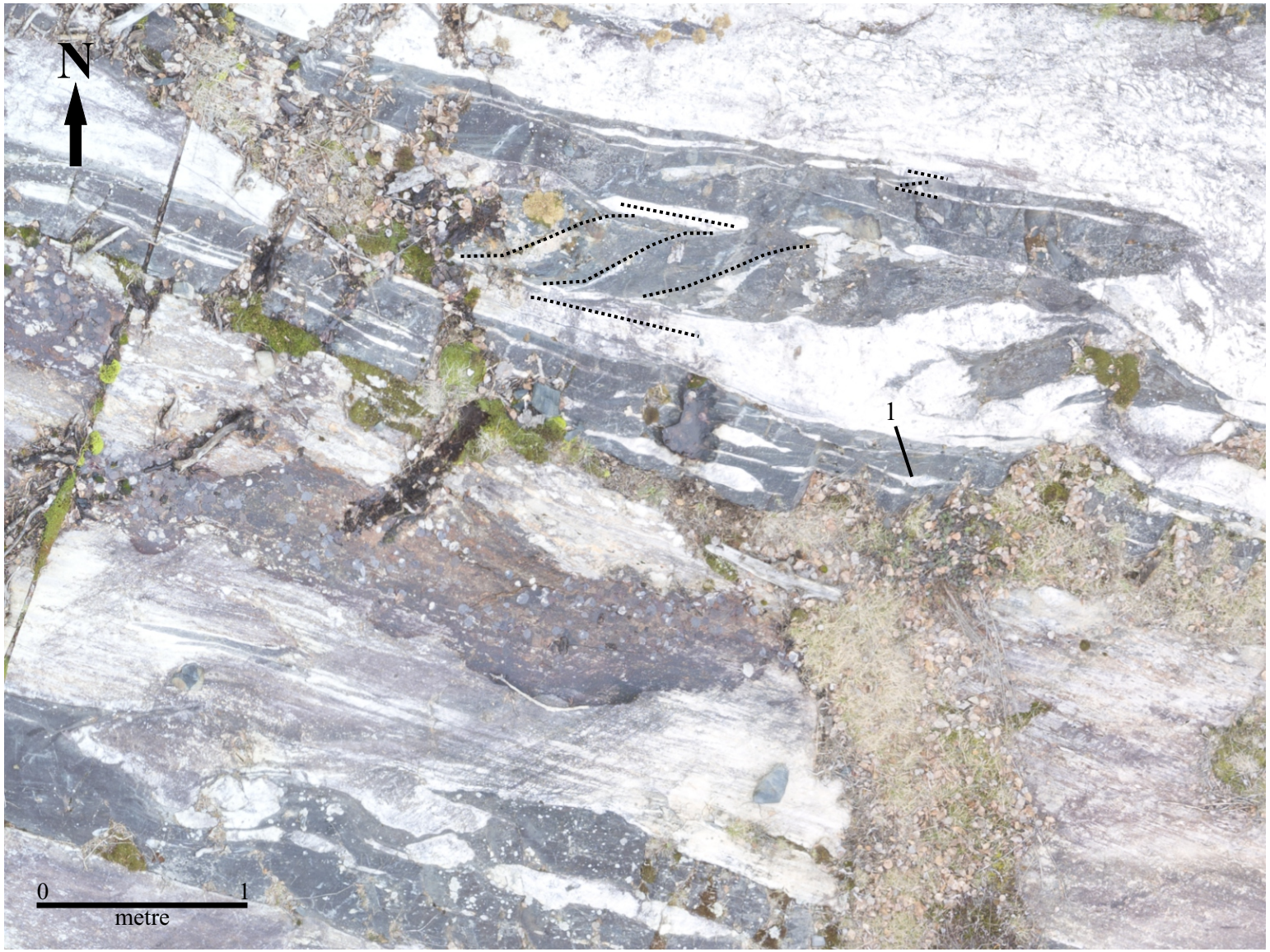

Figure 4.37. Dextral asymmetry in thin dikes similar to s-c fabric in deformed rock in the lepidolite zone of the SRp. Asymmetric boudin (1) in boudin train. Deformed septum of basalt (2) between multiple impinging pegmatite dikes to form composite bridge structure.

Figure 4.38. Arcuate dike linkage at the Snowbank pegmatite. Two overlapping dikes in basalt connected by a thin linkage with dextral asymmetry (centre). Basalt foliation, traced in green, is partially folded and re-oriented from its usual northwest-southeast trend to form flexure folds along the convex margins of the dikes. Dextral en-echelon shearband boudin train (1; cf. Goscombe *et al*., 2004) traces flexure in S_2 foliation.

Figure 4.39. Section view of two dikes cropping out in vertical plane of Snowbank pegmatite. Sample 19SNO11b collected and analyzed (see Section 5.1.3) across basalt bridge between dikes.

planes, holmquistite defines a weak, inconsistently developed, horizontal to slightly eastward-plunging lineation. In thin section, holmquistite transects and overprints biotite oblique to S_2 (Figure 4.40). Garnet occurs as embayed crystals within altered country rock that is cut by pegmatite and as euhedral to embayed crystals with original in pegmatite (Figs. 4.23, 4.26).

4.3.7 Deformation and metamorphism

In this study, at least two greenschist-facies metamorphic and deformation events postdating crystallization of the pegmatites have been identified and are recorded by localized solid-state deformation along the margins of the pegmatites. One event is non-penetrative in pegmatite and is accommodated by the adjacent wallrock along the periphery of the pegmatites. The second event is recorded only at the Big Mack pegmatite, where its northern and southern contacts show evidence of strike-slip dominant, sinistral features and greenschist-facies mineral assemblages. Sinistral drag folds along the southern contact coeval with pegmatite emplacement overprint initial dextral drag of the composite regional S_2 foliation (Figure 4.41). Discordance (up to 15^o) between the pegmatite arms and S_2 folia results in local, sinistral, flexural folds along the southern contact near sample BM6 (Figs. 4.3, 4.41). Along the northern contact of the pegmatite, a 10 cm wide, sinistral, brittle fault zone disrupts the wallrock (Figure 4.42). Slickenlines plunge shallow (<10^o) to the east (Fig. 4.3). Dextral deformation is noted adjacent to the peripheral contacts of the Big Whopper and Glitter and Snowbank pegmatites (*e.g.,* Fig. 4.26). Deformation is predominantly accommodated by the biotite-altered wallrock at all these locales (Table 4.3).

In thin section, solid-state shear bands overprint altered wallrock. Locally developed, recrystallized biotite forms dextral mica fish and felsic σ-type augen comprising quartz and albite (Figure 4.43). Based on the studied thin sections, greenschist-facies deformation textures in pegmatite are only developed in one location at the Snowbank pegmatite and penetrate less than

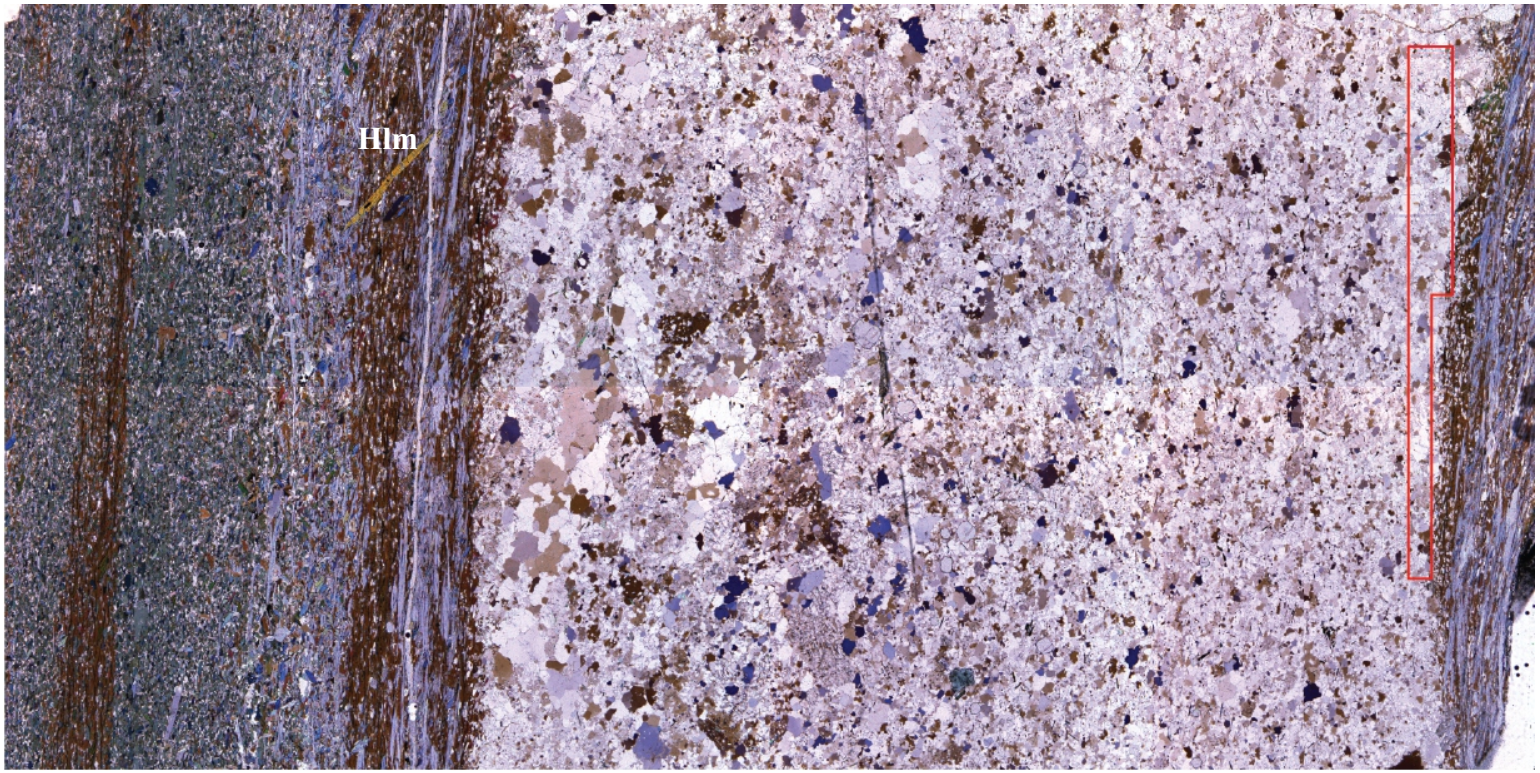

Figure 4.40. Thin section of 19GL1b in profile across thin dike. Brown biotite and purple holmquistite overprint dark green hornblende. Euhedral holmquistite upper left oriented at angle to S_2 foliation, pegmatite contact, and alteration halo. Hlm - Holmquistite Long axis 46mm. See Section 5.1.3 for analyses within red box at right.

Figure 4.41. Drag folds in basalt adjacent to Big Mack pegmatite. Initial dextral drag folding (blue) is overprinted by sinistral drag folding (green) of the composite regional S_2 hornblende-bearing schistosity evident along the western arm of the Big Mack pegmatite.

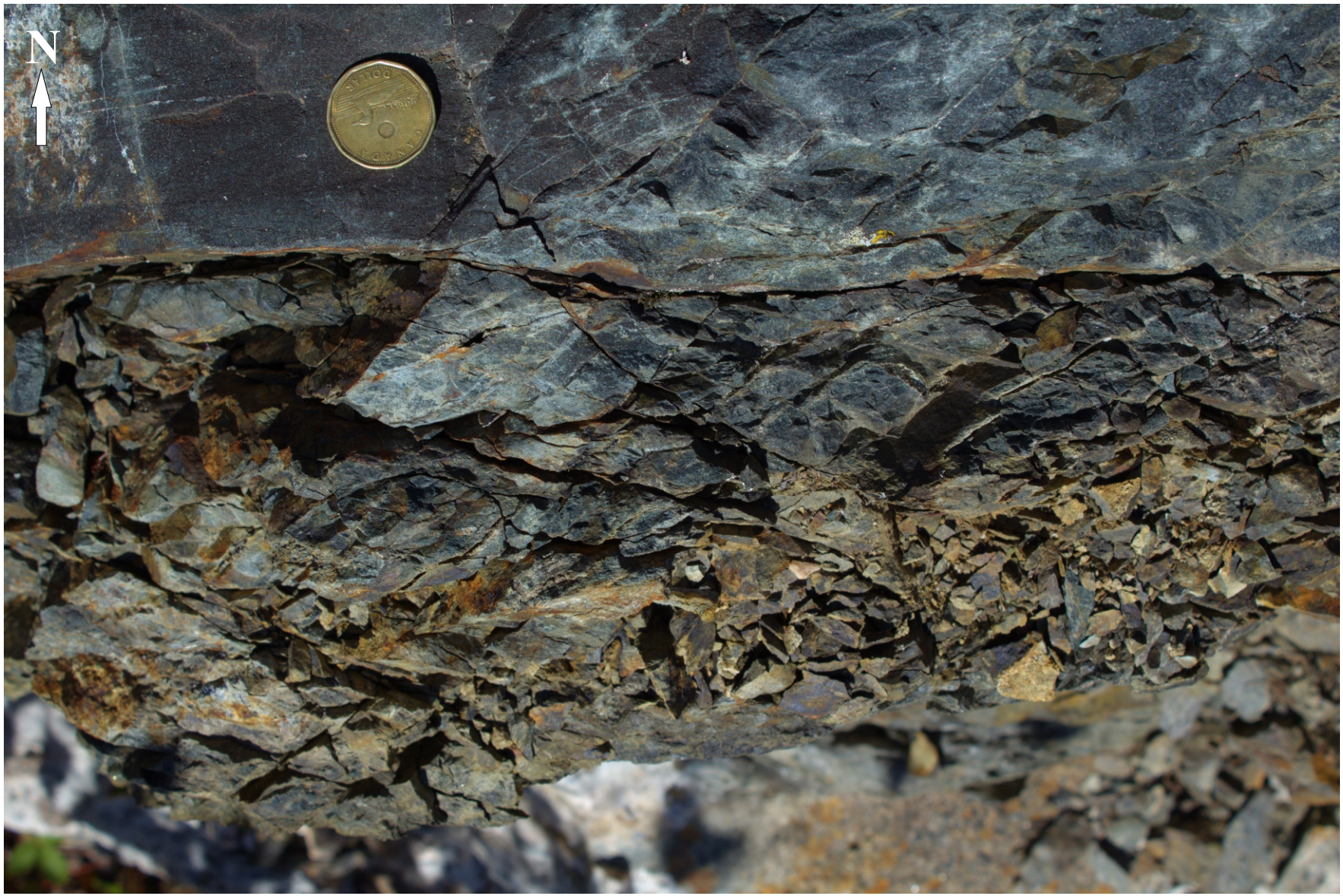

Figure 4.42. Brittle fault zone along northern contact of Big Mack pegmatite. Principle stress orientations derived from conjugate faulting indicates sinistral transcurrent movement with a minor dip-slip component.

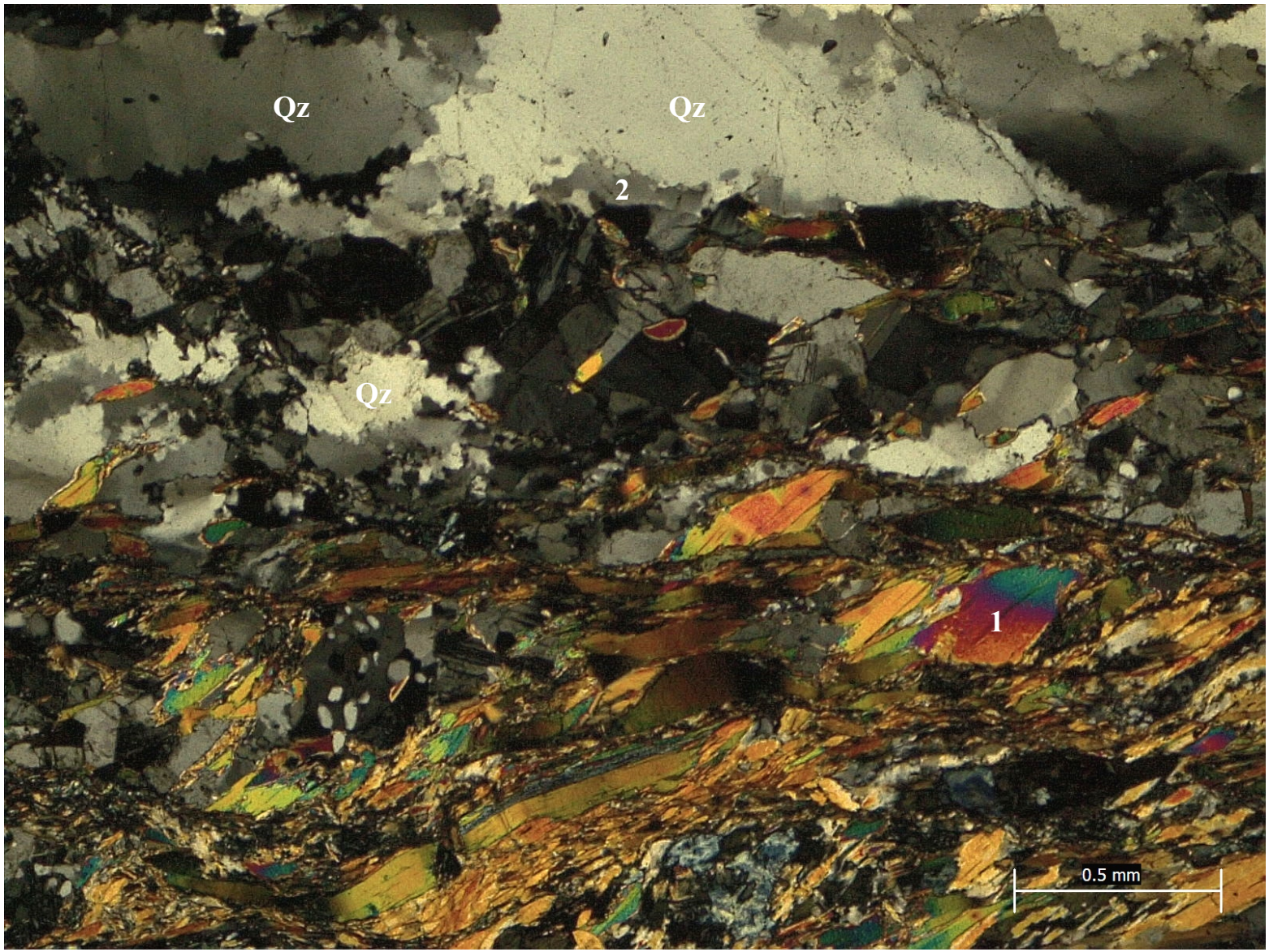

Figure 4.43. Crossed-nicols photomicrograph of deformed contact at the Snowbank pegmatite. (1) Biotite-altered basalt with dextral fish. (2) Grain size reduction in quartz grains adjacent to contact in pegmatite.

one centimetre into the pegmatite near sample SNO8 (Figs. 4.4, 4.43). Quartz at this location has experienced recovery during strain through grain size reduction and sub-grain rotation to form fine-grained aggregates. Fine-grained albite is recrystallized with equidimensional bent and tapered lamellae in augen.

Attenuated and recrystallized aplitic phases ("GWN aplites" in Tables 4.1, 4.2, 4.3) are identified in outcrop along the drill-access road northwest of the Big Whopper (Fig. 2.1). These aplites are fine grained, mineralogically homogeneous, and comprise albite, quartz ± orange-red garnet with trace amounts of very fine-grained, euhedral monazite and fine-grained, twinned cassiterite blebs. Recrystallized quartz augen are evident in hand sample. Thin sections oriented perpendicular to the foliation and parallel to the lineation indicate both albite and quartz are deformed in the aplite. Albite {010} forms an igneous layering parallel to the lineation and is recrystallized by transformation twinning to form equidimensional, bent, and tapered lamellae. Grain boundaries in elongated quartz are anhedral and affected by strain recovery and sub-grain rotation. All quartz crystals have low-grade undulatory extinction. Elongation in quartz and alignment of twin planes in albite-rich zones define a foliation that overprints possible magmatic layering.

4.3.8 Rock Fabrics

Disturbance to the regional foliation at each pegmatite is evident in outcrops examined (see Sections 4.2.2; 4.3.1-4; 4.3.6) with composite S_2 fabrics commonly rotated, truncated or obliterated adjacent to the intrusion contacts. The regional trend of S_2 is defined by hornblende along a northwest-southeast trend with pole distributions that occur near margins of the stereonet (Figure 4.44A), although some scatter is evident across the locations studied (Figure 4.44B). Measured hornblende lineations (L_2) plunge ~ 72° to the east-northeast. Local discordance of S_2 is present at

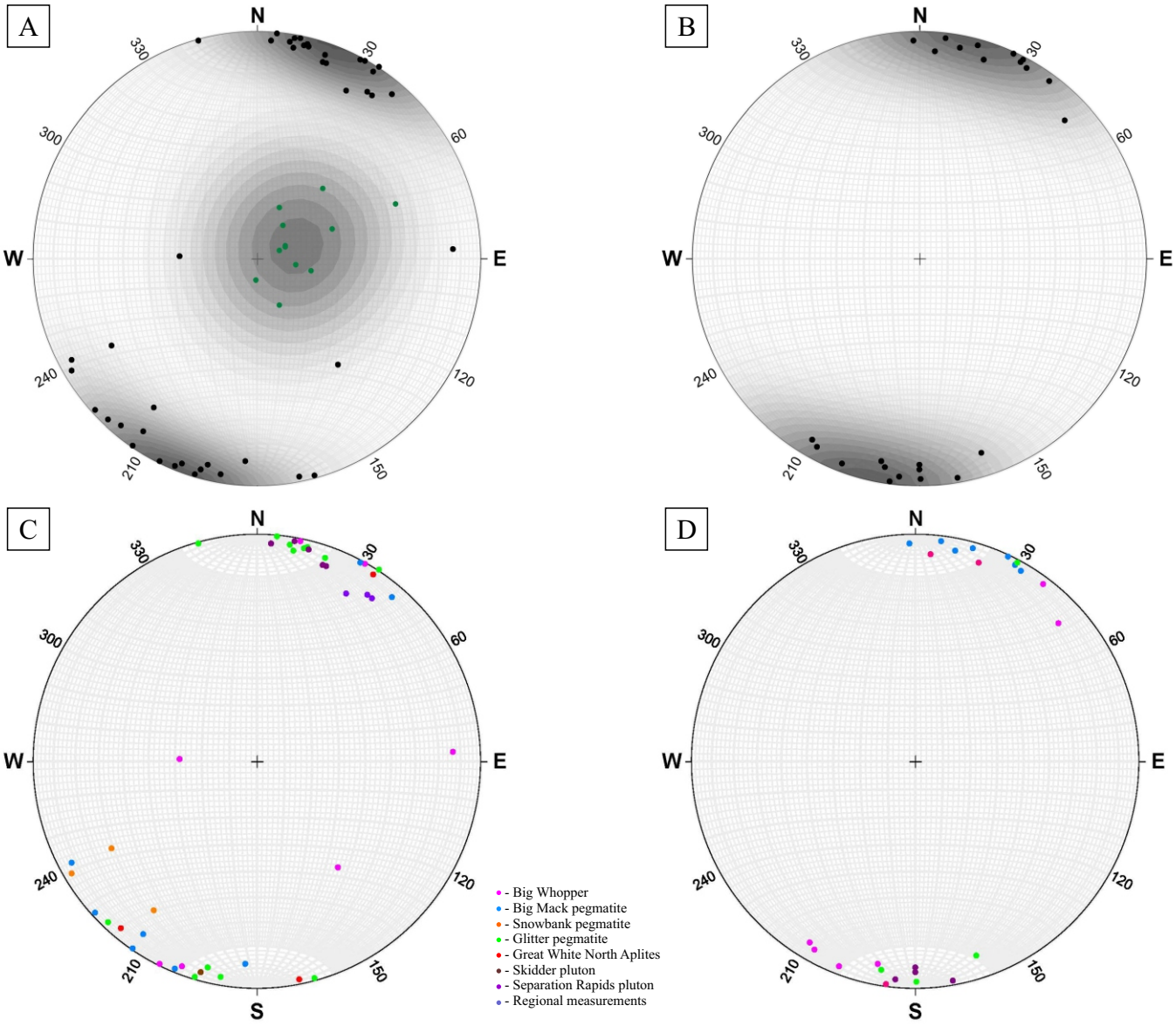

Figure 4.44. A) Contoured pole plot of measured S_2 foliations across the study area. Contours centre around 20 degree trend near the margins of the stereonet. Steeply plunging lineation for hornblende contoured trending east northeast in green; B) Contoured plot of P_L within each pegmatite illustrating similar trend as S_2; C) Grouped S_2 measurements colourized by nearby intrusion. Spread of data approaches 60 degrees for trend variation; D) Grouped P_L and S_L measurements colourized by intrusions illustrating minor discordance between units.

each pegmatite, with poles plotting over a spread approaching 60° along the primitive. At the Big Whopper a larger spread of data occurs with several measurements taken within xenoliths are markedly discordant in both trend and dip to both the regional S_2 and P_L trends (Figs. 4.27, 4.44C).

Mineral lineations in the pegmatites are rarely observed. Compiled orientations of P_L are subvertical with northwest-southeast trend among all pegmatites. Comparisons of the two compiled datasets for S_2 and P_L indicate a slight discordance of trend of ~5 degrees (Figure 4.44C). Comparisons between individual pegmatites indicates P_L within each pegmatite is oriented oblique to each other across the study area (Figure 4.44D).

4.3.9 Summary

Extensive planar and linear elements associated with solid-state deformation are not evident in the internal layers of the pegmatites, nor along xenolith margins, nor penetrating the pegmatite – country rock contact. Interactions between pegmatite and wallrock produced textures and structures, such as quench zones, granophyre, and magmatic schlieren (P_L), that trend easterly with subvertical dips subparallel to S_2. Regional S_2 folia are consistently truncated, rotated and obliterated along xenolith margins, and along dike contacts normal to S_2, S_L and P_L. Internal zones of the pegmatites lack penetrative foliations and recovery and recrystallization textures.

Chapter 5 Analytical Results

This chapter presents results from *in-situ* analytical techniques applied to both pegmatites and host rocks – specifically, textural analyses by electron back-scatter diffraction (EBSD) and U-Pb geochronological analyses by laser ablation–inductively coupled plasma–mass spectrometry (LA-ICP-MS). Various domains in the Separation Rapids pluton (section 4.2.2) and the Separation Rapids, Snowbank and Glitter pegmatites (section 4.3) were analyzed by EBSD. Uranium-bearing minerals in the Separation Rapids, Big Mack, Snowbank, Glitter and Marko's pegmatites (section 4.3), and the Great White North aplite (section 4.3.5), were analyzed to determine crystallization ages. Mafic volcanic host rock (section 4.1) and granitoid plutons (section 4.1.2) were also dated by LA-ICP-MS to determine the age of regional metamorphism and deformation.

5.1 Electron Back-Scatter Diffraction

Mesoscopic features documented in Chapter 4 such as boudinage, asymmetry, and folding, among others, would be expected to retain a crystallographic record of strain-induced recrystallization and recovery. Thin sections were produced from seven specimens and were analysed by EBSD to determine the level of strain in the rocks. Images of the thin sections analysed by EBSD are provided in Appendix A. Specimens were selected to characterize strain in (1) different textural layers within the main pegmatite intrusions, (2) fine-grained quench zones adjacent to country rock xenoliths in pegmatite, and (3) fine-grained quench zones on thin pegmatite dikes adjacent to the main pegmatite intrusions in locations where strain localization might be expected during solid-state deformation due to strength anisotropy between pegmatite and wall rock. The latter two types of specimens focus on the pegmatite–wall rock interface, where rheology contrast is also expected to be greater, and thus would be expected to be a locus for ductile strain.

Background

Background information for EBSD summarized below involves recovery, recrystallization, and the concept of misorientation of White (1977). Greater detail can be found in works by Hobbs *et al.,* (1976), White (1977), Lloyd *et al.,* (1997) and Vernon (2004).

In deformed crystals, the process of recovery and recrystallization develops characteristic microstructures. Grain boundaries of phases in rock are particularly important during deformation as multiple processes (e.g., dislocation creep, grain boundary sliding, phase transformation and twinning, grain growth, and diffusion) results in changes to the boundaries between neighbouring grains (Lloyd *et al.*, 1997; Vernon, 2004). Modification of grain shapes occur through dislocations of the crystal lattice, whereby defects in the crystal structure shift in response to deformation (Hobbs *et al.*, 1976; Vernon, 2004). As dislocations traverse the crystal lattice, interactions between multiple slip planes may result in "tangling" of dislocations where further progress and deformation is inhibited and hardens the crystal structure (White, 1977; Vernon, 2004).

To facilitate further deformation, recovery and recrystallization processes attempt to return the crystal to an undeformed state by reducing the number of tangled dislocations (Vernon, 2004) Recovery processes permit formation of strain-free sub-grains by organizing tangled dislocations into sub-grain boundaries, forming no new high angle (high energy) grain boundaries. Increased strain accommodated across the subgrain boundary will increase the angular rotation (misorientation) of the lattice between adjacent crystals (White, 1977). If during strain the recovery rate can mitigate increases in dislocation density, the subgrains or clusters of subgrains will misorient until they are discrete grains in relation to the original grain. Maximum misorientations are mineral specific and usually taken as a rough guide, with 10^{o} of misorientation the maximum in quartz (White, 1977). Recrystallization produces new grains by encapsulating strain free

volumes of material by the creation of, or movement of, grain boundaries in response to deformation within the same mineral (White, 1977; Vernon, 2004). New strain free crystal aggregates are typically the product of recrystallization and permit continued deformation (Vernon, 2004).

The following EBSD background information outlines the concepts of lattice orientation and misorientation between grains to quantify strain imparted to crystals. This is referenced to work by Vernon *et al.,* (1983); Lloyd *et al.,* (1997); Trimby *et al.*, (1998); Prior *et al.*, (1999); Wheeler *et al*, (2001); Passchier and Trouw, (2005); Wright *et al.*, (2011); Cross *et al.*, (2017a, b); and Morales *et al.*, (2018).

Electron back-scatter diffraction (EBSD) is a method that allows the quantification of strain imparted in specific microstructural environments to relict and recrystallized crystals *in situ* such as quartz, feldspars, hornblende, olivine and garnet (Trimby *et al.*, 1998; Prior *et al.*, 1999; Wheeler *et al*, 2001; Wright *et al.*, 2011; Cross *et al.*, 2017a, b; Morales *et al.*, 2018). Lattice orientations between two grains in a specimen can be described via rotation angles around unique axes where the rotation of one grain would map the lattice of the second grain, regardless of which grain is selected first (Lloyd *et al.*, 1997; Wheeler *et al.*, 2001). Plotting of the misorientation between grains on stereonets in the specimen reference frame can then be used to infer processes impacting crystals, such as sub-grain rotation recrystallization (Lloyd *et al.*, 1997). Utilizing EBSD, it is possible to quantify the extent to which deformation processes overprint original magmatic textures and orientations, such as imparting a crystallographic preferred orientation (CPO) and/or a reduction in grainsize through recrystallization and neocrystallization (Vernon *et al.*, 1983; Passchier and Trouw, 2005). Where a CPO exists solid state deformation processes such as dislocation creep or twinning are active (Passchier and Trouw, 2005; Prior *et al.*, 1999). Where no

CPO exists, deformation occurs by mechanisms not controlled by the crystallography such as frictional or diffusion accommodated grain boundary sliding (Prior *et al.*, 1999).

5.1.1 Layers within pegmatite (specimens BW14a, DL1)

To test for strain-induced recovery and recrystallization of the minerals that form primary layering, east-trending P_L at the Big Whopper (BW14a, Fig. 4.2) and S_L at the Separation Rapids pluton were analyzed by EBSD. Specimens were collected along the northern extent of the Big Whopper and from a fine-grained layer along the southern margin of the Separation Rapids pluton near the River Outcrop.

Specimen BW14a was collected along the northern extent of the Big Whopper in a zone rich in basalt xenoliths (Figs. 4.2, 4.25; Figure 5.1). In thin section, layering (P_L) in BW14a is defined by the preferred orientation of twinned albite and biotite laths. Uncommon, simple twins are evident in thin section. Quartz occurs in fine- to coarse grain sizes and undulatory extinction is present. Recovery and recrystallization textures in a few albite crystals is inferred from tapered and bent twin lamellae.

Specimen DL1, in the Separation Rapids pluton, was collected at the River outcrop (Fig. 2.1) immediately north of the dike swarm. Fine- to medium-grained layers show boudinage with pinch and swell textures present (Figure 5.2). Along trend to a zone of augen and shearband boudins illustrating dextral asymmetry, specimen DL1 was selected to test the degree of strain, if any, incorporated into the crystals. Albite and biotite define S_L with deflection of the latter locally around garnet crystals. Anhedral quartz shows undulatory extinction with growth twinned albite crystals typical. Recovery and recrystallization textures are not common in albite with biotite retaining pristine linear cleavages and sub- to euhedral forms.

Figure 5.1. Specimen BW14a in outcrop at the Big Whopper. Specimen collected from fine-grained muscovite-biotite-garnet schlieren in pegmatite near to basalt xenolith.

Figure 5.2. Specimen DL1 in outcrop at the the Separation Rapids pluton. Oriented sample taken of fine- to medium-grained boudinaged pegmatite sandwiched between megacrystic pegmatite. Shearband boudin train (1), augen (2) and possible S-C fabric (3) show dextral asymmetry and suggest crystals have experienced solid-state deformation.

Indexing indicates quartz-albite in BW14a and quartz-orthoclase in DL1 constitute the bulk of the minerals for both specimens (Figures 5.3A, 5.4A). The grain orientation spread (GOS; see Section 3.3) of the indexed phases is <2° of misorientation between grain pixels and the parent grain orientation, with uncommon maxima greater than 5° in the Big Whopper (Fig. 5.3B) and 5-6° in the Separation Rapids pluton (Fig. 5.4B). Quartz shows poor lattice-preferred orientation (LPO) with a moderately strong LPO in albite (Figs. 5.3C, 5.4C). Point maxima along Y for albite $[01\bar{0}]$ in BW14a record a preferred orientation of (010) parallel to layering (Fig. 4.44D), whereas $[01\bar{0}]$ in DL1 shows a LPO in both north-south trends parallel to layering as well as northwest-southeast trends oblique to layering and regional S_2 folia (Fig. 4.44C).

Frequency plots of the interphase misorientation angle between quartz and albite (Figs. 5.3D, 5.4D) show a uniform distribution where both the angles of misorientation between non-neighbour and neighbour grains trace an expected distribution in a random (uniform) texture (cf. Grimmer, 1979) in low strain environments (cf. Trimby *et al.,* 1998). Annotated with crystallographic axes for quartz and albite, inverse pole figure projections of the interphase misorientation axis are unevenly distributed (2.5 kernel density; Figs. 5.3E, 5.4E) and record a lack of preferred orientations between quartz and albite.

5.1.2 Pegmatite adjacent to xenoliths (specimens BW18a, GL3d)

To determine the extent of strain-induced recovery and recrystallization in the Big Whopper and Glitter pegmatites adjacent to xenoliths, specimens BW18a (Fig. 4.2, 4.25; Figure 5.5) and GL3d were collected (Fig. 4.5; Figure 5.6) respectively. Lineations in pegmatite are not evident. Specimens were cut orthogonal to the contact with basalt with thin sections cut in profile to include biotite alteration in basalt, the pegmatite quench, and pegmatite (e.g. Figs. 4.23, 4.26).

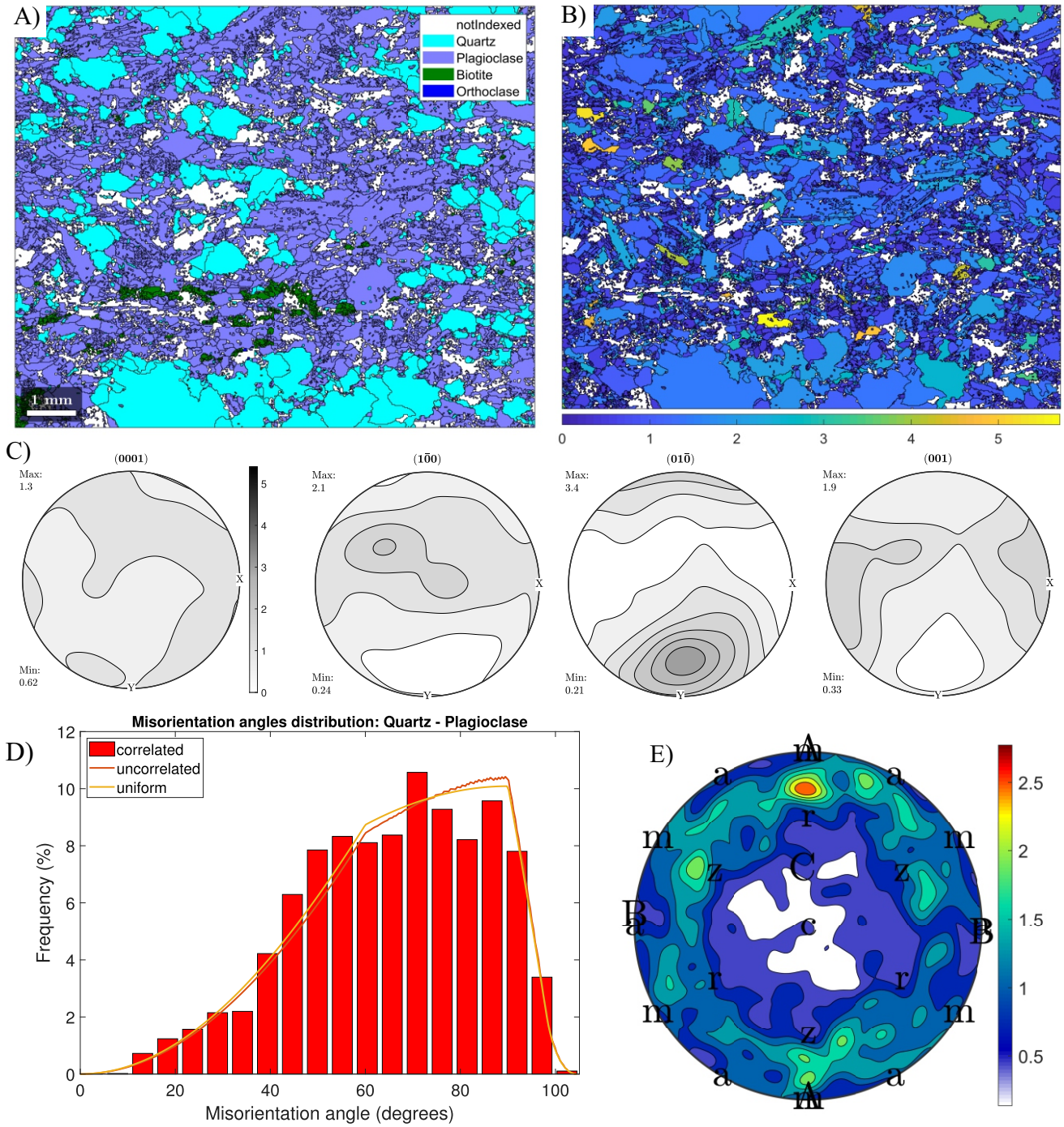

Figure 5.3. EBSD results for section BW14a. All plots contoured using a kernel density function estimation via diffusion (Botev et al., 2010) with a halfwidth of 10 degrees. A) Mineral index map; B) GOS map illustrating <2° misorientation. Infrequent grains of up to 5° misorientation recorded; C) Quartz (0001) and Albite (100; 010; 001) lower hemisphere plotting low preferred orientation. Point maxima in (010) represents alignment of b-planes parallel to layering (XZ plane). D) Frequency plot of misorientation angle distributions between quartz and plagioclase approaching uniform distribution. Adjacent neighboring grains are correlated where recrystallization may impact the adjacent crystal, uncorrelated are non-neighbor grains where recrystallization of one grain would not impact the other. Uniform textures are a random distribution of misorientations expected in a crystallite (Grimmer, 1979); E) Inverse Pole Figure (IPF) of the misorientation axis distributions illustrating low preferred orientation between quartz and albite crystals.

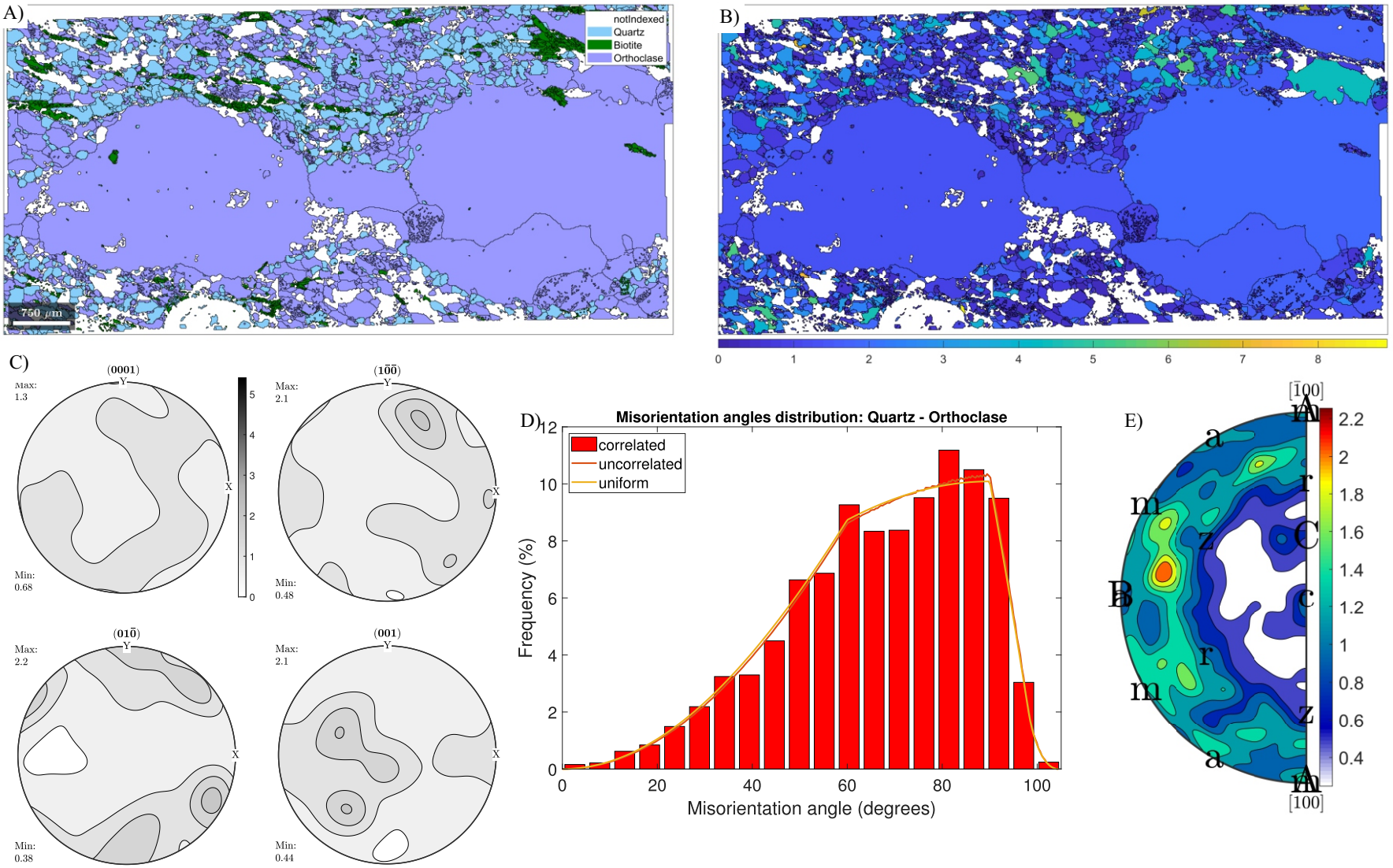

Figure 5.4. EBSD results for specimen DL1. A) Mineral index map; B) GOS map of indexed phases of differing grain size domains. Coarse grained phases contain <2° of misorientation between individual pixels and parent grain orientation. Fine grained phases contain up to 5-6° misorientation in irregularly distributed grains; C) Weak to moderate lattice preferred orientation in Quartz (0001) and orthoclase (100; 010; 001). D) Frequency plot of misorientation angle between quartz and orthoclase tracing a uniform distribution; E) IPF map of the misorientation axis distribution between quartz and orthoclase lattices. Plot records low kernel density (<2.2) and uneven distribution of maxima.

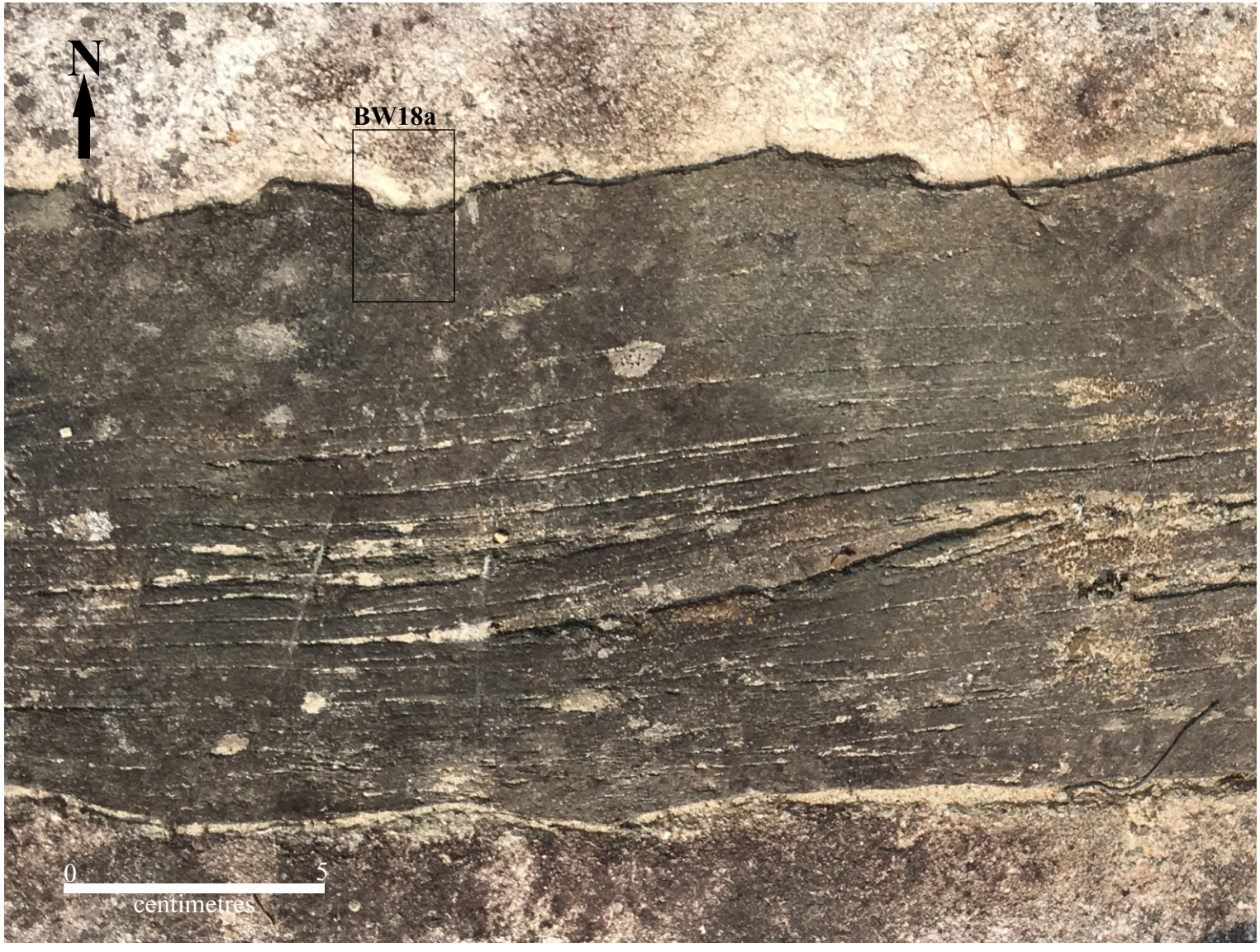

Figure 5.5. Specimen BW18a collection site. Thin section for EBSD cut facing West through contact between pegmatite and basalt xenolith.

Figure 5.6. Specimen GL3d collection site at the Glitter Pegmatite the contact between pegmatite and xenolith. Thin section cut facing West across contact.

Analyses were completed in the quenched pegmatite to verify if strain-induced modification penetrated the pegmatite or is confined to the basalt.

In BW18a thin section altered basalt shows deformation textures and anastomosing fabric in biotite altered domain inferred to be dextral (Figure 5.7). Adjacent to pegmatite, basalt shows irregularly oriented pristine biotite growth at the contact. The pegmatite quench is very fine- to fine-grained quartz-albite that abruptly shifts to medium-grained quartz-albite pegmatite.

Records of strain induced deformation in GL3d occur as millimetre scale en echelon quartz-albite drawn boudins and minor shear band development adjacent to pegmatite (Figure 5.8). Biotite replaces hornblende in basalt throughout the thin section. Sub-millimetre scale quenched albite-quartz pegmatite transitions into fine-grained pegmatite <1 cm from the basalt contact. Linear growth twins are common in albite. Minor amounts of corroded subhedral garnet are present within the quenched pegmatite. Anhedral quartz and albite grains show sparsely distributed recrystallized crystals with low-grade undulatory extinction and tapered twins respectively.

Mineral indexing records quartz and albite as the major phases in the pegmatite of BW18a with biotite concentration increasing into the quench approaching the contact (Figures 5.9A, 5.10A). A uniform GOS of <2º is determined within the quench zones adjacent to the basalt with an increase of up to 8º (BW18a) and 6º (GL3d) present in sparsely distributed crystals in coarser-grained layers (Fig. 5.9B, 5.10B).

Lattice-preferred orientation (LPO) for quartz *c*-axis analyses plot a point maximum oriented parallel to the pegmatite – xenolith contact in the plane of XZ but oblique to the orientation of albite for BW18a (Fig. 5.9C), and a weakly defined lineation lying in the plane defined by a single girdle parallel to the contact in GL3d (Fig. 5.10C).

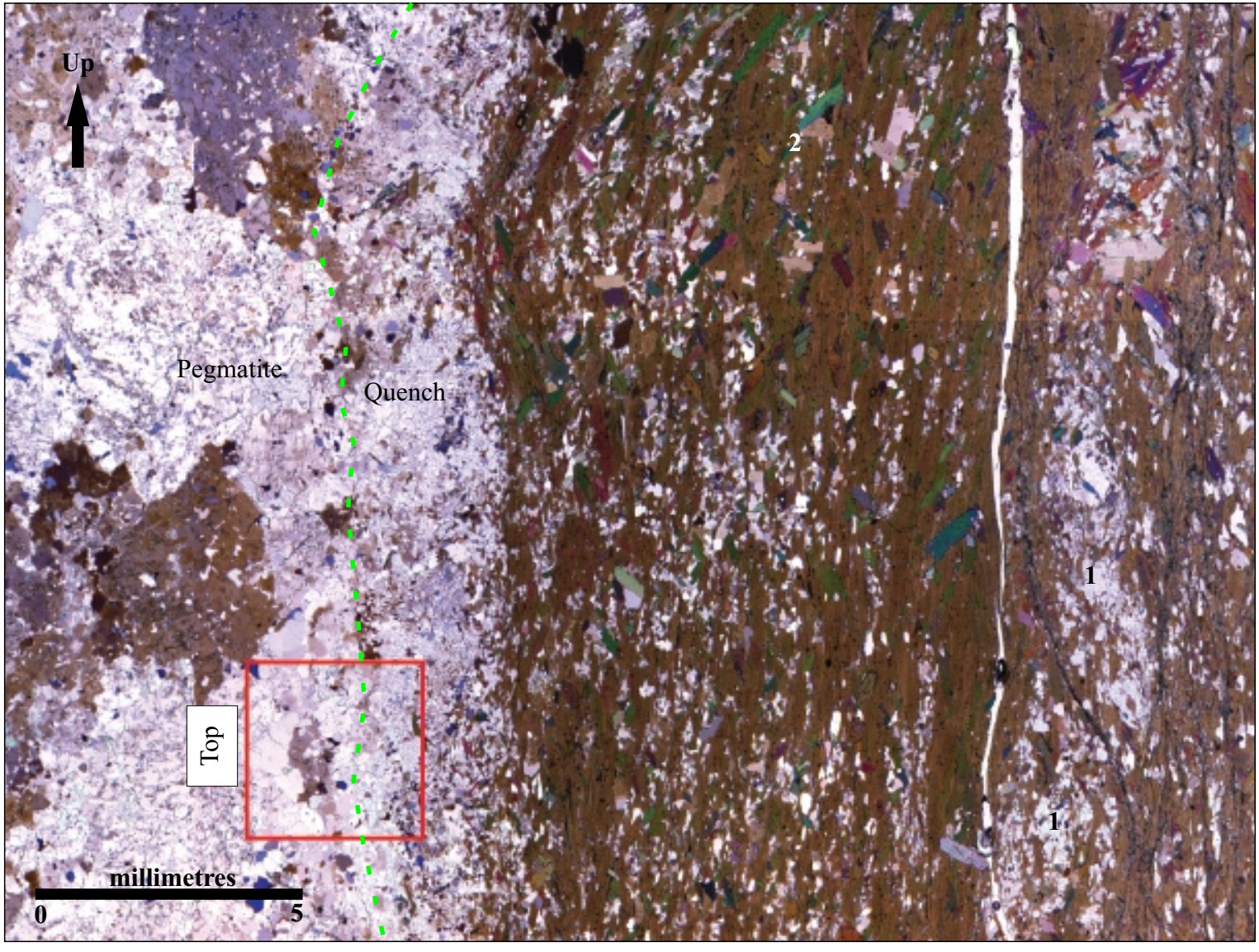

Figure 5.7. Thin section scan of BW18a in profile across the contact between pegmatite and xenolith. Pegmatite quench demarked by green line. Anastomosing structures enveloping quartz-albite (1) and irregularly oriented pristine biotite (2) in altered basalt. EBSD analysis region and orientation given in red.

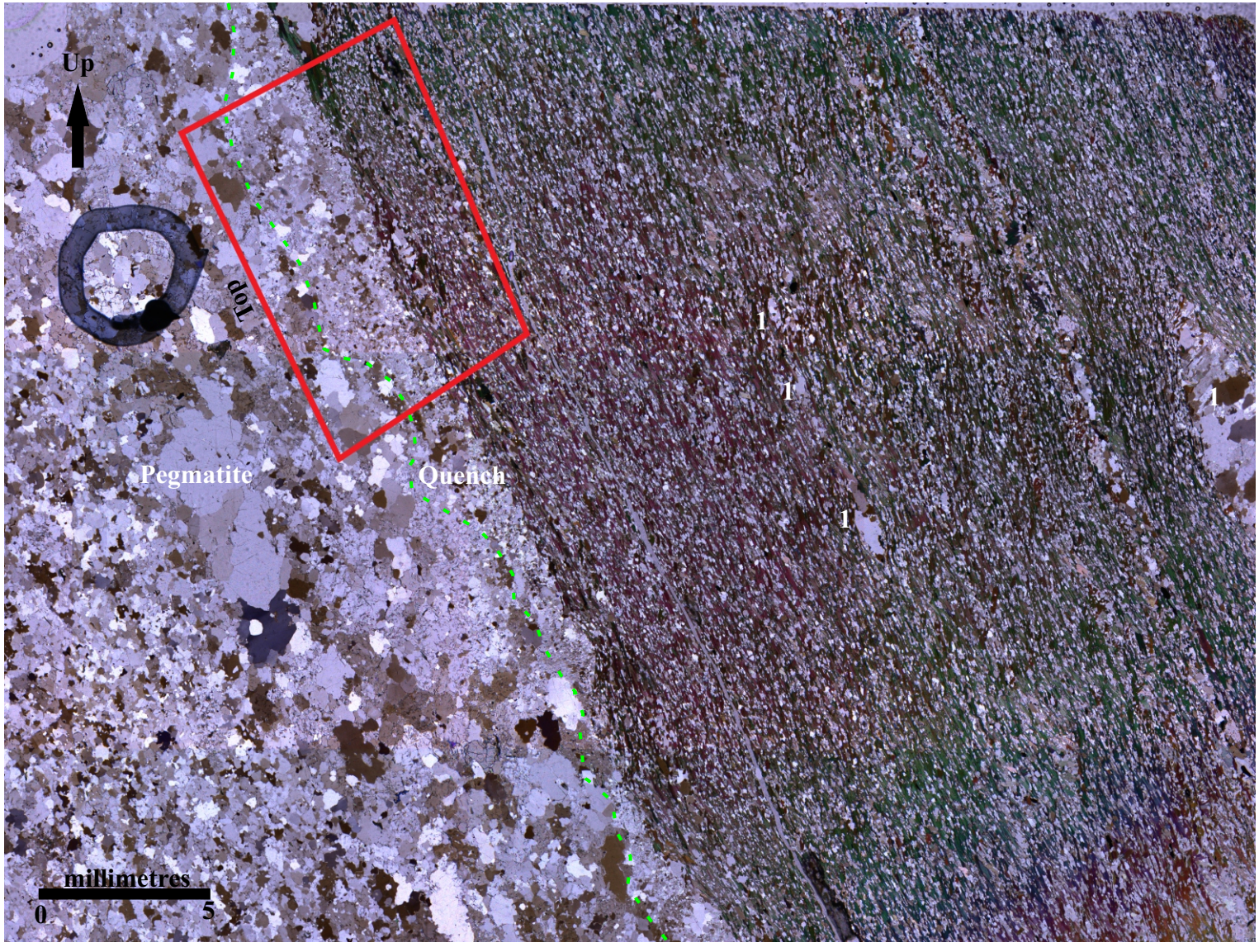

Figure 5.8. Thin section scan of GL3d in profile across the contact between pegmatite and xenolith. Pegmatite quench demarked by green line. Quartz-albite boudins at left (1) and a millimetre-thick zone of shear bands adjacent to the contact suggest normal movement (sinistral) in relation to pegmatite.

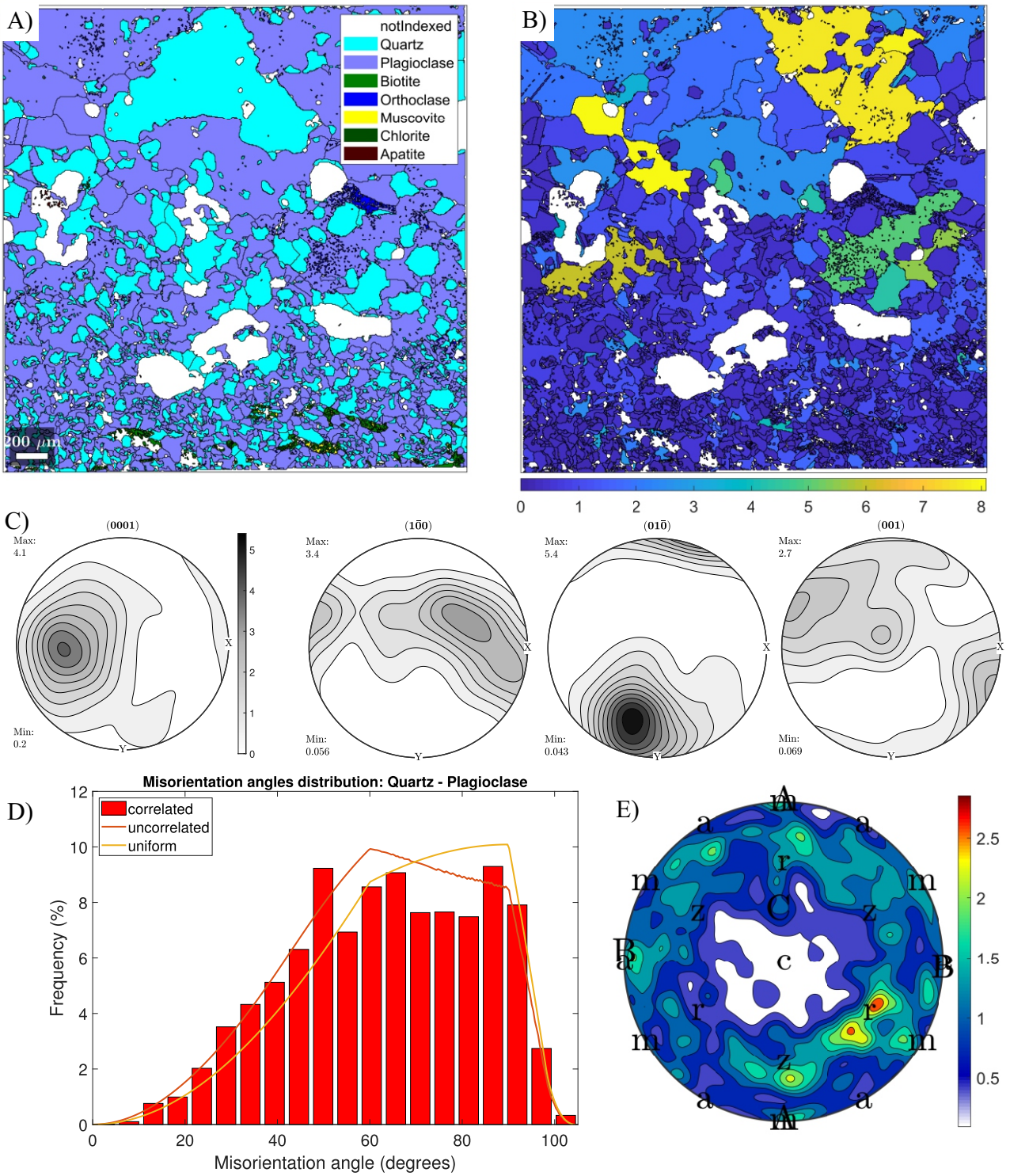

Figure 5.9. EBSD results for specimen BW18a. A) Mineral index map; B) GOS map recording <2° spread in fine grained crystals. Coarser grained crystals indicate a spread up to 7° misorientation between individual pixels and the grain orientation. C) Lower hemisphere pole plots of quartz (0001) and albite planes (100; 010; 001). Point maxima in quartz, (0001), lie parallel to the contact in the plane of XZ and oblique to the albite orientation. Point maxima in [010] reflects b-plane orientations of albite parallel to the contact; D) Frequency plot of misorientation angles diverging from a uniform distribution; E) IPF plot of crystal lattices of quartz and albite illustrating low preferred crystallographic orientation.

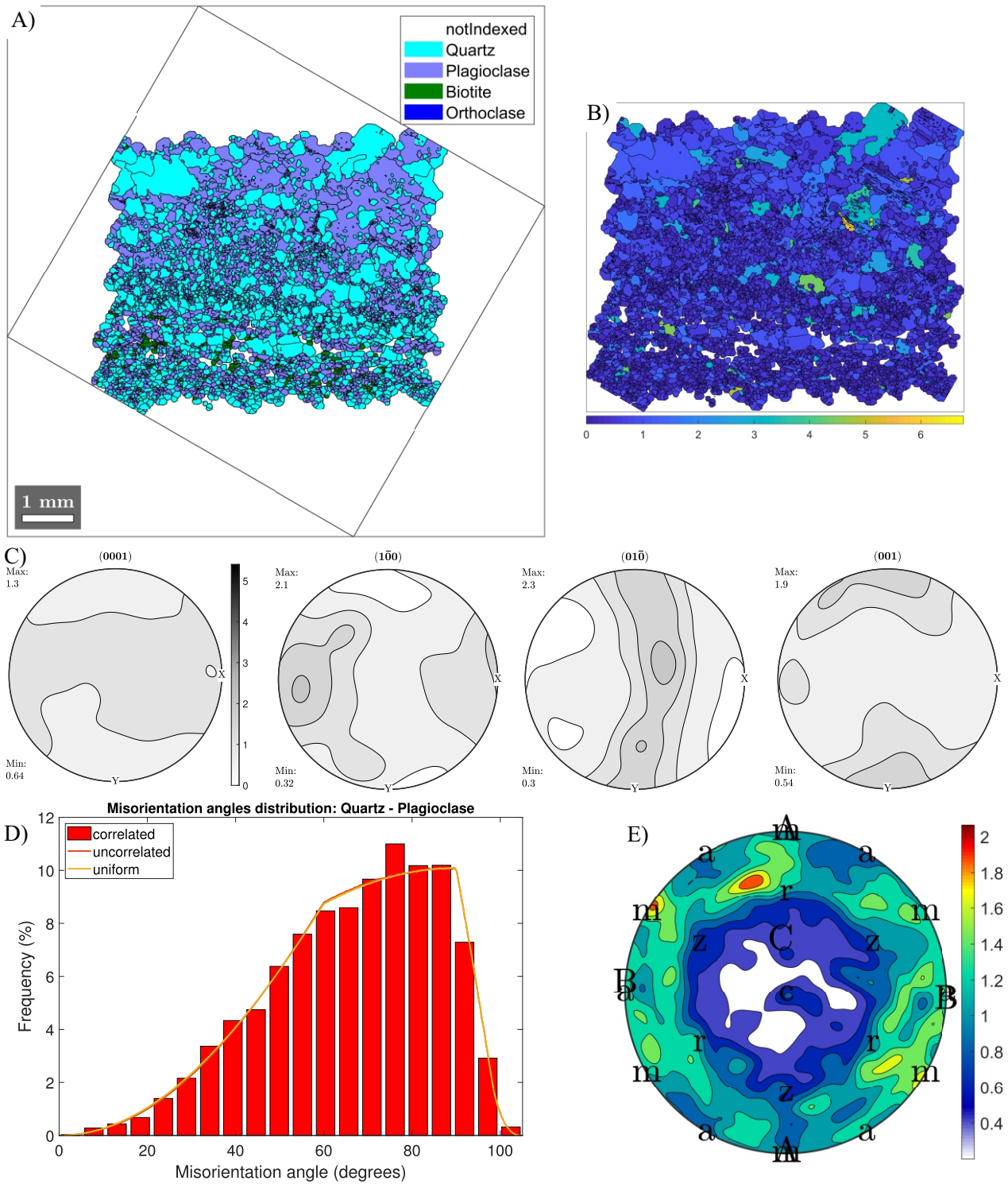

Figure 5.10. EBSD results for specimen GL3d. A) Mineral indexing; B) GOS map expressing <2° of spread between pixels and average orientation of the grain; C) A single girdle of poles in (0001) display a weak single girdle that define a plane parallel to the contact. Albite fabrics display a point maxima in [100] parallel to the contact and a plane defined by a single girdle in [010] orthogonal to the contact. D) Frequency plots of the misorientation angle between quartz and plagioclase follow that of a uniform trend; E) IPF plots of the interaction between quartz and albite lattices illustrate a lack of preferred orientation (maxima <2.2).

LPO plots for albite $[1\bar{0}0]$ in BW18a record a single girdle parallel to the contact between the pegmatite and xenolith (XZ plane) with point maxima defined by $[01\bar{0}]$ orthogonal to the contact with resultant twin interfaces oriented subparallel to the contact with basalt. Specimen GL3d, however, records point maxima for $[1\bar{0}0]$ oriented subparallel to the contact, while $[01\bar{0}]$ plots a plane defined by a single girdle orthogonal to the contact.

Interphase (quartz-albite) misorientation angle plots of specimen BW18a (Fig. 5.9D) illustrate a maximum in misorientation from 10 to 50° for adjacent albite and quartz and a weak correlation by the misorientation axis (Fig. 5.9E) to indicate a low preferred orientation. In specimen GL3d, interphase misorientation angles follow a uniform distribution (Fig. 5.10D) and there is a weak correlation of the interphase misorientation axis (<2.2 kernel density, Fig 5.10E).

5.1.3 Thin pegmatite dikes (specimens 19SNO11b, 19GL1b, 19GL2b)

Extensive solid-state deformation inferred by previous authors is tested along the margins of thin dikes at the Snowbank and Glitter pegmatites. Volumetrically minor, thin pegmatite dikes were selected to highlight the rheology contrast between pegmatite and basalt. In rock deformed in the solid state, strain-induced recrystallization and recovery would be expected and recorded in boudin necks and linear attenuated dikes representative of rocks in tension as well as along limbs or hinges of folds in rocks experiencing compression. Three sites were selected for analysis: (1) boudin neck at the Snowbank pegmatite (19SNO11b; Figs. 4.4, Fig. 4.39); (2) thin planar dikes oriented parallel to S_2 folia at the Glitter pegmatite (19GL1b; Fig. 4.5; Figure 5.11); and (3) folded dikes that dismember S_2 folia in the Glitter pegmatite (19GL2b; Figs. 4.5; 4.29). Metasomatic haloes of biotite ± holmquistite overprint the S_2 foliation in basalt adjacent to the pegmatite in all three specimens.

Figure 5.11. Attenuated dike in the Glitter pegmatite. Specimen 19GL1b collected to test for record of strain in volumetrically minor pegmatite.

Specimen 19SNO11b was sectioned in profile and targeted an arcuate linkage in a boudin neck (Fig. 4.39; Figure 5.12). Fine-grained anhedral quartz and fine- to medium-grained growth twinned albite crystals intergrown with quartz occur adjacent to the contact. Albite crystals with sub-to euhedral crystal faces occur and distort the contact between pegmatite and basalt to form cusps. The dip of S_2 is oriented at angle to contacts with biotite-altered basalt fabrics reoriented to parallel the pegmatite contact.

Specimen 19GL1b was collected across a thin dike in basalt at the Glitter pegmatite. Contacts between pegmatite and basalt are curvi-linear in outcrop and irregular at thin-section scale (Fig. 5.9; Figure 5.13). Albite and quartz are the dominant minerals in pegmatite with hornblende, biotite, quartz, albite, and holmquistite present in basalt. Anhedral fine- to medium-grained quartz shows low-grade undulatory extinction with granophyric albite present throughout the thin section. Poikilitic albite with quartz is common with infrequent simply twinned alkali feldspar crystals present. Minor biotite and flakes of muscovite comprise the mica present in the pegmatite. Holmquistite laths overprint biotite metasomatic fabrics (Fig. 5.13).

A folded, thin dike (specimen 19GL2b) was selected for EBSD to determine whether a fabric was imparted on the pegmatite during folding. A several mm wide weakly developed sinistral S-C fabric is developed in altered basalt which is in sharp contact with fine-grained pegmatite (Fig. 4.29; Figure 5.14). Contact parallel layers of medium-coarse skeletal quartz define P_L. Quartz and albite are the main minerals with garnet, apatite, biotite and muscovite present. Undulatory extinction is present. Transformation twinning is not well developed in section with growth-twinned albite lamellae typical. Textures indicative of crystals accommodating strain are uncommon.

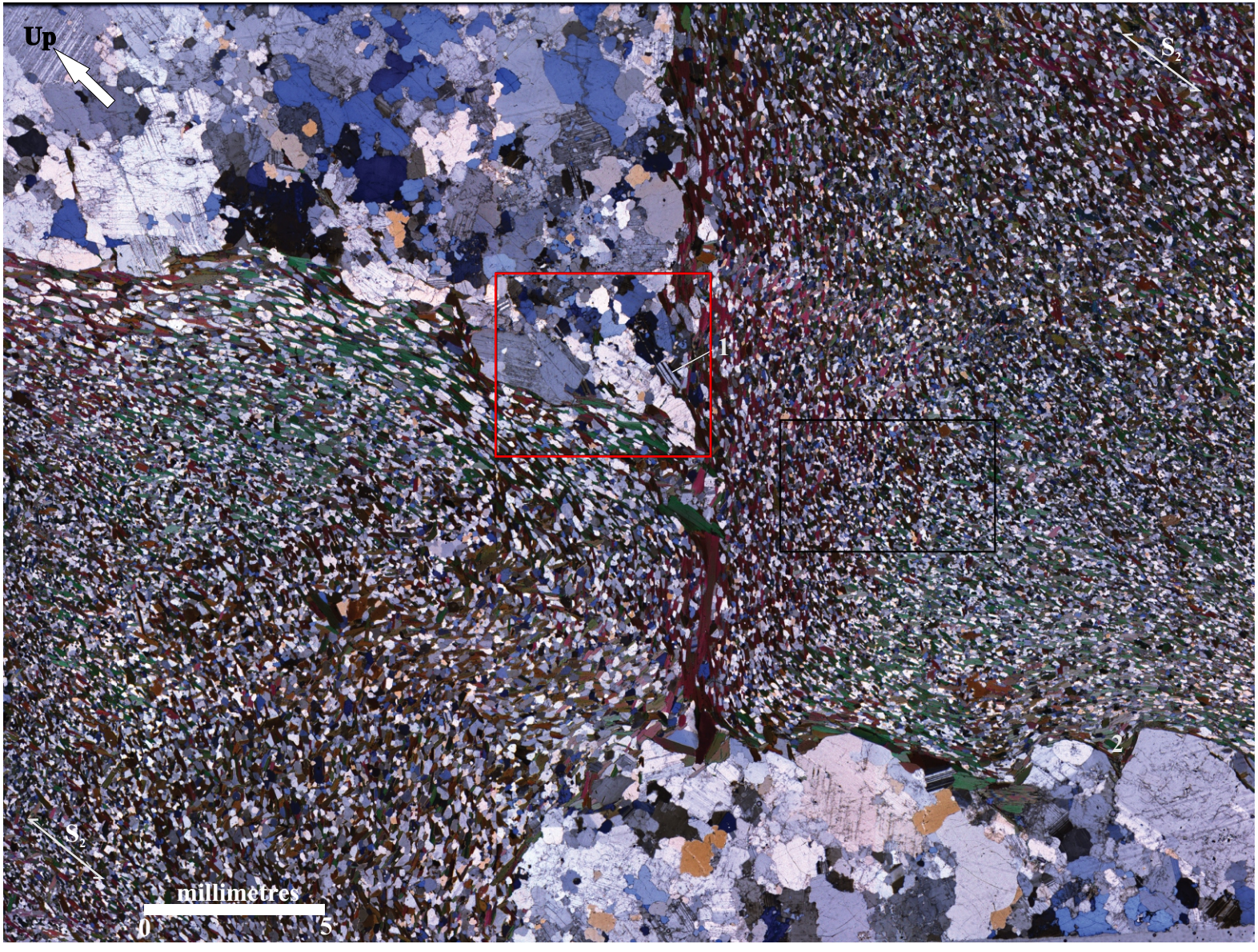

Figure 5.12. Section scan of sample 19SNO11b cut through dike linkage at the Snowbank pegmatite. Basalt S_2 fabric trend disrupted to parallel dike contacts. Growth twinned albite (1) adjacent to euhedral crystals in dike neck and cusp development (2) between pegmatite and basalt developed. Analysis region in red, second mapped but not analyzed region at right in black.

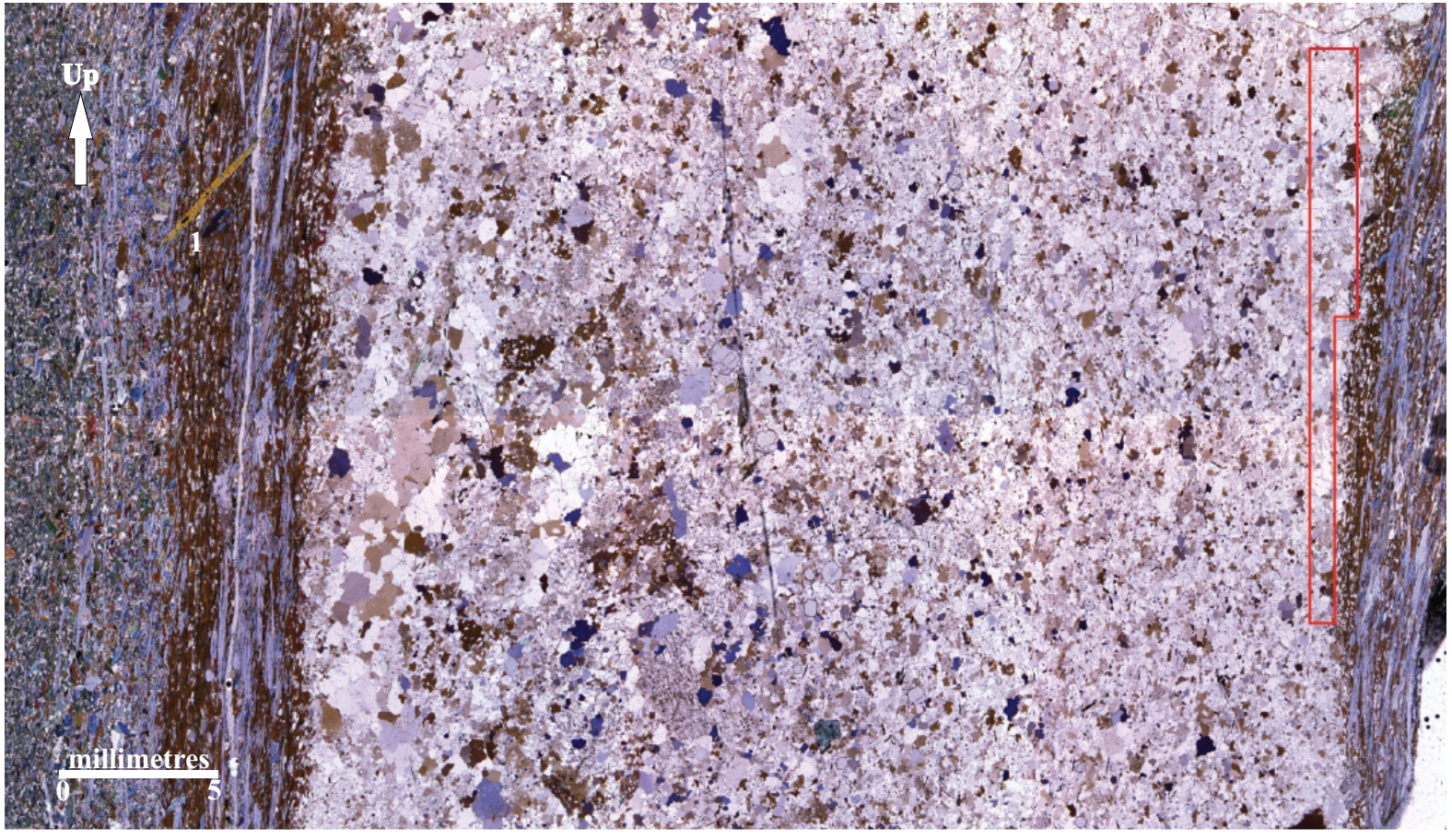

Figure 5.13. Section scan of sample 19GL1b cut in profile orthogonal to thin dike contacts at the Glitter pegmatite. lath-shaped holmquistite (1) at angle to contact parallel biotite alteration fabric. Analysis region given in red.

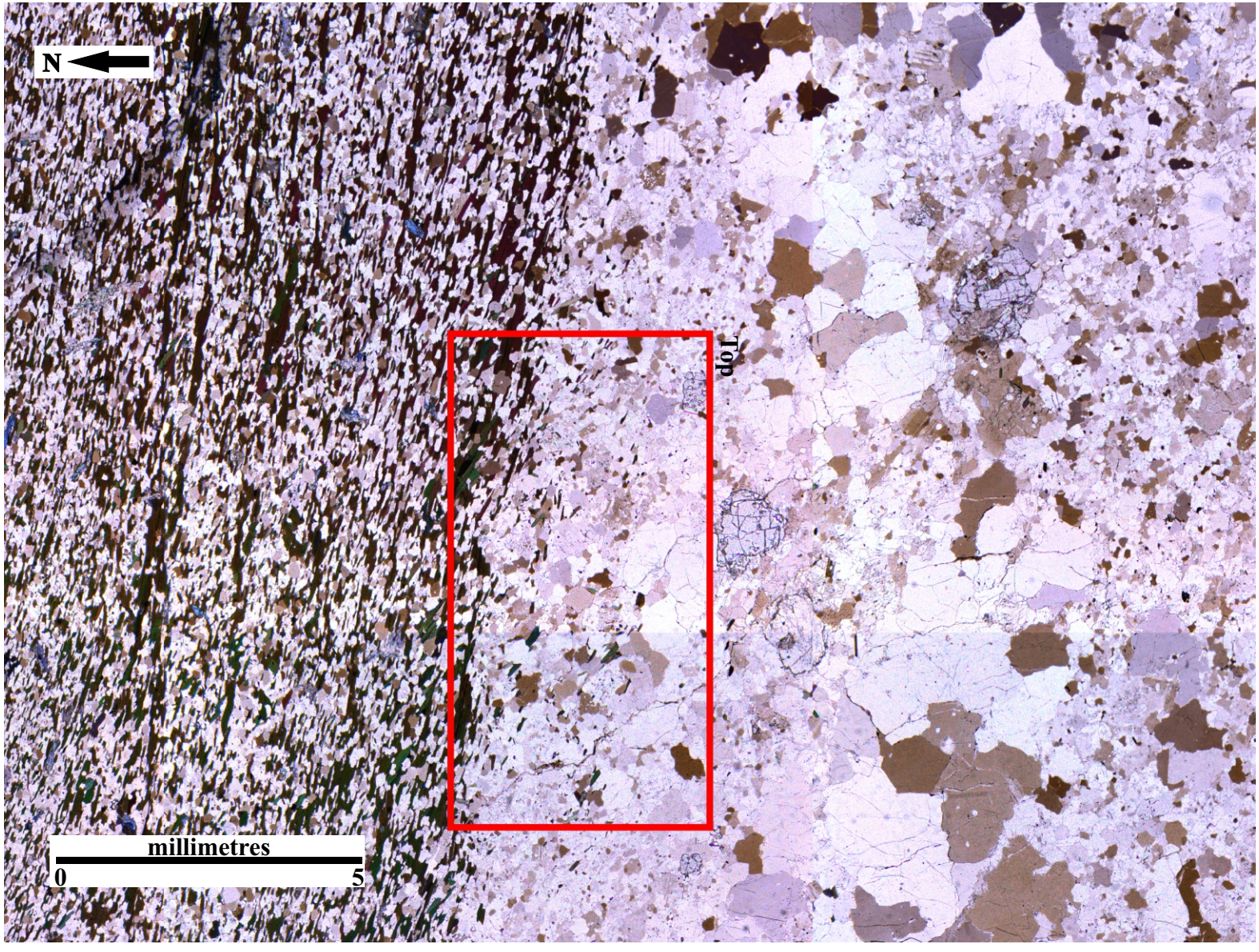

Figure 5.14. Section scan of sample 19GL2b cut in plan view at the Glitter pegmatite. Weak sinistral S-C fabric in basalt is developed adjacent to mm-scale irregular pegmatite quench. Pegmatite transitions to medium-coarse grained crystals that define P_L layering parallel to the contact.

Mineral index maps record quartz, albite, and biotite as the major phases in pegmatite (Figures 5.15A, 5.16A, 5.17A) with a minor component of orthoclase in 19GL1b (Fig. 5.15A). All specimens record grains with GOS of <3° between individual pixels and the parent grain orientation with occasional grains up to 6° GOS (Figs. 5.15B, 5.16B, 5.17B).

Lattice-preferred orientations of quartz and plagioclase in specimens 19SNO11b and 19GL2b present poorly defined fabrics (Figs. 5.15C, 5.17C). Similarly, poorly defined fabrics are recorded in 19GL1b (Fig. 5.16C) except in albite. In albite $[1\bar{0}0]$ forms a single girdle oriented parallel to the contact with the country rock (XZ) and a point maximum for $[01\bar{0}]$ lies parallel to Y to indicate the long axis of albite is weakly parallel to the contact.

Both specimens 19GL1b (Fig. 5.16D) and 19GL2b (Fig. 5.17D) plot quartz-plagioclase interphase misorientation distributions with a high frequency of correlated misorientation angles of 40 to 70° above the expected uniform distribution. The relative lattice orientation between these grains does not show a high maximum. Specimen 19SNO11b, however, shows moderately correlated misorientation angles between quartz and plagioclase with a maximum in the distribution of the misorientation angles parallel to plagioclase <111> or <1-1-1> faces and the quartz trigonal bipyramid axis (Figs. 5.15D, 5.15E).

5.1.4 Summary

Grain orientation spreads are consistently less than 2° and quartz and albite illustrate poorly defined preferred orientations in all lower-hemisphere plots. Uncommon GOS in excess of 5° is recorded and suggests local grain-scale strain is present (see Section 6.3 Discussion). Grain size reduction, expected in environments experiencing strain, is absent to minimal as the lack of bimodal distribution with a low angle peak in all frequency plots is absent (cf. Trimby *et al.,* 1998),

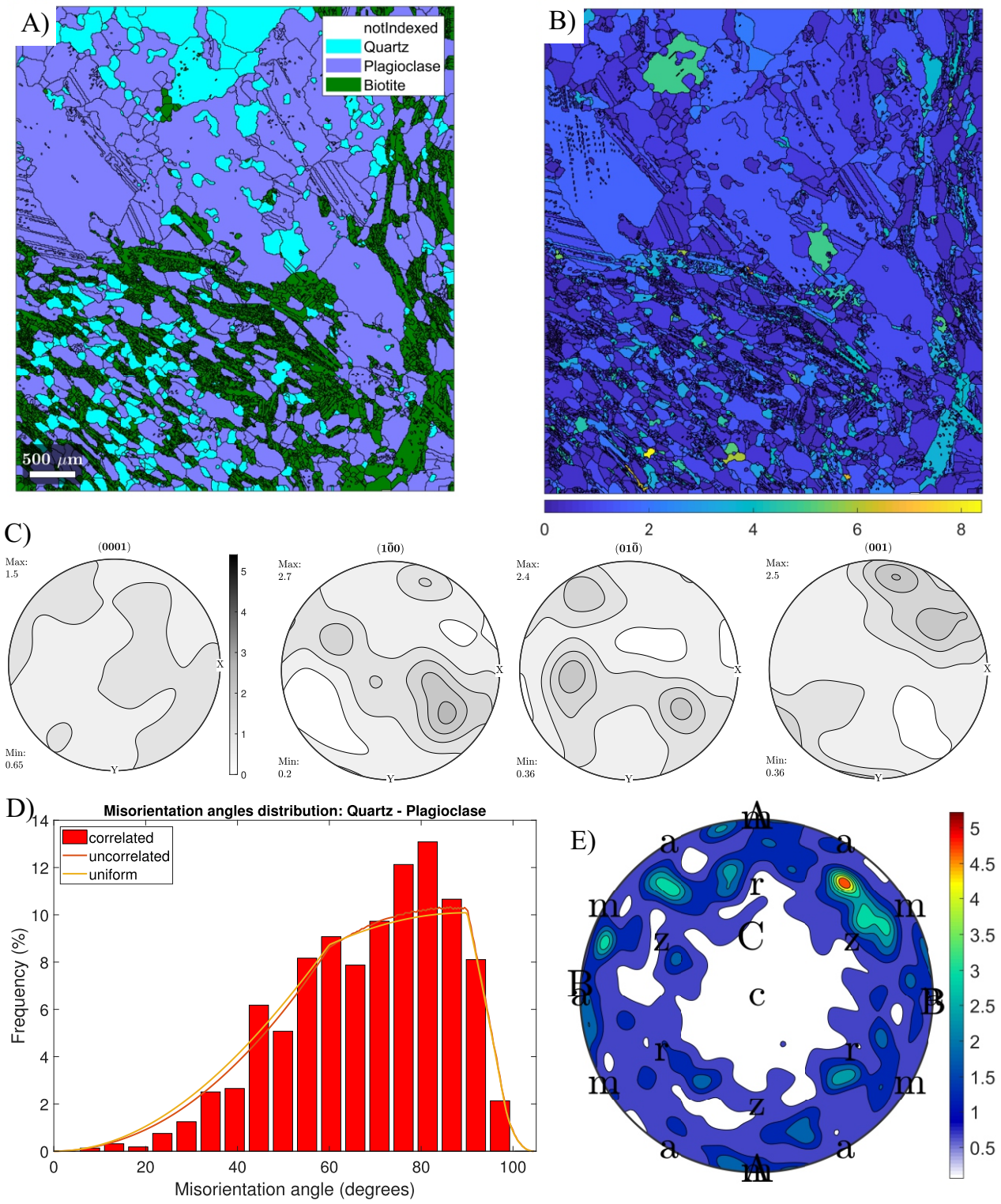

Figure 5.15. EBSD results for specimen 19SNO11b. A) Mineral index map; B) GOS map recording <2° misorientation between individual pixels and that of the parent grain; C) Poorly defined lattice preferred orientations of quartz (0001) and albite; D) Frequency plot of misorientation angle distribution between major phases approaching uniform distribution for quartz; E) IPF plot between quartz and albite recording moderately correlated misorientation axes parallel to albite and the quartz trigonal bipyramid axis.

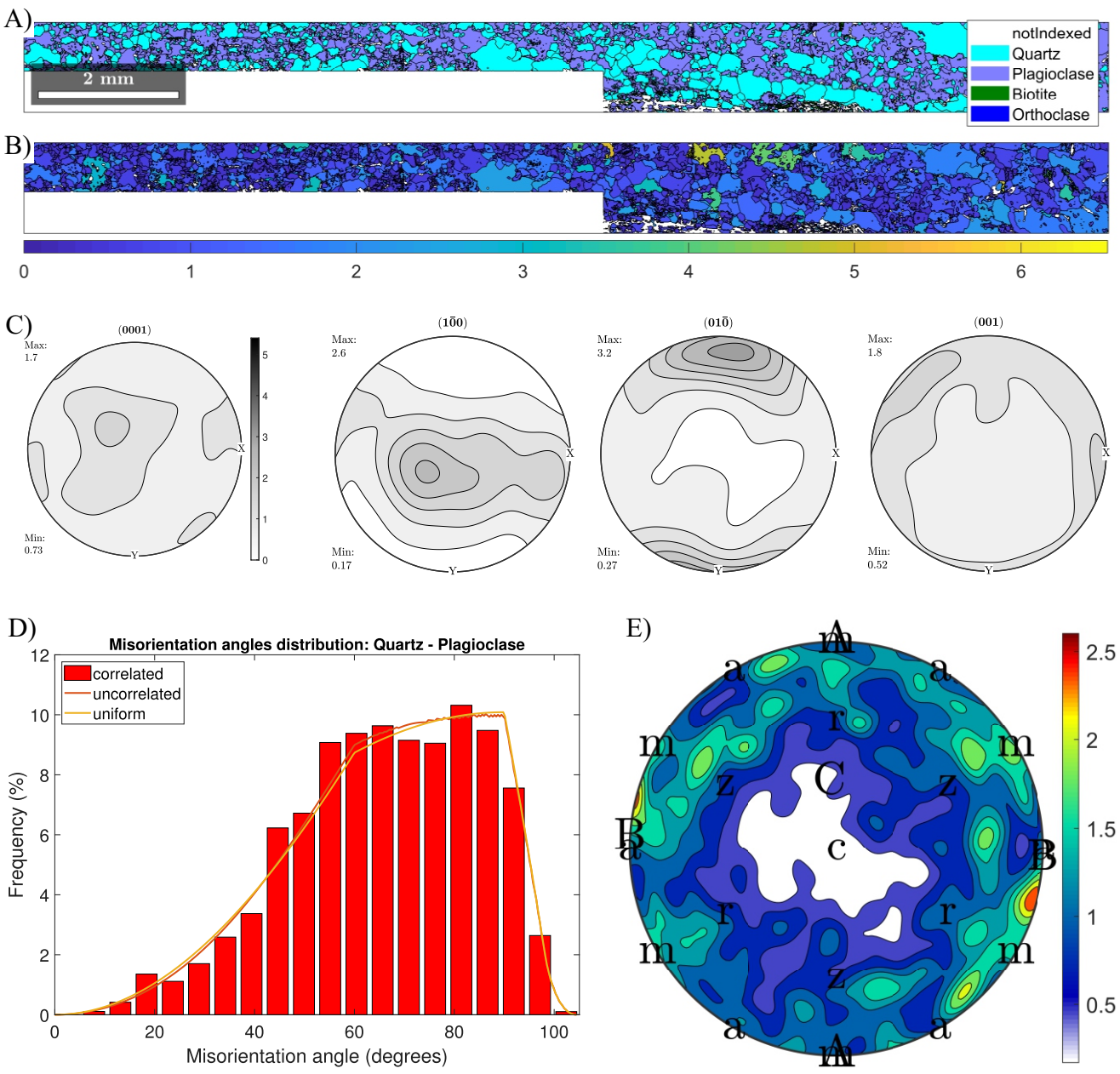

Figure 5.16. EBSD results for specimen 19GL1b. A) Mineral index map; B) GOS map of indexed minerals; C) Low preferred orientation and fabric development of quartz (0001) and albite. Weak single girdle in [100] occurs parallel to the contact of the xenolith and [010] defines a maxima parallel to Y; D) Frequency distribution of quartz - plagioclase crystals plotted against that of a uniform distribution. Increased frequency of correlated grain misorientation from 40 to 70 degrees: E) IPF plot of quartz-albite misorientation axes displaying low correlation between the misorientation axes of quartz and albite.

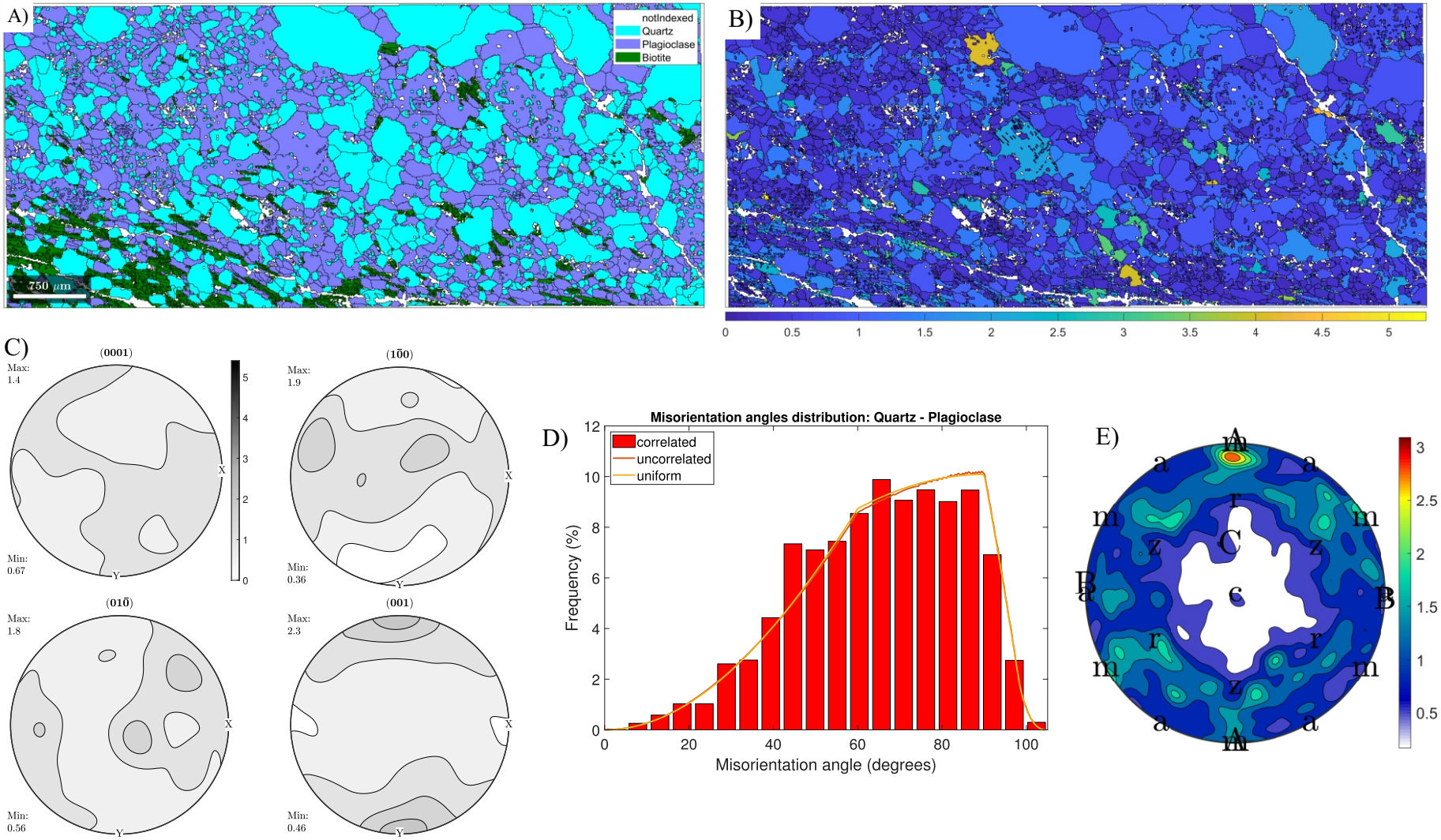

Figure 5.17. EBSD results for section 19GL2b. A) Mineral index map; B) GOS map recording <1.5° of misorientation. Irregularly distributed GOS values up 4-5° comprise a minor component of specimen; C) Poorly defined fabrics in Quartz (0001) and albite (100; 010; 001) displayed as lower hemisphere plots; D) Frequency plot of misorientation angle distributions between phases approaching that of a uniform distribution for quartz. Increased frequency of correlated misorientation angles above the uniform distribution from 40 to 70 degrees; E) IPF plot of misorientation axis distribution corroborating low preferred orientation between quartz and albite.

and rather closely follows the uniform distribution for quartz (cf. Grimmer, 1979). Crystal lattices between quartz and albite all indicate a low preferred orientation and an uneven distribution of maxima.

5.2 Geochronology

Geochronological analyses were completed to establish the timing of amphibolite-facies metamorphism and deformation, and the crystallization age of pegmatites and aplites. Results are tabulated in Appendix B.

5.2.1 Timing of regional metamorphism and deformation

Two rock specimens from two different units of country rock were analyzed by *in-situ* LA-ICP-MS to establish the timing of metamorphic mineral growth. Specimens were cut in the kinematic reference frame orthogonal to the S_2 composite foliation and along the L_2 lineation to identify phases crystallized during regional fabric development. Analytical results are tabulated in Appendix B.1 with metamorphic age plots compiled in Figure 5.18.

Specimen 19MS1 is a feldspathic arenite collected in a clastic metasedimentary unit along the northern margin of the SLgb near the ERS boundary (Fig. 2.1). Biotite defines the S_2 foliation, trending eastward and dipping 45° to the south, in agreement with the orientation reported by Blackburn and Young (2000). Lineated biotite plunges 40-60° to the west. In thin section, elongate laths of biotite include very fine (30-50 μm) crystals of monazite. These monazite crystals are rounded to ellipsoidal, surrounded by an equidimensional metamict halo, and irregularly distributed within the host biotite. Sixteen grains of monazite were identified for a total of 20 spot analyses. Of these, seven analyses represented scatter and were removed from the U-Pb isochron plot. The remaining data yield an upper intercept age of 2647 ± 5 Ma (MSWD 2.7; Fig. 5.18A).

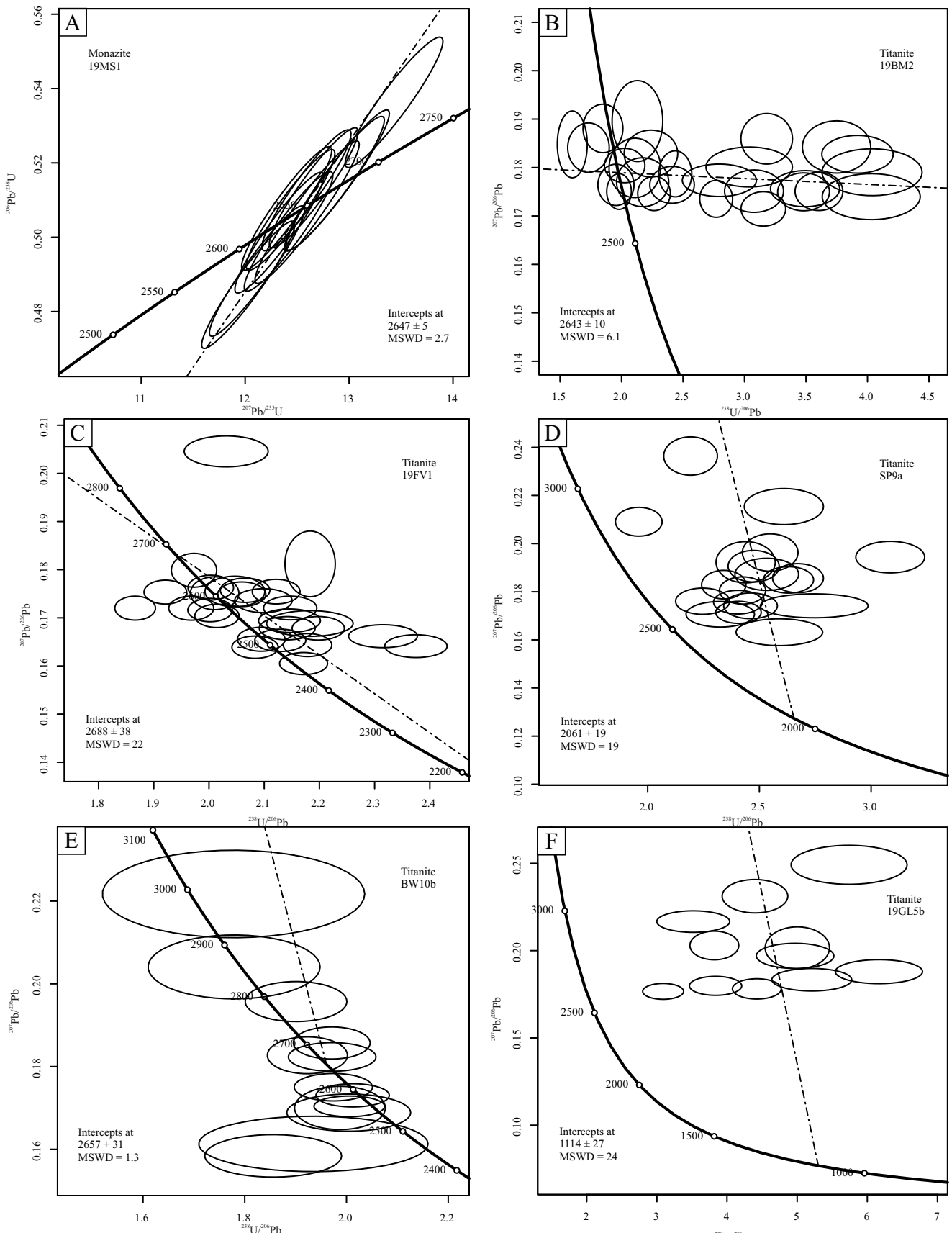

Figure 5.18. Uranium-Pb plots for metamorphic age of country rock specimens. A) Peak amphibolite metamorphism and D_2 fabric development in feldspathic arenite; B) Calc-silicates coeval with Big Mack intrusion; D-F) Additional titanite analyses with inconclusive results.

This monazite age is comparable to the age of NW-SE dextral transpression in the region focused on Subprovince boundaries (Corfu, 1988; Menard *et al.,* 1997; Melnyk *et al.,* 2006). This result is interpreted to reflect the age of S_2 fabric development during amphibolite-facies metamorphism in the SLgb.

Specimen 19BM2 was collected approximately 20 m north of the Big Mack pegmatite and includes both massive basalt and calc-silicate after hyaloclastite (Fig. 4.3). Hornblende in the basalt defines a mineral lineation plunging 80^{o} to the east in the plane of the dominant subvertical S_2 composite fabric. Fine-grained titanite trails occur in the plane of the S_2 foliation. In thin section, the calc-silicate consists of fine- to coarse-grained polygonal assemblages of hornblende, actinolite, epidote, clinopyroxene, clinozoisite, and minor amounts of quartz and calcite with accessory titanite. Nineteen titanite grains were analyzed for a total of 34 spots; of these, eight results were removed due to excess scatter. The remaining 26 analyses return an upper intercept age of 2643 ± 10 Ma (MSWD = 6.1; Fig. 5.18B), which is within error of the age of the Big Mack pegmatite (see Section 5.2.2 below).

Metamorphic age determinations were inconclusive for several additional specimens hosting titanite grains that included: 1) a unit of felsic volcanic rock below the Feldspathic Arenite (Fig. 2.1; Fig. 5.18C); xenoliths of the 2) Separation Rapids pluton (Fig. 5.18D) and 3) Big Whopper pegmatite (Fig. 5.18E); and 4) a basalt sample adjacent to unmineralized pegmatite near the Glitter pegmatite (Fig. 5.18F).

5.2.2 Timing of Pegmatite/Aplite Crystallization

Crystallization ages of pegmatites and aplites were determined by in-situ U-Pb analyses of primary igneous minerals that include monazite, zircon, wodginite, and cassiterite using LA-ICP-

MS. The monazite results for Glitter, Snowbank, Big Mack, and Big Whopper dikes are tabulated in Appendix B.2. Very fine- to fine-grained, euhedral monazite with pristine grain boundaries indicative of primary growth (Parrish, 1990) is typical in these pegmatites. In addition to the four principal pegmatites of this study, analyses of cassiterite, microlite, zircon and wodginite were completed on grains recovered from the Marko's pegmatite, located farther to the east in the SLgb and are tabulated in Appendices B.3 and B.4. Cassiterite and monazite were utilized to determine the age of the GWN aplite with results tabulated in Appendix B.4. Crystallization age plots are presented in Figures 5.19 and 5.20.

Anchored through the origin U-Pb results indicate a range of monazite crystallisation ages for the pegmatites: 2637 ±4 Ma for Big Mack (MSWD = 0.8; Fig. 5.19A), 2623 ±10 Ma for Snowbank (MSWD = 0.7; Fig. 5.19B), 2617 ±4 Ma for Big Whopper (MSWD = 1.3; Fig. 5.19C) and 2617 ±4 Ma for Glitter (MSWD = 1.4; Fig. 5.19D). In the Marko's pegmatite, zircon and wodginite ages of 2602 ±5 Ma (MSWD = 0.7; Fig. 5.19E) and 2602 ±6 Ma (MSWD = 0.7; Fig. 5.19F), respectively, are considered to reflect the timing of igneous crystallization. Analyses of microlite and cassiterite grains in the Marko's pegmatite were inconclusive (Fig. 5.20A, B).

Attenuated and recrystallized aplitic phases interpreted by previous authors (see Pedersen, 1998; Pedersen *et al.,* 2017) as exploration vectors to lithium pegmatite were sampled in an outcrop ~400m northwest of the SRp. Near the GWN pegmatite, these aplites ("Great White North aplites") were described by previous authors (Aiken *et al*., 2016; Pedersen *et al.*, 2017; Gowans *et al.*, 2018) as part of the SRLD system. A lineated specimen was selected for U-Pb analysis. Two U-bearing phases occur within the recrystallized fabric: (1) fine-grained blebby cassiterite and (2) very fine- to fine-grained monazite. A shape-preferred orientation of corroded an- to subhedral cassiterite occurs parallel to the foliation defined by deformed albite. Seven of twenty-three spot analyses

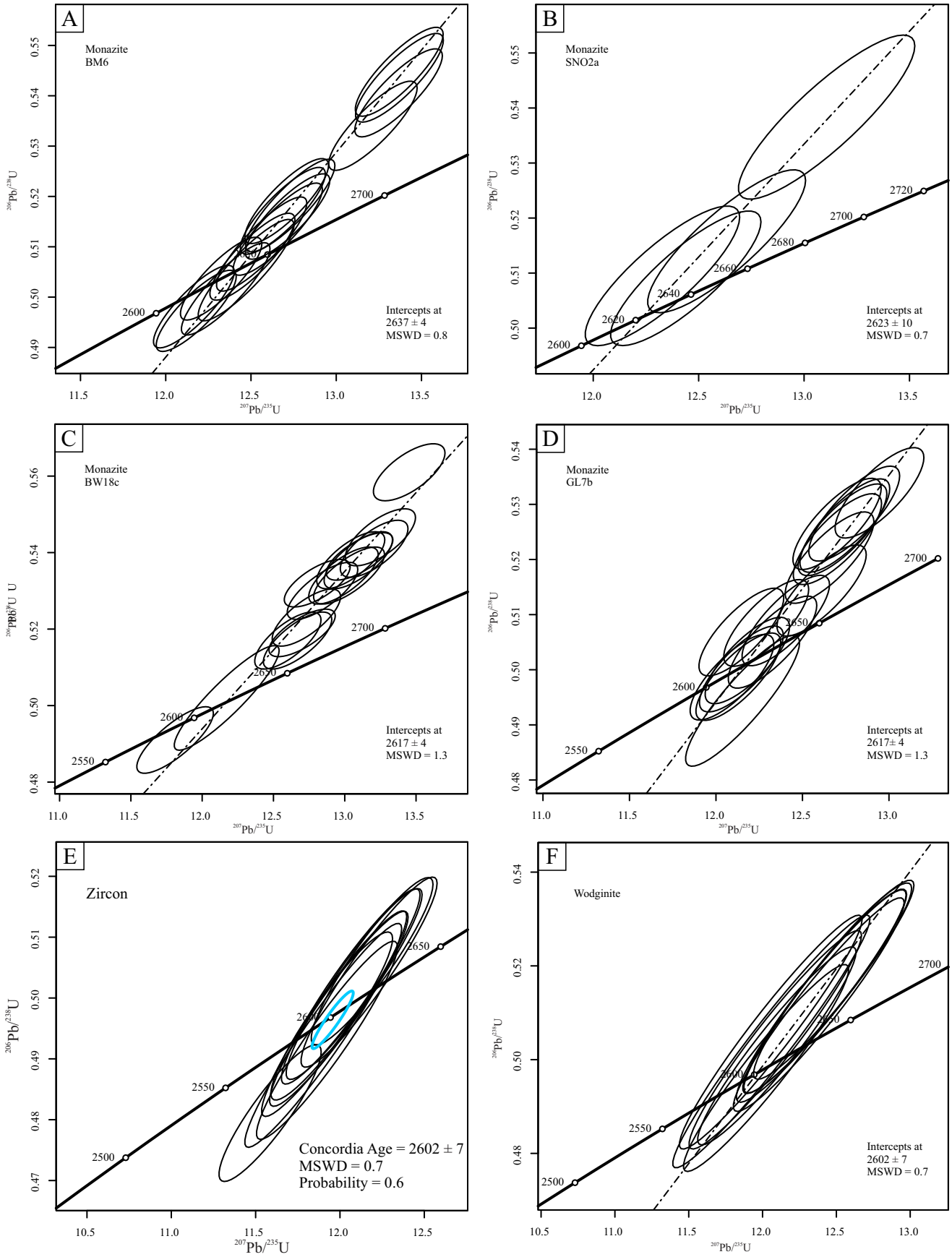

Figure 5.19. Pegmatite crystallization ages. A-D) *In-situ* euhedral monazite for Big Mack, Snowbank, Big Whopper and Glitter pegmatites; E-F) Grain analyses for Marko's pegmatite.

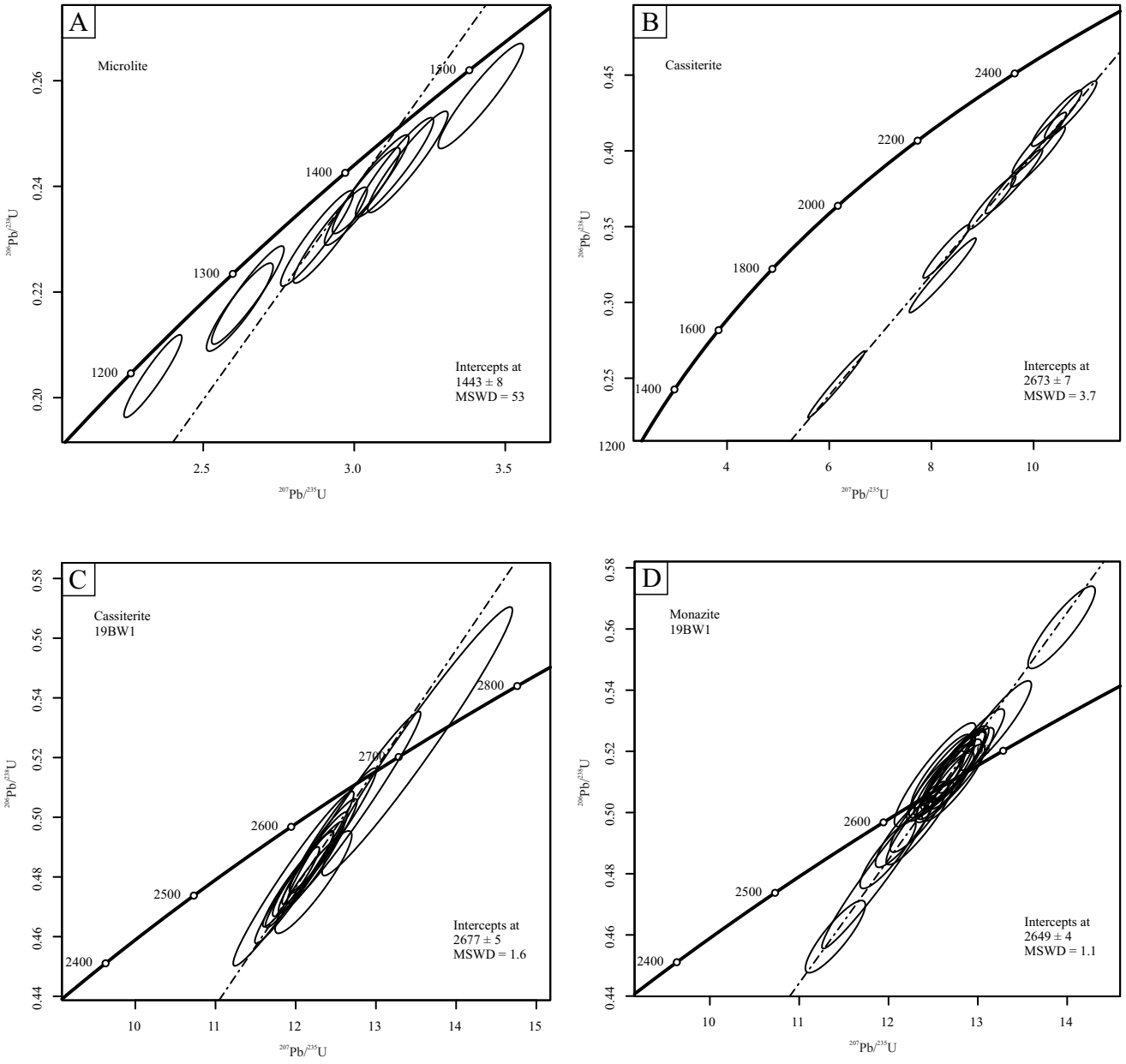

Figure 5.20. A-B) Microlite and cassiterite grain analyses for Marko's pegmatite; C-D) *In-situ* analyses for cassiterite blebs and euhedral monazite in the GWN Aplites

were omitted due to lead loss with the remainder yielding an upper intercept age of 2677 ±5 Ma (MSWD = 1.6; Figure 5.20C) and is comparable to other metamorphic ages of ca. 2680 Ma in regions near the SLgb (cf. Corfu *et al.,* 1995). Monazite is subhedral with rounded grain margins. Twenty-two analyses (3 analyses omitted) on eight grains yielded an age of 2649 ±4 Ma (MSWD = 1.1; Figure 5.20D), which is comparable to peak metamorphism in the SLgb (Section 5.2.1).

5.2.3 Summary

The Skidder pluton dated by Macdonald *et al.,* (2023) pre-dates peak D_2 amphibolite-facies metamorphism established in this study at ca. 2650 Ma. As it is older than the 2646 ±2 Ma (Larbi *et al.*, 1999) Separation Rapids pluton, the Skidder pluton cannot be derived from the Separation Rapids pluton. Crystallization ages for the lithium pegmatites of the SLgb ca. 2640 Ma, ca. 2620 Ma, and ca. 2600 ma all post-date the D_2 event. Protracted pegmatite emplacement over ~44 Ma brings into question the genetic link between the ca. 2620 Ma and ca. 2600 Ma lithium pegmatites and the Separation Rapids pluton. In addition a genetic link between the GWN aplites and the Big Whopper, and possibly the SRLD system is also unlikely with an age variation of at least 60 Ma (Fig. 5.20C). Age determinations for this study and from literature are overlain on the regional geology in Figure 5.21.

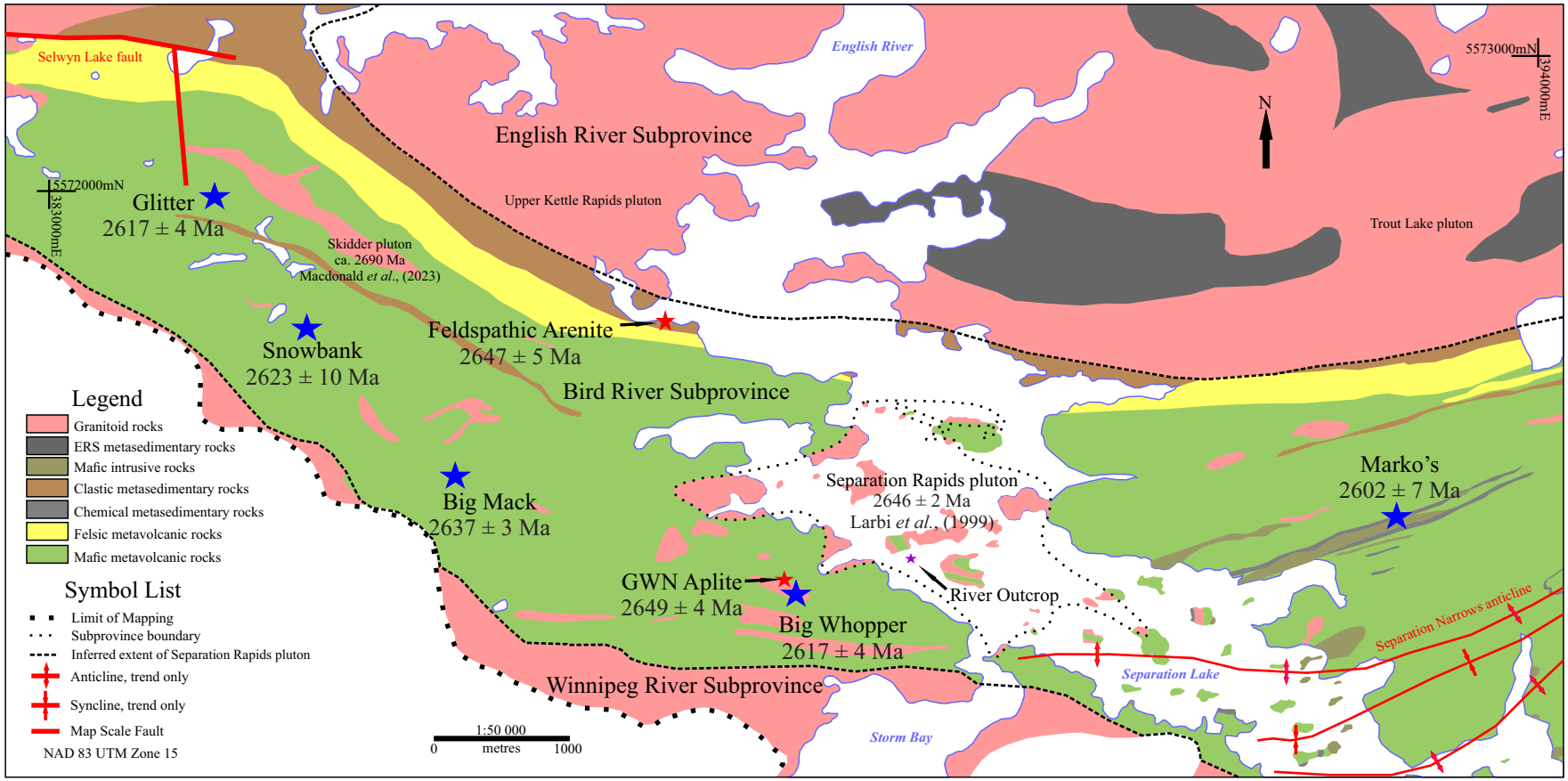

Figure 5.21. Intrusion ages determined in this study; previously known ages from other studies are also plotted. Simplified geology from Blackburn *et al.*, (2008). Red Stars - metamorphic ages; blue stars - crystallization ages; purple star - river outcrop location.

Chapter 6 Discussion

6.1 To what extent did the pegmatites in the SLgb experience solid-state deformation?

Past work on the SLgb pegmatites has led to the idea that they experienced significant, post-emplacement high-strain deformation. Breaks and Tindle (1997) inferred that strong ductile deformation had affected the pegmatites, based on their observations of Z folds, σ-type K-feldspar porphyroclasts with clockwise rotation, and rotated boudins in outcrop indicative of dextral shear. They interpreted that this deformation resulted in pegmatite minerals with spindle and lensoid shapes. Breaks and Tindle (1997) also reported petalite with a net-like polygonal form (Photo 17.1 *in* Breaks and Tindle, 1997) mantled by very fine-grained quartz–spodumene intergrowth (SQUI). This interpretation has particularly influenced mineral exploration strategies. Pedersen (1998) suggested that the Big Whopper represents a series of coeval dikes that tectonically coalesced in a dilatant flexure, producing boudinaged dike swarms and pinch-and-swell structures. Pryslak and Chastko (2001) reported variable strain throughout pegmatite dikes near the Big Mack pegmatite, describing isoclinal to open Z- and S-type folds. However, Chastko (2001) briefly mentioned that pegmatites cut the foliation in the basalt, with variable internal foliation in the pegmatites, thus interpreting the timing of the deformation experienced in the pegmatites to be late in the structural evolution of the belt. Most recently, Pedersen (2017) highlighted competency contrasts at the Glitter pegmatite occurrence, inferring that rheological differences between basalt and pegmatite under stress were the cause of flame-and-mullion structures.

However, results of this current project bring interpretations of extensive post-emplacement metamorphism and deformation into question. Petrographic observations and EBSD analyses show that the pegmatites do not preserve penetrative, solid-state deformation fabrics and

the minerals lack a CPO (Section 5.1), respectively. In addition, the age determinations show that pegmatite crystallization took place after regional metamorphism and deformation (Figure 6.1; see Section 5.2). Rounded to pill-shaped monazite indicative of metamorphic crystallization (Parrish, 1990) place upper-amphibolite facies metamorphism coeval with the development of the dominant S_2 fabric during D_2 at *ca.* 2650 Ma and would have influenced textures and microstructures in the pegmatites as evidenced in the Skidder pluton (*ca.* 2690 Ma; Macdonald *et al.,* 2023; Section 4.2.1) and the GWN aplites (*ca.* 2649 Ma; Section 4.3.7). While textures and microstructures associated with deformation were observed in the Skidder pluton and Great White North aplites, these features were not observed in any pegmatites in this study. The presence of transformation twinning in albite; myrmekite overprinting partially tartan-twinned K-feldspar (Fig. 4.9; Eggleton and Buseck, 1980; Bell and Johnson, 1989); anhedral to subhedral recrystallized quartz with undulatory extinction, bulging at grain boundaries, and grain-size reduction (Stipp *et al.*, 2012); support the interpretation that the Skidder and GWN aplites were emplaced prior to D_2 deformation.

Truncated, rotated, and obliterated S_2 fabrics in the host rocks adjacent to the pegmatites is evidence for pegmatite emplacement after D_2 (Sections 4.3.4, 4.3.5, 5.2). Pegmatite contacts discordant to the regional S_2 schistosity have also been previously reported by de la Fuente (1998), Chastko (2001), and Pryslak and Chastko (2001).

To summarize, the pegmatites examined in this study do not contain internal fabrics or textures indicative of ductile deformation, whereas such features are pervasive in the adjacent host rocks. Although the pegmatites do exhibit mesoscopic features such as fold and boudin-like structures that have been attributed to regional ductile deformation by previous workers, the absence of associated fabrics within the pegmatites preclude this interpretation. To explain this discrepancy, an alternative interpretation is proposed (Section 6.2.3) wherein the pegmatites of the

Figure 6.1. Bar Graph of the relative timing of metamorphism and deformation and rare-element mineralization in the SLgb as compared to the ERS, WRS, and Bird River Subprovinces (see Sections 2.1, 2.2, 5.2.1, 5.2.2). 1- Beakhouse, 1991; 2 - Corfu *et al.*, (1995); 3 - Gilbert *et al*., (2008); 4 - Melnyk *et al*., 2006; 5 - Macdonald *et al*., (2023); 6 - Larbi *et al.*, (1999).

SLgb were not subject to extensive post-emplacement deformation but did influence the structures and fabrics in the host rocks locally through intrusion-induced deformational processes. In this interpretation, mesoscopic structures (Section 6.2.3) and crystal textures (Section 6.3.1) are not the products of recrystallization and recovery but are magmatic and developed during emplacement by rapid crystallization of an undercooled, flux-rich melt.

6.2 How did the intrusion dynamics of the pegmatites influence the host rock fabrics?

6.2.1 Controls on pegmatite transport and emplacement

Publications are sparse on the mechanics of pegmatite intrusion with Brisbin (1986), Baker (1998), and Bons *et al.* (2004), among others, focused specifically on pegmatites. Brisbin (1986) summarized factors including fluid pressures, regional lithostatic stress, directed (tectonic) stress, rheological state of the host rock, and rock anisotropy that affect intrusion dynamics. In addition, a heat flow model developed by Rubin (1995) and applied to pegmatites by Baker (1998) indicates that dike propagation is arrested until sufficient heat is added to the country rock, either through the cooling of the source pluton, or via heat influx from tectonic activity.

Turcotte (1987) suggested three modes for the transport of melt: porous flow, diapiric, and fracture. For pegmatites exsolved from a source pluton the typical mode of transport is by fracture. To dilate a fracture, the melt pressure must exceed the normal stress and the tensile strength of the host rock (Brisbin, 1986). To maintain dilation, sufficient magma supply is required – such as in mafic systems at spreading centres or plumose hot-spots. Felsic melts from which LCT pegmatites are derived are unable to maintain the fracture dilation due to insufficient melt volume, and instead, migrate preferentially via stepwise batches by hydrofracturing (Clemens and Mawer, 1992; Bons, 2001; Bons *et al.,* 2001).

6.2.2 Mesoscopic features of sheet intrusion propagation and emplacement

The following section is summarized from works of multiple authors to provide background information into features indicative of brittle (faulting) and ductile (folding, ductile shear) response of the country rock to sheet intrusion. Comparison can then be made to features documented in this study to intrusion models and work of Robson and Barr (1964), Pollard (1973), Lister (1990), Rubin (1993), Merle and Donnedieu (2000), Ziv *et al*. (2000), Khodayar and Einarsson (2002), Mathieu *et al*. (2008), Abdelmak *et al*. (2012) Schofield *et al.* (2010, 2012a, b), and Spacapan *et al*. (2016, 2017) in Section 6.2.3 that follows. A table of sheet intrusion models and diagnostic outcrop features is provided here as Table 6.1, modified from Figure 1 of Spacapan *et al.* (2017).

Dike propagation requires mechanical energy to overcome resistance: (1) the flow resistance of the magma, (2) the resistance of the host rock to intrusion dilation, and (3) the resistance of the host rock to local deformation by compression, folding and faulting (Pollard, 1973; Pollard *et al.*, 1975). Dike and sill propagation is controlled by multiple factors: the rheology of the country rock; the lithostatic and directional stress present at the intrusion site; pre-existing fabrics such as fractures, cleavage, schistosity and layering; magma viscosity, buoyancy and pressurization; heat transport; and volatile content (Pollard, 1973; Brisbin, 1986; Clemens and Mawer, 1992; Bons, 2001; Bons *et al.*, 2001; Spacapan *et al.*, 2017). Modelling of these components indicates several mechanisms by which the mechanical energy of a dike may overcome the resistance to propagation (Table 6.1; Spacapan *et al.*, 2017). To propagate from their source melt, dikes can (1) induce a local fracture network through increased overpressure by brittle or ductile deformation processes (Pollard, 1973; Clemans and Mawer, 1992; Bons *et al.*, 2001; Spacapan *et al.*, 2017; Bertelsen *et al*., 2018), or (2) exploit planes of weakness in the country rock

Table 6.1. Sheet intrusion emplacement models and diagnostic outcrop features adjacent to intrusions, after Spacapan *et al.*, (2017). Features observable perpendicular to the propagation direction (parallel to the x axis), and in the plane of the intermediate (y) and short (z) axes in section unless otherwise noted.

Dike emplacement models and diagnostic features in country rocks adjacent to intrusions

Model Type	Variance	Features	Reference
Linear elastic fracture mechanics (LEFM)	LEFM	Failure by extensional fracture (Mode I). Dilation parallel to σ_3. High length (x) to width (y) ratios. Consistent with brittle response in shallow crust\	Pollard (1973) Lister (1990)
	LEFM - Barenblatt	Similar to LEFM but has plastic (ductile) cohesive zone of country rock at the intrusion tip of dike. Predicts occurrence of compression perpendicular to fracture due to suction in tip cavity	Rubin (1993)
Induced Faulting	Brittle	Fault surfaces contain σ_2 with faults oriented <45° to plane of intrusion (x-y). Occur at depths of 4-5 km under moderate confining pressure	Pollard (1973) Robson and Barr (1964)
	Ductile	Fault surfaces contain σ_2 with faults oriented >45° to plane of intrusion (x-y). An increase in radius of curvature of propagation fronts results in blunt ends.	
	Viscous Indenter	Shortens country rock in plane of intrusion ahead of intrusion. Viscous shear force at propagation tip overcomes the strength of the host rock by conjugate faulting and folding. Typical of viscous magmas.	Merle and Donnedieu (2000) Mathieu *et al.* (2008) Abdelmak *et al.* (2012) Spacapan *et al.* (2017)
Fluidization	Triggered	Rapid drop in hydrostatic pressure accompanies tensile failure. Locally disaggregates the country rock adjacent to the sill. Fluid-fluid interface induces and forms finger-like intrusions with chaotic country rock fabrics adjacent to fracture. Depths <2 km.	Schofield *et al.* (2010) Kokelaar (1982)
	Thermal	Occurs by heating and volatilization of pore fluids by the intrusion when pore-fluid pressure overcomes mechanical strength between grains. Chaotic country rock fabrics adjacent to intrusion. Depths <2 km	Schofield *et al.* (2010, 2012)
Pre-existing deformation		May facilitate intrusion in any orientation as compared to regional stress field if overpressure is sufficiently high. Dike morphology and extent controlled by maturity of fault zones. A local effect: it is hard to maintain unless (1) fracture is orthogonal to σ_3, (2) the shear stress is small compared to overpressure, and (3) dike normal stress << host tensile strength.	Ziv *et al.* (2000) Khodayar and Einarsson (2002) Spacapan *et al.* (2016, 2017)

such as bedding planes, contacts and deformation structures, including joints and faults (Vigneresse *et al.*, 1999; de Saint-Blanquat *et al.*, 2006; Burchardt, 2008; Spacapan *et al.*, 2017). The mechanical energy expended by the magma to dilate and propagate is lower in brittle regimes where dikes form continuous sheets rather than ductile environments where tube-like structures are preferred.

Dike intrusion into brittle country rock

In an isotropic brittle host rock, singular sheet intrusions propagate normal to their contacts at the position of maximum tangential stress (Pollard, 1973). Accommodation of the intrusion by the country rock is depth dependant: brittle (faulting) *vs.* ductile (folding, ductile shear) (Table 6.1; Pollard, 1973; Thomson and Hutton, 2004; Thomson, 2007). Mechanical fracturing of the country rock ahead of the intrusion front facilitates dike propagation and is modelled by Linear Elastic Fracture Mechanics (LEFM; Pollard, 1973; Lister, 1990) and variants (1) LEFM – Barenblatt cohesive zone (Rubin, 1993), (2) brittle faulting, and (3) ductile faulting (Table 6.1; Pollard, 1973). All variants of LEFM models represent a continuum between variations in rock type, confining pressure, temperature, pore fluid pressure, and strain rates (Pollard, 1973; Spacapan *et al.*, 2017). In an isotropic medium, propagation (elongation) occurs parallel to the intermediate principal stress axis (σ_2). Magma pressures are uniform about the (σ_2) axis, herein labelled as x, with the maximum (σ_1) and minimum (σ_3) compressive stresses orthogonal to the x-axis. Dilatant cracks propagate along principal stress axes and are oriented normal to the direction of least compressive stress (tensile; σ_3) (Pollard *et al.*, 1975, 1982). The intermediate stress (σ_2) direction lies within the plane of brittle or ductile faults, whereby conjugate fault orientations occur at $<45^o$ to σ_1 in brittle conditions and $>45^o$ to σ_1 in ductile conditions (Pollard, 1973).

In regions with sufficient magma supply, a series of interconnected dikes and sills can form macroscopic saucer- or cup-shaped morphologies when viewed in the XZ plane (Figure 6.2; Pollard *et al.,* 1975; Schofield *et al.*, 2012a, b). In these instances, near-field stress axes adjacent to the intrusion can become misoriented to the far-field stresses as dike inflation re-orients the local stress field. This results in (1) climbing of the intrusion to form saucer-like profiles, or (2) rotation to produce *en echelon* segments of dikes along the margins of intrusions (Fig. 6.2; Pollard, 1973; Pollard *et al.,* 1975, 1982; Nicholson, 1985; Nicholson and Pollard 1985; Hutton, 2009; Schofield *et al.*, 2012b; Wyrick *et al.*, 2020). Reductions in over-pressurization as the magma supply dwindles may force the magma to seek planes of weakness for continued propagation that may result in an inconsistent up-down offset or stair-step morphology (Pollard, 1973; Pollard *et al.*, 1975, 1982; Nicholson and Pollard, 1985; Hutton, 2009; Schofield *et al.*, 2010).

Distal to a magma source, step and bridge structures form in the YZ plane of the finite strain ellipsoid in both brittle and ductile regimes (Figure 6.3; Nicholson and Pollard, 1985). Dike inflation may concentrate and re-orient the local stress field and cause fractures to propagate ahead of the intrusion or along the margins between contemporaneous dikes (Pollard, 1973; Pollard *et al.*, 1982). In regions where the tensile stress exceeds the strength of the country rock, continued fracture propagation may lead to infilled linkages of nearby dikes, step and bridge structures or magmatic-induced *en-echelon* intrusion tips (Fig. 6.2B; Pollard, et al. 1982; Nicholson and Pollard, 1985; Hutton; 2009; Schofield *et al.*, 2012a, b; Thomson and Hutton, 2004; Magee *et al.*, 2019; Wyrick *et al.*, 2020).

Bridge structures develop in the YZ plane of the intrusion as overlap forms a septum of country rock between sheets on separate planes or *en-echelon* intrusions (Pollard, 1973; Nicholson and Pollard, 1985; Hutton, 2009; Schofield *et al.*, 2012a, b; Magee *et al.*, 2019). Dike inflation and

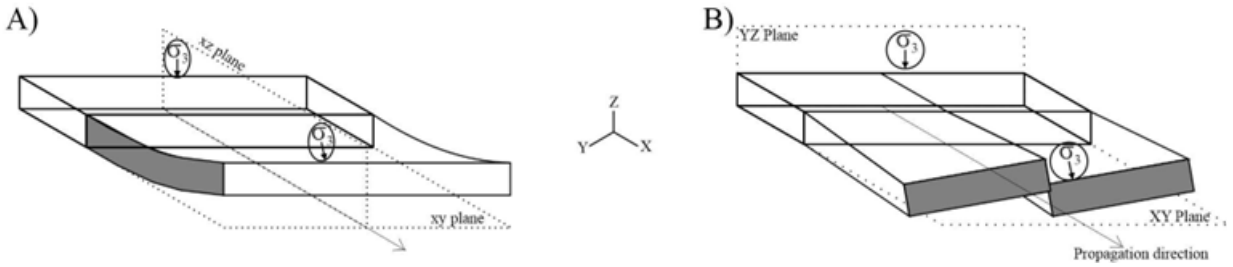

Figure 6.2. Changes in sheet morphology as the orientation of the least compressive stress (σ_3) changes over the length of a sheet, *after* Pollard *et al.*, (1975). (A) Rotation of σ_3 acting normal to the contact of the intrusion that results in climbing of the sheet; (B) Rotation of σ_3 in the plane of YZ to form rotated *en echelon* segments during propagation of the sheet eintrusion along X.

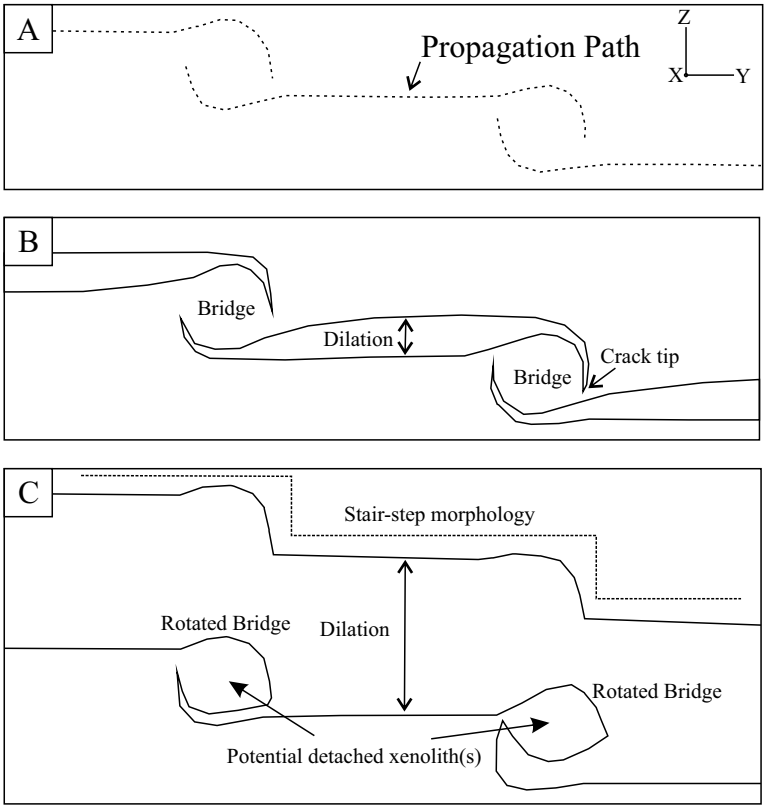

Figure 6.3. Schematic illustration of *en echelon* cracks that form along curved interfaces to develop stair-step morphology, *after* Nicholson and Pollard, (1985). (A) Propagation path separates adjacent cracks prior to bridge development. (B) Early propagation where some dilation is accommodated with crack walls defined as two curved distal parts and a rectilinear central part. (C) After linkage of crack tip to XY plane intersection dilation increases following detachment. Continued inflation may lead to complete detachment to form xenoliths.

propagation impart a local stress field to the bridge of country rock, and thus facilitate deformation and failure. Failure of a bridge may manifest as either (1) fractures orthogonal to the convex surface of the overlapping dikes at the point of maximum tangential stress, or (2) by layer-parallel contraction on the concave interior of bridge structures between adjacent dikes and initiation of tension cracking at a high angle to the convex outer surface (Fig. 6.3; Pollard, 1982; Nicholson, 1985; Nicholson and Pollard, 1985; Hutton, 2009; Schofield *et al.*, 2012b). As the process continues, the broken bridges may continue to rotate and detach into xenoliths within a stepped sheet of igneous rock (6.1B; Schofield *et al.*, 2012b).

Dike intrusion into ductile country rock

Intrusion of magma within a ductile system requires the host rock have very low mechanical strength resulting in a low shear modulus, unless strain rates are very high (Duffield *et al.*, 1986; Schofield *et al*., 2012b). In this case, the fabric of the host rock will deform and be displaced around the tip of the intruding magma. To produce a low shear modulus, intruding magma can either destabilize the rock through direct heating during intrusion or induce fluidization of the country rock (Table 6.1) to assist in the propagation of the intrusion at a fluid-fluid interface analogous to a Saffman-Taylor instability (Saffman and Taylor, 1958; Pollard *et al., 1975;* Schofield *et al*., 2010). This fluid-fluid interface leads to arcuate, bulbous to lobate, and roughly elliptical dike morphologies (YZ plane) perpendicular to the direction of propagation (X axis; Figure 6.4; Pollard *et al.*, 1975; Schofield *et al.*, 2012b). First termed as magma fingers by Pollard *et al.,* (1975) these structures are indicative of ductile conditions. At the intrusion front, fingers may taper to a blunted form or propagate and develop into lobes where the tip of intrusion dilates in the plane of YZ (Schofield *et al.*, 2010, 2012a,b). The propagation of a magma finger is controlled by the rates of cooling, crystallization, and increased drag between dike and country

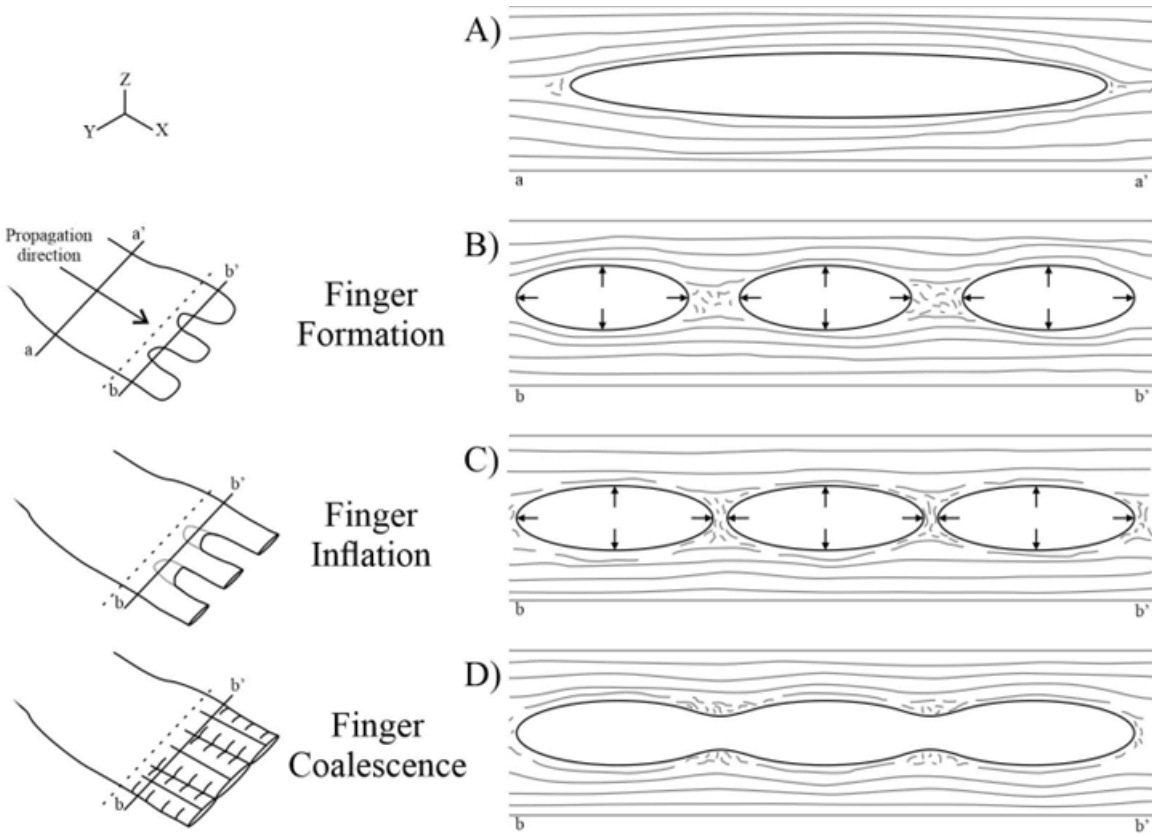

Figure 6.4. Sheet morphologies in the YZ plane intruding isotropic ductile crust parallel to the fabric of the country rock, Modified from Pollard *et al.* (1975) and Schofield *et al.*, (2012). Dikes propagate parallel to the x-axis. Reference frame top left. Dotted lines signify stationary sheet intrusion front at time T_1 . A) Dike profile from a-a' as a laterally continuous sheet; B) Initiation and formation of finger development at the interface between viscous magma and viscous country rock along the intrusion front at time T_1 along section b-b'. Country rock fabrics are overprinted, with the greatest shortening parallel to the intermediate (Y) axis of the dike, and minor compaction parallel to Z; C) Magma overpressure at T_2 inflates fingers orthogonal to contacts and shortens the country rock between fingers through folding, faulting, or compaction. The intrusion front advances at a similar rate to finger coalescence. D) Fingers coalesce during continued advance of the intrusion front. Cuspate morphologies develop between fingers at the point of coalescence, time T_3. Continued magma supply is required for an extended period for coalescence and formation of a continuous sheet from T_1 to T_3. Dikes may crystallize at any time prior to T_3 or continue to act as conduits for magma to feed other sills (Holness and Humphreys, 2003; Schofield *et al.*, 2012).

rock until steady state flow is achieved, at which point the total length of the finger is established from the front of the intrusion back to the point of coalescence (Pollard *et al.*, 1975).

Magma fingers induce deformation in ductile country rock at the leading edge of the fingers. This deformation facilitates continued intrusion and subsequent dike inflation to encroach and coalesce nearby fingers into sheet-like structures in the YZ plane. Shortening and compression of the country rock is greatest between fingers along Y (Fig. 6.4B-C) as dike inflation progresses during propagation (Fig. 6.4B-C; Pollard *et al.*, 1975; Schofield *et al.*, 2010, 2012b). When viewed down the propagation axis (X) the coalesced fingers will produce mesoscopic and microscopic structures analogous to pinch and swell or boudinage through time (Fig. 6.4D). Cuspate contact morphologies develop as fingers coalesce (Fig 6.3C) with the potential for second- generation dikes termed "horns" by Pollard *et al. (1975)* that propagate in the plane of XZ (Schofield *et al*., 2010; Schofield *et al*., 2012b).

Dike intrusion into country rock with pre-existing fabrics

It is assumed that faults influence magma transport and emplacement, as the potential weakness of earlier developed structures permits propagation through otherwise competent rock (Spacapan *et al*., 2016). Care must be taken with this assumption as local dilation may not parallel the regional orientation of σ_3 if dike overpressure is sufficiently high (Ziv *et al.,* 2000; Khoyadar and Einarsson, 2002). An increase in fluid pressure may (1) develop new fractures as the fluid input can overcome the tensile strength of the rock or (2) dilate preexisting fractures to focus intrusions by overcoming the effective normal stress that closed older fracture systems; where effective normal stress is a measure of the total normal stress (σ_n) acting on the fracture minus the fluid pressure (P_f) (Sibson, 2003; Cox, 2010). The ability of a fluid to overpressure is contingent on the tectonic regime, local state of differential stress, and the presence or absence of pre-existing

heterogeneities (Sibson, 2003). For fractures misaligned to the principal stress directions mathematical modelling by Ziv *et al*. (2000) found that even if magma pressure exceeds the ambient normal stress, it is very hard for the dike to follow existing structures unless one or more of the following conditions are met: (1) the fracture is nearly perpendicular to the least compressive stress, (2) the shear stress is small compared to the magma overpressure, or (3) the ambient normal stress of the dike is small in relation to the tensile strength of the host rock. As the intrusion progresses away from its source, reduction in overpressure results in preferential intrusion into weaker lithologies until an obstacle is encountered, at which point, continued melt supply would inflate and renew the process or dike arrest occurs (Thomas and Hutton, 2004; Thomson, 2007; Abdelmak *et al.*, 2012; Magee *et al.*, 2016).

The role of fluid overpressure for melt transport through fractured rock

Unlike mafic magmas, felsic magmas are unlikely to be voluminous enough to maintain critical levels of over pressurization to sustain fracture opening for continued magma transport over long distances from the melt source (Clemans and Mawer, 1992; Bons, 2001; Bons *et al.*, 2001). In felsic systems, small volumes of melt are transported by batches or pulses through repetitive opening and closing along fractures (Clemans and Mawer, 1992; Bons, 2001; Bons *et al.*, 2001). Melt passage permits buoyancy forces to overpressure the leading tip of the rising melt, dilate the fracture, and simultaneously underpressure the trailing tip to permit lithostatic pressure or regional stress to close the fracture (Bons, 2001). Melt transport by these mobile hydrofractures (Bons, 2001) is not controlled by viscosity, fracture-tip mechanics, or host-rock elasticity, but rather by the input rate of magma and any obstacles encountered during melt transport. As successive magma batches encounter impermeable regions and merge, batch sizes increase under confinement and cause the fluid pressure to exceed the effective normal stress; this dilates or

induces fractures, permitting continued propagation (Bons, 2001). As such, mobile hydrofractures are interpreted to form in primary ascent systems where a steady flow of magma is restricted by the absence of a magma reservoir that can be tapped — such as in granitic systems (Bons *et al.*, 2001).

6.2.3 Intrusion mechanism of the Separation Rapids pegmatites

Described by previous authors as sourced from the Separation Rapids pluton (Breaks and Tindle, 1997; Pan and Breaks, 1997) the melts that crystallized to form the Separation Rapids pegmatites preserve a history of magmatic processes, as shown by poikilitic textures, high-angle crystal growth, simply twinned feldspars, and euhedral crystals (Figs. 4.13, 4.16, 4.17, 4.23, 4.24). In addition, EBSD results (Section 5.1) illustrate that a preferred orientation is not developed for crystallographic or grain orientations in these pegmatites, instead indicating a uniform or random texture along layers, contacts, and in zones where solid-state modification of fabrics otherwise would be expected to occur. Mesoscopic textures in the pegmatites of the SLgb manifest in outcrop (*see* Table 4.2) through a combination of thermal fluidization (Kokelaar, 1982; Schofield *et al.,* 2010) and viscous indentation by induced faulting (Merle and Donnedieu, 2000), as magma fingers intruded into ductile host rock (Pollard *et al.,* 1975; *see* Table 6.1). Country rock xenoliths are common with irregular contacts and ridges and depressions on surfaces normal to flow in viscous indentation, as modelled by Mathieu *et al*. (2008).

The primary propagation direction can be derived from the orientation of mesoscopic finger structures in outcrop. In magma fingers, linear to curvi-linear host fabrics parallel to the pegmatite margins would be expected orthogonal to the Z axis of the finger intrusion (Fig. 6.4B-C) as is observed along the southwest and northeast contacts of the intrusions (Figs. 4.15, 4.22, 4.25). Along these contacts, minimal deformation of the S_2 fabric is recorded with the country rock

typically tracing the contact (e.g., Figs. 4.15, 4.28), except where ptygmatic subordinate dikes inject across the country rock fabric (Figs. 4.26, 4.27, 4.33, 4.36). Disordered and truncated country rock fabrics are greatest in YZ where local compression is active between finger intrusions along Y as lobes impinge (Fig. 6.4). Mantled by a biotite ± holmquistite metasomatic halo the pegmatites intrude subparallel to S_2 and truncate (Figs. 4.12, 4.14, 4.16, 4.17, 4.27, 4.28), wedge open (Figs. 4.28, 4.29, 4.33) or obliterate (Fig. 4.26) the country rock fabric along contacts at high angles to the long dimension of the pegmatite in outcrop. In the pegmatites studied, this approximates a southeasterly trend with subvertical dip with the trend defining either the maximum (X) or intermediate (Y) axis of the intrusion. The X axis would be expected to have laterally continuous form along the finger without impinging dikes, possible secondary high-angle "horns" (Pollard, 1973) of pegmatite at high angle to the contacts, and structures indicative of shortening of the country rock where propagation as a viscous indenter would record faulting, folding and compression of the country rock at the blunted terminus of the finger (Spacapan *et al.*, 2017). However, in the study pegmatites, local deformation of the country rock and impingement of pegmatite lobes is prevalent. Dikes possess arcuate, bulbous to lobate forms that impinge to form cusps, mullions and flames of interleaved basalt and pegmatite (See Section 4.3.4; Figs. 4.15, 4.17, 4.22, 4.27, 4.30, 4.33, 4.36, 5.12); infilled linkages between dikes (Figs 4.39, 5.12); bridges of country rock (Figs. 4.15, 4.37, 4.31, 4.38, 4.39) and stair-step structures (Figs. 4.31, 4.38), ptygmatic branched "horns" (Figs. 4.27, 4.30, 4.36; Pollard, 1973), and flanking dike blebs that form asymmetric en echelon boudin trains that cut S_2 (Figs. 4.30, 4.33, 4.38). This extent of deformation suggests that the intrusions approximate the minor (Z), and intermediate (Y) length axes of the pegmatites in outcrop (see Section 6.2.2; Fig. 6.4C; Pollard *et al*., 1975; Schofield *et*

al., 2012; Magee *et al.,* 2016, 2019). This would infer the primary propagation direction (X) is oriented subvertical with the secondary Y approximating the trend of the pegmatites.

Asymmetry in the intrusions may be a product of (1) non-coaxial strain and subsequent shearing coeval with intrusion, or (2) changes in the local stress field across the intrusion to form *en echelon* cracks infilled by pegmatite along the flanks of the intrusion (Pollard, 1973; Pollard *et al.,* 1975, 1982; Nicholson, 1985; Nicholson and Pollard 1985; Hutton, 2009; Schofield *et al.*, 2012b; Wyrick *et al.*, 2020). Dextral, non-coaxial strain would have controlled emplacement of the Big Mack pegmatite evidenced by deposit-scale dextral asymmetry and drag folds along the contacts (See Section 4.3.5; Figs. 4.3, 4.34, 4.35). The Glitter, Snowbank, and Big Whopper, however, illustrate asymmetry that may be a combination of (1) and (2) above. Physical analogue modelling by Wyrick *et al*. (2020) illustrated a rotation of second-generation dike branches by ca. 30^{o} off the main dike unit with a stepped morphology in section (Figure 6A-B *in* Wyrick *et al.,* 2020). Similar orientations of thin dikes near to or diverging off the main units are observed in the pegmatites of the SLgb with thin dikes oriented at roughly 30^{o} conjoining coeval dikes at the Separation Rapids pluton (Fig. 4.1), rotated *en echelon* dike blebs adjacent to the dikes at the Snowbank (Fig. 4.30, 4.38), thin dikes approaching S-C geometries at the Big Whopper (Fig. 4.37), and tapered *en echelon* boudins at the Glitter (Fig. 4.33). Correa-Gomes *et al.* (2001) compared dike symmetry in deforming rock with respect to magma shear flow and suggests this type of asymmetry is magmatic, with 'branch' structures similar to tension gashes developed parallel to the magma flow direction. These subordinate dikes suggest the main intrusion is buried at some distance below outcrop, with the current erosional surface between times T_2 and T_3 of Figure 6.4 (C-D; Pollard *et al.,* 1975; Schofield *et al.,* 2012b).

To summarize, mesoscopic structures observed in outcrop correlate with intrusive structures documented in literature (Pollard, 1973, 1975, 1982; Nicholson, 1985; Nicholson and Pollard 1985; Mathieu *et al.,* 2008; Hutton, 2009; Schofield et al., 2012b; Wyrick et al., 2020). These structures indicate the pegmatites of the SLgb intruded into ductile country rock as viscous indenters with a component of fluidization, represented by metasomatic haloes of biotite ± holmquistite, adjacent to the pegmatite. The outcrop surfaces of pegmatites are sub-horizontal and are thus, subparallel to the YZ plane of Fig. 6.4 with the propagation (X) axis oriented subvertical.

6.3 Pegmatite crystallization and magmatic microstructures

The following section provides background information into crystallization processes and resultant microstructures in pegmatites. This is summarized from multiple authors and include concepts of myrmekite vs granophyre, undercooling, and the generation of pegmatitic textures. Additional detail is available in the original works as referenced below. Comparison can then be made from these works to that of the textures and microstructures documented in this study in Section 6.3.1.

In this study, poikilitic intergrowths of albite and quartz occur as two forms (1) myrmekite and (2) granophyre. Herein, the term 'myrmekite' follows the convention of Vernon *et al.* (1983), Simpson and Wintsch (1989), and Vernon (1991, 2000), among others, where myrmekite develops as a subsolidus deformation texture. Myrmekite as defined nucleates along the margins of K-feldspar grains and replaces the original crystals. In the Skidder pluton, this texture is well developed along the penetrative foliation and indicates the Skidder pluton crystallized prior to the *ca.* 2650 Ma amphibolite-facies regional deformation event (ca. 2690 Ma, Macdonald *et al.,* 2023).

Common to the Separation Rapids pluton and all mineralized pegmatites, the second form of quartz-albite intergrowth is granophyre, a quartz - alkali-feldspar intergrowth defined by Fenn (1977) as a magmatic texture indicative of pronounced and sudden undercooling of melts, further applied to pegmatite crystallization by London (2018). Where undercooling is described by Fenn (1977) as the temperature interval between the onset of crystallization and the liquidus for a given composition (Sirbescu *et al.*, 2008, 2017; London, 2009). In unusual cases this may occur at temperatures in the range of 350-450ºC (Morgan and London, 1999; Sirbescu and Nabelek, 2003), well below the melt-saturating rare-element mineral liquidus of 700ºC (*cf.* London, 2016). In undercooled states, crystallization may occur over timeframes as short as days to weeks in thin dikes under disequilibrium to form skeletal or unidirectional crystals (see Section 4.3; Rubin, 1995; Baker, 1998; Sirbescu *et al.*, 2008, 2017; London, 2008, 2009; Morgan and London, 2012).

Crystallization of undercooled melts

Generalized for igneous rocks, large crystal sizes are commonly attributed to slow cooling and unimpeded crystal growth (Winter, 2001). In contrast, however, the crystallization of undercooled, flux-rich melts may facilitate rapid crystallization of large crystals over days to weeks in thin dikes (Rubin, 1995; Baker, 1998; Sirbescu *et al.*, 2008, 2017; London, 2008, 2009; Morgan and London, 2012).

Models of pegmatite crystallization, such as that of early work of Jahns and Burnham (1969), explain the transition from very coarse-grained (pegmatite) to fine-grained (aplite) igneous textures with a two-phase, magma vapour system. In this system, buoyant vapour removes potassium from the melt at the point of H_2O saturation to trigger crystallization of aplite along the footwall, and pegmatitic textures along the hanging wall. London (2009) interprets outer and inner domains of microtextural development in pegmatites. Outer domains may be characterized in part

by fine-grained units, graphic intergrowths between quartz and feldspars, and unidirectional crystal growth. In the outer domain, the high nucleation density of heterogeneous short crystals in water-saturated melts (5-6 wt.% H_2O) imparts quench textures as crystallization progresses (London, 2008, 2009; Sirbescu *et al.*, 2008; 2017). A textural shift takes place from fine-grained aplites, layered aplites, skeletal and graphic crystals, and oriented inward crystal growth in the outer domains to isotropic fabrics and coarse crystal sizes and monocrystalline segregations in the interior domains of the pegmatites (London, 2009).

Internal domains with coarse, blocky crystal textures develop where the rate of lateral diffusion of components approaches that of inward advance of the crystallization front (Section 4.2.2, 4.3.1; Sirbescu and Nabelek, 2003; London, 2009). Flux accumulation and enrichment facilitates crystallization by addition of B, P, F, and H_2O within the haplogranite (Qz-Ab-Or) system, thereby (1) lowering viscosity and (2) promoting the texture formation by enhancing the miscibility among components through constitutional zone-refining (Sirbescu and Nabelek, 2003; Chapter 17 of London, 2008). Although integral to the generation of pegmatitic texture, flux is a minor constituent of the melt with some of the most fractionated pegmatite bodies known to date, such as the Tanco pegmatite, containing less than 1 wt% of fluxing components (Stilling *et al.*, 2006).

Experimental studies reviewed in Paterson *et al. (1989)* and summarized below indicate that melt fabrics have poor strain memory, are easily reset, and preserve only the waning increments of strain during emplacement. A lack of CPO and uniform / random crystal orientations would be expected in magmatic systems. Submagmatic systems, where suspension flow is inhibited would have solid-state deformation super-imposed on magmatic flow, such as c-slip in quartz, recrystallized feldspars, a-slip in quartz and grain size reduction, ‘S-C’ foliations following

same shear sense as imbricated minerals, and late mineral growth in pressure shadows (Paterson *et al.,* 1989). Recent review of mesoscopic magmatic structures by Paterson *et al.* (2019) plot deviatoric stress (flow rate) and strain rate against decreasing temperature and increased crystallization (see Figure 1 *in* Paterson *et al.,* 2019). Characteristics of submagmatic flow are evident in this schematic and share elements of tectonic and magmatic stress dominant textures (Paterson *et al.,* 2019*)*.

6.3.1 Microstructures of the SLgb pegmatites

Breaks and Tindle (1997) inferred recrystallization (Photo 17.1 *in* Breaks and Tindle, 1997) by strong ductile deformation to flatten and recrystallize petalite and develop spindle and lensoid-shaped feldspars. Along the margins of petalite, Breaks and Tindle (1997) inferred secondary growth of SQUI (spodumene-quartz intergrowths). For secondary SQUI to develop through strain-induced recrystallization a CPO would be expected. The lack of preferred orientations in the pegmatites of this study (see Section 5.1) does not support this interpretation. Alternatively, Cerny and Ferguson (1972) documented primary SQUI in the TANCO pegmatite where SQUI formed *en masse* coeval with petalite as the temperature decreased below the petalite stability field (London, 1984). SQUI at TANCO does not show preferred orientations (Cerny and Ferguson, 1972) like those in the pegmatites of this study.

Paterson *et al*. (1989) reviewed four environments where foliations can form in granitoids. These include magmatic (suspension-like) flow, submagmatic flow, high temperature solid-state and low temperature solid-state flow regimes. The lack of penetrative CPO through the fine-grained domains and internal layers in addition to crystallization ages that post-date S_2 fabric development precludes both the high- and low-temperature solid-state fabric generation suggested by previous authors for the pegmatites of the SLgb. However, EBSD analyses (Section 5.1) record

uncommon GOS in excess of 5° (Figs. 5.3, 5.7, 5.14) and suggest that non-pervasive recrystallization and recovery has occurred in places within the pegmatites of the SLgb.

Evidence for the presence of microtextural domains of London (2009) occur in the pegmatites of the SLgb with quenched outer domains comprised of growth-twinned, euhedral, poikilitic to granophyric albite indicative of magmatic growth (e.g. Figs. 4.13, 4.21, 4.24; London, 2009, 2018, 2020; Sirbescu *et* al., 2017; Vernon, 1986, 2000, 2010). These outer domains possess weakly aligned albite in places at the contacts (Figs. 5.3, 5.7, 5.14) as well as in albite-rich internal layers (Fig. 4.21) that in part defines P_L in the pegmatites. Pegmatite layering (P_L) is preserved in the internal domains (see Section 4.3.1; Figs. 4.18, 4.21) with a lack of preferred orientation (Figs. 5.3, 5.4) and are locally monomineralic, with layers of albite-rich or petalite-rich crystals (Fig. 4.21).

Crystal orientations in the SLgb occur in uniform (random) and aligned forms. Comparison of textures documented in the SLgb to textures plotted on Figure 1 of Paterson *et al.* (2019) of infrequent fractured microcline infilled by muscovite and quartz (tectonic influence) as well as transformation twinning of albite (magmatic; See Section 4.3.1) suggest local preservation of submagmatic crystallization and the transition from melt- to grain-supported flow of a viscous magma towards the solidus. Herein, layering in the Separation Rapids pluton and in the pegmatites, indicated elsewhere in this thesis as S_L and P_L respectively, is the product of magmatic flow of a viscous fluid which follows the definition of Paterson *et al*., (1989) to imply deformation by displacement of melt, of which local crystalline deformation, such as the infrequent GOS, would be expected as crystallization progresses through the transition from melt-supported to grain-supported (submagmatic) flow.

6.4 Implications for Rare-element Pegmatite Exploration and Recommendations for Future Work

Results of this study provide new information on pegmatite morphology, structural attitudes, emplacement, and timing in the Separation Lake area and thus, has the potential to refine the exploration for critical element-bearing intrusions in the SLgb. In addition, the findings provide information that may find application in other rare-element pegmatite fields.

Fluidization of the country rock coupled with ductile finger intrusion of rare-element pegmatites has resulted in complex morphologies of arrested intrusions. Lack of crystallographic preferred orientations, non-penetrative regional foliation, and lack of recrystallization (Tables 4.1-4.3) indicate the magmatic micro-, meso-, and macroscopic are the dominant structures and textures preserved in the pegmatites of the SLgb and far outweigh any regional-scale tectonic overprint. Cropping out in the YZ plane of Figure 6.4, the pegmatites would be open at depth with the length of the long axis of the pegmatites yet undefined. The morphology of the Big Whopper supports the interpretation of intrusion of magma fingers into a ductile host rock with the minor (Z, 70 m; Breaks and Tindle, 1997) and intermediate (Y, 350 m; Breaks and Tindle, 1997) axes forming the YZ plane oriented similar to the glaciated surface and the long (X, >560 m, 566 m drilled depth, Avalon Advanced Materials [Press Release], 2023) axis oriented subvertical and infer the direction of propagation. Drilling by Avalon in spring 2023 shows that the deposit is still open at depth below the 566 m pierce point.

A subvertical propagation direction suggests arrest of the intrusions at different levels in the now glaciated topography. The Big Mack and Big Whopper illustrate near complete coalescence of the individual pegmatites at the mesoscale (Fig. 6.4D). Dikes are not similarly coalesced and possess more complex morphologies at the Snowbank and Glitter pegmatites. This

would infer the eroded surface of the Snowbank and Glitter pegmatites is located above, but near to, the point of coalescence (T_2 of Fig. 6.4B-C). Follow up drilling to test for the thickest part of these intrusions as well as delineate the root of these pegmatites to expand the SLgb lithium resource is recommended as the interpreted level of glaciated surface suggests the Glitter and Snowbank pegmatites should open at depth.

Variations in crystallization ages indicate protracted generation (>40 Ma) of lithium-bearing pegmatites in the SLgb. To facilitate intrusion, over-pressure and mobile hydrofractures (Bons, 2001; Bons *et al.,* 2001) to transport melt would have utilized previously fractured or weakened ground, such as lithological contacts or strain zones, such as the interpreted structural corridor of Pedersen (1997). Brisbin (1986) outlines the importance of anisotropies, where schistosity, cleavage, and pre-existing fracture play a part in the orientation of the pegmatites, where the fluid pressure of the pegmatite may overcome the effective normal stress. Field relationships at the Big Mack pegmatite indicate syn-tectonic emplacement ca. 2641 Ma during dextral transcurrent movement. Record of tectonic-induced dilation is not prevalent at the other pegmatites in this study with the peripheral contacts under overburden. Viscous indenter and fluidization intrusion dynamics do not require previously fractured ground, with their mechanisms capable of inducing local deformation and dilation to further propagate, such as at the western limit of the map for the Snowbank pegmatite (Fig. 4.4). At this western limit a thin dike exploited a strain zone at the contact between massive and pillowed basalt ~30 m from the main dikes (Fig. 4.4). This thin dike rotates from subparallel the strain-zone trend to near orthogonal where it exits the strain zone. At this point of divergence from strain-subparallel, the thin dike cuts the country rock fabrics to suggest it post-dates the strain zone and utilized previously strained rock as a conduit.

Limited melt supply and batch delivery of melt, such as is favoured in granitic systems, suggests the pegmatites where exposed may be composite bodies built through successive batches of melt. Field relationships at the Big Mack of K-feldspar pegmatite scoured by petalite pegmatite (Fig. 4.20), as well as contact characteristics and presence or lack of fine-grained domains in dikes within 10's of centimetres of each other at the Snowbank pegmatite (Fig. 4.30) would suggest this possibility. Several groupings of pegmatite crystallization, ca. 2640 Ma, 2620 Ma, and 2600 Ma may support this with additional geochronological determinations needed.

In contrast to the interpretation of Breaks (1991), Pedersen (1998), and Barclay (1998) that have guided exploration methodologies in the region, the role of regional deformation at amphibolite-facies is relatively minor with respect to the distribution, deformation, and modification of pegmatite morphologies. This interpretation is supported by: (1) new mineral growth associated with magmatic fluids overprinting the regional S_2 fabric; (2) undeformed contacts between country rock and pegmatites where rheological contrast would be greatest; (3) EBSD analyses to indicate that the minerals were not deformed by solid-state deformation and are magmatic; and (4) protracted pegmatite intrusion over a period in excess of 40 Ma. The complex morphologies documented in Chapter 4 are the products of magmatic flow and would control the distribution of pegmatites through the SLgb where fluid overpressure overcomes the effective lithostatic pressure to induce fracture and propagation. Mesostructural indicators of propagation suggest that the dominant direction of propagation is now sub-vertical with a component of northwesterly flow from the source of the melt; and the surface expression of several pegmatites record partial coalescence and suggest the bulk of these intrusions, such as the Glitter and Snowbank pegmatites lies buried under the current erosional surface. Lastly, similar emplacement ages across the SLgb and Bird River belt of Eastern Manitoba (Ex. Big Mack, ca. 2637 Ma and

Tanco at ca. 2640 Ma) suggest the ERS/WRS boundary is a locus for mineralized pegmatites and mineralization may occur outside the SLgb and Bird River belt along the boundary.

6.4.1 Recommendations for Future Work

Although not necessarily controlled by structural anisotropies in the country rock, the distribution of pegmatites in the SLgb is not unequivocally determined in this study. Additional work to define the structural and lithological architecture of the SLgb is recommended. In addition, detailed geochronological work across units of individual pegmatites would test for reactivation of previous hydrofractures to build composite intrusions over the protracted crystallization history evidenced in this study, as opposed to single pulse generation of each body.

Reference List

Abdelmak, M.M., Mourgues, R., Galland, O. and Bureau, D. (2012): Fracture Mode Analysis and Related Surface Deformation During Dyke Intrusion: Results from 2D Experimental Modelling; *Earth and Planetary Science Letters*, Volume 359-360, pages 93-105, https://dx.doi.org/10.1016/j.espl.2012.10.008.

Aiken, S.R., Gowans, R., Hawton, K.E., Jacobs, C., Pilcher, B., Spooner, J., Trueman, D.L. (2016): Ni-43-101 Technical Report on the Preliminary Economic Assessment of Lithium Hydroxide Production, Separation Rapids Lithium Project, Kenora Ontario; submitted by Micon International Limited *for* Avalon Advanced Materials, 278 pages.

Aleinikoff, J. N., Schenck, W.S., Plank, M.O., Srogi, L., Fanning, C.M., Kamo, S.L. and Bosbyshell, H. (2006): Deciphering Igneous and Metamorphic Events in High-Grade Rocks of the Wilmington Complex, Delaware: Morphology, Cathodoluminescence and Backscattered Electron Zoning, and SHRIMP U-Pb Geochronology of Zircon and Monazite; *Geological Society of America Bulletin*, 118, pages 39–64.

Ashton, K.E., Heaman, L.M., Lewry, J.F., Hartlaub, R.P. and Shi, R. (1999): Age and origin of the Jan Lake Complex: a glimpse at the buried Archean craton of the Trans-Hudson Orogen; *Canadian Journal of Earth Sciences*, Volume 36, Number 2: pages 185-208. https://doi.org/10.1139/e98-038

Avalon Advanced Materials Inc., (2023): Avalon Announces a Substantive 20% Increase in Deposit Size at its Flagship Separation Rapids Joint-Venture Lithium Project; *Avalon Advanced Materials Inc.*, News Release, August 10, 2023, 7 pages.

Baadsgard, H. and Cerny, P. (1993): Geochronological Studies in the Winnipeg River Pegmatite Populations, southeastern Manitoba; *Geological Association of Canada-Mineralogical Association of Canada*, Joint Annual Meeting, Program with Abstracts, Volume 18, page A5.

Baker, D.R. (1998): The Escape of Pegmatite Dikes from Granitic Plutons: Constraints fomr New Models of Viscosity and Dike Propagation; *Canadian Mineralogist*, Volume 36, pages 255-263.

Barclay, W.A. (1998): Mesoscopic Structural Relations and Preliminary Macroscopic Inferences at the Separation Rapids Rare Metal Pegmatite Property, Kenora Mining Division, Ontario; unpublished company report, *Avalon Ventures Ltd.*, 50 pages.

Beakhouse, G.P. (1977): A subdivision of the Western English River Subprovince; *Canadian Journal of Earth Science*, Volume 14, pages 1481-1489.

Beakhouse, G.P. (1991): Winnipeg River Subprovince; *in* Geology of Ontario, *Ontario Geological Survey*, Special Volume 4, Part 1, pages 279-301.

Bell, T.H. and Johnson, S.E. (1989): The Role of Deformation Partitioning in the Deformation and Recrystallization of Plagioclase and K-Feldspar in the Woodroffe Thrust Mylonite Zone, Central Australia; *Journal of Metamorphic Geology,* Volume 7, pages 151-168.

Bertelsen, H.S., Rogers, B.D., Galland, o., Dumazer, G. and Benanni, A.A. (2018): Laboratory Modeling of Coeval Brittle and Ductile Deformation During Magma Emplacement into Viscoelastic Rocks; *Frontiers in Earth Science*, Volume 6, Article 199, pages 1-16, https://doi.org/10.3389/feart.2018.00199.

Blackburn, C.E. and Young, J.B. (1993): Project Unit 92-03. Geology of the Separation Lake Greenstone Belt, *in* Summary of Field Work and Other Activities 1993, *Ontario Geological Survey*, Miscellaneous Paper 162, pages 68-73.

Blackburn, C.E. and Young, J.B. (2000): Precambrian Geology of the Separation Lake Area, northwestern Ontario; *Ontario Geological Survey*, Open File Report 6001, 84 pages.

Bons, P.D. (2001): The Formation of Large Quartz Vein by Rapid Ascent of Fluids in Mobile Hydrofractures; *Tectonophysics*, Volume 336, pages 1-17.

Bons, P.D., Dougherty-Page, J. and Elburg, M.A. (2001): Stepwise Accumulation and Ascent of Magmas; *Journal of Metamorphic Geology,* Volume 19, pages 627-633.

Bons, P.D., Druguet, E., Hamann, I., Carreras, J. and Passchier, C.W. (2004): Apparent Boudinage in Dykes; *Journal of Structural Geology*, Volume 26, pages 625-636.

Bradley, D.C., McCauley, A.D., and Stillings, L.M. (2017): Mineral-deposit model for lithium-cesium-tantalum pegmatites; *US Geological Survey Scientific Investigations Report* 2010-5070-0, 48 pages, https://doi.org/10.3133/sir20105070O.

Breaks, F.W. (1991): English River Subprovince; *in* Geology of Ontario, *Ontario Geological Survey*, Special Volume 4, Part 1, pages 239-277.

Breaks, F.W. (1993): Project Unit 93-11. Granite-Related Mineralization in northwestern Ontario: I. Raleigh Lake and Separation Rapids (English River) Rare-Element Pegmatite Fields; *in* Summary of Field Work and Other Activities, 1993, *Ontario Geological Survey*, Miscellaneous Paper 162, pages 104-110.

Breaks, F.W. and Bond, W.D. (1993): The English River Subprovince – An Archean Gneiss Belt: Geology, Geochemistry and Associated Metamorphism; *Ontario Geological Survey*, Open File Report 5846, Volume 1, pages 1-483, 884 pages.

Breaks, F.W. and Tindle, A.W. (1994): Granite-Related Mineralization in Northwestern Ontario: II. Detailed examination of the Separation Rapids (English River) Rare-Element Pegmatite Group, *in* Summary of Field Work and Other Activities 1994, *Ontario Geological Survey*, Miscellaneous Paper 163, pages 109-112.

Breaks, F.W. and Tindle, A.W. (1996a): Project Unit 93-11. Granite-Related Mineralization in Northwestern Ontario: IV. New Rare-Element Pegmatite Discoveries in the Separation Lake Area; *in* Summary of Field Work and Other Activities, *Ontario Geological Survey*, Miscellaneous Paper 166, pages 19-22.

Breaks, F.W. and Tindle, A.W. (1996b): New Discovery of Rare-Element Pegmatite Mineralization, Separation Lake Area, northwestern Ontario; *Ontario Geological Survey*, Open File Report 5946, 9 pages.

Breaks, F.W. and Tindle, A.W. (1997): Project Unit 93-11. Rare-Metal Exploration Potential of the Separation Lake Area: an Emerging Target for Bikita-Type Mineralization in the Superior Province of North Western Ontario; *in* Summary of Field Work and Other Activities, *Ontario Geological Survey*, Miscellaneous Paper 168, pages 72-88.

Breaks, F.W. and Tindle, A.W. (2002): Rare-Element Mineralization of the Separation Lake Area, northwest Ontario: Characteristics of a New Discovery of Complex-type, Petalite-subtype, Li-Rb-Cs-Ta Pegmatite; *in* Industrial Minerals in Canada, *Canadian Institute of Mining, Metallurgy and Petroleum*, Special Volume 53, pages 159-178.

Breaks, F.W. and Pan, Y. (1995): Granite Related Mineralization in northwest Ontario. III. Relationship of Granulite Metamorphism to Rare-Element Mineralization in the Separation Lake Area of the English River Subprovince; in Summary of Field Work and Other Activities 1995, *Ontario Geological Survey*, Miscellaneous Paper 164, pages 79-81.

Breaks, F.W., Bond, W.D. and Stone, D. (1978): Preliminary Geological Synthesis of the English River Subprovince, northwestern Ontario and its Bearing Upon Mineral Exploration; *Ontario Geological Survey*, Miscellaneous Paper 72, 55 pages.

Breaks, F.W., Tindle, A.G. and Smith, S.R. (1999): Geology, Mineralogy, and Exploration Potential of the Big Mack Pegmatite System: a Newly Discovered Western Extension of the Separation Rapids Pegmatite Group, NW Ontario; *in* Summary of Field Work and Other Activities, 1999, *Ontario Geological Survey*, Open File Report 6000, pages 25-1 to 25-13.

Breaks, F.W., Selway, J.B and Tindle, A.G. (2001): Project Unit 01-304. Fertile Peraluminous Granites and Related Rare-Element Pegmatite Mineralization, Superior Province, northwest and northeast Ontario; *in* Summary of Field Work and Other Activities 2001, *Ontario Geological Survey*, Open File Report 6070, pages 39-1 to 39-39.

Breaks, F.W., Selway, J.B. and Tindle, A.G. (2003): Fertile peraluminous granites and related rare-element mineralization in pegmatites, Superior Province, Northwest and Northeast Ontario: Operation Treasure Hunt; *Ontario Geological Survey*, Open File Report 6099, 179 pages.

Brisbin, W.C. (1986): Mechanics of Pegmatite Intrusion; *American Mineralogist*, Volume 71, pages 644-651

Blackburn, C.E., Beakhouse, G.P., Young, J.B. (1992): Project Unit 92-03. Geology of the Umfreville-Separation Lakes Area; *in* Summary of Field Work and Other Activities, 1992, *Ontario Geological Survey*, Miscellaneous Paper 160, pages 20-26.

Blackburn, C.E. and Young, J.B. (1993): Project Unit 92-03. Geology of the Separation lake Greenstone Belt; *in* Summary of Field Work and Other Activities 1993, *Ontario Geological Survey*, Miscellaneous Paper 162, pages 68-73.

Blackburn, C.E., Young, J.B. and Breaks, F.W. (2008): Precambrian Geology of the Separation Lake Greenstone Belt – West Sheet; *Ontario Geological Survey*, Preliminary Map P.2673, scale 1:20,000.

Burchardt, S. (2008): New Insights into the Mechanics of Sill Emplacement Provided by Field Observations of the Njardvik Sill, Northeasty Iceland; *Journal of Volcanology and Geothermal Research*, Volume 173, pages 280-288.

Camacho, A., Baadsgaard, H., Davis, D.W. and Cerny, P. (2012): Radiogenic Isotope Systematics of the TANCO and Silverleaf Granitic Pegmatites, Winnipeg River Pegmatite District, Manitoba; *The Canadian Mineralogist*, Volume 50, pages 1775-1792; doi: 10.3749/canmin.50.6.1775.

Card. K.D. and Ciesielski, A. (1986): DNAG#1. Subdivisions of the Superior Province of the Canadian Shield; *Geoscience Canada*, Volume 13, pages 5-13.

Cerny, P. (1989a): Characteristics of Pegmatite Deposits of Tantalum, *in* Lanthanides, Tantalum, and Niobium; Möller, P., Cerny, P. and Saupé, F., Editors, Springer-Verlag, pages 195-239.

Cerny, P. (1989b): Exploration Strategy and Methods for Pegmatite Deposits of Tantalum; *in* Lanthanides, Tantalum, and Niobium, Möller, P., Cerny, P. and Saupé, F., Editors, Springer-Verlag, pages 274-302

Cerny, P. (1991): Rare-element Granitic Pegmatites. Part I : Anatomy and Internal Evolution of Pegmatite Deposits; *Geoscience Canada*, Volume 18, No.2, pages 49-67.

Cerny, P. and Ercit, T.S. (2005): The Classification of Granitic Pegmatites revisited; *The Canadian Mineralogist*, Volume 43, pages 2005-2026.

Cerny, P. and Ferguson, R.B. (1972): The Tanco Pegmatite at Bernic Lake, Manitoba. IV. Petalite and Spodumene Relations; *The Canadian Mineralogist*, Volume 11, pages 660-678.

Cerny, p., Ercit, T.S. and Vanstone, P.J. (1998): Mineralogy and Petrology of the Tanco Rare-Element Pegmatite Deposit, Southeastern Manitoba – Field Trip Guidebook B6; *International Mineralogical Association 17th General Meeting*, Toronto, Ontario, 74 pages.

Cerny, P., Trueman, D.L, Ziehlke, D.V., Goad, B.E. and Paul, B.J. (1981): Economic Geology Report ER80-1, The Cat Lake-Winnipeg River and the Wekusko Lake Pegmatite Fields, Manitoba; *Manitoba Department of Energy and Mines*, 236 pages.

Cerny, P., Ercit, T.S. and Vanstone, P.T. (1996): Petrology and Mineralization of the Tanco Rare-Element Pegmatite, Southeastern Manitoba – Field Trip Guidebook A4; *Geological Association of Canada/Mineralogical Association of Canada Annual Meeting*, Winnipeg, Manitoba, May 27-29, 63 pages.

Cerny, P., London, D. and Novàk, M. (2012): Granitic Pegmatites as Reflections of their Sources; *Elements*, Volume 8, pages 289-294, https://doi.org/10.2113/gselements.8.4.289.

Chastko, L.C. (2001): Report on Rare Element Pegmatite Properties in the Separation, Huston, & Linklater Lakes Areas of northwestern Ontario, Rush ake – Birse Lake of southeastern Manitoba; submitted by Emerald Fields Resource Corporation, *Ontario Geological Survey*, Technical Report, 124 pages.

Clark, J.G. and Siemieniuk, S. (2016): Assessment Report on the Paterson Lake Property, Kenora Mining Division, Ontario; submitted by GoldOn Resources, *Ontario Geological Survey*, Assessment Report 20000014162, 56 pages.

Clemans, J.D. and Mawer, C.K. (1992): Granitic Magma Transport by Fracture Propagation; *Tectonophysics*, Volume 204, pages 339-360.

Corfu, F. (1988): Differential Response of U-Pb Systems in Coexisting Accesssory Minerals, Winnipeg River Subprovince, Canadian Shield: Implication for Archean Crustal Growth and Stabilization; *Contributions to Mineralogy and Petrology*, Volume 98, pages 312-325.

Corfu, F., Stott, G.M. and Breaks, F.W. (1995): U-Pb Geochronology and Evolution of the English River Subprovince, and Archean low-P-high T Metasedimentary Belt in the Superior Province; *Tectonics*, Volume 14, Number 5, pages 1220-1233.

Correa-Gomes, L.C., Filho, C.R.S, Martins, C.J.F.N. and Oliveira, E.P. (2001): Development of Symmetrical and Asymmetrical Fabrics in Sheet-like Igneous Bodies: The Role of Magma Flow and Wall-rock Displacements in Theoretical and Natural Cases; *Journal of Structural Geology,* Volume 23, pages 1415-1428.

Cox, S.F. (2010): The Application of Failure Mode Diagrams for Exploring the Roles of Fluid pressure and Stress States in Controlling Styles of Fracture-controlled Permeability Enhancement in Faults and Shear Zones; *Geofluids*, Volume 10, pages 217-233.

Cross, A.J., Prior, D.J., Stipp, M. and Kidder, S. (2017a): The recrystallized grain size piezometer for quartz: An EBSD-based calibration; *Geophysical Research Letters*, Volume 44, pages 6667–6674. https://doi.org/10.1002/2017GL073836

Cross, A.J., Hirth, G. and Prior, D.J. (2017): Effects of Secondary Phases on Crystallographic Preferred Orientations in Mylonites; *Geology*, Volume 45, No. 10, pages 955-958.

de la Fuente, F. (1998): Structural Analysis of the Tanco's Separation Lake Property. Western Ontario (Canada); *in* Galeschuk, C. (1998) Report on the 1998 Lithogeochemistry, Geological Mapping and Structural Analysis Separation Lake, Ontario (52 L/8 SW) Summer 1998; submitted by Tantalum Mining Corporation of Canada Limited, *Ontario Geological Survey,* 52L08SW2008; 33 pages.

de Saint-Blanquet, M., Habert, G., Horsman, E., Morgan, S.S., Tikoff, B., Launeau, P. and Gleizes, G. (2006): Mechanisms and Duration of Non-Tectonically Assisted Magma Emplacment in the Upper Crust: The Black Mesa Pluton, Henry Mountains, Utah; *Tectonophysics*, Volume 428, pages 1-31.

Duffield, W.A., Bacon, C.R., and Delaney, P.T. (1986): Deformation of Poorly Consolidated Sediment During Shallow Emplacement of a Basalt Sill, Coso Range, California; *Bulletin of Volcanology,* Volume 48, pages 97-107.

Eggleton, R.A. and Buseck, P.R. (1980): The Orthoclase-Microcline Inversion: A High-Resolution Transmission Electron Microprobe Study and Strain Analysis; *Contributions to Mineralogy and Petrology*, Volume 74, pages 123-133.

Fenn, P.M. (1977): The Nucleation and Growth of Alkali Feldspars from Hydrous Melts; *The Canadian Mineralogist,* Volume 15, pages 135-161.

Galeschuk, C.R. (1998): Report on the 1998 Lithogeochemistry, Geological Mapping and Structural Analysis Separation Lake, Ontario (52 L/8 SW) Summer 1998; submitted by Tantalum Mining Corporation of Canada Limited, *Ontario Geological Survey,* Assessment Report 52L08SW2008, 177 pages.

Galeschuk, C.R. and Vanstone, P.J. (2005): Exploration for Buried Rare Element Pegmatites in the Bernic Lake Area, southeastern Manitoba, MAC Short Course, 2004, GAC publication.

Galeschuk, C.R. and Vanstone, P.J. (2007): Exploration Techniques for Rare-Element Pegmatite in the Bird River Greenstone Belt, southeastern Manitoba; *in* Proceedings of Exploration 07: Fifth Decennial International Conference on Mineral Exploration, Milkereit, Editor, Toronto, Ontario, Canada, pages 823-839.

Gilbert, H.P. (2008): Stratigraphic Investigations in the Bird River Greenstone Belt, Manitoba (part of NTS 52L5,6); *in* Report of Activities 2008, Manitoba Science, Technology, Energy and Mines, *Manitoba Geological Survey*, pages 121-138.

Gilbert, H.P., Davis, D.W., Duguet, M., Kremer, P.D., Mealin, C.A. and MacDonald, J. (2008): Geology of the Bird River Belt, southeastern Manitoba (parts of NTS 52L5, 6); Manitoba Science, Technology, Energy and Mines, *Manitoba Geological Survey*. Geoscientific Map MAP2008-1, scale 1:50,000 (plus notes and appendix).

Goscombe, B.D., Passchier, C.W. and Hand, M. (2004): Boudinage Classification: End-Member Boudin Types and Modified Boudin Structures; *Journal of Structural Geology*, Volume 26, pages 739-763.

Gowans, R.M., Jacobs, C., Pilcher, B., Aiken, S.R., Hawton, K.E. and Mercer, W. (2018): NI 43-101 Technical Report on the Preliminary Economic Assessment for the Production of Petalite Concentrate from the Separation Rapids Lithium Deposit, Kenora, Ontario; submitted by Micon International Ltd. *for* Avalon Advanced Materials, 300 pages.

Grasemann, B. and Dabrowski, M. (2015): Winged Inclusinos: Pinch-and-Swell Objects during High-Strain Simple Shear; *Journal of Structural Geology*, Volume 70, pages 78-94.

Grimmer, H. (1979): The Distribution of Disorientation Angles if all Relative Orientations of Neighboring Grains are Equally Probable; *Scripta Metallurgica*, Volume 13, pages 161-164.

Hrabi, R.B. and Cruden, A.R. (2006): Structure of the Archean English River Subprocine: Implications for the Tectonic Evolution of the western Superior Province, Canada; *Canadian Journal of Earth Sciences*, Volume 43, pages 947-966.

Hielscher, R. and Schaeben, H., (2008): A novel pole figure inversion method : specification of the MTEX algorithm; *Journal of Applied Crystallography,* Volume 41, pages 1024–1037. https://doi.org/10.1107/S0021889808030112

Hobbs, B.E., Means, W.D. and Williams, P.F. (1976): An outline of Structural Geology; John Wiley & Sons, New York, 571 pages.

Holness, M.B. and Humphreys, M.C.S. (2003): The Traigh Bhan na Sgurra Sill, Isle of Mull: Flow Localization in a Major Magma Conduit; *Journal of Petrology*, Volume 44, pages 1961-1976.

Hutton, D.H.W. (2009): Insights into Magmatism in Volcanic Margins: Bridge Structures and a New Mechanism of Basic Sill Emplacement – Theron Mountains, Antarctica; *Petroleum Geoscience*, Volume 15, pages 269-278.

Jackson, S.E., Pearson, N.J., Griffin, W.L. and Belousova, E.A. (2004): The Application of Laser Ablation-Inductively Coupled Plasma-Mass Spectrometry to *in situ* U-Pb Zircon Geochronology; *Chemical Geology*, Volume 211, pages 47-69.

Jahns, R.H. and Burnham, C.W. (1969): Experimental Studies of Pegmatite Genesis: I. A model for the Derivation and Crystallization of Granitic Pegmatites; *Economic Geology*, Volume 64, pages 843-864.

Kesler, S.E., Gruber, P.W., Medina, P.A., Keolian, G.A., Everson, M.P. and Wallington, T.J. (2012): Global lithium resources: Relative importance of pegmatite, brine, and other deposits; *Ore Geology Reviews,* Volume 48, pages 55-69.

Kinny, K.D., McNaughton, N.J., Fanning and Maas, R. (1994): 518 Ma Sphene (titanite) from the Khan Pegmatite, Namibia, southwest Africa: A Potential Ion-Microprobe Standard; *in* Abstract presented at the 8th International Conference on Geochronology, Cosmochronology, and Isotope Geology, *United States Geological Survey*, Circular 1107, page 171.

Khodayar, M. and Einarsson, P. (2002): Strike-Slip Faulting, Normal Faulting, and Lateral Dike Injections Along a Single Fault: Field Example of the Gljúfurá Fault Near a Tertiary Oblique Rift-Transform Zone, Borgarfjörður, west Iceland; *Journal of Geophysical Research*, Volume 107, No. B5, pages ETG-5-1 to ETG 5-16.

Kokelaar, B.P. (1982): Fluidization of Wet Sediments During the Emplacement and Cooling of Various Igneous Bodies; *Journal of the Geological Society of London,* Volume 139, pages 21-33.

Larbi, Y., Stevenson, R., Breaks, F.W., Machado, N. and Gariepy, C. (1999): Age and Isotopic Composition of Late Archean Leucogranites: Implications for Continental Collision in the western Superior Province; *Canadian Journal of Earth Sciences*, Volume 36, pages 495-510.

Lister, J.R. (1990): Buoyancy-Driven Fluid Fracture. The Effects of Material Toughness and of low-viscosity precursors; *Journal of Fluid Mechanics*, Volume 210, pages 263-280.

Lloyd, G.E., Farmer, A.B. and Mainprice, D. (1997): Misorientation Analysis and the Formation and Orientation of Subgrain and Grain Boundaries; *Tectonophysics*, Volume 279, pages 55-78.

London, D. (1984): Experimental Phase Equilibria in the System $LiAlSiO_4$-SiO_2-H_2O: A Petrogenetic Grid for Lithium-rich Pegmatites; *American Mineralogist*, Volume 69, pages 995-1004.

London, D. (2008): Pegmatites; *Canadian Mineralogist Special Publication 10*, 368 pages.

London, D. (2009): The Origin of Primary Textures in Granitic Pegmatites; *The Canadian Mineralogist*, Volume 47, pages 697-724.

London, D. (2016): Rare-element Granitic Pegmatites; *in* Rare Earth and Critical Elements in Ore Deposits, Verplanck, P.L, Hitzman, M.W., Editors, *Society of Econonic Geologists*, pages 165-193.

London, D. (2018): Reading Pegmatites: What Quartz and Feldspars Say; *Rocks & Minerals*, Volume 93:4, pages 320-336, https://doi.org/10.1080/00357529.2018.1454105

London, D. (2020): Feldspar Thermometry in Pegmatites: Truth and Consequences; *Contributions to Mineralogy and Petrology,* Volume 175, No.8, 21 pages.

Ludwig, K.R. (2003): Users manual for Isoplot 3.00. A Geochronological Toolkit for Microsoft Excel; Berkeley Geochronology Center, Special Publication No. 4a, Berkeley, California.

Macdonald, J., Camacho, A., Ching, J.G. and Dyck, B. (2023): Emplacement Mechanisms of Rare-Element Pegmatites, Separation Lake Greenstone Belt, Northwest Superior Province; Resourcing the Green Transition, SEG 2023 Conference, *Society of Economic Geologists*, August 26-29, 2023, London, United Kingdom.

Magee, C., Muirhead, J., Schofield, N., Walker, R.J., Galland, O., Holford, S., Spacapan, J., Jackson, C.A.L. and McCarthy, W. (2019): Structural Signatures of Igneous Sheet Intrusion Propagation; *Journal of Structural Geology*, Volume 125, pages 148-154, https://doi.org/10.1016/j.jsg.2018.07.010.

Magee, C., Muirhead, J.D., Karvelas, A., Holford, S.P., Jackson, C.A.L., Bastow, I.D., Schofield, N., Stevenson, C.T.E., McLean, C., McCarthy, W. and Shtukert, O. (2016): Lateral Magma Flow in Mafic Sill Complexes; *Geosphere*, Volume 12, No. 3, pages 1-33, https://doi.org/10.1130/GES01256.1.

Mathieu, L., van Wik de Vries, B., Holohan, E.P. and Troll, V.R. (2008): Dykes, Cups, Saucers and Sills: Analogue Experiments on Magma Intrusion into Brittle Rocks; *Earth and Planetary Science Letters, Volume 271,* pages 1-13.

Melnyk, M., Davis, D.W., Cruden, A.R. and Stern, R.A. (2006): U-Pb Ages Constraining Structural Development of an Archean Terrane Boundary in the Lake of the Woods Area, western Superior Province, Canada; *Canadian Journal of Earth Sciences*, Volume 43, pages 967-993.

Menard, T., Cruden, A.R., Davis, D. and Robin, P.Y-R. (1997): Himalayan Style Metamorphism and Tectonics Between 2700 and 2650 Ma in the Winnipeg River and Wabigoon Subprovinces near Dryden; *in* Western Superior Transect, Lithoprobe Secretariat, University of British Columbia, Vancouver, British Columbia, Lithoprobe Report #63, pages 46-54.

Merle, O. and Donnadieu, F. (2000): Indentation of Volcanic Edifices by the Ascending Magma; *in* Salf, Shale, and Igneous Diapies in and Around Europe, Vendeville, B., Mart, Y., Vigneresse, J.L., Editors; *Geological Society, London*, Special Publications, Volume 174, pages 43-53.

Morales, L.F.G., Mainprice, D. and Kern, H. (2018): Olivine-Antigorite Orientation Relationships: Microstructures, Phase Boundary Misorientations and the Effect of Cracks in the Seismic Properties of Serpentinites; *Tectonophysics*, Volume 724-725, pages 93-115.

Morgan, G.B. and London, D. (1999): Crystallization of the Little Three Layered Pegmatite-aplite Dikem Ramona District, California; *Contributions to Mineralogy and Petrology*, Volume 136, pages 310-330.

Morgan, G.B. and London, D. (2012): Process of Granophyre Crystallization in the Long Mountain Granite, Southern Oklahoma; *Geological Society of America*, Volume 124, No. 7/8, pages 1251-1261.

Natural Resources Canada, (2020): Canada and U.S. Finalize Joint Action Plan on Critical Minerals Collaboration; *Natural Resources Canada,* press release, https://www.canada.ca/en/natural-resources-canada/news/2020/01/canada-and-us-finalize-joint-action-plan-on-critical-minerals-collaboration.html, [2021-05-25].

Natural Resources Canada, (2022): The Canadian Critical Minerals Strategy, From Exploration to Recycling: Powering the Green and Digital Economy for Canada and the World; *Natural Resources Canada*, 58 pages.

Nicholson, R. (1985): The Intrusion and Deformation of Tertiary Minor Sheet Intrusions, West Suardal, Isle of Skye, Scotland; *Geological Journal*, Volume 20, pages 53-72.

Nicholson, R. and Pollard, D.D. (1985): Dilation and Linkage of Echelon Cracks; *Journal of Structural Geology*, Volume 7, No. 5, pages 583-590.

Pan, Y. and Breaks, F.W. (1997): Rare-Earth Elements in Fluorapatite, Separation Lake Area, Ontario: Evidence for S-Type Granite – Rare-Element Pegmatite Linkage; *The Canadian Mineralogist*, Volume 35, pages 659-671.

Parrish, R. (1990): U-Pb Dating of Monazite and its Application to Geological Problems; *Canadian Journal of Earth Sciences,* Volume 27, pages 1431-1450.

Passchier, C.W. and Trouw, R.A.J. (2005): *Microtectonics*; Springer-Verlag, Berlin, 366 pages; https://doi.org/10.1007/3-540-29359-0

Paterson, S.R., Vernon, R.H. and Tobisch, O.T. (1989): A Review of Criteria for the Identification of Magmatic and Tectonic Foliations in Granitoids; *Journal of Structural Geology*, Volume 11, No. 3, pages 349-363.

Paterson, S.R., Ardill, K., Vernon, R. and Žák, J. (2019): A Review of Mesocopic Magmatic Structures and their Potential for Evaluating the Hypersolidus Evolution of Intrusive Complexes; *Journal of Structural Geology*, Volume 125, pages 134-147, https://doi.org/10.1016/j.jsg.2018.04.022.

Pedersen, J.C. (1998): Geological Report 1997-1998 Exploration Program, The Big Whopper Rare Metals Pegmatite, Separation Rapids Property, Kenora Mining Division, Ontario, NTS 52 L7/SE Volume 1: Report; submitted by Avalon Ventures Ltd., *Ontario Geological Survey*, Assessment Report 52L07SE2003, 866 pages.

Pedersen, J.C. (2017): Assessment Report for Summer 2017 Field Work on the Paterson Lake Claims, Paterson Lake Area, Separation Rapids, Ontario; submitted by Avalon Advanced Materials Inc., *Ontario Geological Survey*, Assessment Report 20000015331, 66 pages.

Pedersen, J.C., Ching, J.G.W., Bodeving, S. (2018): Paterson Lake Field Maps, unpublished company report, 3 pages.

Prior, D.J., Boyle, A.P., Brenker, F., Cheadle, M.C., Day, A., Lopex, G., Peruzzo, L., Potts, G.J., Reddy, S., Spiess, R., Timms, N.E., Trimby, P., Wheeler, J. and Zetterström, L. (1999):

The Application of Electron Backscatter Diffrace and Orientation Contrast Imaging in the SEM to Textural Problems in Rocks; *American Mineralogist*, Volume 84, pages 1741-1759.

Pollard, D.D. (1973): Derivation and Evaluation of a Mechanical Model for Sheet Intrusions; *Tectonophysics,* Volume 18, pages 233-269.

Pollard, D.D., Muller, O.H. and Dockstader, D.R. (1975): The Form and Growth of Fingered Sheet Intrusions; *Geological Society of America Bulletin,* Volume 86, No. 3, pages 351-363.

Pollard, D.D., Segall, P. and Delaney, P.T. (1982): Formation and Interpretation of Dilatant Echelon Cracks; *Geological Society of America Bulletin,* Volume 93, No. 12, pages 1291-1303.

Pryslak, A.P. and Chastko, L.C. (2001): Report on Diamond Drilling, Separation Rapids Area, Northwest Ontario, Paterson Lake Claim Sheet, G-2634; submitted by Emerald Field Resource Corporation, *Ontario Geological Survey*, Assessment Report 52L07SE2011, 140 pages.

Rubin, A.M. (1993): Tensile Fracture of Rock at High Confining Pressure: Implications for Dike Propagation; *Journal of Geophysical Research: Solid Earth*, Volume 98, pages 15919-15935.

Rubin, A.M. (1995): Getting Granite Dikes out of the Source Region; *Journal of Geophysical Research*, Volume 100B, pages 5911-5929.

Robson, G.R. and Barr, K.G. (1964): The Effect of Stress on Faulting and Minor Intrusions in the Vicinity of a Magma Body; *Bulletin of Volcanology*, Volume 27, pages 315-330, https://doi.org/10.1007/BF02597528.

Sanborne-Barrie, M. (1988): Project Number 88-21. Geology of the Tectonic Boundary Zone Between the English River and Winnipeg River Subprovinces, northwestern Ontario; *in* Summary of Field Work and Other Activities 1988, *Ontario Geological Survey*, Miscellaneous Paper 141, pages 98-107.

Saffman, P.G. and Taylor, G. (1958): The Penetration of a Fluid into a Porous Medium or Hele-Shaw Cell Containing a more Viscous Fluid; *Proceedings of the Royal Society of London, Series A*, Volume 245, pages 312-329.

Schofield, N., Stevenson, C. and Reston, T. (2010): Magma Fingers and Host Rock Fluidization in the Emplacement of Sills; *Geology*, Volume 38, No. 1, pages 63-66, https://doi.org/10.1130/G30142.1.

Schofield, N., Heaton, L., Holford, S.P., Archer, S.G., Jackson, C.A.L and Jolley, D.W. (2012a): Seismic Imaging of 'Broken Bridges': Linking Seismic to Outcrop-Scale Investigations of Intrusive Magma Lobes; *Journal of the Geological Society, London*, Volume 169, pages 421-426, https://doi.org/10.1144/0016-76492011-150.

Schofield, N.J., Brown, D.J., Magee, C. and Stevenson, C.T. (2012b): Sill Morphology and Comparison of Brittle and Non-Brittle Emplacement Mechanisms; *Journal of the Geological Society, London*, Volume 169, pages 127-141, https://doi.org/10.1144/0016-76492011-078.

Selway, J.B., Breaks, F.W. and Tindle, A.G. (2005): A Review of rare-Element (Li-Cs-Ta) Pegmatite Exploration Techniques for the Superior Province, Canada, and Large Worldwide Tantalum Deposits; *Exploration and Mining Geology*, Volume 14, Nos 1-4, pages 1-30, https://doi.org/10.2113/gsemg.14.1-4.1.

Sears., S.M and Pryslak, A.P. (1999): Separation Rapids Project, Snook Lake Claim Block Area, Geological Mapping, Prospecting and Sampling of Pegmatite Intrusions for Rare Metal Potential; submitted by Champion Bear Resources Ltd., *Ontario Geological Survey*, Assessment Report 52L07SE2006, 38 pages.

Sears, S.M. and Pryslak, A.P. (2001): Report on a Stripping Program on the Snook Lake Claim Block, Separation Rapids Project, Paterson Lake Map Area, Ontario, Separation Rapids Project, Snook Lake Claim Block Area; submitted by Champion Bear Resources Ltd., *Ontario Geological Survey*, 52L07SE2009, 20 pages.

Sibson, R.H. (2003): Brittle-failure Controls on Maximum Sustainable Overpressure in Different Tectonic Regimes; *AAPG Bulletin,* Volume 87, No. 6, pages 901-908.

Simonetti A. Heaman, L.M., Hartlaub, R.P., Creaser, R.A., MacHattiea, T.G., and Bohm, C. (2005): U–Pb zircon dating by laser ablation-MC-ICP-MS using a new multiple ion counting Faraday collector array; *Journal of Analytical Atomic Spectrometry*, 20, 677-686.

Simonetti A. Heaman, L.M., Chacko, T.., Banerjee, N.R., (2006): In situ petrographic thin section U–Pb dating of zircon, monazite, and titanite using laser ablation–MC–ICP-MS; *International Journal of Mass Spectrometry*, 253, 87-97.

Simpson, C. and Wintsch, R.P. (1989): Evidence for Deformation-Induced K-feldspar Replacement by Myrmekite; *Journal of Metamorphic Geology*, Volume 7, pages 261-275.

Sinclair, W.D. (1996): Granitic Pegmatites; *in* Geology of Canadian Mineral Deposit Types, Eckstrand, O.R., Sinclair, W.D. and Thorpe, R.I., Editors, Geological Survey of Canada, Geology of Canada, No. 8, pages 503-512.

Sirbescu, M.L.C. and Nabelek, P.I. (2003): Crustal Melts below 400 ºC; *Geology*, Volume 31, No. 8, pages 685-688.

Sirbescu, M.L.C., Hartwick, E.E. and Student, J.J. (2008): Rapid crystallization of the Animikie Red Ace Pegmatite, Florence county, northeastern Wisconsin: inclusion microthermometry and conductive-cooling modelling; *Contributions to Mineralogy and Petrology*, Volume 156, pages 289-305, https://doi.org/10.1007/s00410-008-0286-0.

Sirbescu, M.L.C., Schmidt, C., Veksler, I.V., Whittington, A.G. and Wilke, M. (2017): Experimental Crystallization of Undercooled Felsic Liquids: Generation of Pegmatitic Texture; *Journal of Petrology*, Volume 58, No. 3, pages 539-568. doi: 10.1093/petrology/egx027.

Slama, J., Kosler, J., Condón, D.J., Crowley, J.L., Gerdes, A., Hanchel, J.M., Horstwood, S.A., Morris, G.A., Nasdala, L., Norberg, N., Schaltegger, U., Schoene, B., Tubrett, M. and

Whitehouse, M.J. (2008): Plesovice Zircon – A New Natural Reference Material for U-Pb and Hf Isotopic Microanalysis; *Chemical Geology*, Volume 249, pages 1-35.

Smith, S.R., Foster, G.L., Romer, R.L., Tindle, A.G., Kellely, S.P., Noble, S.R., Horstwood, M. and Breaks, F.W. (2004): U-Pb Columbite-Tantalite Chronology of Rare-Element Pegmatites using TIMS and Laser Ablation-Multi Collector-ICP-MS; *Contributions to Mineralogy and Petrology*; Volume 147, pages 549-564.

Spacapan, J.B., Galland, o., Leanza, H.A. and Planke, S. (2016): Control on Strike-slip Fault o Dyke Emplacement and Morphology; *Journal of the Geological Society,* Volume 173, pages 573-576, https://doi.org/10.1144/jgs2015-166.

Spacapan, J.B., Galland, O., Leanza, H.E. and Planke, S. (2017): Igneous Sill and Finger Emplacement Mechanism in Shale-Dominated Formations: a Field Study at Cuesta del Chihuido, Neuquén Basin, Argentina, *Journal of the Geological Society*, Volume 174, pages 422-433, https://doi.org/10.1144/jgs2016-056.

Stern, R.A., Bodorkos, S., Kamo, S.L., Hickman, A.H. and Corfu, E. (2009): Measurement of SIMS Instrumental Mass Fractionation of Pb Isotopes During Zircon Dating; *Geostandards and Geoanalytical Research,* Volume 33, pages 145-168.

Stilling, A., Cerny, P. and Vanstone, P.J. (2006): The Tanco Pegmatite at Bernic Lake, Manitoba. XVI. Zonal and Bulk Compositions and their Petrogenetic Significance; *The Canadian Mineralogist*, Volume 44, pagegs 599-623.

Stipp, M., Stünitz, H., Heilbronner, R. and Schmid, S.M. (2002): The Eastern Tonale Fault Zone: a 'Natural Laboratory' for Crystal Plastic Deformation of Quartz Over and Temperature Range from 250 to 700 ºC; *Journal of Structural Geology*, Volume 24, pages 1861-1884.

Stockwell, C.H. (1932): Lithium Deposits; *in* Geological Survey of Canada, Memoir 169, pages 108-126.

Thomson, K. (2007): Determining Magma Flow in Sills, Dykes, and Laccoliths and their Implications for Sill Emplacement Mechanisms; *Bulletin of Volcanology*, Volume 70, pages 183-201, https://doi.org/10.1007s00445-007-0131-8.

Thomson, K. and Hutton, D. (2004): Geometry and Growth of Sill Complexes: Insights using 3D Seismic from the North Rockall Trough; *Bulletin of Volcanology*, Volume 66, pages 364-375. https://doi.org/10.1007/s00445-003-0320-z.

Tindle, A.W. and Breaks, F.W. (1998): Oxide Minerals of the Separation Rapids Rare-Element Granitic Pegmatite Group, northwestern Ontario; *The Canadian Mineralogist*, Volume 36, pages 609-635.

Tindle, A.W. and Breaks, F.W. (2000a): Columbite-Tantalite Mineral Chemistry from Rare-Element Granitic Pegmatites: Separation Lake Area, N.W. Ontario, Canada; *Mineralogy and Petrology*, Volume 70, pages 165-198.

Tindle, A.W. and Breaks, F.W. (2000b): Tantalum Mineralogy of the Rare-Element Granitic Pegmatites from the Separation Lake Area, northwestern Ontario; *Ontario Geological Survey*, Open File Report 6022, 378 pages.

Tindle, A.W., Breaks, F.W. and Webb, P.C. (1998): Wodginite-Group Minerals from the Separation Rapids Rare-Element Granitic Pegmatite Group, northwestern Ontario; *The Canadian Mineralogist*, Volume 36, pages 637-658.

Trimby, P.W., Prior, D.J. and Wheeler, J. (1998): Grain Boundary Hierarchy Development in a Quartz Mylonite; *Journal of Structural Geology*, Volume 20, No. 7, pages 917-935.

Trueman, D.L. (1980): Stratigraphy, Structure, and Metamorphic Petrology of the Archean Greenstone Belt at Bird River, Manitoba; unpublished Ph.D. Thesis; University of Manitoba, 214 pages.

Trueman, D.L. and Cerny, P. (1982): Exploration for Rare-Metal Granitic Pegmatites; *in* Cerny, P, Editor, Granitic Pegmatites in Science and Industry, *Mineralogical Association of Canada*, Short Course Handbook, 8, pages 463-493.

U.S. Geological Survey, (2021): Mineral Commodity Summaries 2021; *U.S. Geological Survey*, 200 pages, https://doi.org/10.3133/mcs2021.

Vernon, R.H. (1986): K-Feldspar Megacrysts in Granites – Phenocrysts, not Porphyroblasts; *Earth Science Reviews*, Volume 23, pages 1-63.

Vernon, R.H. (1991): Questions about Myrmekite in Deformed Rocks; *Journal of Structural Geology*, Volume 13, No. 9, pages 979-985.

Vernon, R.H. (2000): Review of Microstructural Evident of Magmatic and Solid-State Flow; *Electronic Geosciences*, Volume 5, No. 2, pages 1-23.

Vernon, R.H. (2004): A practical guide to rock microstructure; Cambridge: Cambridge University Press; https://10.1017/9781108654609.

Vernon, R.H. (2010): Granites Really Are Magmatic: Using Microstructural Evidence to Refute Some Obstinate Hypotheses; *Journal of the Virtual Explorer, Electronic Edition*, Forster, M.A. and Fitz Gerald, J.D, Editors, Volume 35, paper 1

Vernon, R.H., Williams, V.A. and D'arcy, W.F. (1983): Grain-Size Reduction and Foliation Development in a Deformed Granitoid Batholith; *Tectonophysics*, Volume 92, pages 123-145.

Vermeesch, P. (2018): IsoplotR: A Free and Open Toolbox for Geochronology; *Geoscience Frontiers*, Volume 9, pages 1479-1493, https://doi.org/10.1016/j.gsf.2018.04.001.

Winter, J.D. (2001): An introduction to Igneous and Metamorphic Petrology; *Prentice Hall,* New Jersey, 643 pages.

Wheeler, J., Prior, D.J., Jiang, Z., Spiess, R. and Trimby, P.W. (2001): The Petrological Significance of Misorientations Between Grains; *Contributions to Mineralogy and Petrology*, Volume 141, pages 109-124.

Wright, S.I., Nowell, M.M. and Field, D.P. (2011): A Review of Strain Analysis Using Electron Backscatter Diffraction; *Microscopy and Microanalysis*, Volume 17, pages 316–329.

Wyrick, D.Y., Morris, A.P., Todt, M.K. and Watson-Morris, M.J. (2020): Physical Analogue Modelling of Martian Dyke-Induced Deformation; *Volcanism and Tectonism Across the Inner Solar System,* Platx, T., Massironi, M., Byrne, P.K. and Heisinger, H., Editors, Geological Society, London, Special Publications, Volume 401, pages 395-403, https://dx.doi.org/10.1144/SP401.15.

Ziv, A., Rubin, A.M. and Agnon, A. (2000): Stability of Dike Intrusion Along Preexisting Fractures; *Journal of Geophysical Research,* Volume 105, No. B3, pages 5947-5961.

Appendix A:

Thin section images of *in-situ* crystals analyzed through Electron Back Scatter Diffraction.

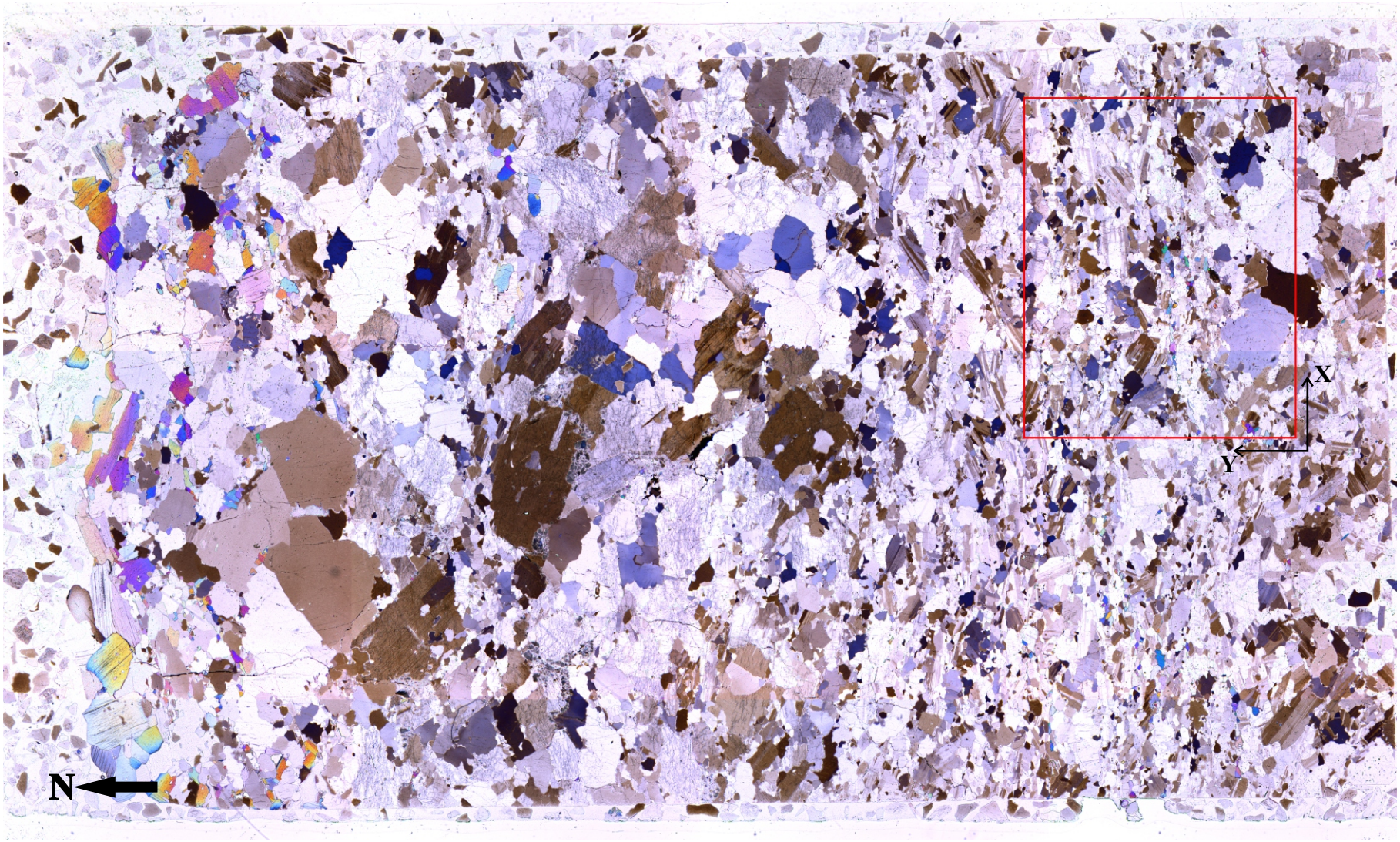

Appendix A1. Oriented thin section from specimen BW14a cut parallel to plane of outcrop, short axis is 26mm in all sections. Location reference Fig. 4.2. EBSD analyses performed across contact between fine and medium grained layers in red highlighed region in upper right with plot axes given in black.

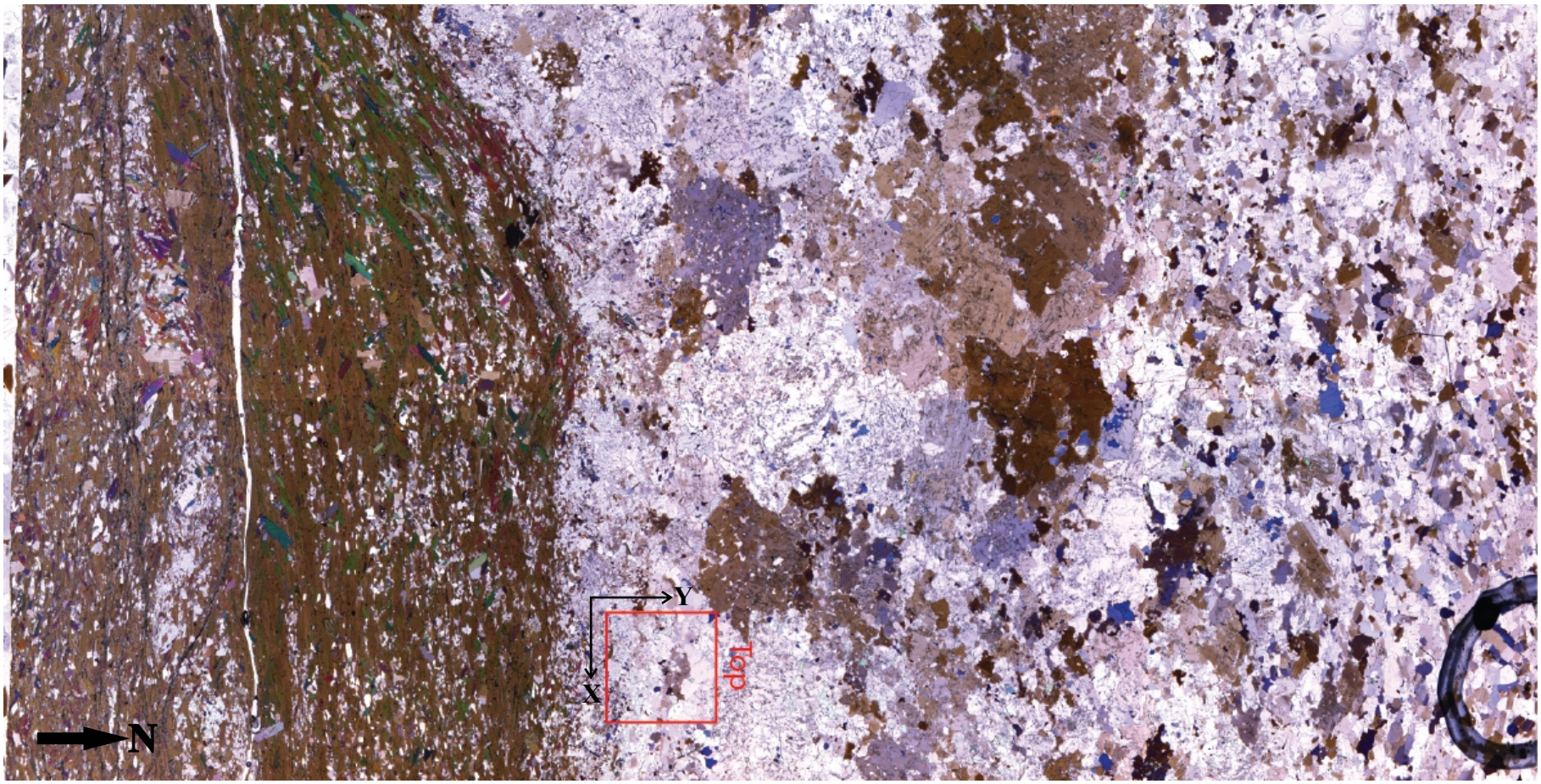

Appendix A2. Oriented thin section from specimen BW18b. Location reference Fig. 4.2 Section is cut in profile through contact between basalt (left) and pegmatite (right). Region analyzed given in red box left of bottom centre with plot axes in black.

Appendix A3. Oriented thin section cut from specimen GL3d. Location reference Fig. 4.5. Section faces west in profile perpendicular to contact trend between basalt xenolith (left) and Glitter pegmatite. EBSD analyses completed in red box bottom centre with plot axes given in white.

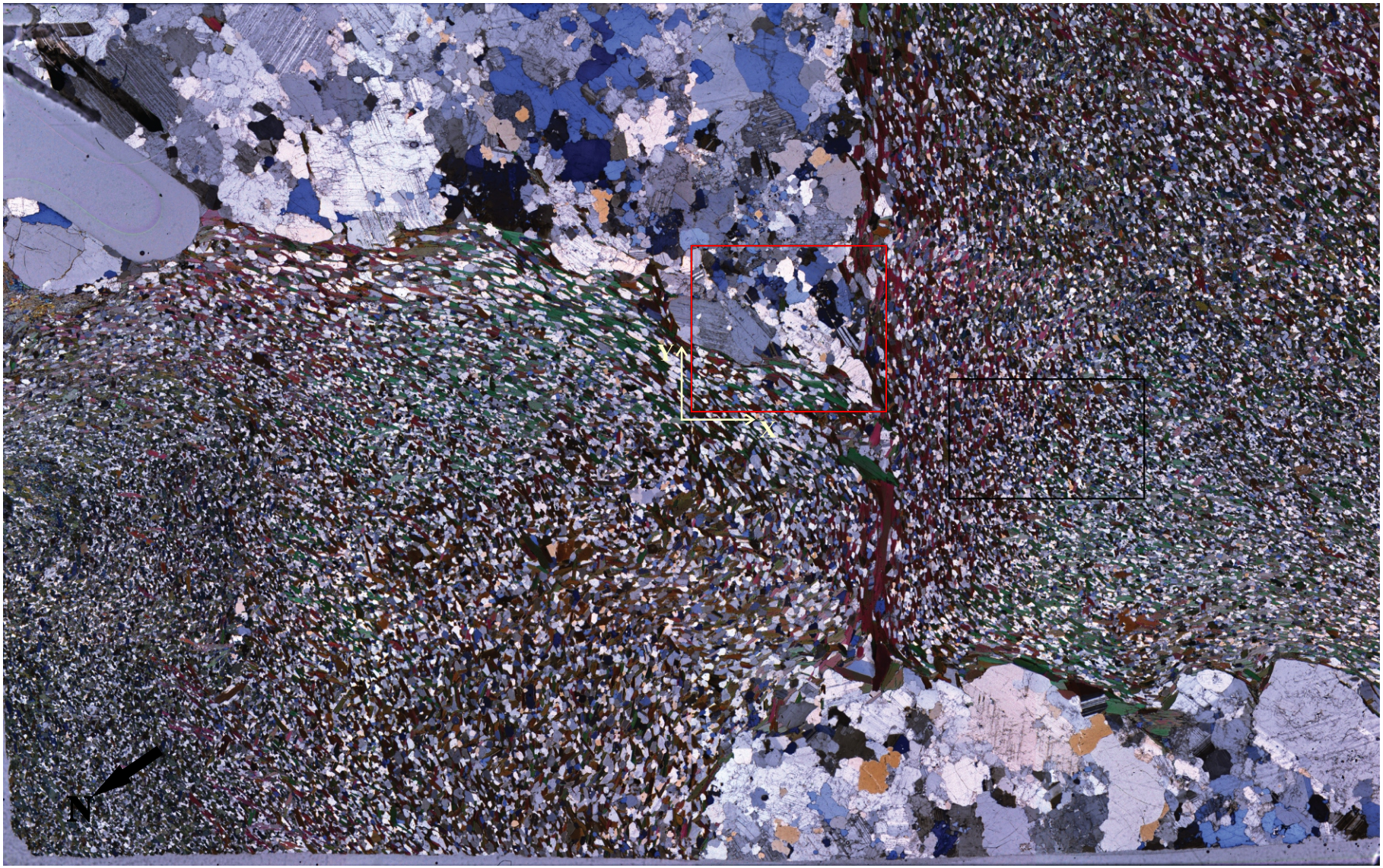

Appendix A4. Oriented thin section cut from specimen 19SNO11b through boudin neck between two thin dikes. Location reference Fig. 4.4. Section cut in profile perpendicular to pegmatite trend. EBSD analyses completed in red box centre image with plot axes given. Black box right of red box not analysed.

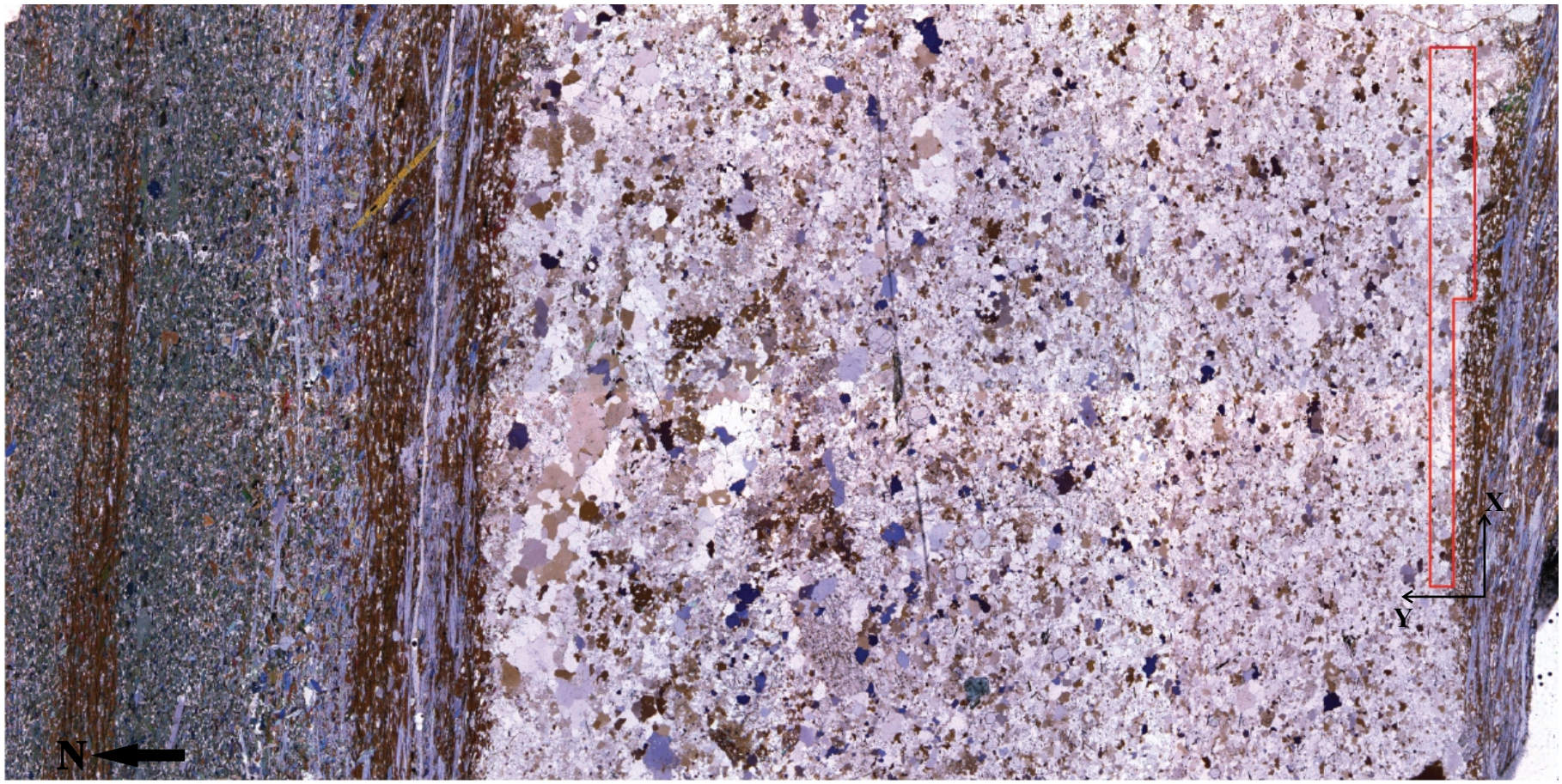

Appendix A5 Oriented thin section from section 19GL1b cut across thin dike in profile perpendicular to trend of pegmatite. Location reference Fig. 4.5. Coarse holmquistite oblique to contact (yellow-orange crystal upper left) overprints biotite alteration in basalt. Region analyzed in red box at right with plot axes in black.

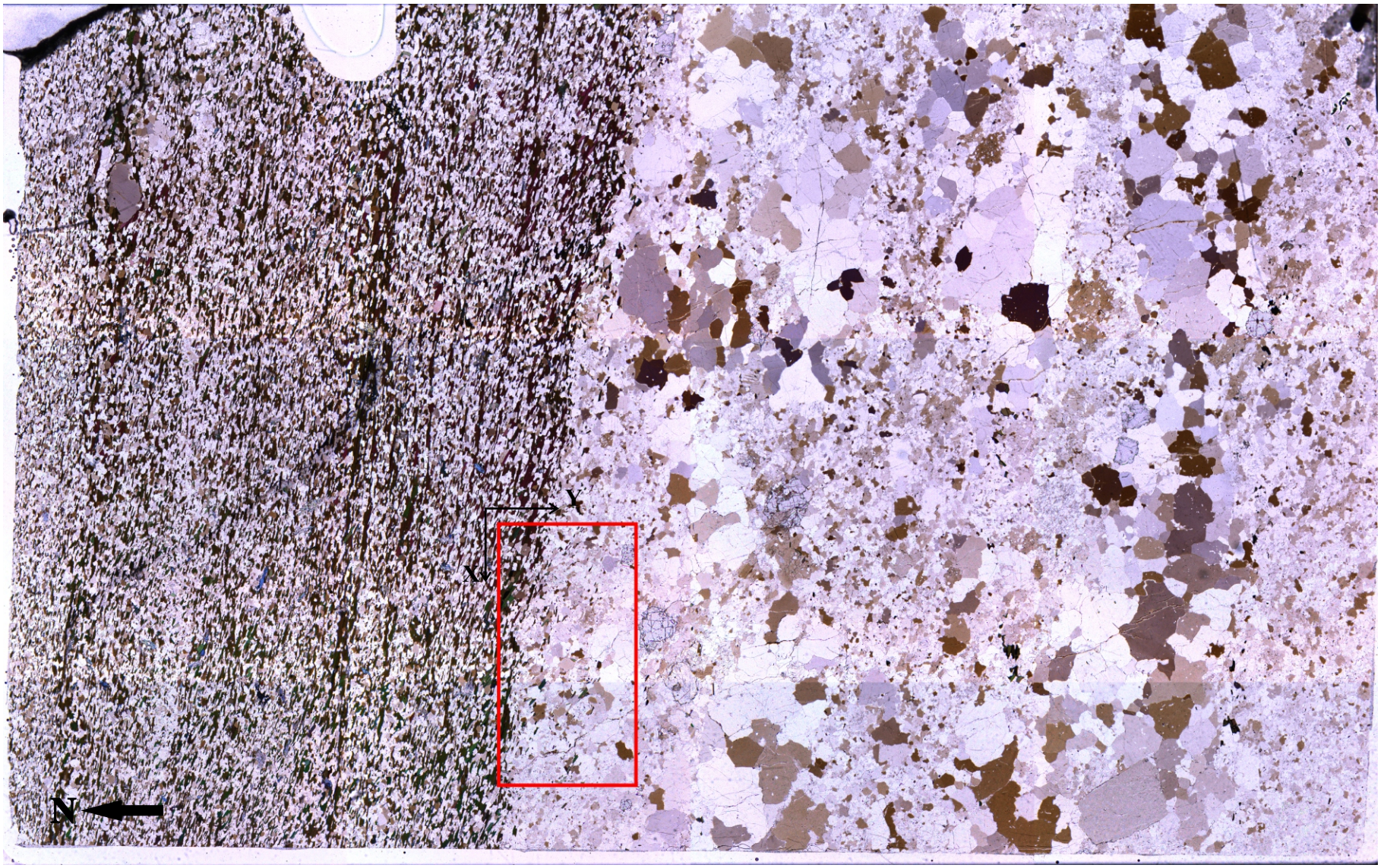

Appendix A6. Oriented thin section cut from specimen 19GL2b along northen limb of folded dike in Glitter pegmatite. Location reference in Fig. 4.5. Section cut in plan view parallel to outcrop. Region analyzed given in red with plot axes in black.

Appendix B:

LA-ICP-MS result tables for metamorphic and crystallization ages of selected specimens.

* - Asterisk denotes analyses excluded from plot due to scatter or erroneous results.

Appendix B.1. Age of metamorphism results from *in-situ* LA-ICP-MS analyses on monazite and titanite

Lithology	Specimen - Spot	^{206}Pb (cps)	^{204}Pb (cps)	^{207}Pb/^{206}Pb	2 s	^{207}Pb/^{235}U	2 s	^{206}Pb/^{238}U	2 s	r	^{207}Pb/^{206}Pb age (Ma)	2 s error (Ma)	^{207}Pb/^{235}U age (Ma)	2 s error (Ma)	^{206}Pb/^{238}U age (Ma)	2 s error (Ma)	% discordance	^{238}U/^{206}Pb	2 s	^{207}Pb/^{206}Pb	2 s
Feldspathic arenite	19MS1-1a*	656774	35	0.18426	0.00202	13.78611	0.46465	0.54287	0.01730	0.946	2692	18	2736	31	2795	72	-3.7	1.842	0.059	0.184	0.002
	19MS1-1b	1946858	46	0.17896	0.00179	12.65962	0.34942	0.51329	0.01321	0.932	2643	16	2655	26	2671	56	-1.0	1.948	0.050	0.179	0.002
	19MS1-2a	3437736	31	0.17848	0.00178	12.32875	0.34932	0.50122	0.01329	0.936	2639	16	2630	26	2619	57	0.8	1.995	0.053	0.178	0.002
	19MS1-2c*	105707	688	0.28889	0.00371	4.59298	0.15413	0.11536	0.00358	0.924	3412	20	1748	28	704	21	384.7	8.668	0.269	0.289	0.004
	19MS1-3a	1825308	139	0.18036	0.00182	12.59609	0.40989	0.50674	0.01568	0.951	2656	17	2650	30	2643	67	0.5	1.973	0.061	0.180	0.002
	19MS1-4a	3573169	109	0.17787	0.00179	12.43666	0.34882	0.50735	0.01328	0.933	2633	17	2638	26	2645	57	-0.5	1.971	0.052	0.178	0.002
	19MS1-8a	3761068	85	0.17721	0.00177	12.39948	0.35451	0.50771	0.01360	0.937	2627	16	2636	27	2647	58	-0.8	1.970	0.053	0.177	0.002
	19MS1-8b*	229677	45	0.20738	0.00219	17.01107	0.65783	0.59520	0.02215	0.962	2885	17	2936	36	3010	89	-4.2	1.680	0.063	0.207	0.002
	19MS1-9a*	57897	3	0.18823	0.00200	13.56792	0.53683	0.52302	0.01993	0.963	2727	17	2720	37	2712	84	0.5	1.912	0.073	0.188	0.002
	19MS1-9a2*	77060	1	0.18741	0.00202	13.00789	0.53568	0.50362	0.02002	0.965	2720	18	2681	38	2629	85	3.4	1.986	0.079	0.187	0.002
	19MS1-9a3*	88894	15	0.18793	0.00198	15.52807	0.47449	0.59953	0.01719	0.939	2724	17	2849	29	3028	69	-10.0	1.668	0.048	0.188	0.002
	19MS1-10a*	46	26	-0.13285	-0.28071	0.23521	0.56722	-0.01285	-0.01493	0.482	Erroneous	Erroneous	215	384	-83	-98	Erroneous	-77.842	-90.473	-0.133	-0.281
	19MS1-11b*	382825	44	0.20157	0.00208	15.39056	0.43836	0.55402	0.01470	0.932	2839	17	2840	27	2842	61	-0.1	1.805	0.048	0.202	0.002
	19MS1-15b*	88097	17	0.20257	0.00306	3.17989	0.22994	0.11390	0.00805	0.978	2847	24	1453	54	695	46	309.4	8.779	0.621	0.203	0.003
	19MS1-15a*	235982	1	0.18174	0.00185	13.43258	0.38442	0.53629	0.01435	0.935	2669	17	2711	27	2768	60	-3.6	1.865	0.050	0.182	0.002
	19MS1-16a*	2571058	12	0.18147	0.00183	12.88955	0.40726	0.51538	0.01543	0.948	2666	17	2672	29	2680	65	-0.5	1.940	0.058	0.181	0.002
	19MS1-16b*	2109763	67	0.18139	0.00182	12.85915	0.39240	0.51438	0.01482	0.944	2666	17	2670	28	2675	63	-0.4	1.944	0.056	0.181	0.002
	19MS1-18a1	1842423	6	0.17964	0.00181	12.41768	0.34855	0.50157	0.01315	0.934	2650	17	2637	26	2621	56	1.1	1.994	0.052	0.180	0.002
	19MS1-18a2	1807984	12	0.17907	0.00180	12.11453	0.37471	0.49089	0.01436	0.946	2644	17	2614	29	2575	62	2.7	2.037	0.060	0.179	0.002
	19MS1-18a3	2010256	18	0.17916	0.00180	12.02958	0.36640	0.48720	0.01401	0.944	2645	17	2607	28	2559	60	3.4	2.053	0.059	0.179	0.002
	19MS1-18a4	1665448	90	0.17821	0.00178	12.58996	0.35057	0.51262	0.01332	0.933	2636	17	2650	26	2668	57	-1.2	1.951	0.051	0.178	0.002
Calc-silicates in basalt	19BM2-1a-1	4070	24	0.17697	0.00408	11.230	0.921	0.460	0.036	0.960	2625	38	2543	74	2442	158	7.5	2.172	0.171	0.177	0.004
	19BM2-2a-2	3134	14	0.18426	0.00433	6.774	0.434	0.267	0.016	0.930	2692	38	2083	55	1524	80	76.6	3.749	0.224	0.184	0.004
	19BM2-2b-3	4494	20	0.18012	0.00330	8.171	0.776	0.329	0.031	0.981	2654	30	2251	82	1834	147	44.7	3.038	0.283	0.180	0.003
	19BM2-2b-4	3968	37	0.18479	0.00556	15.923	1.088	0.625	0.038	0.898	2696	49	2873	63	3131	150	-13.9	1.599	0.098	0.185	0.006
	19BM2-2f-5	3917	49	0.18808	0.00404	14.019	1.035	0.541	0.038	0.957	2725	35	2751	68	2787	158	-2.2	1.849	0.131	0.188	0.004
	19BM2-2g-6	2866	14	0.18290	0.00387	11.257	0.913	0.447	0.035	0.965	2679	35	2545	73	2380	154	12.6	2.239	0.175	0.183	0.004
	19BM2-2g-7	2366	16	0.18960	0.00672	12.272	1.050	0.470	0.037	0.910	2739	57	2626	77	2482	159	10.3	2.129	0.166	0.190	0.007
	19BM2-2g-8	3771	33	0.17993	0.00493	11.760	0.995	0.474	0.038	0.946	2652	45	2586	76	2502	164	6.0	2.109	0.169	0.180	0.005
	19BM2-2i-9	5926	47	0.17643	0.00305	10.086	0.633	0.415	0.025	0.961	2620	28	2443	56	2237	113	17.1	2.411	0.146	0.176	0.003
	19BM2-3b-11	6835	50	0.17466	0.00286	10.630	0.532	0.442	0.021	0.945	2603	27	2492	45	2358	93	10.4	2.265	0.107	0.175	0.003
	19BM2-3b-12	7412	40	0.17871	0.00383	10.108	0.499	0.410	0.018	0.901	2641	35	2445	45	2217	83	19.1	2.437	0.108	0.179	0.004
	19BM2-3b-13	9492	46	0.17737	0.00273	8.744	0.771	0.358	0.031	0.985	2628	25	2312	77	1971	146	33.3	2.796	0.243	0.177	0.003
	19BM2-3e-16	4812	29	0.17643	0.00343	12.441	0.791	0.512	0.031	0.952	2620	32	2639	58	2664	131	-1.7	1.954	0.118	0.176	0.003
	19BM2-4b-17	3263	29	0.18411	0.00412	14.656	1.197	0.578	0.045	0.962	2690	36	2794	75	2939	183	-8.5	1.731	0.136	0.184	0.004
	19BM2-4b-18	7277	43	0.17504	0.00296	12.185	0.537	0.505	0.021	0.923	2606	28	2619	41	2636	87	-1.1	1.980	0.081	0.175	0.003
	19BM2-6a-21	5045	38	0.18041	0.00288	12.275	0.826	0.494	0.032	0.972	2657	26	2626	61	2587	138	2.7	2.026	0.132	0.180	0.003
	19BM2-7a-22	6901	67	0.17564	0.00299	6.931	0.464	0.286	0.019	0.967	2612	28	2103	58	1623	92	60.9	3.493	0.226	0.176	0.003
	19BM2-7a-23	5574	72	0.17498	0.00314	6.929	0.360	0.287	0.014	0.938	2606	30	2103	45	1628	70	60.0	3.480	0.170	0.175	0.003
	19BM2-7b-25	6233	68	0.18594	0.00420	8.057	0.465	0.314	0.017	0.920	2707	37	2238	51	1762	81	53.6	3.181	0.169	0.186	0.004
	19BM2-7c-26	6418	60	0.17146	0.00287	7.494	0.370	0.317	0.015	0.941	2572	28	2173	43	1776	72	44.8	3.153	0.146	0.171	0.003
	19BM2-7d-28	8836	183	0.17354	0.00307	8.636	0.369	0.361	0.014	0.910	2592	29	2301	38	1987	66	30.4	2.770	0.108	0.174	0.003
	19BM2-7p-29	5574	170	0.17513	0.00353	7.842	0.516	0.325	0.020	0.952	2607	33	2213	58	1814	98	43.8	3.078	0.193	0.175	0.004
	19BM2-7p-30	6275	160	0.17509	0.00320	6.693	0.315	0.277	0.012	0.922	2607	30	2072	41	1578	60	65.2	3.605	0.156	0.175	0.003
	19BM2-7p-31	6543	150	0.18274	0.00315	6.427	0.399	0.255	0.015	0.961	2678	28	2036	53	1465	78	82.8	3.919	0.234	0.183	0.003
	19BM2-7p-32	5389	153	0.17399	0.00380	5.949	0.491	0.248	0.020	0.964	2596	36	1969	69	1429	101	81.7	4.031	0.321	0.174	0.004
	19BM2-7p-33	5894	144	0.17903	0.00392	6.112	0.514	0.248	0.020	0.966	2644	36	1992	71	1427	103	85.3	4.037	0.328	0.179	0.004
Basalt xenolith	BW10b-2a-1	30479	42	0.17297	0.00229	11.85299	0.38083	0.49700	0.01455	0.911	2587	22	2593	30	2601	62	-0.6	2.012	0.059	0.173	0.002
	BW10b-2b-2	2018	38	0.22163	0.00862	17.18666	2.14356	0.56243	0.06665	0.950	2993	61	2945	113	2877	269	4.0	1.778	0.211	0.222	0.009
	BW10b-3a-3*	377	51	0.37989	0.01643	-0.57371	-19.97015	-0.01095	-0.38126	1.000	3831	64	-866	Erroneous	-71	-3139	-5496.4	-91.299	-3177.989	0.380	0.016
	BW10b-4a-4	15388	44	0.17493	0.00271	12.21781	0.43251	0.50654	0.01613	0.899	2605	26	2621	33	2642	69	-1.4	1.974	0.063	0.175	0.003
	BW10b-5a-5*	426	47	0.26808	0.02350	5.84368	7.99241	0.15810	0.21579	0.998	3295	131	1953	786	946	1101	248.2	6.325	8.633	0.268	0.023
	BW10b-6a-6	9013	73	0.18224	0.00283	12.74323	0.49594	0.50714	0.01810	0.917	2673	25	2661	36	2644	77	1.1	1.972	0.070	0.182	0.003
	BW10b-7a-7	3591	69	0.20399	0.00630	15.81001	1.32151	0.56210	0.04366	0.929	2858	49	2865	77	2875	178	-0.6	1.779	0.138	0.204	0.006
	BW10b-7a-8	6814	87	0.19563	0.00395	14.19062	0.67350	0.52609	0.02260	0.905	2790	33	2763	44	2725	95	2.4	1.901	0.082	0.196	0.004
	BW10b-7b-9*	941	115	0.78687	0.03552	167.44273	204.11309	1.54334	1.88005	0.999	4898	63	5205	806	6018	3568	-18.6	0.648	0.789	0.787	0.036
	BW10b-7b-10*	175	82	0.58182	0.06013	-0.57640	-4.22956	-0.00719	-0.05272	1.000	4463	143	-872	Erroneous	-46	-352	-9701.4	-139.177	-1021.169	0.582	0.060
	BW10b-8a-11*	2233	78	0.20943	0.00573	19.85234	2.83390	0.68749	0.09632	0.981	2901	44	3084	129	3373	358	-14.0	1.455	0.204	0.209	0.006
	BW10b-9a-12	11578	83	0.18265	0.00364	13.09495	0.50967	0.51999	0.01739	0.859	2677	33	2687	36	2699	73	-0.8	1.923	0.064	0.183	0.004
	BW10b-10a-13	12325	132	0.18562	0.00316	12.98483	0.46284	0.50736	0.01588	0.878	2704	28	2679	33	2645	68	2.2	1.971	0.062	0.186	0.003
	BW10b-10b-14*	3367	81	0.19161	0.00504	11.89449	0.56251	0.45023	0.01770	0.831	2756	43	2596	43	2396	78	15.0	2.221	0.087	0.192	0.005
	BW10b-11a-15	57608	103	0.17031	0.00205	11.70852	0.35997	0.49861	0.01411	0.921	2561	20	2581	28	2608	60	-1.8	2.006	0.057	0.170	0.002
	BW10b-12a-16	7797	39	0.16992	0.00428	11.79045	0.52499	0.50324	0.01848	0.825	2557	42	2588	41	2628	79	-2.7	1.987	0.073	0.170	0.004
	BW10b-14a-17*	1323	64	0.15497	0.00634	18.15446	3.95997	0.84962	0.18204	0.982	2402	68	2998	191	3964	605	-39.4	1.177	0.252	0.155	0.006
	BW10b-14b-18	3776	105	0.15834	0.00420	11.76364	0.76346	0.53883	0.03191	0.913	2438	44	2586	59	2779	132	-12.3	1.856	0.110	0.158	0.004
	BW10b-15a-19	2392	87	0.16123	0.00546	11.48862	1.16041	0.51680	0.04918	0.942	2469	56	2564	90	2686	206	-8.1	1.935	0.184	0.161	0.005
	BW10b-15a-20	5266	56	0.16879	0.00368	11.61053	0.62956	0.49890	0.02477	0.916	2546	36	2574	49	2609	106	-2.4	2.004	0.100	0.169	0.004

	SP9a-1a-1	6065	29	0.19051	0.00537	10.61677	0.50040	0.40417	0.01527	0.802	2747	46	2490	43	2188	70	25.5	2.474	0.093	0.191	0.005
	SP9a-1b-2*	1122	24	0.23508	0.01170	4.79294	0.49190	0.14787	0.01327	0.874	3087	77	1784	83	889	74	247.2	6.763	0.607	0.235	0.012
	SP9a-1c-3	8958	20	0.18044	0.00463	10.26072	0.44442	0.41242	0.01439	0.806	2657	42	2459	39	2226	65	19.4	2.425	0.085	0.180	0.005
	SP9a-1d-4	4789	30	0.19217	0.00702	10.86648	0.62479	0.41012	0.01822	0.773	2761	59	2512	52	2215	83	24.6	2.438	0.108	0.192	0.007
	SP9a-2a-5	6343	21	0.17136	0.00375	9.81925	0.40186	0.41559	0.01437	0.845	2571	36	2418	37	2240	65	14.8	2.406	0.083	0.171	0.004
	SP9a-2c-6	5934	32	0.17407	0.00404	8.74291	0.66011	0.36427	0.02617	0.951	2597	38	2312	67	2002	122	29.7	2.745	0.197	0.174	0.004
	SP9a-2d-7	7467	109	0.23630	0.00650	14.86440	0.78200	0.45623	0.02045	0.852	3095	43	2807	49	2423	90	27.7	2.192	0.098	0.236	0.007
	SP9a-3a-8	3206	63	0.16311	0.00456	8.68560	0.58459	0.38621	0.02365	0.910	2488	46	2306	60	2105	109	18.2	2.589	0.159	0.163	0.005
	SP9a-3b-9	5846	60	0.17598	0.00447	10.80349	0.54944	0.44524	0.01962	0.867	2615	42	2506	46	2374	87	10.2	2.246	0.099	0.176	0.004
Basalt xenolith	SP9a-3c-10	3873	47	0.17056	0.00435	10.11528	0.60276	0.43013	0.02316	0.904	2563	42	2445	54	2306	104	11.1	2.325	0.125	0.171	0.004
	SP9a-4a-11	6719	67	0.19431	0.00536	8.68290	0.42800	0.32409	0.01324	0.829	2779	44	2305	44	1810	64	53.6	3.086	0.126	0.194	0.005
	SP9a-4a-12	8107	77	0.21529	0.00613	11.37526	0.70969	0.38321	0.02127	0.890	2946	45	2554	57	2091	98	40.9	2.610	0.145	0.215	0.006
	SP9a-4b-13	6559	38	0.17406	0.00436	9.75465	0.45962	0.40645	0.01623	0.847	2597	41	2412	42	2199	74	18.1	2.460	0.098	0.174	0.004
	SP9a-4c-14	8603	37	0.18287	0.00485	10.77261	0.47044	0.42723	0.01482	0.794	2679	43	2504	40	2293	67	16.8	2.341	0.081	0.183	0.005
	SP9a-5a-15	6942	52	0.18484	0.00449	9.69023	0.41223	0.38021	0.01327	0.821	2697	40	2406	38	2077	62	29.8	2.630	0.092	0.185	0.004
	SP9a-5a-16	4610	21	0.18715	0.00545	10.18697	0.55478	0.39479	0.01817	0.845	2717	47	2452	49	2145	83	26.7	2.533	0.117	0.187	0.005
	SP9a-5a-17	5705	47	0.19619	0.00635	10.61546	0.54552	0.39242	0.01567	0.777	2795	52	2490	47	2134	72	31.0	2.548	0.102	0.196	0.006
	SP9a-5a-18	7612	59	0.18555	0.00494	9.57207	0.41994	0.37415	0.01304	0.795	2703	43	2394	40	2049	61	31.9	2.673	0.093	0.186	0.005
	SP9a-6a-19	6768	57	0.20900	0.00488	14.70148	0.72710	0.51018	0.02224	0.881	2898	37	2796	46	2657	94	9.0	1.960	0.085	0.209	0.005
	SP9a-6b-20	9034	42	0.17559	0.00402	10.07056	0.44053	0.41595	0.01550	0.852	2612	38	2441	40	2242	70	16.5	2.404	0.090	0.176	0.004
	19FV1-1a-1*	154720	197	0.16027	0.00186	10.82371	0.22227	0.49001	0.00830	0.825	2459	19	2509	19	2571	36	-4.4	2.041	0.035	0.160	0.002
	19FV1-1b-2	77152	192	0.17511	0.00279	12.00492	0.28738	0.49744	0.00888	0.746	2607	26	2605	22	2603	38	0.2	2.010	0.036	0.175	0.003
	19FV1-1c-3*	110659	260	0.17202	0.00203	12.70280	0.25380	0.53582	0.00864	0.807	2577	20	2658	19	2766	36	-6.8	1.866	0.030	0.172	0.002
	19FV1-2a-4	90332	196	0.17572	0.00207	11.72559	0.24968	0.48417	0.00860	0.834	2613	19	2583	20	2545	37	2.7	2.065	0.037	0.176	0.002
	19FV1-2b-5	106611	195	0.17201	0.00205	12.04678	0.24891	0.50816	0.00859	0.818	2577	20	2608	19	2649	37	-2.7	1.968	0.033	0.172	0.002
	19FV1-2c-6	92980	204	0.17535	0.00203	12.57990	0.25309	0.52056	0.00857	0.818	2609	19	2649	19	2702	36	-3.4	1.921	0.032	0.175	0.002
	19FV1-2d-7	89485	187	0.16390	0.00190	10.84152	0.21822	0.47996	0.00790	0.818	2496	19	2510	19	2527	34	-1.2	2.084	0.034	0.164	0.002
	19FV1-2e-8*	86852	323	0.18121	0.00558	11.43931	0.40298	0.45806	0.00782	0.485	2664	50	2560	32	2431	34	9.6	2.183	0.037	0.181	0.006
	19FV1-2f-9	118698	195	0.17041	0.00198	11.65845	0.23322	0.49642	0.00808	0.813	2562	19	2578	19	2598	35	-1.4	2.014	0.033	0.170	0.002
	19FV1-2f-10	85206	211	0.17357	0.00203	11.39905	0.26680	0.47652	0.00966	0.866	2592	19	2557	22	2512	42	3.2	2.099	0.043	0.174	0.002
	19FV1-3a-11	67986	128	0.16782	0.00200	10.52340	0.22351	0.45498	0.00801	0.828	2536	20	2482	20	2417	35	4.9	2.198	0.039	0.168	0.002
	19FV1-3a-12*	67915	151	0.16784	0.00198	10.80028	0.24432	0.46691	0.00902	0.854	2536	20	2507	21	2470	39	2.7	2.142	0.041	0.168	0.002
	19FV1-3a-13	82561	152	0.16618	0.00194	9.89309	0.24634	0.43195	0.00950	0.883	2520	19	2425	23	2315	43	8.9	2.315	0.051	0.166	0.002
	19FV1-4a-14	88461	48	0.17548	0.00259	11.81449	0.30982	0.48853	0.01059	0.826	2611	24	2590	24	2564	46	1.8	2.047	0.044	0.175	0.003
Felsic volcanics	19FV1-4a-15	72505	132	0.17987	0.00288	12.56526	0.29326	0.50687	0.00862	0.729	2652	26	2648	22	2643	37	0.3	1.973	0.034	0.180	0.003
	19FV1-5b-16	94610	186	0.17162	0.00199	11.81401	0.23787	0.49949	0.00823	0.818	2573	19	2590	19	2612	35	-1.5	2.002	0.033	0.172	0.002
	19FV1-5c-17	83758	138	0.16555	0.00204	10.89279	0.22717	0.47742	0.00804	0.807	2513	21	2514	19	2516	35	-0.1	2.095	0.035	0.166	0.002
	19FV1-5d-18*	90242	133	0.16050	0.00188	10.18749	0.20487	0.46056	0.00753	0.813	2461	20	2452	18	2442	33	0.8	2.171	0.036	0.160	0.002
	19FV1-6a-19	86618	143	0.16434	0.00195	10.39632	0.21108	0.45902	0.00756	0.811	2501	20	2471	19	2435	33	2.7	2.179	0.036	0.164	0.002
	19FV1-6b-20	76890	138	0.17204	0.00201	11.04312	0.24031	0.46574	0.00855	0.843	2578	19	2527	20	2465	37	4.6	2.147	0.039	0.172	0.002
	19FV1-6c-21	104601	166	0.17490	0.00209	11.70491	0.24593	0.48560	0.00840	0.823	2605	20	2582	19	2552	36	2.1	2.059	0.036	0.175	0.002
	19FV1-7a-22	70804	136	0.16412	0.00194	9.52438	0.21677	0.42109	0.00819	0.855	2499	20	2390	21	2265	37	10.3	2.375	0.046	0.164	0.002
	19FV1-7b-23*	68825	312	0.20457	0.00263	13.88072	0.46086	0.49233	0.01507	0.922	2863	21	2742	31	2581	65	10.9	2.031	0.062	0.205	0.003
	19FV1-7c-24	62098	93	0.16882	0.00218	10.65941	0.34180	0.45815	0.01345	0.915	2546	21	2494	29	2431	59	4.7	2.183	0.064	0.169	0.002
	19FV1-8a-25	77899	132	0.16940	0.00200	10.87996	0.26554	0.46603	0.00995	0.875	2552	20	2513	22	2466	44	3.5	2.146	0.046	0.169	0.002
	19FV1-8a-26	89233	143	0.16532	0.00189	10.70098	0.22558	0.46966	0.00832	0.840	2511	19	2498	19	2482	36	1.2	2.129	0.038	0.165	0.002
	19FV1-9a-27	91804	183	0.17628	0.00210	12.12749	0.25023	0.49919	0.00840	0.816	2618	20	2615	19	2610	36	0.3	2.003	0.034	0.176	0.002
	19FV1-9a-28	66493	159	0.17544	0.00209	11.39614	0.23353	0.47133	0.00786	0.814	2610	20	2557	19	2489	34	4.9	2.122	0.035	0.175	0.002
	19FV1-10a-29*	65471	198	0.17380	0.00212	10.00839	0.31630	0.41785	0.01218	0.923	2595	20	2436	29	2251	55	15.3	2.393	0.070	0.174	0.002
	19FV1-10b-30*	1480455	134	0.17451	0.00197	13.88734	0.33204	0.57741	0.01217	0.881	2601	19	2742	22	2938	50	-11.5	1.732	0.036	0.175	0.002
	19GL5b-1a-1	2102	36	0.20296	0.00670	7.32387	0.59706	0.26183	0.01952	0.914	2850	53	2152	70	1499	99	90.1	3.819	0.285	0.203	0.007
	19GL5b-1b-2	3493	27	0.17810	0.00476	5.54686	0.38672	0.22599	0.01455	0.924	2635	44	1908	58	1313	76	100.6	4.425	0.285	0.178	0.005
	19GL5b-1c-3	2864	46	0.23118	0.00783	7.24317	0.67635	0.22734	0.01978	0.932	3060	53	2142	80	1321	103	131.7	4.399	0.383	0.231	0.008
	19GL5b-1d-4	2026	28	0.18334	0.00530	4.85119	0.45593	0.19199	0.01717	0.952	2683	47	1794	76	1132	92	137.0	5.209	0.466	0.183	0.005
	19GL5b-2a-5	2155	33	0.17983	0.00446	6.45958	0.53782	0.26063	0.02072	0.955	2651	41	2041	71	1493	105	77.6	3.837	0.305	0.180	0.004
Basalt	19GL5b-2a-6	1483	30	0.18796	0.00561	4.20124	0.36833	0.16218	0.01337	0.940	2724	48	1675	69	969	74	181.2	6.166	0.508	0.188	0.006
	19GL5b-2b-7	1607	30	0.19698	0.00591	5.46173	0.52308	0.20118	0.01830	0.950	2801	48	1895	79	1182	97	137.1	4.971	0.452	0.197	0.006
	19GL5b-2c-8	2604	57	0.20160	0.00982	5.55421	0.49636	0.19991	0.01498	0.838	2839	77	1909	74	1175	80	141.7	5.002	0.375	0.202	0.010
	19GL5b-2d-9	1383	6	0.24916	0.00917	5.98212	0.73835	0.17421	0.02052	0.955	3179	57	1974	102	1035	112	207.1	5.740	0.676	0.249	0.009
	19GL5b-3a-10	3567	1	0.17666	0.00372	7.88124	0.63136	0.32370	0.02502	0.965	2622	35	2218	70	1808	121	45.0	3.089	0.239	0.177	0.004
	19GL5b-3b-11	2668	10	0.21664	0.00504	8.48581	1.04499	0.28421	0.03437	0.982	2956	37	2285	106	1613	170	83.3	3.519	0.425	0.217	0.005

Appendix B.2. Results of *in-situ* LA-ICP-MS analyses on monazite for the crystallization ages of the Glitter, Snowbank, Big Mack, and Big Whopper pegmatites

Pegmatite	Specimen - Spot	^{206}Pb (cps)	^{204}Pb (cps)	^{207}Pb/^{206}Pb	2 s	^{207}Pb/^{235}U	2 s	^{206}Pb/^{238}U	2 s	r	^{207}Pb/^{206}Pb age (Ma)	2 s error (Ma)	^{207}Pb/^{235}U age (Ma)	2 s error (Ma)	^{206}Pb/^{238}U age (Ma)	2 s error (Ma)	% discordance	^{238}U/^{206}Pb	2 s	^{207}Pb/^{206}Pb	2 s
Glitter	GL7b-1a-1*	939597	1326	0.19612	0.00223	11.22103	0.51006	0.41497	0.01827	0.968	2794	18	2542	42	2238	83	24.9	2.410	0.106	0.196	0.002
	GL7b-2a-2	760194	215	0.17830	0.00180	12.15370	0.26500	0.49437	0.00955	0.886	2637	17	2616	20	2590	41	1.8	2.023	0.039	0.178	0.002
	GL7b-2a-3	952352	39	0.17781	0.00181	12.61065	0.20751	0.51437	0.00665	0.786	2633	17	2651	15	2675	28	-1.6	1.944	0.025	0.178	0.002
	GL7b-2b-4	1664921	35	0.17638	0.00177	12.12918	0.19723	0.49874	0.00638	0.787	2619	17	2614	15	2608	27	0.4	2.005	0.026	0.176	0.002
	GL7b-3a-5	1035096	27	0.17703	0.00178	12.32684	0.20571	0.50501	0.00672	0.797	2625	17	2630	16	2635	29	-0.4	1.980	0.026	0.177	0.002
	GL7b-4a-6*	2642596	80	0.16645	0.00294	13.17421	0.35844	0.57404	0.01188	0.761	2522	29	2692	25	2924	48	-13.8	1.742	0.036	0.166	0.003
	GL7b-5a-7	984927	52	0.17530	0.00178	12.29050	0.19743	0.50849	0.00633	0.774	2609	17	2627	15	2650	27	-1.6	1.967	0.024	0.175	0.002
	GL7b-6a-8	1772686	79	0.17381	0.00177	12.14669	0.19717	0.50684	0.00640	0.778	2595	17	2616	15	2643	27	-1.8	1.973	0.025	0.174	0.002
	GL7b-7a-9	1136669	67	0.17614	0.00177	12.14678	0.19503	0.50014	0.00627	0.781	2617	17	2616	15	2614	27	0.1	1.999	0.025	0.176	0.002
	GL7b-7a-10	1086784	58	0.17610	0.00177	12.18129	0.19624	0.50168	0.00631	0.781	2617	17	2618	15	2621	27	-0.2	1.993	0.025	0.176	0.002
	GL7b-9a-11	1804685	52	0.17676	0.00177	12.40350	0.20343	0.50893	0.00660	0.791	2623	17	2635	15	2652	28	-1.1	1.965	0.025	0.177	0.002
	GL7b-9a-12	2373070	59	0.17575	0.00176	12.73117	0.20633	0.52539	0.00669	0.786	2613	17	2660	15	2722	28	-4.0	1.903	0.024	0.176	0.002
	GL7b-9a-13*	2525121	47	0.17054	0.00171	11.77360	0.19129	0.50070	0.00640	0.787	2563	17	2587	15	2617	27	-2.1	1.997	0.026	0.171	0.002
	GL7b-10a-14	834837	50	0.17589	0.00178	12.09262	0.19484	0.49864	0.00625	0.778	2614	17	2612	15	2608	27	0.2	2.005	0.025	0.176	0.002
	GL7b-11a-15*	491133	323	0.15980	0.00173	8.46968	0.16667	0.38440	0.00632	0.835	2454	18	2283	18	2097	29	17.0	2.601	0.043	0.160	0.002
	GL7b-12a-16*	1103739	389	0.17947	0.00187	15.63257	0.28527	0.63175	0.00946	0.820	2648	17	2855	17	3157	37	-16.1	1.583	0.024	0.179	0.002
	GL7b-13a-17	1951513	89	0.17641	0.00177	12.65639	0.20626	0.52034	0.00667	0.787	2619	17	2654	15	2701	28	-3.0	1.922	0.025	0.176	0.002
	GL7b-14a-18	2128800	107	0.17496	0.00176	12.69985	0.20517	0.52645	0.00666	0.783	2606	17	2658	15	2726	28	-4.4	1.899	0.024	0.175	0.002
	GL7b-14a-19	1965568	58	0.17645	0.00177	12.94510	0.20649	0.53209	0.00660	0.778	2620	17	2676	15	2750	28	-4.7	1.879	0.023	0.176	0.002
	GL7b-15a-20	3000558	67	0.17571	0.00176	12.79914	0.21120	0.52832	0.00693	0.795	2613	17	2665	15	2734	29	-4.4	1.893	0.025	0.176	0.002
	GL7b-15a-21	2389353	49	0.17568	0.00176	12.74468	0.20885	0.52615	0.00682	0.791	2612	17	2661	15	2725	29	-4.1	1.901	0.025	0.176	0.002
	GL7b-15a-22	2029025	36	0.17591	0.00176	12.70200	0.20524	0.52369	0.00663	0.784	2615	17	2658	15	2715	28	-3.7	1.910	0.024	0.176	0.002
Snowbank	SNO2a-1a-1	2005493	28	0.17763	0.00224	12.63254	0.30137	0.51578	0.01045	0.850	2631	21	2653	22	2681	44	-1.9	1.939	0.039	0.178	0.002
	SNO2a-1a-2	2582809	113	0.17658	0.00225	13.10683	0.33652	0.53834	0.01200	0.868	2621	21	2687	24	2777	50	-5.6	1.858	0.041	0.177	0.002
	SNO2a-2a-3*	10454	8	0.31001	0.00456	240.94821	375.87146	5.63689	8.79298	1.000	3521	23	5573	952	12201	5439	-71.1	0.177	0.277	0.310	0.005
	SNO2a-2a-4*	9108	6	0.31789	0.00476	178.42012	188.48093	4.07071	4.29982	1.000	3560	23	5270	729	10466	3959	-66.0	0.246	0.259	0.318	0.005
	SNO2a-3a-5*	397	42	0.43294	0.03128	4.76301	16.75976	0.07979	0.28070	1.000	4028	104	1778	1384	495	1490	713.9	12.533	44.091	0.433	0.031
	SNO2a-4a-6	2836700	80	0.17722	0.00223	12.43875	0.28698	0.50905	0.00984	0.838	2627	21	2638	21	2653	42	-1.0	1.964	0.038	0.177	0.002
	SNO2a-4a-7	1626367	113	0.17549	0.00229	12.32814	0.29468	0.50949	0.01021	0.839	2611	22	2630	22	2654	43	-1.6	1.963	0.039	0.175	0.002
Big Mack	BM6a-1-1	1274759	49	0.17898	0.00151	12.47133	0.22611	0.50536	0.00811	0.885	2643	14	2641	17	2637	35	0.3	1.979	0.032	0.179	0.002
	BM6a-1-2	1968464	55	0.17858	0.00149	12.35159	0.20903	0.50164	0.00738	0.870	2640	14	2632	16	2621	32	0.7	1.993	0.029	0.179	0.001
	BM6a-1-3	1527904	32	0.17857	0.00150	12.50828	0.20067	0.50803	0.00695	0.852	2640	14	2643	15	2648	30	-0.3	1.968	0.027	0.179	0.001
	BM6a-1-4	1138308	33	0.17846	0.00149	12.56255	0.21301	0.51054	0.00753	0.870	2639	14	2647	16	2659	32	-0.8	1.959	0.029	0.178	0.001
	BM6a-2-5	3643456	29	0.17763	0.00148	12.17879	0.18877	0.49727	0.00649	0.842	2631	14	2618	14	2602	28	1.1	2.011	0.026	0.178	0.001
	BM6a-2-6	4203324	64	0.17713	0.00148	12.16512	0.19075	0.49811	0.00660	0.845	2626	14	2617	15	2606	28	0.8	2.008	0.027	0.177	0.001
	BM6a-3-7	6617508	69	0.17792	0.00149	12.68691	0.20059	0.51715	0.00694	0.849	2634	14	2657	15	2687	29	-2.0	1.934	0.026	0.178	0.001
	BM6a-3-8	2407544	28	0.17758	0.00149	12.70953	0.19748	0.51908	0.00679	0.842	2630	14	2658	15	2695	29	-2.4	1.926	0.025	0.178	0.001
	BM6a-4-9	2599608	42	0.17840	0.00149	13.37068	0.20719	0.54358	0.00709	0.842	2638	14	2706	15	2798	30	-5.7	1.840	0.024	0.178	0.001
	BM6a-4-10	3003665	49	0.17799	0.00149	13.36950	0.20727	0.54477	0.00711	0.842	2634	14	2706	15	2803	30	-6.0	1.836	0.024	0.178	0.001
	BM6a-4b-11	3361635	30	0.17871	0.00150	12.71465	0.19926	0.51601	0.00683	0.844	2641	14	2659	15	2682	29	-1.5	1.938	0.026	0.179	0.002
	BM6a-4b-12	8781386	37	0.17877	0.00150	12.65718	0.21049	0.51350	0.00737	0.864	2641	14	2654	16	2672	31	-1.1	1.947	0.028	0.179	0.001
	BM6a-4b-13	7109908	28	0.17817	0.00149	12.73009	0.21077	0.51819	0.00741	0.864	2636	14	2660	15	2691	31	-2.1	1.930	0.028	0.178	0.001
	BM6a-5-14	4117656	17	0.17947	0.00151	13.21515	0.20862	0.53404	0.00713	0.846	2648	14	2695	15	2758	30	-4.0	1.873	0.025	0.179	0.002
	BM6a-5-15	3056625	54	0.17932	0.00150	13.36560	0.20666	0.54058	0.00704	0.842	2647	14	2706	15	2786	29	-5.0	1.850	0.024	0.179	0.001
	BM6a-6-16	4712151	57	0.17748	0.00149	12.32496	0.19208	0.50367	0.00662	0.844	2629	14	2629	15	2630	28	0.0	1.985	0.026	0.177	0.001
Big Whopper	BW18c-1a-1	3458574	65	0.17463	0.00182	12.807	0.186	0.532	0.005	0.693	2602	17	2666	14	2750	22	-5.3	1.880	0.019	0.175	0.002
	BW18c-1a-2	3546331	76	0.17657	0.00190	13.250	0.198	0.544	0.006	0.692	2621	18	2698	14	2801	23	-6.4	1.837	0.019	0.177	0.002
	BW18c-2a-3	4882639	70	0.17588	0.00180	12.844	0.199	0.530	0.006	0.749	2614	17	2668	14	2740	26	-4.6	1.888	0.022	0.176	0.002
	BW18c-2b-4	4216123	71	0.17661	0.00181	12.731	0.193	0.523	0.006	0.735	2621	17	2660	14	2711	25	-3.3	1.913	0.021	0.177	0.002
	BW18c-2c-5	4889249	54	0.17589	0.00181	12.172	0.296	0.502	0.011	0.906	2614	17	2618	23	2622	47	-0.3	1.992	0.044	0.176	0.002
	BW18c-2d-6	3275658	62	0.17661	0.00182	13.095	0.193	0.538	0.006	0.714	2621	17	2687	14	2774	24	-5.5	1.859	0.020	0.177	0.002
	BW18c-3a-7	3039654	54	0.17667	0.00181	12.601	0.187	0.517	0.006	0.723	2622	17	2650	14	2688	24	-2.4	1.933	0.021	0.177	0.002
	BW18c-3b-8*	1038218	41	0.16596	0.00451	13.352	0.481	0.583	0.014	0.656	2517	45	2705	34	2963	56	-15.0	1.714	0.041	0.166	0.005
	BW18c-3c-9	5556081	108	0.17640	0.00181	12.991	0.196	0.534	0.006	0.733	2619	17	2679	14	2759	25	-5.1	1.872	0.021	0.176	0.002
	BW18c-3d-10	5616629	112	0.17629	0.00181	13.104	0.188	0.539	0.005	0.698	2618	17	2687	13	2780	23	-5.8	1.855	0.019	0.176	0.002
	BW18c-3e-11	5468787	126	0.17595	0.00180	13.042	0.192	0.538	0.006	0.717	2615	17	2683	14	2773	24	-5.7	1.860	0.020	0.176	0.002
	BW18c-4a-12	2306999	92	0.17765	0.00182	12.669	0.193	0.517	0.006	0.740	2631	17	2655	14	2687	25	-2.1	1.933	0.022	0.178	0.002
	BW18c-4a-13	2501710	110	0.17734	0.00182	12.701	0.187	0.519	0.005	0.718	2628	17	2658	14	2697	23	-2.6	1.925	0.020	0.177	0.002
	BW18c-4b-13	6770509	131	0.17686	0.00182	13.030	0.200	0.534	0.006	0.744	2624	17	2682	14	2760	26	-4.9	1.871	0.021	0.177	0.002
	BW18c-4c-14*	631635	122	0.16709	0.00176	11.771	0.182	0.511	0.006	0.731	2529	18	2586	14	2661	25	-5.0	1.957	0.022	0.167	0.002
	BW18c-5a-15	3499794	120	0.17692	0.00183	13.206	0.191	0.541	0.006	0.701	2624	17	2694	14	2789	23	-5.9	1.847	0.019	0.177	0.002
	BW18c-5b-16	5182197	158	0.17450	0.00191	11.810	0.216	0.491	0.007	0.800	2601	18	2589	17	2574	31	1.0	2.037	0.030	0.175	0.002
	BW18c-6a-17	2281871	114	0.17386	0.00193	13.452	0.202	0.561	0.006	0.674	2595	18	2712	14	2872	23	-9.6	1.782	0.018	0.174	0.002

Appendix B.3. Results of LA-ICP-MS wodginite, zircon, microlite, and cassiterite grain analysis from Marko's pegmatite.

Mineral	Spot	^{206}Pb (cps)	^{204}Pb (cps)	^{207}Pb/^{206}Pb	2 s	^{207}Pb/^{235}U	2 s	^{206}Pb/^{238}U	2 s	r	^{207}Pb/^{206}Pb age (Ma)	2 s error (Ma)	^{207}Pb/^{235}U age (Ma)	2 s error (Ma)	^{206}Pb/^{238}U age (Ma)	2 s error (Ma)	% discordance	^{238}U/^{206}Pb	2 s	^{207}Pb/^{206}Pb	2 s
Wodginite	M-wod-1	1418969	110	0.17516	0.00204	12.39752	0.46979	0.51357	0.01852	0.952	2608	19	2635	35	2672	78	-2.4	1.947	0.070	0.175	0.002
	M-wod-2	1438116	200	0.17365	0.00202	12.05930	0.54563	0.50389	0.02204	0.967	2593	19	2609	42	2630	94	-1.4	1.985	0.087	0.174	0.002
	M-wod-3	1468282	98	0.17516	0.00203	12.47426	0.43757	0.51675	0.01711	0.944	2608	19	2641	32	2685	72	-2.9	1.935	0.064	0.175	0.002
	M-wod-4	1444940	106	0.17554	0.00204	12.38039	0.47286	0.51174	0.01862	0.953	2611	19	2634	35	2664	79	-2.0	1.954	0.071	0.176	0.002
	M-wod-5	1390503	185	0.17292	0.00201	12.05540	0.50556	0.50587	0.02039	0.961	2586	19	2609	39	2639	87	-2.0	1.977	0.080	0.173	0.002
	M-wod-6	1481053	170	0.17511	0.00203	12.02382	0.45727	0.49822	0.01804	0.952	2607	19	2607	35	2606	77	0.0	2.007	0.073	0.175	0.002
	M-wod-7	1402478	143	0.17392	0.00201	12.08610	0.47725	0.50423	0.01904	0.956	2596	19	2612	36	2632	81	-1.4	1.983	0.075	0.174	0.002
	M-wod-8	1439042	117	0.17515	0.00203	12.42072	0.45355	0.51457	0.01782	0.948	2607	19	2637	34	2676	75	-2.6	1.943	0.067	0.175	0.002
	M-wod-9	1411252	168	0.17520	0.00204	12.44910	0.47079	0.51558	0.01855	0.952	2608	19	2639	35	2680	78	-2.7	1.940	0.070	0.175	0.002
	M-wod-10	1407381	105	0.17452	0.00203	12.09683	0.43841	0.50293	0.01726	0.947	2602	19	2612	33	2626	74	-0.9	1.988	0.068	0.175	0.002
Zircon	M-z-1	1312433	57	0.17547	0.00169	11.92300	0.34156	0.49305	0.01331	0.942	2610	16	2598	26	2584	57	1.0	2.028	0.055	0.175	0.002
	M-z-2	1733423	40	0.17516	0.00168	12.17245	0.32964	0.50425	0.01277	0.935	2608	16	2618	25	2632	55	-0.9	1.983	0.050	0.175	0.002
	M-z-3	1728812	76	0.17480	0.00167	12.19057	0.29499	0.50603	0.01125	0.919	2604	16	2619	22	2640	48	-1.3	1.976	0.044	0.175	0.002
	M-z-4	1728688	56	0.17454	0.00168	11.96554	0.35155	0.49743	0.01381	0.945	2602	16	2602	27	2603	59	0.0	2.010	0.056	0.175	0.002
	M-z-5	2155496	30	0.17474	0.00167	11.58566	0.24745	0.48109	0.00919	0.894	2604	16	2572	20	2532	40	2.8	2.079	0.040	0.175	0.002
	M-z-6	2063197	67	0.17447	0.00167	11.95123	0.29475	0.49704	0.01129	0.921	2601	16	2601	23	2601	48	0.0	2.012	0.046	0.174	0.002
	M-z-7	1953486	65	0.17467	0.00167	11.99332	0.33561	0.49823	0.01310	0.940	2603	16	2604	26	2606	56	-0.1	2.007	0.053	0.175	0.002
	M-z-8	1884504	45	0.17456	0.00167	12.08386	0.32933	0.50230	0.01282	0.936	2602	16	2611	25	2624	55	-0.8	1.991	0.051	0.175	0.002
	M-z-9	1838726	38	0.17485	0.00168	11.90078	0.38014	0.49386	0.01504	0.954	2605	16	2597	29	2587	65	0.7	2.025	0.062	0.175	0.002
	M-z-10	2298633	47	0.17441	0.00167	12.06377	0.33592	0.50190	0.01312	0.939	2600	16	2609	26	2622	56	-0.8	1.992	0.052	0.174	0.002
Microlite	M-micro-1	4160063	408	0.09183	0.00107	2.92066	0.09857	0.23077	0.00731	0.939	1464	22	1388	25	1339	38	9.4	4.333	0.137	0.092	0.001
	M-micro-2	3962948	388	0.08759	0.00121	2.62106	0.08873	0.21714	0.00671	0.913	1373	26	1307	25	1267	35	8.4	4.605	0.142	0.088	0.001
	M-micro-3	4176963	499	0.09424	0.00110	3.17741	0.10691	0.24463	0.00772	0.938	1513	22	1452	26	1411	40	7.3	4.088	0.129	0.094	0.001
	M-micro-4	3705643	398	0.09069	0.00105	2.87668	0.09690	0.23015	0.00728	0.939	1440	22	1376	25	1335	38	7.9	4.345	0.137	0.091	0.001
	M-micro-5	3249379	272	0.08296	0.00098	2.33333	0.07713	0.20408	0.00630	0.934	1268	23	1223	23	1197	34	5.9	4.900	0.151	0.083	0.001
	M-micro-6	3816555	368	0.09333	0.00108	3.13353	0.10380	0.24361	0.00756	0.937	1495	22	1441	25	1405	39	6.3	4.105	0.127	0.093	0.001
	M-micro-7	3763221	328	0.09223	0.00107	3.02654	0.10068	0.23810	0.00743	0.937	1472	22	1415	25	1377	39	6.9	4.200	0.131	0.092	0.001
	M-micro-8	4193744	452	0.09649	0.00112	3.41897	0.11362	0.25711	0.00801	0.937	1557	22	1509	26	1475	41	5.6	3.889	0.121	0.096	0.001
	M-micro-9	4031941	354	0.09218	0.00107	3.05411	0.10194	0.24040	0.00752	0.938	1471	22	1422	25	1389	39	5.9	4.160	0.130	0.092	0.001
	M-micro-10	3677567	258	0.08755	0.00113	2.64764	0.09651	0.21942	0.00748	0.935	1373	25	1314	27	1279	39	7.3	4.557	0.155	0.088	0.001
Cassiterite	M-cas-1*	296	38	0.18306	0.02819	0.31066	0.05238	0.01231	0.00085	0.407	2681	234	275	40	79	5	3298.0	81.212	5.579	0.183	0.028
	M-cas-2*	206	26	0.21630	0.02872	0.60706	0.13641	0.02036	0.00369	0.807	2953	200	482	83	130	23	2172.6	49.106	8.902	0.216	0.029
	M-cas-3	30288	60	0.17989	0.00235	10.45120	0.39359	0.42155	0.01489	0.938	2652	21	2476	34	2268	67	17.0	2.372	0.084	0.180	0.002
	M-cas-4	31574	55	0.18108	0.00227	10.11221	0.42539	0.40520	0.01627	0.955	2663	21	2446	38	2193	74	21.4	2.468	0.099	0.181	0.002
	M-cas-5	30775	51	0.18035	0.00229	8.29259	0.36696	0.33363	0.01414	0.958	2656	21	2264	39	1856	68	43.1	2.997	0.127	0.180	0.002
	M-cas-6	31938	46	0.18223	0.00239	10.72549	0.40967	0.42707	0.01532	0.939	2673	22	2500	35	2292	69	16.6	2.342	0.084	0.182	0.002
	M-cas-7*	491	39	0.16603	0.01108	0.88891	0.11230	0.03885	0.00417	0.849	2518	108	646	59	246	26	924.9	25.742	2.761	0.166	0.011
	M-cas-8	28465	116	0.18472	0.00244	10.08468	0.42936	0.39614	0.01603	0.951	2696	22	2443	39	2151	74	25.3	2.524	0.102	0.185	0.002
	M-cas-9	30753	112	0.18210	0.00237	9.18255	0.37717	0.36588	0.01425	0.948	2672	21	2357	37	2010	67	32.9	2.733	0.106	0.182	0.002
	M-cas-10*	32616	187	0.21484	0.00369	10.89129	0.74711	0.36785	0.02443	0.968	2942	27	2514	62	2019	114	45.7	2.719	0.181	0.215	0.004
	M-cas-11*	116	138	0.66594	0.08566	0.97816	0.22399	0.01066	0.00202	0.827	4659	174	693	109	68	13	6717.1	93.828	17.776	0.666	0.086
	M-cas-12	21825	141	0.18119	0.00227	6.14166	0.44962	0.24594	0.01774	0.985	2664	21	1997	62	1418	91	87.9	4.066	0.293	0.181	0.002
	M-cas-13	26032	147	0.18369	0.00241	9.61530	0.45008	0.37982	0.01707	0.960	2686	21	2399	42	2075	79	29.4	2.633	0.118	0.184	0.002
	M-cas-14*	23541	172	0.21504	0.00367	12.01502	0.49272	0.40541	0.01512	0.910	2944	27	2606	38	2194	69	34.2	2.467	0.092	0.215	0.004
	M-cas-15	21793	112	0.18765	0.00272	8.22032	0.52572	0.31786	0.01980	0.974	2722	24	2256	56	1779	96	53.0	3.146	0.196	0.188	0.003

Appendix B.4. Results of LA-ICP-MS in-situ analyses of monazite and cassiterite in the Great White North aplite

Mineral	Specimen	^{206}Pb (cps)	^{204}Pb (cps)	^{207}Pb/^{206}Pb	2 s	^{207}Pb/^{235}U	2 s	^{206}Pb/^{238}U	2 s	r	^{207}Pb/^{206}Pb age (Ma)	2 s error (Ma)	^{207}Pb/^{235}U age (Ma)	2 s error (Ma)	^{206}Pb/^{238}U age (Ma)	2 s error (Ma)	% discordance	^{238}U/^{206}Pb	2 s	^{207}Pb/^{206}Pb	2 s
Monazite	19BW1-5a-1	4595042	30	0.17953	0.00178	12.34225	0.26093	0.49860	0.00931	0.883	2649	16	2631	20	2608	40	1.6	2.006	0.037	0.180	0.002
	19BW1-5a-2	377496	25	0.18116	0.00182	13.19921	0.32237	0.52844	0.01176	0.911	2663	17	2694	23	2735	49	-2.6	1.892	0.042	0.181	0.002
	19BW1-5a-3	254081	3	0.18063	0.00181	12.81211	0.29585	0.51443	0.01071	0.901	2659	16	2666	22	2676	45	-0.6	1.944	0.040	0.181	0.002
	19BW1-5b-1	108302	1	0.17724	0.00217	12.52088	0.36702	0.51236	0.01364	0.908	2627	20	2644	27	2667	58	-1.5	1.952	0.052	0.177	0.002
	19BW1-5c-1	2929488	1	0.17960	0.00179	12.78475	0.27209	0.51627	0.00971	0.884	2649	16	2664	20	2683	41	-1.3	1.937	0.036	0.180	0.002
	19BW1-5c-2	59504	2	0.18004	0.00208	11.40505	0.27035	0.45944	0.00951	0.873	2653	19	2557	22	2437	42	8.9	2.177	0.045	0.180	0.002
	19BW1-5c-3	1974232	0	0.17978	0.00179	12.73983	0.27843	0.51394	0.01000	0.890	2651	16	2661	20	2673	42	-0.8	1.946	0.038	0.180	0.002
	19BW1-5d-1	3707921	3	0.17886	0.00177	11.99382	0.25178	0.48636	0.00901	0.882	2642	16	2604	19	2555	39	3.4	2.056	0.038	0.179	0.002
	19BW1-5d-2	4547475	25	0.17889	0.00177	12.17254	0.25655	0.49350	0.00919	0.883	2643	16	2618	20	2586	40	2.2	2.026	0.038	0.179	0.002
	19BW1-5e-1*	1279436	5	0.17639	0.00176	11.96727	0.27427	0.49206	0.01015	0.900	2619	17	2602	21	2580	44	1.5	2.032	0.042	0.176	0.002
	19BW1-5c-2*	319177	0	0.16673	0.00197	9.65477	0.50309	0.41998	0.02131	0.974	2525	20	2402	47	2260	96	11.7	2.381	0.121	0.167	0.002
	19BW1-5e-3*	1729278	1	0.17548	0.00176	12.14463	0.27113	0.50193	0.01002	0.894	2611	17	2616	21	2622	43	-0.4	1.992	0.040	0.175	0.002
	19BW1-5f-1	2674815	1	0.17943	0.00177	12.72120	0.29157	0.51419	0.01063	0.902	2648	16	2659	21	2675	45	-1.0	1.945	0.040	0.179	0.002
	19BW1-5f-2	2605031	2	0.17853	0.00181	12.60107	0.29851	0.51192	0.01096	0.904	2639	17	2650	22	2665	47	-1.0	1.953	0.042	0.179	0.002
	19BW1-5f-3	842844	9	0.17945	0.00179	11.88989	0.51178	0.48053	0.02012	0.973	2648	16	2596	40	2530	87	4.7	2.081	0.087	0.179	0.002
	19Bw1-6a-1	887905	0	0.18032	0.00181	12.35016	0.30250	0.49674	0.01110	0.912	2656	17	2631	23	2600	48	2.2	2.013	0.045	0.180	0.002
	19Bw1-6a-2	655394	0	0.18107	0.00184	12.72803	0.28360	0.50981	0.01011	0.890	2663	17	2660	21	2656	43	0.3	1.962	0.039	0.181	0.002
	19Bw1-6a-3	1101829	0	0.18018	0.00179	12.92142	0.30321	0.52013	0.01106	0.906	2654	16	2674	22	2700	47	-1.7	1.923	0.041	0.180	0.002
	19Bw1-6a-4	2144760	1	0.17999	0.00178	12.67833	0.29043	0.51088	0.01055	0.901	2653	16	2656	21	2660	45	-0.3	1.957	0.040	0.180	0.002
	19Bw1-6a-5	1453358	2	0.17783	0.00177	12.58982	0.26903	0.51348	0.00971	0.885	2633	16	2649	20	2671	41	-1.5	1.947	0.037	0.178	0.002
	19Bw1-7a-1	4978109	510	0.18034	0.00178	13.93758	0.30249	0.56054	0.01083	0.890	2656	16	2745	20	2869	45	-7.4	1.784	0.034	0.180	0.002
	19Bw1-7a-2	2555274	31	0.17965	0.00180	12.76210	0.26614	0.51521	0.00943	0.877	2650	17	2662	19	2679	40	-1.1	1.941	0.036	0.180	0.002
	19Bw1-7a-3	3837758	1	0.17861	0.00177	12.52736	0.25985	0.50869	0.00928	0.879	2640	16	2645	19	2651	40	-0.4	1.966	0.036	0.179	0.002
	19Bw1-7a-4	5909555	13	0.17920	0.00177	12.61770	0.26822	0.51068	0.00961	0.885	2645	16	2652	20	2660	41	-0.5	1.958	0.037	0.179	0.002
	19Bw1-7a-5	3317236	2	0.18018	0.00178	12.62908	0.26334	0.50836	0.00933	0.881	2655	16	2652	19	2650	40	0.2	1.967	0.036	0.180	0.002
Cassiterite	19BW1-cas1a-1	25103	143	0.18231	0.00149	12.04779	0.34292	0.47928	0.01307	0.958	2674	13	2608	26	2524	57	5.9	2.086	0.057	0.182	0.001
	19BW1-cas1a-2	18978	147	0.18300	0.00164	12.19420	0.32960	0.48329	0.01233	0.944	2680	15	2619	25	2542	53	5.5	2.069	0.053	0.183	0.002
	19BW1-cas1a-3*	213954	298	0.12870	0.00085	7.34411	0.16396	0.41387	0.00882	0.955	2080	12	2154	20	2233	40	-6.8	2.416	0.052	0.129	0.001
	19BW1-cas1b-1*	5305	86	0.18345	0.00271	10.48390	0.74715	0.41447	0.02890	0.978	2684	24	2478	64	2235	130	20.1	2.413	0.168	0.183	0.003
	19BW1-cas1b-2	4537	106	0.18654	0.00294	13.51476	0.95617	0.52545	0.03624	0.975	2712	26	2716	65	2722	151	-0.4	1.903	0.131	0.187	0.003
	19BW1-cas1b-3*	31065	128	0.10816	0.00098	4.07295	0.10287	0.27312	0.00644	0.933	1769	16	1649	20	1557	33	13.6	3.661	0.086	0.108	0.001
	19BW1-cas1b-4	7679	131	0.18339	0.00205	12.72642	0.66963	0.50330	0.02588	0.977	2684	18	2660	48	2628	110	2.1	1.987	0.102	0.183	0.002
	19BW1-cas2a-1	13735	115	0.18233	0.00173	12.46628	0.43365	0.49587	0.01659	0.962	2674	16	2640	32	2596	71	3.0	2.017	0.067	0.182	0.002
	19BW1-cas2a-2*	573864	672	0.16124	0.00100	12.16614	0.32094	0.54724	0.01403	0.972	2469	10	2617	24	2814	58	-12.3	1.827	0.047	0.161	0.001
	19BW1-cas2a-3	8617	115	0.18111	0.00218	11.97257	0.60551	0.47945	0.02355	0.971	2663	20	2602	46	2525	102	5.5	2.086	0.102	0.181	0.002
	19BW1-cas2a-4*	286347	368	0.15658	0.00100	12.05932	0.26543	0.55859	0.01176	0.957	2419	11	2609	20	2861	48	-15.4	1.790	0.038	0.157	0.001
	19BW1-cas3a-1	17765	126	0.18533	0.00234	12.22099	0.38509	0.47826	0.01381	0.916	2701	21	2622	29	2520	60	7.2	2.091	0.060	0.185	0.002
	19BW1-cas3a-2*	24984	119	0.18948	0.00315	12.48072	0.47393	0.47773	0.01631	0.899	2738	27	2641	35	2517	71	8.7	2.093	0.071	0.189	0.003
	19BW1-cas3a-3*	24081	136	0.16645	0.00399	9.55579	0.49366	0.41636	0.01906	0.886	2522	40	2393	46	2244	86	12.4	2.402	0.110	0.166	0.004
	19BW1-cas3a-4*	50064	146	0.13904	0.00133	4.82954	0.11389	0.25192	0.00543	0.915	2215	16	1790	20	1448	28	53.0	3.970	0.086	0.139	0.001
	19BW1-cas3a-5*	21711	205	0.23261	0.00379	16.86875	0.54941	0.52595	0.01484	0.866	3070	26	2927	31	2724	62	12.7	1.901	0.054	0.233	0.004
	19BW1-cas4a-1*	21950	136	0.17719	0.00324	11.94499	0.36879	0.48892	0.01215	0.805	2627	30	2600	29	2566	52	2.4	2.045	0.051	0.177	0.003
	19BW1-cas4a-2	29531	119	0.18234	0.00160	12.09090	0.30490	0.48092	0.01137	0.938	2674	14	2611	23	2531	49	5.6	2.079	0.049	0.182	0.002
	19BW1-cas4a-3	35721	114	0.18169	0.00134	11.94208	0.28405	0.47670	0.01078	0.951	2668	12	2600	22	2513	47	6.2	2.098	0.047	0.182	0.001
	19BW1-cas4a-4	26270	112	0.18253	0.00148	12.23873	0.32894	0.48631	0.01246	0.954	2676	13	2623	25	2555	54	4.7	2.056	0.053	0.183	0.001
	19BW1-cas4a-5*	29807	172	0.18184	0.00162	2.91492	0.90154	0.11626	0.03594	1.000	2670	15	1386	210	709	204	276.5	8.601	2.659	0.182	0.002
	19BW1-cas4a-6	18336	148	0.18254	0.00166	12.34261	0.33946	0.49038	0.01273	0.944	2676	15	2631	26	2572	55	4.0	2.039	0.053	0.183	0.002
	19BW1-cas4a-7	15062	148	0.18234	0.00160	11.97984	0.39400	0.47651	0.01511	0.964	2674	14	2603	30	2512	66	6.5	2.099	0.067	0.182	0.002